UNIVERSITÉ DE STRASBOURG

ÉCOLE DOCTORALE MATHEMATIQUES, SCIENCES DE L'INFORMATION ET DE L'INGÉNIEUR

Laboratoire des sciences de l'Ingénieur, de l'Informatique et de l'Imagerie (ICube) - Institut pour l'ingénierie Médicale et l'informatique Médicale (IM2)

THÈSE présentée par:

Duc-Vinh NGUYEN

Soutenue le : 16/12/2020

Pour obtenir le grade de: **Docteur de l'université de Strasbourg**
Discipline/ Spécialité: **Micro-électronique**

Sonde portable de spectroscopie par résonance magnétique nucléaire

---

Rapporteur externe :	Marie Poirier-Quinot	*Professeure (Univ. Paris-Saclay)*
Rapporteur externe :	Stéphane Serfaty	*Professeur (Univ. Cergy-Pontoise)*
Examinateur :	Gilles Jacquemod	*Professeur (Polytech'Nice Sophia)*
Examinateur :	Joris Pascal	*Professeur (FHNW – Muttenz, Suisse)*
Examinateur :	Latifa Fakri-Bouchet	*Maître de Conférences (Univ. Lyon 1)*
Examinateur :	Norbert Dumas	*Maître de conférences (Univ. De Strasbourg)*
Co-directeur de thèse :	Wilfried Uhring	*Professeur (Univ. de Strasbourg)*
Directeur de thèse :	Luc Hébrard	*Professeur (Univ. De Strasbourg)*

UNIVERSITY OF STRASBOURG

DOCTORAL SCHOOL OF MATHEMATICS, INFORMATION SCIENCES AND ENGINEERING

Laboratory of engineering science, computer science and imaging (ICube) - Institute for Medical Engineering and Medical Informatics (IM2)

PhD Thesis by:

Duc-Vinh NGUYEN

Defended on : 16/12/2020

To obtain the degree: **PhD, Doctor of University of Strasbourg**
Discipline/ Specialty: **Micro-electronics**

Portable Nuclear Magnetic Resonance Spectroscopy Probe

Referee :	Marie Poirier-Quinot	*Professor (Univ. Paris-Saclay)*
Referee :	Stéphane Serfaty	*Professor (Univ. Cergy-Pontoise)*
Inspector :	Gilles Jacquemod	*Professor (Polytech'Nice Sophia)*
Inspector :	Joris Pascal	*Professor (FHNW – Muttenz, Suisse)*
Inspector :	Latifa Fakri-Bouchet	*Associate Professor (Univ. Lyon 1)*
Inspector :	Norbert Dumas	*Associate Professor (Univ. De Strasbourg)*
Thesis co-director :	Wilfried Uhring	*Professor (Univ. de Strasbourg)*
Thesis Director :	Luc Hébrard	*Professor (Univ. De Strasbourg)*

Contents

Acknowledgement

Chapter 1

Introduction and context

1   Environmental and sanitary issues

World population growth and human activity are driving many environmental changes. Recent global awareness for a better environmental balance has led to the development of ecological processes in several areas to ensure the human society sustainability. Air, soil and water pollution are leading to a sharp increase in health concerns. The World Health Organization estimates that only one person out of ten lives in a place where air is at a considered safe level. Air pollution kills 6.5 million people every year. Deaths related to the respiratory tract are among the top 10 causes of death. Soil pollution, caused by rainfall (fallout from air pollution) and the use of biocidal plant protection products, raises health concerns as the chemicals found in the soil could potentially finish in foods and drinking water. Moreover, in addition to these biocidal products, medicinal products are also found in drinking water, being discharged into the wastewater circuit by urines. Water treatment method being not always very efficient, or simply not implemented, the medicinal residues are then ingested by the population [1, 2]. This "cocktail" causes health problems, genetic mutations and behavioural changes are strongly observed in the animal environment subject to this pollution [3]. Numerous efforts are being made to develop water purification techniques [4], as well as detection systems to control the water quality. In 2000 the World Health Organization (WHO) estimated that 4.6% of deaths worldwide are due to a lack of hygiene and poor water quality [5, 6, 7]. In addition, according to the United Nations (UN), we are observing an increase in natural disasters, leading to significant health hazards for developing countries. Unrestrained urban growth and density are one of the reasons these countries are exposed to bigger concerns and higher risks such as flooding and fire. Furthermore, victims often have restricted access to utility services and public healthcare which encourages the spread of diseases throughout communities already fragile. Further efforts must be made to increase the environmental quality of those areas, and also to obtain rapid tests that can be easily and cheaply deployed so that everyone can have access to a health diagnosis and thus combat medical desertification.

2   Nuclear Magnetic Resonance application fields

Nuclear Magnetic Resonance (NMR) is a powerful tool for the detection of chemical elements. It allows determining precisely the composition of a sample, and is the benchmark tool in several fields requiring a thorough knowledge of the sample under observation. Table 1.1 presents some possible applications of NMR. From the pharmaceutical industry, through the environment, to health and food control, each of these fields is increasingly using NMR spectrometers to test their products. Aside from the "Tesla hunting" for ever more powerful spectrometers to push the limits of chemical detection, these systems follow the miniaturization trend that has always been observed in the electronic and instrumental world. Such miniaturization helps reducing the cost of NMR systems considerably. These fields do not necessarily need a tiny limit of detection, but a system adapted to their needs. Pharmaceutical companies aim to control the purity of their drugs, but also to be able, during the design phase, to test molecules in a very short time and thus make multiple combinations with a higher sensitivity than what they currently use. NMR spectrometry can replace in a unique tool many possible alternative techniques for testing, identification and analysis, and thus allows improving the production lines by a continuous analysis, i.e. switching from a batch production system to a continuous production system (often impossible in biotechnology production) [8, 9].

Concerning health stakes, health is certainly the field where NMR systems are developing the most. It is possible to carry out in-vivo monitoring, which consists in following the evolution of diseases in real time to better understand their development. The use of laboratory animals genetically modified (e.g. rat) in which known human diseases are instilled, can be used to observe brain metabolites and follow, for example, the evolution of Alzheimer's disease while the animal is still alive [10]. This avoids the current morbidity of stage analyses when using biopsy, i.e. taking a piece of tissue from each stage of the disease that one wishes to observe, and then analysing it. Biopsy method requires larger number of animals to be sacrificed (one per observation stage) and also represents a significant cost, whereas, in-vivo exploration allows only one animal to be used for the duration of the experiment while having real-time observation of the disease development. Besides, the death and biopsy of the animal may affect the observable elements, hence, in-vivo techniques are preferable. Another example of an application in health care is the detection of cancer, which is also developing rapidly. Thanks to the avidin protein, for example, it becomes possible to detect the presence of cancer cells [11]. It is also possible to observe the different chemical elements contained in blood and to diagnose diseases such as Lyme disease or anaemia. Another project such as the non-invasive method of detecting glucose through the skin using NMR is still ahead of us but it seems achievable [12, 13]. Thus, NMR, with the development of portable and rapid screening tools will allow a faster and more efficient management in the diagnostic of patients (also called "Point of Care diagnosis") with a lower cost, thus fighting against the saturation of health facilities and medical deserts.

The NMR analysis of food is also very recent. Honey and Wine quality control are two examples that are grabbing more attention [14]. Indeed, the possibility of obtaining rapid results on the

origin, composition and purity by harvesting only a very small sample, is of interest for many food industries to guaranty the quality of their products.

Due to the contemporary ecological stakes, another recent facet of NMR use is the environmental field. Nuclear Magnetic Resonance should allow the detection of pollutants in water coming from phytosanitary products that contaminate drinking water. It is also the case of dialysis, where it could be possible to observe the discharged water. This Ph.D. work brings its contributions in this field by exploring the possibility to design a portable NMR spectrometer for detection of pollutants in water.

	Type	Applications	Existing techniques	Existing portable NMR ?	References
Pharmaceutics	Pharmaceutical industry	Identification of molecules, determination of purity...	Chromatography, Mass Spectrometry, NMR...	Yes	[15, 8, 16, 17, 18]
Health	In-vivo monitoring	Evolution of diseases	Biopsy, animal experimentation	No	[10, 19, 20, 21]
	Detection of biomarkers	Detection of cancer markers and pathogens (S Aureus, E. Faecalis...)	Laboratory analysis (ELISA test, Scanning Electron Microscopy...)	Yes	[22, 23, 11, 24, 25, 26, 27]
	Blood tests	Non-invasive glucose detection, anemia, methemoglobin...	Skin puncturing (glucose), Laboratory analysis	Yes	[28, 26]
Food Industries	Quality/ composition	Composition: Allergens, proteins, sugar...	Conventional chemical processes, or NMR spectroscopy	Yes	[23, 29, 30]
	Traceability	Provenance			
	Security	Contamination, fraud...			
Environment	Pollutant detection	Detection of glyphosate, drug residues, dialysis rejects...	Conventional chemical processes	No	[26]

Table 1.1: Possible uses of the NMR (Not exhaustive).

Finally, we may also cite some niche fields, like history and art, where NMR spectrometers may be useful to determine the composition of old paintings, or the origin of different materials [31].

3   Pollutants detection

We saw the different possibilities of NMR uses and we presented the issues to be addressed in the context of global health as well as towards an ecological transition. Our work is part of this latter area. Indeed, we aim to design a system capable of detecting the presence of pollutants in water using NMR spectroscopy since it seems a versatile and powerful tool.

The European directive 2008/105/EC of the European parliaments and European Council established the water quality standard for human health. A watch list resulting from it includes 63-priority chemical compounds. However, it remains difficult to obtain high requirements as it is difficult to get a substantial amount of decent quantitative measures. Quality control of water is made from accredited laboratories directly from water sources and distribution networks. Nevertheless, the low control frequency, which is directly related to the water catchment area and the population size, leads to serious health risks. Consequently, accidental spills of pesticide cannot be detected in time. In France, it is estimated that 680 000 individuals consumed in 2013 untested water [32]. Albeit, the water quality in west Europe tends to be satisfactory, some events have affected the population. In 2014 in France, 100 000 people were affected by non-conformity situations. More recently, at the time of writing, in Switzerland in February 2020, banned pesticides have been found in drinking water in 12 cantons [33]. As the population increases and the future safety requirements tighten, the need for cheapest, better performing, ever-rising water pollutants sensors strengthen.

Commercial devices detecting water pollution are already available. Continuous measures of temperature, pH, conductivity, or turbidity on water grid are carried out. However, concerning measures of the chemical compounds, i.e. the main potential pollutants traces, the different measurement methods that have been published and demonstrated involve bulky equipment (mass spectroscopy) or a regulated environment (biosensors), which uses expensive consumables. ICube laboratory (University of Strasbourg, France), in collaboration with the Institute for Medical Engineering and Medical Informatics (IM2 - University of Applied Sciences – FHNW, Muttenz, Switzerland), the BSC laboratory (University of Strasbourg, France), the Institute for microsystems techniques (University of Applied Sciences – HFU, Furtwangen, Germany), the IMTEK laboratory (University of Friburg, Germany), and the Department of Chemistry of the Technical university of Kaiserlautern (Germany) are investigating an alternative that can be easily generalized to different pollutants, small enough for field study and affordable for large-scale deployment to monitor water pollution in real time and to prevent risk. All those points make NMR a perfect candidate to be economically viable. With the development of the internet of things, it can also lead to a massive collection of data and analysis to create new health standard in hormone

disruptors.

This PhD work, which was performed during its three first years at ICube, and for its last year at IM2, is partly at the genesis of this new pollutants probe project, and provides a pre-study on the possibility of detecting water pollutants through portable NMR spectrometry. The water pollutants probe focuses on highly disturbing pollutants, i.e. the glyphosate, which is sold as a broad spectrum herbicide and is highly controversial, as well as the atrazine, the second most widely use herbicide after glyphosate in 2014 (in the USA). In Europe, researches have been carried out on this herbicide and it seems to be the factor of health trouble for small animals since it provokes mutagenic reactions and health malfunctions. In some countries such as France, atrazine is prohibited, but residues are still present. The acceptable pollutants concentrations limits are very low to ensure safe consumption. It is why before detection through NMR spectrometry, pollutants have to be concentrated. This concentration will be done through molecular imprinted polymer where water flows through a selective polymer that traps a specific pollutant. Then, an eluent, i.e. the acetonitrile, is used to flush the polymer, and extract the highly concentrated pollutants that will be analyzed through NMR spectrometry (see figure 1.1).
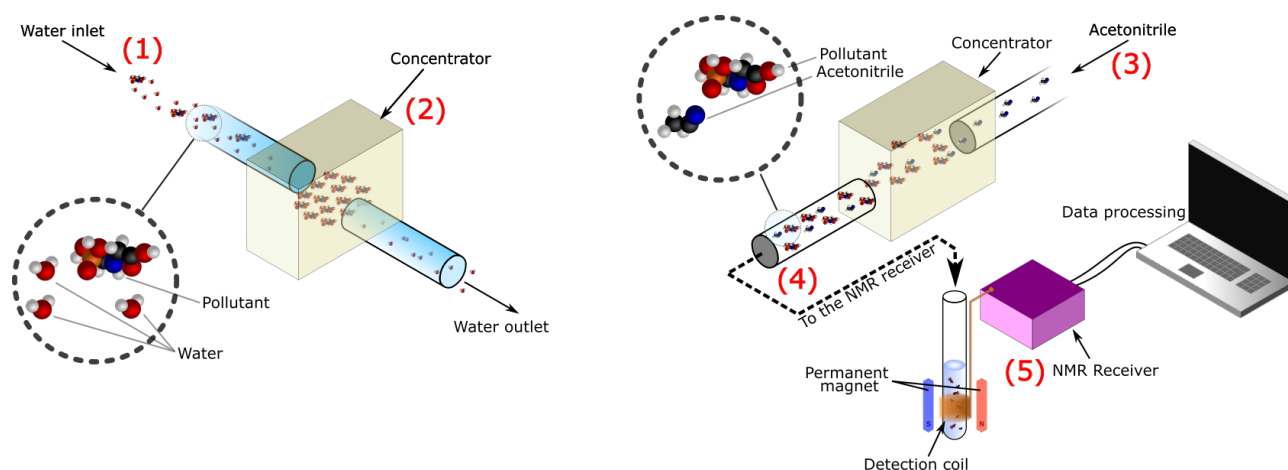
Figure 1.1: Shematic principle of the complete pollutants NMR probe, (1) drinking water is collected from the grid (2) pollutants are concentrated with a polymer cartridge, (3) acetonitrile is used to release the trapped pollutant from the polymer, (4) the highly concentrated pollutants solution is sent to the portable NMR spectrometer, (5) the solution is analyzed through NMR spectrometry.

4   State of the art of portable NMR systems

NMR spectrometer used in laboratories and industries are designed for samples requiring high sensitivity and temperature stability. Such systems are most of the time helium-cooled and have several cabinets for regulation, control, power, requiring extra space. These NMR spectrometers are thus bulky, and fixed, and cannot be moved without appropriate means. They are generally higher than $800000\$US$ but they provide the best resolution. Typically they occupy a whole dedicated room (Height of 2m for the example on figure 1.2).

Figure 1.2: Specialized helium-cooled spectrometer for food from Brucker.

Benchtop NMR spectrometers are usually small sized (Height: 40cm for the Magritek in figure 1.3). Due to their weight (60Kg) they are also movable if necessary. Their detection limit is suitable for many applications. However, their cost, around $100000\$US$, as well as their size, do not allow a wide deployment of such NMR spectrometers, as required in our applications, where the portable NMR spectrometer is expected to be deployed in many water stations.

Figure 1.3: 60MHz Magritek Spectrometer.

Portable NMR devices are recent systems that have not been commercialized yet for most of them, and that are mainly found in research. In spite of their interesting characteristics we have to take into account that the analysis time may be very long. Indeed, to compensate for the lack of signal-to-noise ratio, it is interesting to average several measurements. This is the case of the Mini NMR shown on figure 1.4, which can have a measurement time up to one hour [34]. The Mini NMR was created for the detection of bacteria as the avidin protein to monitor cancerous cells. It is around 20x20x20cm3, and its cost is estimated between $300\$US$ and $2000\$US$. However, it is not available on the market yet.
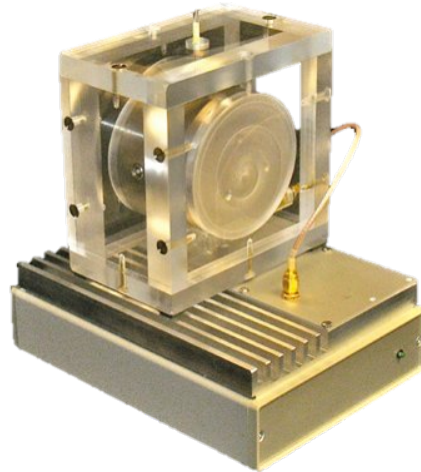
Figure 1.4: "Mini-NMR" NMR relaxometer [34].

Over the last twenty years, different portable NMR relaxometers or NMR spectrometers (see section 2.2 of chapter 2 for the difference between relaxometry and spectroscopy) have been proposed in the scientific literature. Table 1.2 provides, to our knowledge, an exhaustive list of these research devices with their main characteristics defined as:

- Frequency: This column corresponds to the Larmor frequency of use of the system, noting that above 34MHz it is highly likely that the system uses a magnetic field from an MRI scanner.

- Rx Antenna: If the system has a receiving antenna or not, it may be discrete.

- Technology: The technology used to design the system.

- Tx Antenna: The presence or absence (or single-antenna system i.e. same as "Rx") of a transmitting antenna. In the case where there is no transmitting antenna, this means that the system requires an external antenna to be connected.

- Antenna type: If the antenna is volumetric (typically solenoidal, but can also be a birdcage, horse saddle etc).

- Shape: The shape of the antenna.

- Connection: The connection between the antenna and the system.

- Type: If the coil is integrated directly into the system or if it is external

- Designer: Designer and System Reference

- Year: Year of system publication

Frequency	Rx Antenna	Technology	Tx Antenna	Antenna type	Shape	Connection	Type	Designer	Year
360 MHz		GaAs FET	no	Volumetric	Solenoidal	Wire bonding	non-Integrated	MacFarland [35]	1992
300 MHz		GaAs FET	no	Surface	square	Wire bonding	Integrated	Stocker [36]	1995
85 MHz	Yes	0.7 µm CMOS	no	Surface	round	Wire bonding	Integrated	Boero [37]	1998
300 MHz	Yes	0.5µm CMOS	Yes	Surface	square	Integrated	Integrated	Boreo [38]	2001
-	-	FPGA	-	-	-	-	discrete	Dalal [39]	2006
500 MHz	Yes	0.18µm CMOS	Yes	-	-	-	Integrated	Fan [40]	2007
21 MHz	Yes	0.18µm CMOS	Rx	Volumetric	Saddle	Wire bonding	Integrated	Liu [11]	2008
300 MHz	Yes	0.35µm CMOS	no	Surface	square	Integrated	Integrated	Anders [41]	2008
21 MHz	discrete	0.18µm CMOS	discrete	Surface	octogonal	Wire bonding	Integrated	Sun [42]	2009
34 MHz	discrete	0.12µm SiGe BiCMOS	discrete	-	-	Wire bonding	Integrated	Hassibi [43]	2009
300 MHz	Yes	0.35µm CMOS	discrete	Surface	square	Integrated	Integrated	Anders[44]	2009
21 MHz	Yes	0.18µm CMOS	Rx	Surface	-	Wire bonding	Integrated	Haun [22]	2010
86 MHz	discrete	0.13µm CMOS	no	-	-	Wire bonding	Integrated	Kim [19]	2010
300 MHz	Yes	0.13µm CMOS	no	Surface	square	Integrated	Integrated	Anders [45]	2010
21 MHz	Yes	-	Rx	Volumetric	Solenoidal	Wire bonding	Integrated	Haun [46]	2011
21 MHz	Yes	0.18µm CMOS	Rx	Surface	square	Integrated	Integrated	Sun [24]	2011
21 MHz	Yes	-	Rx	Volumetric	Solenoidal	Wire	discrete	Issadore [34]	2011
402 MHz	Yes	0.35µm CMOS	no	Volumetric	Solenoidal	Wire bonding	Integrated	Badilita [47]	2011
9 MHz	discrete	-	Rx	Surface	butterfly	Wire	discrete	Danieli [48]	2012
300 MHz	discrete	0.13µm CMOS	Rx	Volumetric	Solenoidal	Wire	Integrated	Kim [15]	2012
28 MHz	discrete	-	Rx	Surface	round	Wire bonding	discrete	Wu [49]	2013
300 MHz	Yes	0.13µm CMOS	discrete	Surface	square	Integrated	Integrated	Anders [50]	2013
21 MHz	discrete	0.18µm CMOS	no	Surface	round	Wire bonding	Integrated	Zhao [51]	2014
21 MHz	discrete	-	Rx	Surface	butterfly	Wire	discrete	Lei [52]	2014
22 MHz	discrete	0.18µm CMOS	Rx	Volumetric	Solenoidal	Wire bonding	Integrated	Dongwan [53]	2014
300 MHz	Yes	-	-	Surface	rectangulaire	-	Integrated	Trejo-Rosillo [54]	2014
21 MHz	discrete	0.13µm CMOS	Rx	Volumetric	Solenoidal	Wire bonding	Integrated	H. Pourmodheji [55]	2015
23 MHz	discrete	-	discrete	Volumetric	Solenoidal	-	discrete	Chen [56]	2015
300 MHz	Yes	0.13µm CMOS	no	Stacked	octogonal	Integrated	Integrated	H. Pourmodheji [57]	2015
300 MHz	Yes	0.13µm CMOS	Rx	Surface	octogonal	Integrated	Integrated	Grisi [25]	2015
20 MHz	Yes	0.18 µm CMOS	Rx	Surface	octogonal	Integrated	Integrated	Lei [58]	2016
20 MHz	discrete	0.18µm CMOS	Rx	Surface	butterfly	Wire bonding	Integrated	Lei [58]	2016
300 MHz	Yes	0.13µm CMOS	no	Stacked	octogonal	Integrated	Integrated	H. Pourmodheji [59]	2016
20 MHz	Yes	0.18 µm CMOS	Rx	Surface	octogonal	Integrated	Integrated	Lei [23]	2017
21 MHz	discrete	0.18 µm CMOS	Rx	Volumetric	Solenoidal	Wire bonding	Integrated	Dongwan [53]	2017
300 MHz	Yes	0.13µm CMOS	Rx	Surface	octogonal	Integrated	Integrated	Grisi [60]	2017
300 MHz	Yes	0.13µm CMOS	Rx	Surface	square	Integrated	Integrated	Handwerker [61]	2017
21 MHz	Yes	0.18 µm CMOS	Rx	-	-	-	Integrated	Hossein-Zadeh [62]	2018
6 MHz	discrete	-	Rx	Volumetric	Solenoidal	Wire	discrete	Louis-Joseph [63]	2019

Table 1.2: Listing of miniaturized NMR systems.

Some of these realizations, that we consider as the most representative, are now briefly discussed. In 2012, Kim and al. [15, 19] demonstrated a NMR spectrometer for drug discovery and development (figure 1.5 and 1.6). The system is designed to work from 0.5T to 5T. And has an input referred noise of $3.5nV/\sqrt{Hz}$. The channel has a total gain of 120dB. The coil is external (discrete) and has not been discussed in detail. Even if the system is designed to also work with permanent magnets, the system is currently not completely portable because the testing and validation has been done using the magnet of a 5T magnetic resonance imager (MRI) and no portable magnet has been developed nor used.
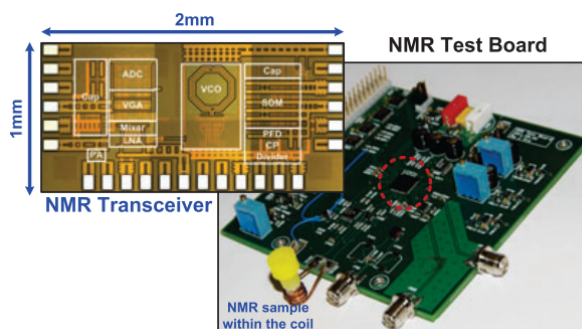

Figure 1.5: NMR system for drug discovery and development [15].
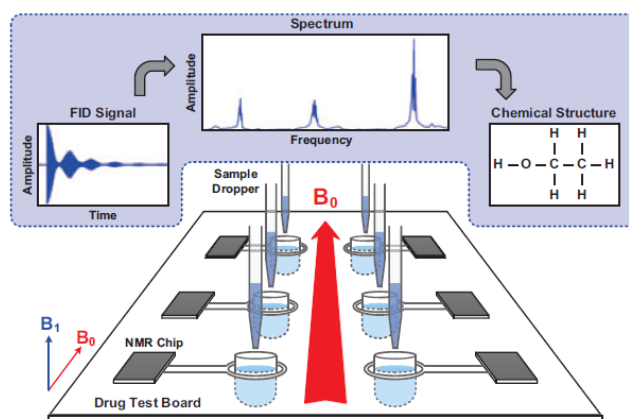

Figure 1.6: Schematic Diagram of the NMR Application System for Pharmaceuticals [15].

Almost all so-called portable NMR systems are used in health care for the detection of cancer cells. We list here the few NMR systems that have a proof of concept and have a specific purpose in this field.

In 2008, Liu designed a relaxometer based on the detection of avidin [11], like most of his successors. Acting as a link between the biotin and the magnetic particles added to the solution, avidin indicates whether cancer cells are present since the relaxation time is shorter in the latter case (figure 1.7 and 1.8). The coil is a planar coil on a glass substrate that was realized for this system. It uses a fist size permanent magnet of 0.5T from Metrolab®. The input referred noise of the channel is $2.5nV/\sqrt{Hz}$ but the channel amplification has not been reported.
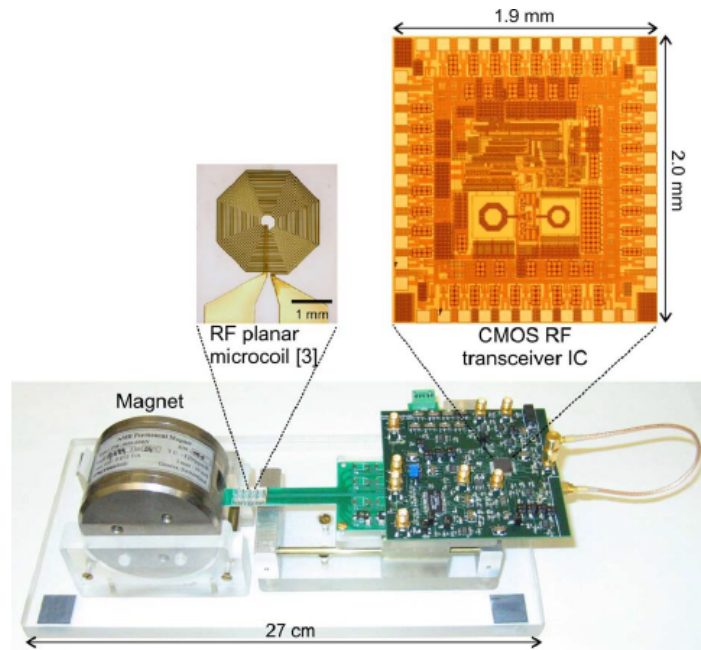
Figure 1.7: Relaxometer "CMOS mini-NMR" for the detection of cancer cells with avidin [11].
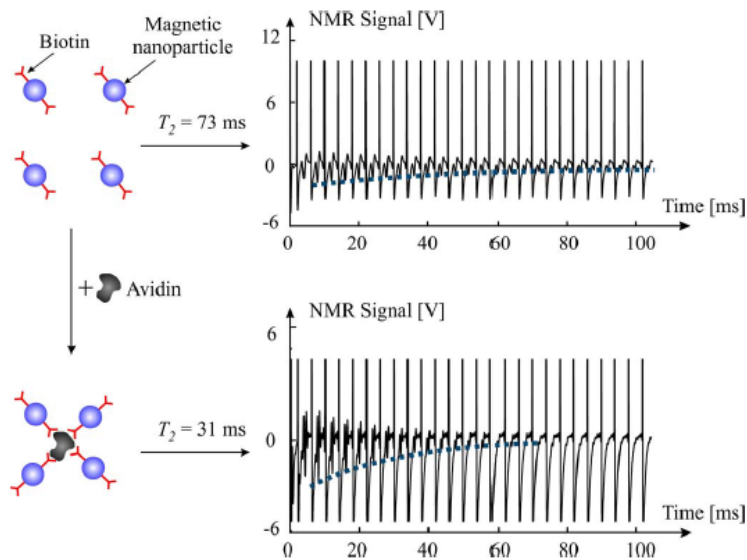
Figure 1.8: Relaxation differences in the absence or presence of avidin [11].

The DMR (Diagnostic Magnetic Resonance, figure 1.9) relaxometer designed in 2010 by Haun, allows one to test multiple solutions to detect enzymes and proteins (such as the Telomerase "hTERT"). The system is based on microfluific channels that bring the samples to be measured to planar microcoils. Thank to magnetic particles that bind to cells it allows one to observe the evolution of these biological elements. It can also detect the presence of numerous elements, small molecules (Folate, Glucose...) and organisms (Herpes Simplex Virus "HSV", adenovirusm S. Aureus...). As Liu (figure 1.7), the authors use the same magnet of 0.5T from Metrolab® and they also conceived a coil on a glass substrate.
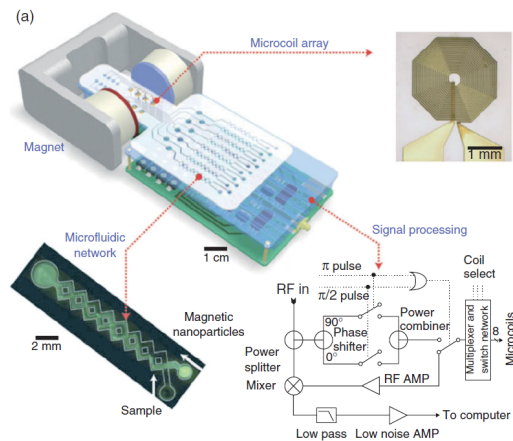
Figure 1.9: Micro-fluidic NMR relaxometer "DMR" for the detection of carcinogenic cells [22].

The "Palm Hand NMR" was designed by Sun in 2011 [24] uses also the 0.5T NMR magnet from Metrolab® but this time the surface coil is directly on chip, realized in a CMOS technology. The receiver input referred noise is $1.26nV/\sqrt{Hz}$. The relaxometer is focused on the rapid detection of carcinogenic cells and in particular those of kidney cancer (figure 1.10 and 1.11).
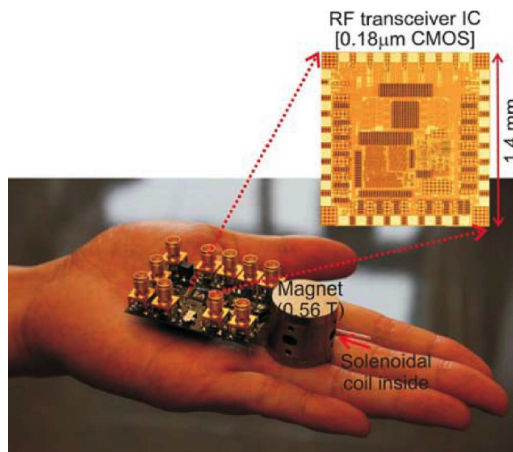
Figure 1.10: Relaxometer "Palm Hand NMR" for the detection of kidney cancer cells [24].
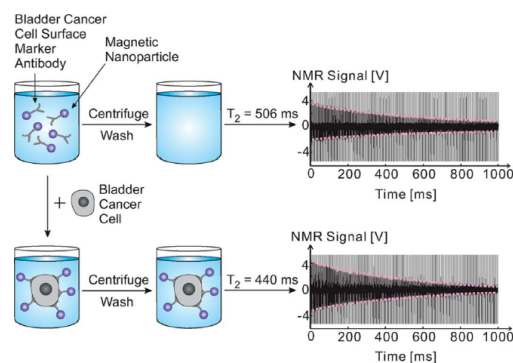
Figure 1.11: Detection of human liver-derived carcinogenic cells resulting in a shorter observed signal in the presence of carcinogenic cells [24].

The latest relaxometer designed by Lei in 2017, and shown on figure 1.12, is an improved

version resulting from his research, using again the Metrolab® magnet of 0.5T. The coil is also a planar coil made with CMOS lithographic process. The input referred noise reported is below $1nV/\sqrt{Hz}$. This relaxometer aims to detect several elements, including certain diseases such as methemoglobin, lyme disease etc.. through DNA or blood tests. It was also tested for cancer markers detection (S. Aureus, E. Faecalis pathogens for example).
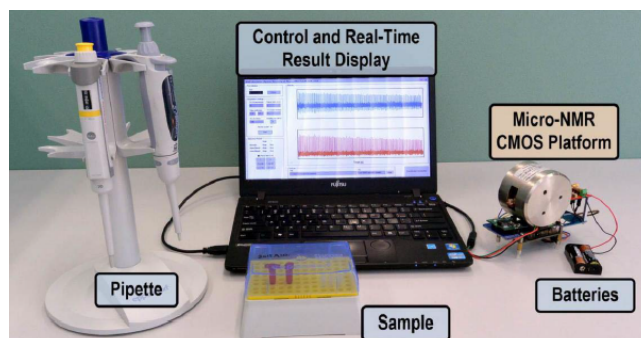
Figure 1.12: NMR relaxometer for biological and chemical detection (DNA & proteins) [23].

From this short state-of-the-art, we see that all NMR systems are intended to detect some cancer cells or specific chemical components through relaxometry (see section 2.2 of chapter 2 for the difference between relaxometry and spectrometry). As will be shown in this work, spectrometry is highly demanding in terms of system design, especially for the highly homogeneous magnet that is required to be able to separate the peaks of the NMR spectrum, as well as low-noise electronics in order to see the smallest peaks. This is certainly why all portable realizations that were published focused on relaxometry. Spectrometry has however the advantage of being able to detect easily several components from one measurement. So portable NMR may find very useful applications in all the application fields discussed above. It is the aim of this PhD work to highlight the main challenges to face, and to provide some possible solutions, especially for the receiver electronics.

$$*$$
$$* \quad *$$

Summary

This chapter has presented the context and the objective of this PhD work, which is to assess the possibility of designing a NMR portable probe for water pollutants detection. The global architecture of the pollutants detection system was presented, followed by a state-of-the-art of portable systems already published in the literature. Most of them are focused on medical applications, and are relaxometers instead of spectrometers. However, from these realizations, we may expect that a portable spectrometer is achievable.

Chapter 2

The Nuclear magnetic resonance

The notion of spin was first introduced by *Wolfgang Pauli* in 1924. In 1938 *Isidor Isaac Rabi* described, and measured the Nuclear Magnetic Resonance (NMR) by extending the Stern–Gerlach experiment that demonstrates the spatial orientation of angular momentum to be quantized. *Felix Bloch*, and *Edward Purcell* improved this technique to use it on liquid, and solid in 1946, and modelled it in what is called the *Bloch-Torrey equations*. This was the foundation of Nuclear Magnetic Resonance. In the following years improvement were added. The use of echo sequences (Erwin Hahn, 1950), and the Fourier transformation (Richard Ernst, 1966) to analyze the NMR signal, are two fundamental improvements that permit the actual use of NMR technology in many fields, allowing to observe different compounds in a sample. Thus, since 1970 fields like oil industry, pharmaceutical, etc. used the NMR techniques for quantitative measurement. The first use of NMR in medicine was by Raymond Damadian in 1974. This led to the Magnetic Resonance Imaging (MRI) development, but we will not discuss MRI in this manuscript since we are interested in detecting compounds in a liquid sample, and not in imaging. The figure 2.1 summarizes the main steps in NMR history.
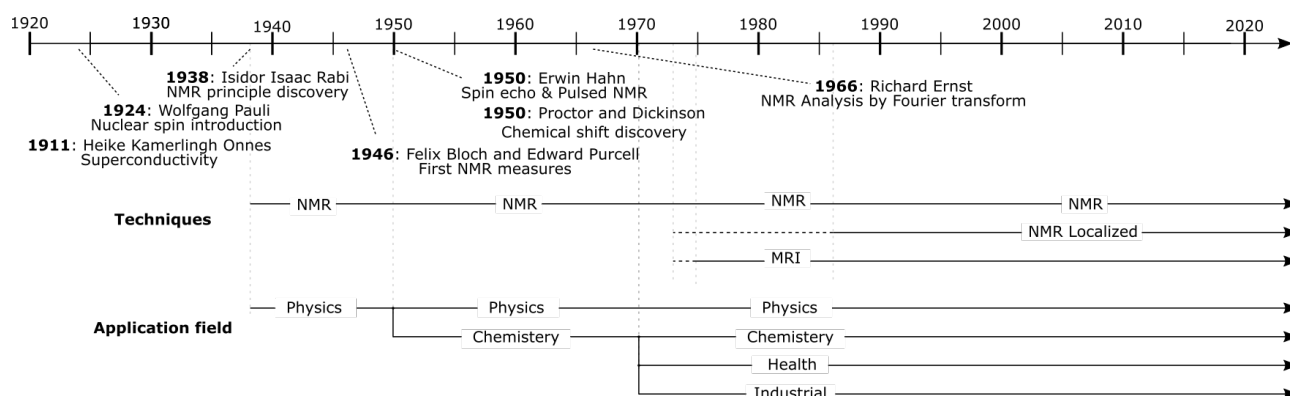

Figure 2.1: General History of the foundation of Nuclear Magnetic Resonance field.

1 Material-magnetic field interaction

1.1 Angular momentum, and magnetic moment

Pauli introduced the notion of spin as an intrinsic angular momentum of the elementary particles, i.e. the elementary particles would undergo a rotational motion on themselves.

Fermions (Quarks, and Leptons) are elementary particles (i.e. particle without sub-particles) that feature a spin. Thus we can define the spin of an electron, one of the six Leptons, as $\vec{s_e}$. The same way protons, and neutrons, which are composed of Quarks having different charges q, also possess a spin (figure 2.2). Neutrons, and protons possess a spin, $\vec{s_n}$, and $\vec{s_p}$ respectively, that are the sum of all angular momentums of the quarks that compose them.

The magnetic moment μ_e, μ_n, and μ_p of the electron, neutron, and proton respectively, is linked to the *intrinsic angular momentum* of the particule by the gyromagnetic ratio γ. This ratio can be seen as a quantitative measure of the "magnetic force" of the particle. It is defined as:

$$\vec{\mu_x} = \gamma \cdot \vec{s_x} = \gamma \cdot \hbar \cdot \sqrt{s(s+1)} \cdot \vec{u_x} \tag{2.1}$$

where $\vec{u_x}$ is a unitary vector in the direction of $\vec{\mu_x}$
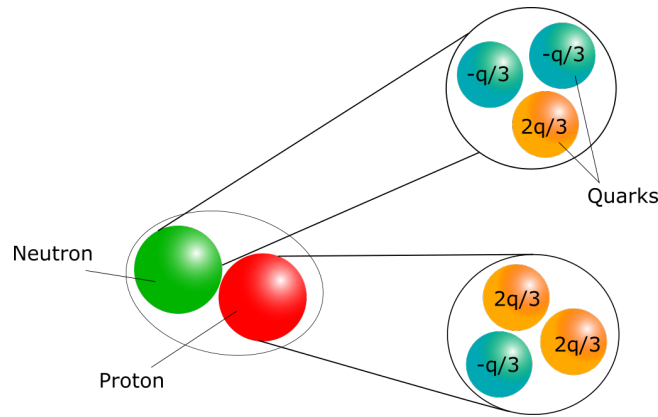
Figure 2.2: Protons, and neutrons nucleus composed of quarks. It is what produces the nuclear angular momentum.

In the previous equation $\hbar = h/2\pi$, where $h = 6.626\,070\,04 \times 10^{-34}\,\mathrm{m^2\,kg\,s^{-1}}$ is the Planck constant, and s corresponds to the quantum spin number. This number differs according to the particle. It can take different values such as : $s = 0, \frac{1}{2}, \frac{3}{2}, 2...$

At the nucleus level (shown on figure 2.3) all sub-particle spins sum up to form the *nuclear angular momentum*

$$\vec{S}_N = \sum_{\substack{neutron \\ proton}} \vec{s} \tag{2.2}$$

leading to the *nuclear magnetic moment* :

$$\vec{\mu}_N = \gamma.\vec{S}_N \tag{2.3}$$

The sum of all electron spin angular momentums in orbit gives $\vec{S}_e = \sum_{electron} \vec{s}_e$. In addition, the electrons movement around the nucleus gives rise to an *orbital angular momentum*, noted $\vec{L}$. The spin angular momentum $\vec{S}_e$ sums up with the orbital angular momentum $\vec{L}$, and gives the total angular momentum $\vec{J}$ of the electrons (figure 2.3).

$$\vec{J} = \vec{L} + \vec{S}_e \tag{2.4}$$
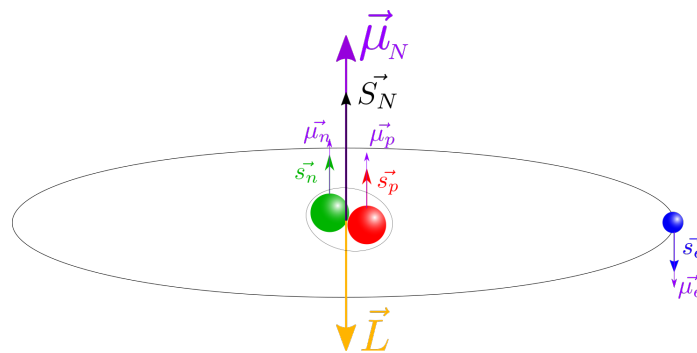
Figure 2.3: Nomenclature of atomic moments on a planetary model of the atom.

1.2 Magnetic moment quantification

The notion of spin by Wolfgang Pauli made possible to interpret the strange effect of spectral multiplets observed by the Irish physicist *Thomas Preston* in 1897, during his experiments based on the work of Pieter Zeeman a few years earlier on the effect of magnetic fields on the frequency of light. He was expecting to see two or three lines in accordance with Lorentz's theory. But Thomas Preston observed up to six lines. He called this strange effect the "Anomalous Zeeman Effect" as the spin was yet to be discovered. Several years later, with the discovery of the spin, and the Pauli exclusion principle (quantum mechanical principle expressing that two fermions cannot occupy the same quantum state simultaneously, stated in 1925), it was possible to explain what Preston noticed almost 30 years before.

Anomalous Zeeman effect

The quantum state of a particle outside a magnetic field is said degenerated, i.e. we can find several distinct quantum states at the same energy level. In other terms, an element (particle, nucleus, molecule) with an angular momentum of $\vec{s}$, and a spin number s have $2s + 1$ possible quantum states (also called multiplicity, from the Hund's first rule). With the application of a magnetic field B_0 there is a lifting of degeneracy, separating the values of available energies into several levels, corresponding to the numbers of quantum states (Figure 2.4). This is at the origin

of the anomalous Zeeman effect which appears when the total spin is non-zero.

In NMR we mostly use the proton isotope protium $^1_1$H, thus calling it *Proton NMR*. For the protium the spin number is $s = 1/2$, therefore the number of potential states for this nucleus is $2s + 1 = 2$. Moreover, as s is non-zero, a nuclear magnetic moment $\vec{\mu}$ exists, and under a magnetic field it creates a torque $\vec{\tau} = \vec{\mu} \wedge \vec{B_0}$ which modifies the energy state of the protium by $E = \pm\vec{\mu}.\vec{B_0}$ depending on the quantum state α or β (figure 2.4):

$$E_\alpha = -\frac{1}{2}.\hbar.\gamma.B_0 \tag{2.5}$$

$$E_\beta = +\frac{1}{2}.\hbar.\gamma.B_0 \tag{2.6}$$

Under such a torque, the nucleus undergoes a precession around the axis of the magnetic field. It is the same principle as a spinning top subjected to the gravitational field.
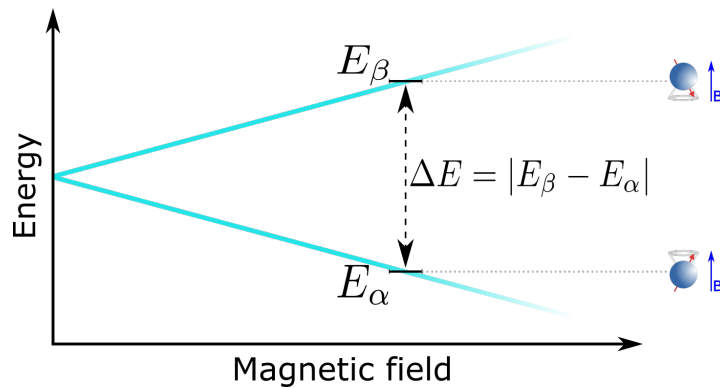
Figure 2.4: Separation of energy levels for a spin 1/2 against the magnetic field. The possible quantum states are noted α, and β.

A nucleus at the energy level E_α can switch to the energy level E_β if it absorbs an energy corresponding to the potential barrier height:

$$\Delta E = \gamma.\hbar.B_0 \tag{2.7}$$

Since the atomic nucleus can only have two different levels of energy, it may switch from one to the other either by gaining the ΔE energy or by releasing it, these exchanges being associated to an electromagnetic radiation. This phenomenum is the basis of Nuclear Magnetic Resonance. The Planck's relationship allows us to associate the energy with the frequency of the electromagnetic wave by the fundamental relationship :

$$E = h.\nu \tag{2.8}$$

The frequency ν_0 of the wave involved during nuclear magnetic resonance is thus :

$$\nu_0 = \Delta E/h = \gamma.B_0/2.\pi \tag{2.9}$$

It can be expressed in angular frequency by:

$$\omega_0 = 2.\pi.\nu_0 = \gamma.B_0 \tag{2.10}$$

$\nu_0 = \omega_0/2\pi$ corresponds to what is called the **Larmor frequency**, i.e. the frequency to switch from one energy level to the other one (equation 2.7).

Statistical distribution of energy levels

The distribution of nucleus states in both energy levels E_β or E_α follows the Maxwell-Boltzmann statistic [64] as:

$$\frac{n_\beta}{n_\alpha} = \frac{N_s.P_\alpha}{N_s.P_\beta} = e^{-\frac{\Delta E}{k.T}} = e^{-\frac{\gamma\hbar.B_0}{k.T}} \tag{2.11}$$

with:

n_α the number of nuclei at energy level E_α

n_β the number of nuclei at energy level E_β

N_s the total number of spins per unit volume from the expression 2.13

P_α the probability of presence at equilibrium of a particle at state α : $P_\alpha = e^{-\frac{E_\alpha}{k.T}}$

P_β the probability of presence at equilibrium of a particle at state β : $P_\beta = e^{-\frac{E_\beta}{k.T}}$

k the Boltzmann constant

T the sample temperature in Kelvin

Since the net nuclear angular momentum $\vec{S}_N$ is the sum of all elementary angular momentums of all proton nucleus in the sample, and since spins up and down cancel each other, the NMR signal is proportional to the difference between α and β nuclei :

$$n_\beta - n_\alpha = N_s \cdot \frac{P_\beta}{P_\beta + P_\alpha} - N_s \cdot \frac{P_\alpha}{P_\beta + P_\alpha} = N_s \cdot \frac{e^{-\frac{\Delta E}{k.T}} - 1}{e^{-\frac{\Delta E}{k.T}} + 1} \approx Ns \cdot \frac{\Delta E}{2.k.T} = N_s \cdot \frac{\gamma.\hbar.B_0}{2.k.T} \tag{2.12}$$

For B_0 = 7 T we get around 1.5 spin taking part in the nuclear magnetic resonance over 10000 spins. This very small number explains why NMR exhibits a low sensitivity. However, hyperpolarization techniques are promising, especially at low B_0.

The number of spins per unit volume N_s, depends on the number of nucleus participating in the resonance of a molecule, n_h, the molecular concentration c_i (expressed in Mol/Kg), the Avogadro number Na, and the abundance P_{ab} of the chemical element observed.

$$N_s = n_h \cdot \frac{P_{ab}}{100} \cdot c_i \cdot N_a \tag{2.13}$$

Each chemical elements have variants i.e. elements with different number of neutrons. There are called isotopes. Each isotope of an element has a percentage of abundance P_{ab} relative to

it's main element. For example, on the first line of table 2.1 considering all hydrogens atoms existing, 99.985% of them are the isotope ^{1}H. [54].

Isotope	P_{ab}(%)	Spin	Gyro ratio (MHz/T)
^{1}H	99.985	1/2	42.576
^{13}C	1.10	1/2	10.705
^{17}O	0.048	5/2	-5.772
^{23}Na	100	3/2	11.262
^{31}P	100	1/2	17.235

Table 2.1: Main nuclei properties studied in NMR.

Hydrogen atoms being one of the most common element in matter, and the abundance of ^{1}H being very high, it is why protium NMR is widely used.

1.3 Electromagnetic Interaction

Resonance of the sample in NMR is obtained by the application of a Radio Frequency (RF) electromagnetic wave. The interaction between the RF excitation wave, and the nuclei of the molecules under study being at the foundation of NRM experiment, we give here a few insight about this interaction. First a microscopic point of view is presented, followed by a macroscopic description.

Microscopic interpretation A good way to visualize the magnetic interaction is to use classical mechanics, where the atomic nucleus is seen as a sphere with an intrinsic angular momentum, and a magnetic moment $\vec{\mu}$. Due to the thermal energy in the sample, this magnetic moment has a random, and spatially varying orientation [65].
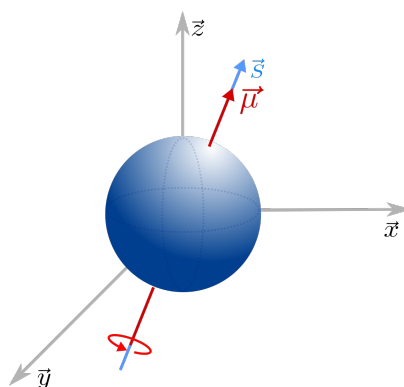

Figure 2.5: Classical representation of the angular momentum $\vec{s}$, and magnetic moment $\vec{\mu}$ when no field is applied. The orientation of μ is free when $B_0 = 0$.

Under no external magnetic field, the norm of the magnetic moment is:

$$|\vec{\mu}| = \sqrt{\mu_x^2 + \mu_y^2 + \mu_z^2} = \hbar.\gamma.\sqrt{s(s+1)} = \hbar.\gamma.\frac{\sqrt{3}}{2} \tag{2.14}$$

Thus, the norm of μ is known, but not its orientation which is totally free (figure 2.5).

If a static magnetic field B_0 is added, the magnetic spin moment will undergo a precession around the axis of the magnetic field, at the Larmor frequency, with a quantification of its component aligned along B_0 due to the energy splitting (equations 2.5, and 2.6, and figure 2.4). Assuming B_0 along the z axis, we thus have (figure 2.6):

$$E = \pm\vec{\mu}.\vec{B} = \mu_z.B_0 \tag{2.15}$$

Therefore μ_z, the magnetic moment along the z axis, can be expressed as :

$$\mu_z = \pm\frac{1}{2}\hbar\gamma \tag{2.16}$$

whereas the other components of μ (μ_x, and μ_y) are such that:

$$|\vec{\mu_{xy}}| = \sqrt{|\vec{\mu}|^2 - |\vec{\mu_z}|^2} = \sqrt{2}\,|\vec{\mu_z}| \tag{2.17}$$
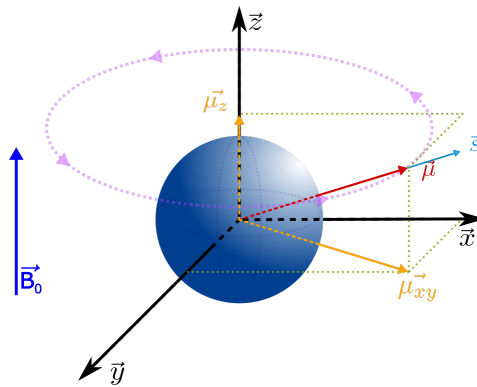
Figure 2.6: Precession of the magnetic spin moment around the magnetic field axis.

In summary, the nuclear magnetic moment of norm $\hbar.\gamma.\frac{\sqrt{3}}{2}$ is oriented, and moves randomly in space. The addition of a static field $\vec{B_0}$, assumed to be parallel to the z axis, makes the nuclear magnetic moment to precess at the Larmor frequency (equation 2.9) around this axis with two possible values of μ_z depending of the energy state of the proton.

Macroscopic interpretation   It is not possible to measure the magnetic moment precession of a single proton. In a NMR experiment, the precession of a wide number of proton's magnetic moments that are in the sample under test is sensed. Thus, we measure the average value of the magnetic moment of the sample $\vec{M}$, and a macroscopic interpretation of the result is necessary. When no magnetic field is applied, $\vec{M}$ averages to zero, and no NMR signal can be detected

(figure 2.7).

$$\vec{M} = \sum \vec{\mu} = 0$$
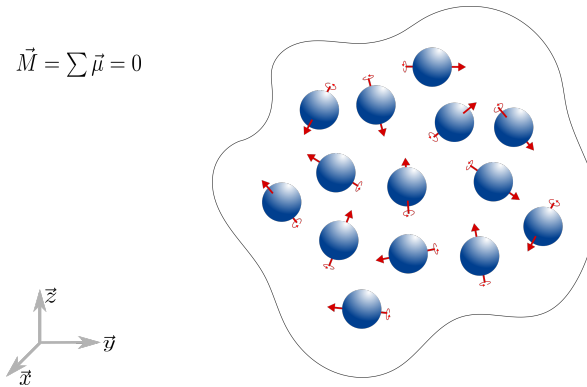
Figure 2.7: Random orientation of magnetic moments but with a zero mean value.

When a static magnetic field $\vec{B_0} = B_0 \vec{z}$ is applied, the z-components of the magnetic moments are quantified with two possible values (equation 2.5, and 2.6) as shown on figure 2.8. The minimization of energy breaks the equilibrium, and a non-zero net magnetization vector $\vec{M}$ appears. This phenomenon is called the nuclear paramagnetism.
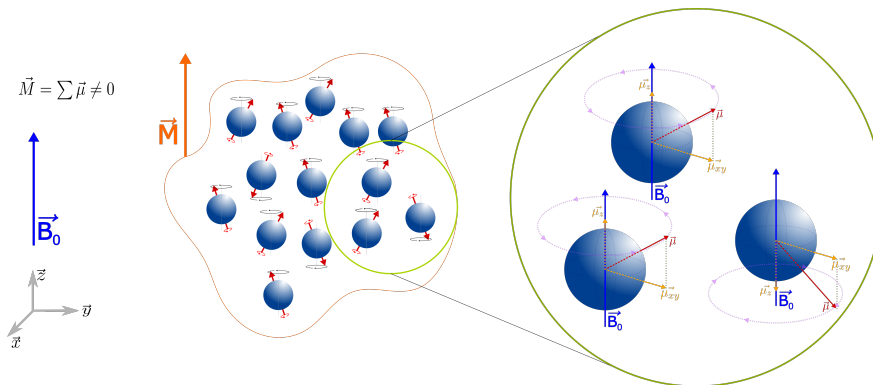
Figure 2.8: Nuclear paramagnetism due to the orientation of the magnetic moments parallel, and anti-parallel, along the axis of the magnetic field.

At absolute zero the atoms' magnetic moment are perfectly aligned with the magnetic field, and the net magnetization of the sample is $M = Ns \cdot \mu$. However, under conventional experimental conditions, i.e. at temperature T, the thermal agitation of the magnetic moments has to be taken into account, and leads to a net magnetization expressed by the Curie's law [66, 67]:

$$\vec{M} = \frac{N_s \mu^2}{3kT} \cdot \vec{B_0} \tag{2.18}$$

Introducing the equation 2.1 into the equation 2.18 provides the widely used expression for $\vec{M}$ [54, 60, 68]:

$$\vec{M} = \frac{N_s (\gamma\hbar)^2 s(s+1)}{3kT} \cdot \vec{B_0} \tag{2.19}$$

It is worth noticing that the magnetization vector is intimately linked to the magnetic field value B_0, and the abundance of the molecule in the sample (equation 2.13).

2 Nuclear Magnetic Resonance Experiment

In this section, we develop the background to get an NMR signal, and determine the chemical species in the sample.

2.1 Radio Frequency excitation Wave

We previously stated that in order to perform a change in the energy state of the nucleus, and thus toggle its magnetic moment parallel or antiparallel to the applied static magnetic field, it is necessary to provide or harvest energy from the nucleus. This can be done using an electromagnetic wave at the Larmor frequency, defined by its amplitude, and duration. Applied perpendicularly to $\vec{B_0}$, this Radio Frequency (RF) wave flips $\vec{M}$ by an angle proportional to the amplitude, and the time window of the excitation. Indeed, under such condition the magnetic component of the RF wave, named B1, applies a constant torque on the magnetization vector since it is rotating at the same frequency as the vector $\vec{M}$ precesses, i.e. at the Larmor frequency (figure 2.9).

In the reference frame of the laboratory, $\mathcal{R}_0(x, y, z)$, the vector coordinates in the xy plane write $\vec{r} = cos(\theta) \cdot \vec{x} + sin(\theta) \cdot \vec{y}$. Therefore, assuming $\vec{B_0}$ parallel to the z-axis, and placing an excitation coil whose axis is aligned to $\vec{r}$, i.e. perpendicular to $\vec{B_0}$, the xy components of the planar magnetic excitation wave B_1 applied with the coil reads:

$$
\begin{aligned}
\vec{B_1}(t) &= 2.B_1.cos(\omega.t).\vec{r} \\
&= 2.B_1.cos(\omega.t).cos(\theta).\vec{x} + 2.B_1.cos(\omega.t).sin(\theta).\vec{y} \\
&= 2.B_1.\frac{1}{2} \left\{ [cos(\omega.t + \theta) - cos(\omega.t - \theta)] .\vec{x} + [sin(\omega.t + \theta) - sin(\omega.t - \theta)] .\vec{y} \right\} \\
&= B_1. \left\{ [cos(\omega.t + \theta) + cos(\omega.t - \theta)] .\vec{x} + [sin(\omega.t + \theta) - sin(\omega.t - \theta)] .\vec{y} \right\} \\
&= B_1. [cos(\omega.t + \theta).\vec{x} + sin(\omega.t + \theta).\vec{y}] + B_1. [cos(\omega.t - \theta).\vec{x} - sin(\omega.t - \theta).\vec{y}] \\
&= \underbrace{B_1. [cos(\omega.t + \theta).\vec{x} + sin(\omega.t + \theta).\vec{y}]}_{\text{Positive turning field}} + \underbrace{B_1. [cos(-\omega.t + \theta).\vec{x} + sin(-\omega.t + \theta).\vec{y}]}_{\text{Negative turning field}}
\end{aligned}
$$

Consequently, the magnetic component of the RF wave is composed of two fields turning in opposite direction, i.e. two circularly polarized magnetic fields. Only one is useful for resonance, that is the one turning in the same direction as the magnetization precession. We will name it $\vec{B_1}$ from now, like the planar wave from which it comes. It applies a constant torque to the magnetization i.e. $-\vec{M} \times \vec{B_1}$, and makes $\vec{M}$ to rotate around the axis defined by the cross product of $\vec{M}$ and $\vec{B_1}$, as well as around the z-axis (i.e. $\vec{B_0}$). In other words, both vectors $\vec{M}$ and $\vec{B_1}$ remain perpendicular while the tip of the vector $\vec{M}$ exhibits an helical trajectory on a sphere whose radius is the norm of $\vec{M}$ (see Figure 2.9).
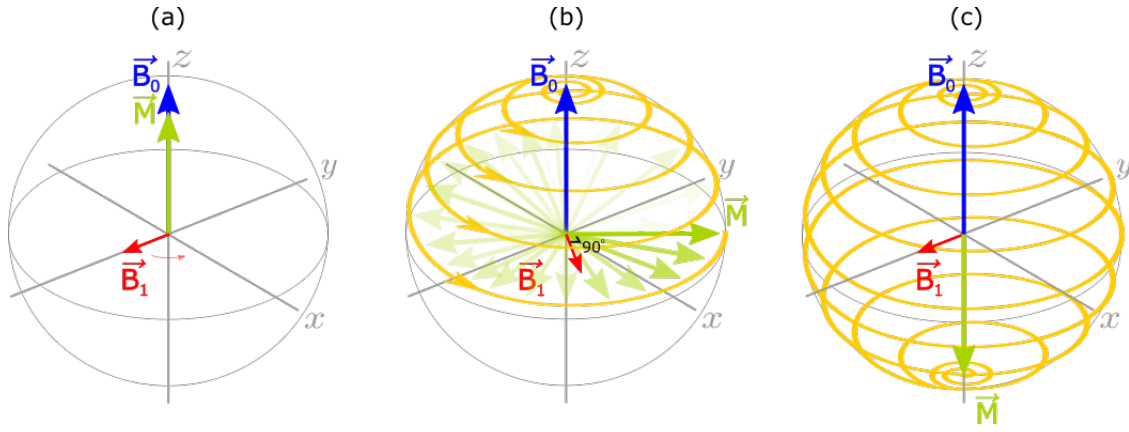
Figure 2.9: The application of the RF excitation wave leads to a rotating excitation magnetic field $\vec{B_1}$ in the xy plane that makes the magnetization $\vec{M}$ to exhibit an helical motion. It is worth to notice that because $\vec{B_1}$ rotates at the Larmor frequency, $\vec{M}$ and $\vec{B_1}$ remains perpendicular, and a constant torque is applied to $\vec{M}$. (a) We are at the beginning of the excitation phase, and $\vec{M}$ is aligned with the z axis, (b) $\vec{M}$ is moving along its helical trajectory, (c) The duration of the excitation phase has been so long that $\vec{M}$ has been reversed. If we keep the excitation wave, $\vec{M}$ will move back to its initial position following the same helical trajectory.

The representation of figure 2.9, which is in the fixed frame $\mathcal{R}_0(x, y, z)$ of the laboratory, provides a complete view of the behavior of the magnetization $\vec{M}$ during the excitation phase of the NMR experiment. However, it is not very practical for NMR interpretation, nor for the determination of the optimal amplitude, and duration of the excitation phase. It is much better to consider what happens for $\vec{M}$ in the frame defined by $\vec{B_1}$, and the plane perpendicular to $\vec{B_1}$ which passes through the z-axis, i.e. in a frame rotating at the Larmor frequency. From the above discussion, we see that in this frame $\mathcal{R}_1(x_1, y_1, z_1)$, $\vec{M}$ rotates around the axis defined by $\vec{B_1}$ because of the torque $-\vec{M} \times \vec{B_1}$ it feels (figure 2.10). In other words, in this rotating frame, $\vec{M}$ precesses around $\vec{B_1}$ at a frequency f_1 which is proportional to B_1 through the gyromagnetic ratio of the proton:

$$f_1 = \frac{\gamma \cdot B_1}{2 \cdot \pi} \tag{2.20}$$

As a consequence, if the RF wave is applied during a time t_p, then $\vec{M}$ rotates by the angle θ defined by (see figure 2.10):

$$\theta = \gamma \cdot B_1 \cdot t_p \cdot \frac{360}{2 \cdot \pi} \tag{2.21}$$

where θ is expressed in degree, and B_1 is the magnitude of the magnetic field component of the RF wave, the circularly polarized magnetic field.
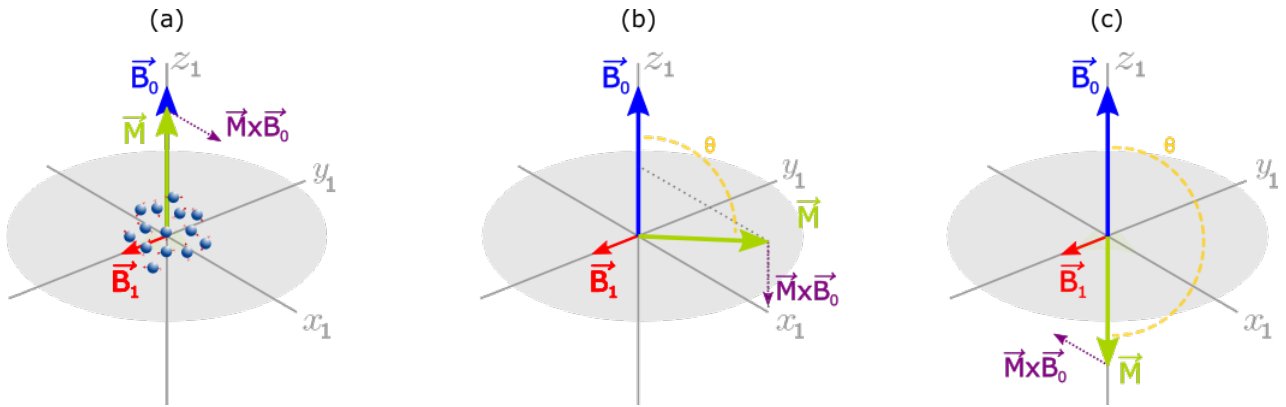
Figure 2.10: RF pulse creating a $\vec{B}_1$, which is fixed, here along y_1, in the rotating frame $\mathcal{R}_1(x_1, y_1, z_1)$. It makes the magnetization $\vec{M}$ to flip by the angle θ in the (x_1, z_1) plane. (a) At the beginning of the pulse, (b) the pulse brings the tip angle to 90°, (c) to 180° and so on if the pulse is not stopped.

Besides, it is possible to choose a large spectral excitation or a small one, to select some nuclei to resonate. Indeed each nucleus resonates at a peculiar frequency which is close to the Larmor frequency but slightly shifted (see section 2.3). Therefore, if one of the nuclei is outside the excitation bandwidth, it will not resonate. According to the Fourrier transform, we can define two types of excitation for the RF wave (see figure 2.11):

- Non selective excitation, "Hard pulse", is a very high power, and quick duration pulse to have a large excitation bandwidth.

- Selective excitation, "Soft pulse" longer and weaker excitation to minimize the selection bandwidth.

Thus the field power and duration can be tuned to select the excitation bandwidth while preserving the tip angle θ (also called flip angle).
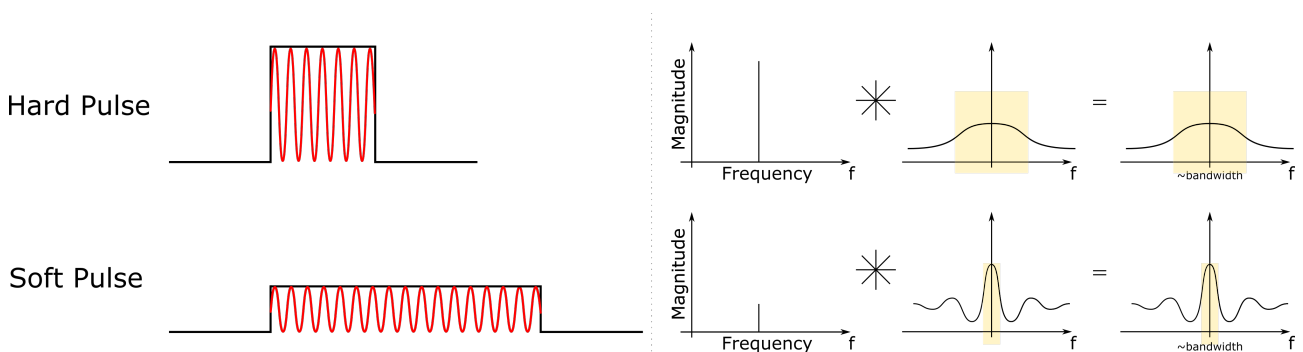
Figure 2.11: Hard, and soft pulses comparison in time, and frequency domain.

Hard, and soft pulses are the two basic pulses of NMR. They derive form a rectangle convoluted with a sine at Larmor frequency, leading to a rectangular-shaped pulse. There are many

other shapes that can be used to produce different excitation profiles, and make selective windows in the frequency domain. The representation of those excitations in literature shows only the shape of the pulse (figure 2.12) as it is a more convenient representation.

Figure 2.12: Representation of hard, soft, and selective pulse in NMR field.

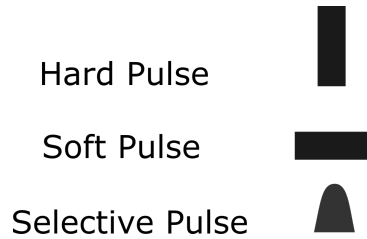Finally, if the applied RF wave is stopped at the time where $\vec{M}$ is in the xy plane, the flip angle is 90°, and corresponds to an equal population of states α, and β. We say that the spins possess a *phase coherence*. If we toggle the magnetization vector to 180°, then there is a "population reversal" (more β than α).

2.2 Free Induction Decay - relaxometry versus spectroscopy

Now that we understood how the magnetization vector $\vec{M}$ is flipped when applying a rotating field, we discuss here what happens after the $\vec{B}_1$ field is stopped.

Once the RF wave is stopped, the magnetization goes back to equilibrium exponentially with two relaxation times depending on which component of $\vec{M}$ we are measuring, i.e. the longitudinal relaxation time T_1 when M_z is sensed, and the transverse relaxation time T_2 (T_2^* will be discussed later) when M_x or M_y (noted M_{xy} on figure 2.13 for simplicity) is sensed (see figure 2.13). Those phenomena are linked to the molecules present in the observed sample, and thus, linked to the spin environment. The longitudinal relaxation of M_z with the time constant T_1, also called *spin–lattice relaxation time*, corresponds to the nuclear magnetic moment relaxing from a higher energy state to equilibrium with the surrounding spins (the "lattice"). The transverse component, M_x or M_y, decays exponentially with a time constant T_2 called *spin-spin relaxation time*. The resulting signal is a sine that dampens over time named the Free Induction Decay (FID). On a general point of view, it comes from the interactions of an ensemble of spins dephasing from each other.

In spectroscopy $M_{xy}(t)$ is measured. In relaxometry, as well $M_{xy}(t)$ is sensed and it is mainly T_2 that is measured. However T_1 could also be of interest.

Relaxometry   The T_2 decay is the main measure. The difference in its length gives an information of the presence of certain molecules (cancer cells for example) compared to a reference sample. Relaxometry can also, with the uses of contrast, lead to MRI technology where each tissues produces different relaxation times, therefore different contrasts that differentiate tissues.
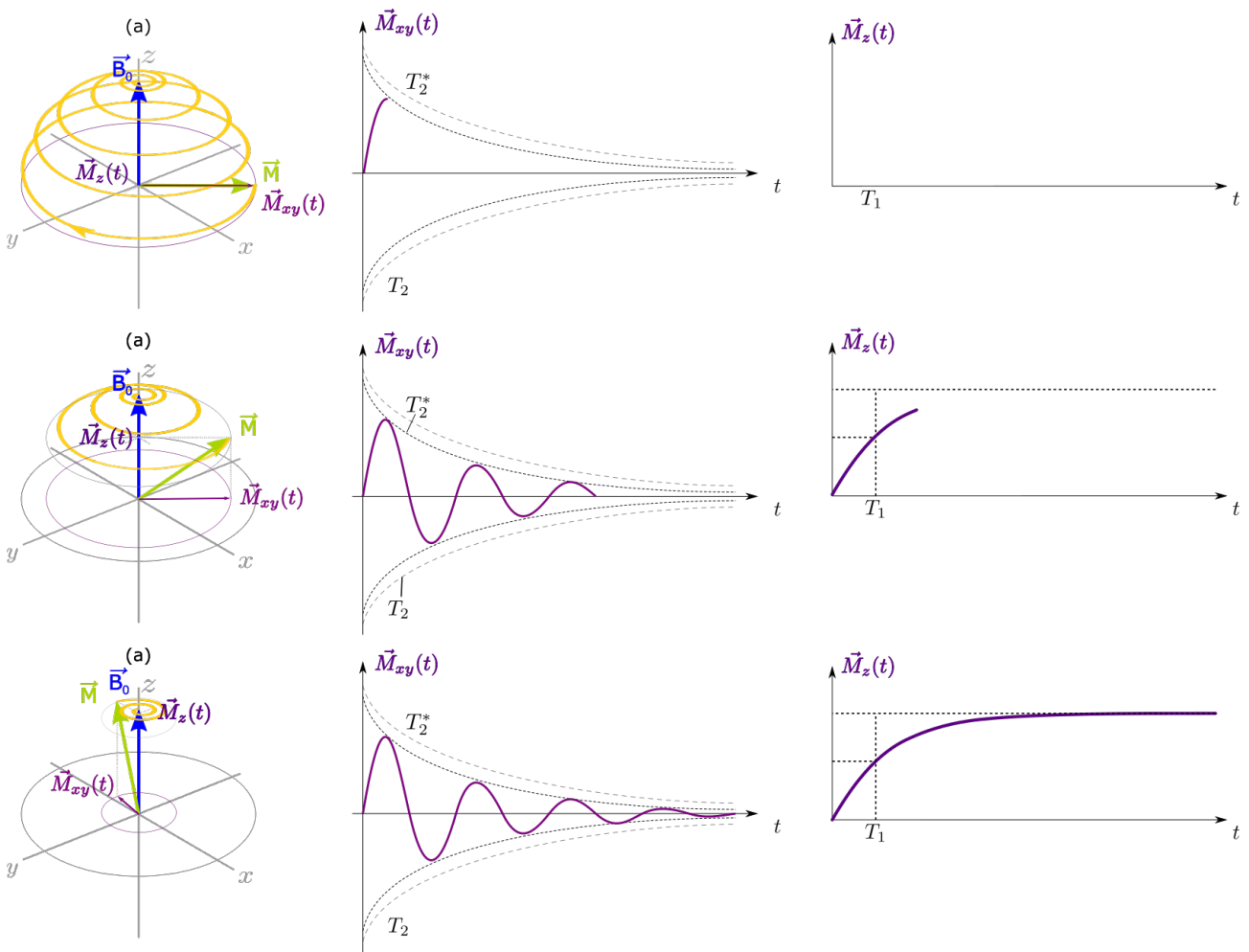
Figure 2.13: Longitudinal (T1), and Transverse (T2) relaxation when the magnetization vector recovers to equilibrium. T1 is represented when $\vec{M}_z(t)$ reaches 63% of its maximum value.

Spectroscopy   When different molecules are present, due to their local environment, they will exhibit slightly different Larmor frequencies (c.f 2.3). It means that different FID are superposed. Therefore, to distinguish the different molecules it is judicious to transform the time domain signal to the frequency domain. By doing so we can distinguish the different frequencies in the total FID, and then, differentiating the compounds present in the sample through spectroscopy.

2.3   Chemical Shift

The chemical shift is important in NMR spectroscopy as it gives the relevant information on the sample composition. In a sample, each nucleus interacts with the total field it feels. This field is the sum of the static field $\vec{B}_0$, and the small field coming from the elements surrounding the nucleus. It means that, depending on the chemical bonds in a molecule, each nucleus will interact differently leading to different resonance frequencies according to the nucleus environment.

In particular, each nucleus senses a local magnetic field depending on the electrons in their vicinity. Therefore, different chemical bonds in a molecule lead to slightly different Larmor frequencies as they do not sense the same magnetic field. If a nucleus senses a higher field $\vec{B}_0$ it

is called deshielded (lower electron density, magnetic induction...). In contrast, due to the motion of electrons, if the nuclei feels a weaker magnetic field $\vec{B_0}$ because of a high electrons density in its vicinity, it is said shielded. In NMR spectroscopy, the local magnetic field B_{0_n} is generally expressed as $B_{0_n} = (1 - \sigma)B_0$ where σ is the shielding constant.

Thus, the local Larmor frequency of the nucleus of interest becomes (remind equation 2.9) [69]:

$$\nu_n = \frac{\gamma . B_{0_n}}{2\pi} \tag{2.22}$$

The Larmor frequency is thus shifted from its nominal value corresponding to a reference sample. The resulting shift is always expressed in parts per million (ppm). It is important to note that for a given molecule in a given sample, the chemical shift, which is a relative quantity expressed in ppm, is the same whatever the static magnetic field used for the NMR experiment. Therefore the shift equation is:

$$\Delta f = \frac{\nu_n - \nu}{\nu} \cdot 10^6 \tag{2.23}$$

It is also worth mentioning that the shielding constant is also affected by the electrons in the molecule environment, i.e. the other molecules, and the solvent molecules of the sample contribute to the shielding constant σ. So for each group of nucleus, there is a slightly different frequency, and the FID will be composed of multiple frequency signals.

2.4 Spin-spin coupling

Besides the chemical shift, due to spin-spin interaction in the nucleus vicinity, the corresponding peak in the NMR spectrum may be splitted into subpeaks, as it can be seen in figure 2.14 that represents the NMR spectrum of ethanol. Main peaks are splitted into subsidiarity peaks.
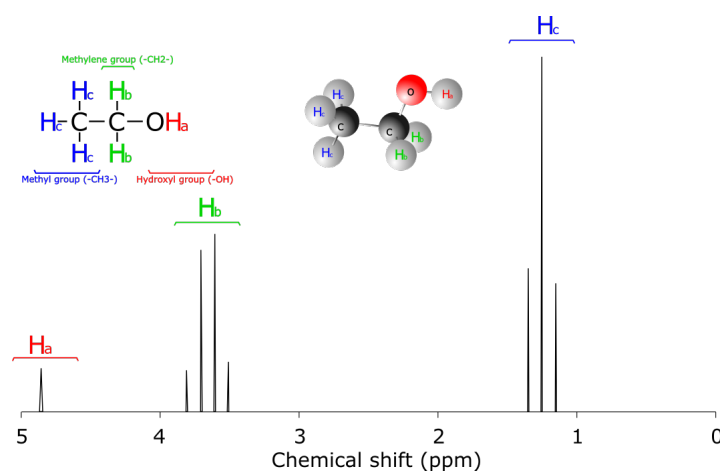

Figure 2.14: A typical "^{1}H-NMR spectra of Ethanol" with the main chemical shifts, and their splitting into sub-peaks for each group of the molecule.

One can see in the spectrum of ethanol more than one peak. This provides a lot of information about the molecules in the sample. Starting at the right side of figure 2.14, shifted by roughly 1.25 ppm, the Methyl group H_c (i.e. the "CH3 group") can be observed. It splits into three sub-peaks with the middle peak higher than its adjacent peaks. It is worth to mention that if each sub-peaks is integrated, the middle one exhibit an area around twice the area of its adjacent sub-peaks for a triplet, i.e. a cluster of three peaks, and so on depending on the number of sub-peaks (see figure 2.15). For the Methylene group H_b (CH2 group), the sub-peaks form a quartet, and for the Hydroxyl group H_a (OH group) only one peak is appearing, i.e. it is a singlet.

This separation into sub-peaks is due to what is called the spin-spin coupling, since it describes the magnetic interactions between non-equivalent non-zero spin nucleus in the vicinity.

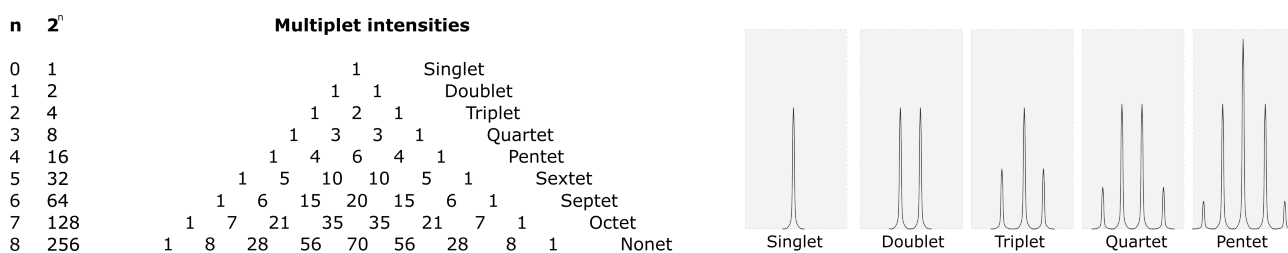| n	2^n					Multiplet intensities					
0	1					1	Singlet				
1	2					1 1	Doublet				
2	4				1	2 1	Triplet				
3	8				1 3	3 1	Quartet				
4	16			1 4	6	4 1	Pentet				
5	32		1 5	10	10	5 1	Sextet				
6	64		1 6	15 20	15	6 1	Septet				
7	128	1 7	21	35 35	21	7 1	Octet				
8	256	1 8	28 56	70 56	28	8 1	Nonet				

Figure 2.15: The Pascal triangle representing the peaks ratio intensity, and spectra examples.

Considering the ethanol molecule, there are three distinct groups: first, the Methyl group with three hydrogens that are connected to the same carbon, secondly, the Methylene group with two hydrogens, and lastly, the Hydroxyl group with only one hydrogen. We thus have in the FID three signals, one for each group.

Now looking the three H_c hydrogens, one can notice that they are all linked to the same carbon atom. They do not influence each other, therefore, they are said "equivalent". Next to them the two H_b hydrogen atoms are close, and thus, affects them. Indeed, each H_b hydrogen produces a small magnetic field due to their magnetic moment, and thus H_c hydrogen atoms sense the static magnetic field B_0 plus the effect of the small magnetic field produced in their vicinity by the H_b hydrogens.

The two H_b hydrogens lead to four different states as shown in figure 2.16:

- The two H_b magnetic moments are aligned to the magnetic field, $H_b \uparrow\uparrow$

- The two H_b magnetic moments are aligned opposite to the magnetic field, $H_b \downarrow\downarrow$

- One of H_b magnetic moment is aligned (H_{b_1}) whereas the other one is opposite to the magnetic field (H_{b_2}), $H_{b_{12}} \uparrow\downarrow$.

- The last possibility is the opposite of the previous one, H_{b_2} is aligned while H_{b_1} is opposite to the magnetic field, $H_{b_{12}} \downarrow\uparrow$

In the first case the $\vec{\mu}_{H_b\uparrow\uparrow}$ magnetic field deshields the H_c hydrogens as they senses a higher magnetic field ($B_0 + \mu_{H_b\uparrow\uparrow}$), $\mu_{H_b\uparrow\uparrow}$ being aligned with B_0. On the NMR spectra the ethanol peak

from these Hc will thereby be visible slightly downfield, i.e in the NMR spectrum, these H_c will give a higher ppm value than if they had felt only $\vec{B}_0$. The next case, when $\vec{\mu}_{H_b\downarrow\downarrow}$ is opposite to the magnetic field vector, the H_c hydrogens are shielded since the magnetic field they feel is weaker, due to the magnetic moment being opposite to the static magnetic field. The two last cases ($H_{b_{12}}$ ↑↓, and $H_{b_{12}}$ ↓↑) cancel each other so there is no frequency shift happening, i.e. they exhibit the shift expected for the applied $\vec{B}_0$.

We can have the same discussion with the H_b hydrogens, looking at the proton in their vicinity, and how they interact depending on their spin orientation possibilities. Finally, for H_a, as it is attached to an oxygen atom after the carbon atom, it does not interact with other hydrogen. Thus, only one peak will appear (singlet).

It is worth noticing that we do not observe only one molecule. So, inside the sample, all the possibilities are almost equally present (there is a bit more spin up than $down$). Besides, since there is twice the latest possibility ($\vec{\mu}_{H_b\downarrow\uparrow} = \vec{\mu}_{H_b\uparrow\downarrow}$), the central peak that is not affected is twice the side peaks as previously mentioned.

Moreover, the distance between the sub-peaks is linked to what is called the coupling constant, also known as the *J-Coupling*. The constant is expressed in Hertz (Hz) since the strength of the proton magnetic moment in vicinity is not dependent of the static magnetic field (equation 2.3). Consequently, the *J-Coupling* is always the same regardless of the applied magnetic field [70, 71]. However, the magnetization vector $\vec{M}$ being linked to the strength of the static magnetic field $\vec{B}_0$, a higher magnetic field provides more signal, hence, a easier readability of the peaks.
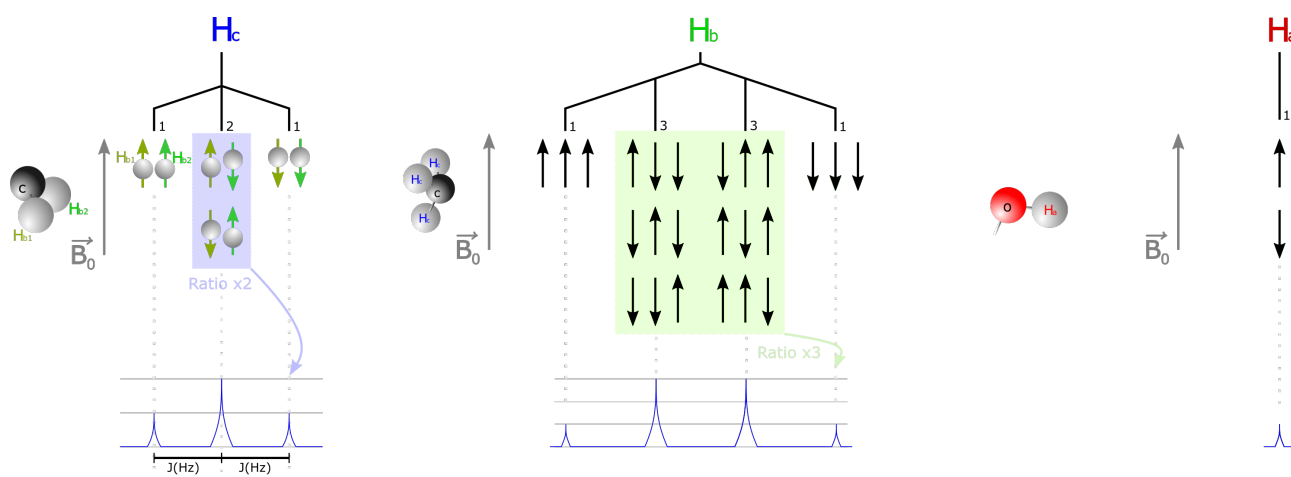

Figure 2.16: Spin-Spin coupling phenomenom in ethanol, depending on the hydrogens in the vicinity, with the spectra representation, and peaks ratio highlighted.

It is worth mentioning a few relevant points :

- The splitting multiplicity is given by the number of hydrogens in vicinity plus 1. It is known as the *n+1 rule*.

- Equivalent nuclei do not split each other.

- More complex coupling exists (see the Pascal triangle, figure 2.15). However, it will not be discussed in this manuscript, but can be found in dedicated NMR books [72, 73].

2.5   Bloch equation

The previous discussions about (i) the magnetization of a sample with application of the B0 field, (ii) its flipping thanks to a RF wave applied perpendicular to B0, (iii) the Free Induction Decay, and (iv) its spectral interpretation, were qualitative. In order to better understand the relevant parameters, and specifications of the portable NMR probe we target to build, as well as demonstrate the equations previously presented, we need a quantitative description. This is the aim of this section which presents the fundamental equations behind NMR. These equations derive from the basic equation of motion law, named Bloch equation in the context of NMR:

$$\frac{d\vec{M}}{dt} = \gamma \cdot \vec{M} \wedge \vec{B} \qquad (2.24)$$

In order to take energy dissipation into account, two relaxation terms are added to the equation 2.24. They allow to introduce both relaxation times T_1, and T_2:

$$\frac{d\vec{M}}{dt} = \gamma . \vec{M} \wedge \vec{B} - \frac{M_x . \vec{x} + M_y . \vec{y}}{T_2} - \frac{(M_z - M_{z0}) . \vec{z}}{T_1} \qquad (2.25)$$

The spin–lattice relaxation time T_1 is generally between 100ms and 10000ms, and the spin-spin relaxation time T_2 is shorter than T_1. When applying an RF pulse to flip the magnetization vector, all spin rotates in coherence (move all together). However, when the RF field is stopped, due to the different spin-spin linkage, this coherence is quickly lost. This lost of coherence happens much faster than the spin lattice relaxation time, consequently, T_2 is shorter than T_1. In addition, any inhomogeneity in the B_0 field makes the same molecules in the sample to have slightly different Larmor frequencies, and leads to an additional incoherence in the precession of the spins. So, due to unavoidable B_0 inhomogeneity, the measured T_2, named in NMR T_2^*, is always smaller than the theoretical one which depends only on the spin-spin relaxation.

The short T_2^* due to B_0 inhomogeneity is a big disadvantages for NMR spectroscopy. Indeed, homogeneity is the key to have a useful NMR signal. Many research projects since the discovery of NMR are dedicated to make the magnetic field more homogeneous [74, 75, 76, 77] or to improve the NMR signal despite the static field inhomogeneity by sending peculiar RF pulses sequences [78]. Nevertheless, inhomogeneities cannot be avoided, and other techniques such as shimming has generally to be applied, by using smartly placed resistive coils, and apply with them a magnetic field that compensates the inhomogeneity of B_0.

Using the laboratory frame $\mathcal{R}_0$, as shown in figure 2.17, the Bloch equation during excitation

phase can be written :

$$\frac{d\vec{M}(\vec{r},t)^{\mathcal{R}_0}}{dt}\bigg|_{\mathcal{R}_0} = \gamma\vec{M} \wedge (\vec{B}_0(\vec{r},t) + \vec{B}_1(t))$$

$$\frac{d\vec{M}(\vec{r},t)^{\mathcal{R}_0}}{dt}\bigg|_{\mathcal{R}_0} = \begin{cases} \frac{dM_x(\vec{r},t)}{dt} = -\omega_0(\vec{r},t).M_y - \omega_1.sin(\omega.t).M_z - \frac{M_x}{T_2} \\ \frac{dM_y(\vec{r},t)}{dt} = \omega_1.cos(\omega.t).M_z + \omega_0(\vec{r},t).M_x - \frac{M_y}{T_2} \\ \frac{dM_z(\vec{r},t)}{dt} = -\omega_1.sin(\omega.t).M_x + \omega_1.cos(\omega.t).M_y - \frac{M_z-M_{z0}}{t} \end{cases}$$

where $\omega_0(\vec{r},t) = B_0(\vec{r}) \cdot \gamma$ is the Larmor angular frequency, and $\omega_1 = B_1(\vec{r})/\gamma$ is the RF angular frequency causing the nutation of the magnetization vector (i.e. the tilt of $\vec{M}$ in the rotating plane $y1z1$). ω states for the rotating frame angular frequency, that is always equal to the Larmor angular frequency ω_0 in NMR.

Due to non constant parameters this equation is not easy to solve. On the contrary, using the rotating frame (see figure 2.17), and the transformation matrix equation 2.27, the Bloch equation becomes :

$$\frac{d\vec{M}(\vec{r},t)^{\mathcal{R}_1}}{dt}\bigg|_{\mathcal{R}_1} = \begin{cases} \frac{dM_x(\vec{r},t)}{dt} = (\omega_0(\vec{r}) - \omega).M_y(\vec{r},t)^{\mathcal{R}_1} - \frac{M_x(\vec{r},t)^{\mathcal{R}_1}}{T_2} \\ \frac{dM_y(\vec{r},t)}{dt} = -(\omega - \omega_0(\vec{r})).M_x(\vec{r},t)^{\mathcal{R}_1} + \omega_1.M_z(\vec{r},t)^{\mathcal{R}_1} - \frac{M_y(\vec{r},t)^{\mathcal{R}_1}}{T_2} \\ \frac{dM_z(\vec{r},t)}{dt} = -\omega_1.M_y(\vec{r},t)^{\mathcal{R}_1} - \frac{M_z-M_{z0}}{t} \end{cases} \quad (2.26)$$
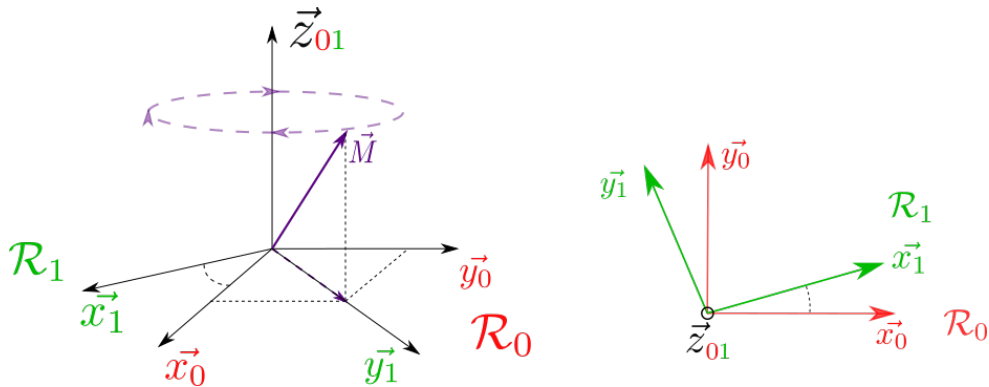
Figure 2.17: Laboratory frame $X_0Y_0Z_0$ related to the rotating frame $X_1Y_1Z_1$.

$$\mathcal{P}_{\mathcal{R}_1}^{\mathcal{R}_0} = \begin{pmatrix} cos(\omega.t) & sin(\omega.t) & 0 \\ -sin(\omega.t) & cos(\omega.t) & 0 \\ 0 & 0 & 1 \end{pmatrix} \quad (2.27)$$

The nutation angle, commonly known as tilt or flip angle in NMR, is one of the three Euler angle (precession, rotation i.e. spin, and nutation, shown on figure 2.18). The magnetization precesses around the static field (z-axis), with a nutation around the x_1 axis, due to the B1 field applied along y_1.
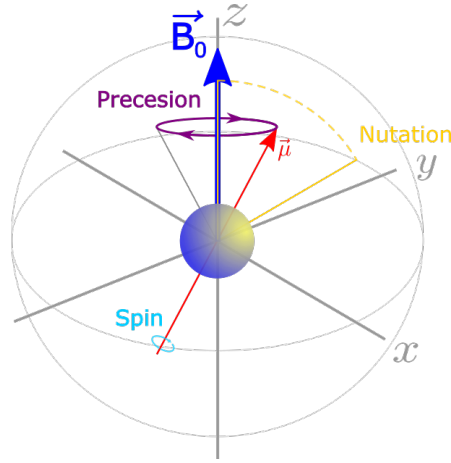
Figure 2.18: The three Euler angles, where the spin is associated to a rotation.

One can notice that the general Bloch equation 2.26 can be simplified by having $\omega = \omega_0$. This condition leads to a tilt in the xy rotating plane according to the simplified theory presented previously in the beginning of this chapter 2. Therefore, neglecting the relaxation times as they are much longer than the RF pulse, and taking the rotating frame angular frequency equal to the Larmor frequency i.e. $\omega = \omega_0$, plus assuming $\vec{M}$ at equilibrium ($M_z(\vec{r}, 0) = M_{z0}$, and $M_x = M_y = 0$) at $t = 0$ (beginning of the relaxation phase) we have:

$$\begin{cases} \frac{dM_x(\vec{r},t)}{dt} = 0 \\ \frac{dM_y(\vec{r},t)}{dt} = -\omega_1.M_z(\vec{r},t)^{\mathcal{R}_1} \\ \frac{dM_z(\vec{r},t)}{dt} = -\omega_1.M_y(\vec{r},t)^{\mathcal{R}_1} \end{cases} \Rightarrow \begin{cases} M_x(\vec{r},t) = 0 \\ M_y(\vec{r},t) = -M_{z0}.sin(\omega_1.t + \phi) \\ M_z(\vec{r},t) = M_{z0}.cos(\omega_1.t + \phi) \end{cases}$$

It is worth mentioning that two types of NMR can be used, pulsed NMR, where an RF pulse is emitted, and Continuous Wave NMR (CW NMR), where the RF field is continuously applied, and its frequency changes overtime. The CW NMR was used in the beginning of NMR. However, it is nearly unused nowadays, as it is a very slow experiment. This old form of NMR will not be discussed here.

In pulsed NMR, the pulse duration will determine the tilt angle $\theta = \omega_1 \cdot \tau$. Using the general equation 2.26, we can solve the longitudinal, and transverse component seen earlier on figure 2.13.

Longitudinal component on z:

$$\frac{dM_z(\vec{r},t)}{dt} = -\frac{(M_z(\vec{r},t) - M_{z0}) \cdot \vec{z}}{T_1(\vec{r})}$$

which solves as:

$$M_z(\vec{r},t) = M_{z0}(\vec{r}) \cdot \underbrace{(1 - e^{-t/T_1(\vec{r})})}_{\text{Equilibrium longitudinal relaxation}} + M_z(\vec{r},0) \cdot \underbrace{e^{-t/T_1(\vec{r})}}_{\substack{\text{Longitudinal} \\ \text{relaxation}}} \qquad (2.28)$$

Transverse component on x and y:

$$\frac{d\vec{M}_{xy}(\vec{r},t)}{dt} = \gamma \cdot [(M_y(\vec{r},t) \cdot B_0(\vec{r},t)) \cdot \vec{x} + (-M_x(\vec{r},t) \cdot B_0(\vec{r},t)) \cdot \vec{y}] - \frac{M_x(\vec{r},t) \cdot \vec{x} + M_y(\vec{r},t) \cdot \vec{y}}{T_2}$$

The equation can be rewritten using complex notation: $M_{xy}(\vec{r},t) = M_x(\vec{r},t) + i \cdot M_y(\vec{r},t)$:

$$\frac{dM_{xy}(\vec{r},t)}{dt} = \left(-\frac{1}{T_2(\vec{r})} - i \cdot \gamma \cdot B_0(\vec{r},t)\right) \cdot M_{xy}(\vec{r},t)$$

Thus, the solution is:

$$M_{xy}(r,t) = M(r,0) \cdot \underbrace{e^{-i \cdot \gamma \cdot \int_0^t B_0(\vec{r},\tau)d\tau}}_{\substack{\text{Rotation} \\ \text{at Larmor frequency}}} \cdot \underbrace{e^{-t/T_2(r)}}_{\substack{\text{Transverse} \\ \text{relaxation}}} \tag{2.29}$$

The FID signal being measured with a receiver coil by induction we can use the reciprocity principle stating that a magnetization at a position r induces an electromotive force in the receiver coil proportional to the magnetic field B_1 this coil would generate at the same position r if 1 ampere would flow through it (equation 2.30) [79, 80, 81]. In our case, the coil being on the x or y axis we have for the FID signal:

$$
\begin{aligned}
s(t) &= -\frac{\partial}{\partial t} \iiint_{V_L} [B_u(\vec{r}) \cdot M_{xy}(\vec{r},t)] \cdot d\vec{r} \\
&\approx -\iiint_{V_L} B_u \frac{\partial}{\partial t}\left[M_{xy}(t) \cdot e^{-i\gamma \cdot B_0 \cdot t} \cdot e^{-\frac{t}{T_2}}\right] d\vec{r} \\
&\Rightarrow \quad B_u(\vec{r}) = cst \; \forall \vec{r} \in V \quad , and \quad M_{xy}(\vec{r},t) = cst \; \forall \vec{r} \in V \\
&\approx -\iiint_{V_L} B_u \cdot M_{xy}(t)(-i\gamma \cdot B_0 . e^{-i\gamma \cdot B_0 \cdot t}) \cdot e^{-\frac{t}{T_2}} d\vec{r} \quad \Rightarrow \quad T_2 \gg \frac{1}{\gamma \cdot B_0} \quad \Leftrightarrow \quad e^{-\frac{t}{T_2}} \approx cst \\
&= -B_u \cdot M_{xy}(t) \cdot V_L \cdot (-i) \cdot \omega_0 \cdot [\cos(\omega_0 \cdot t) + i\sin(\omega_0 \cdot t)] e^{-\frac{t}{T_2}} \\
&= \underbrace{-B_u \cdot M_{xy}(t) \cdot V_L \cdot \omega_0 \cdot \sin(\omega_0 \cdot t) \cdot e^{-\frac{t}{T_2}}}_{\text{component on } \vec{x}} + i \underbrace{B_u \cdot M_{xy}(t) \cdot V_L \cdot \omega_0 \cdot \cos(\omega_0 \cdot t) \cdot e^{-\frac{t}{T_2}}}_{\text{component on } \vec{y}}
\end{aligned}
$$

where w_0 is the Larmor frequency in $rad.s^{-1}$, V_L the sample volume in l, and B_u is the *unitary field of the coil*, i.e. how much magnetic field the coil produces when 1 ampere flows through it. B_u is expressed in $T.A^{-1}$, and due to the reciprocity principle:

$$B_u = \frac{B_1}{I} \tag{2.30}$$

In practice, the RF wave is applied and then stopped at the time at which the magnetization has been tilt by $\theta = 90°$. Once the RF pulse is stopped, under the static magnetic field alone, $\vec{M}$ relaxes to its initial value $\vec{M}_0$ with a rotation at Larmor frequency. In other words, the magnetization vector will aligned back to the longitudinal axis ($\vec{z}$). Since the FID signal $S(t)$ is sensed by a

receiving coil placed on x or y, the FID amplitude at its starting point is given by [25]:

$$S_0 = w_0 \cdot M_0 \cdot V_L \cdot B_u \tag{2.31}$$

Such an equation allows to assess the amplitude of the tiny FID signal we may expect for a given coil, as well as the best Signal to Noise Ratio (SNR) of the NMR spectrometer once the intrinsic noise of the receiving coil is known.

3   NMR measurement system

Before entering into details in the design of the different devices of our portable NMR probe, we give here a brief overview of the key components in a NMR measurement system. As shown in figures 2.21 and 2.22, they are (i) the receiver, (ii) the transmitter, (iii) the magnet which provides the B0 field, and (iv) the data analysis unit.

3.1   Receiver

In order to acquire a signal from the sample, we need to use a *receiver coil*. This element needs to be carefully constructed, and tuned to detect the small NMR signal. One of the key points in the receiver coil construction is to make it resonate at the Larmor frequency. The preamplifier amplifies the small FID signal at the output of the sensing coil possibly without adding noise to get a high signal-to-noise ratio (SNR). It is why the first active element encountered by the NMR signal inside the receiver channel is a low noise amplifier (LNA). As any amplifier, the LNA has a finite gain bandwidth product (GBW). The FID being a RF signal (Larmor frequency at B0=1T is 42MHz), the finite GBW limits the preamplifier gain, which is generally between 20dB and 40dB. In order to get an output signal that can be digitally converted for data analysis, a subsequent amplification is required. However, due to GBW limitation, a down conversion of the signal is first performed thanks to a mixer which provides an image of the FID signal but at a lower frequency. The following amplifier can thus strongly amplify the signal. Fedback at the output of the receiver coil, the noise coming from the mixer and the amplifier are strongly attenuated thanks to the preamplifier gain. As a consequence these sub-blocks do not need to be designed low noise. Nevertheless, we have to keep in mind that the down converted FID signal should remain at a frequency above a few kilohertz in order to avoid any low noise frequency (1/f noise) that is always present in electronics. Once amplified, we may add a filter to reject all unwanted frequencies around the down converted frequency. Then the signal is converted with an Analog to Digital (ADC) converter before being processed thanks to a computer that will determine the NMR spectrum. Figure 2.19 gives a bloc diagram of the NMR receiver.
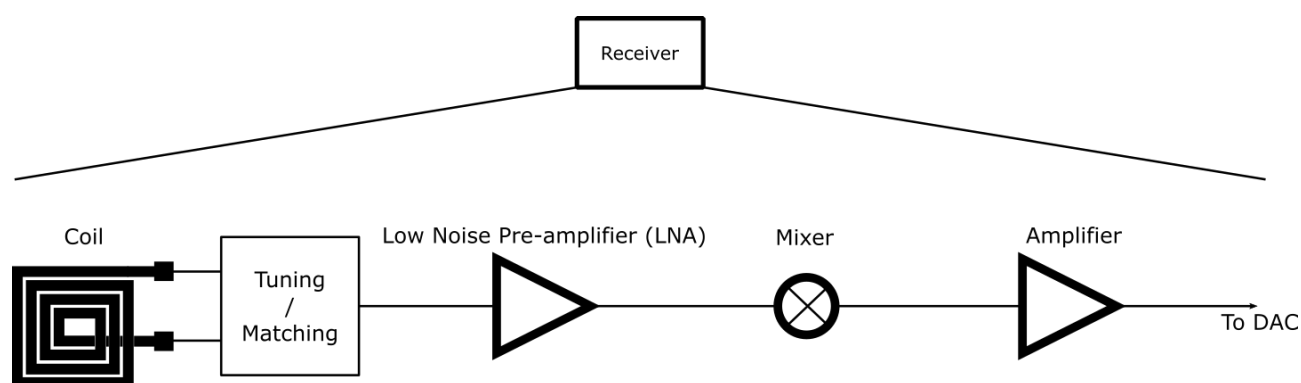
Figure 2.19: Main blocs of a typical NMR receiver.

3.2 Transmitter

The transmitter applies the RF pulse. It must be able to perform a quick pulse, i.e. transmit enough power in a short amount of time. First, the RF signal must be generated. This can be done with a Direct Digital synthesizer (DDS) which can produce a simple pulse or create any shaped pulses that could be interesting for soft pulse emissions (bandwidth selecting pulses as discussed at the end of the section 2.1). Before being transmitted to the sample, the RF signal is amplified by a power amplifier, and applied to the emitting coil with an adequate output power to provide a desired observation frequency window for the sample. The transmitter coil must be tuned, and matched to provide the maximum conversion without energy loss. Figure 2.20 shows the main elements of a transmitter.
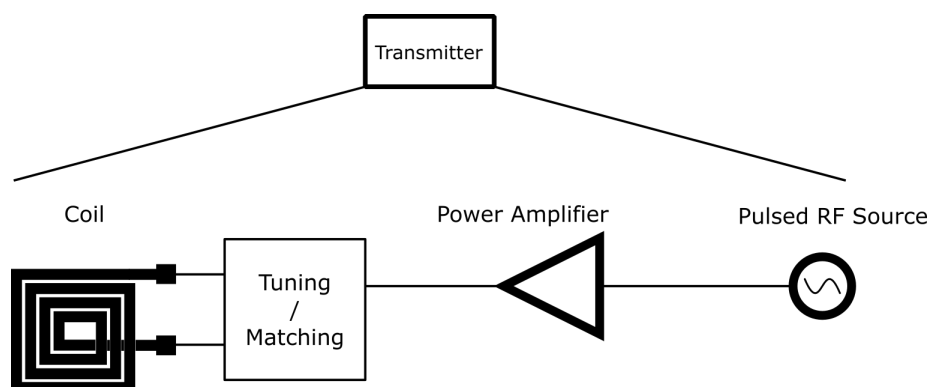
Figure 2.20: Typical NMR transmitter.

3.3 Dual/Single coil

Since the RF wave is applied perpendicularly to B0, and the FID signal has to be sensed with a coil whose axis is perpendicular to B0, the same coil can be used to transmit, and then receive the FID. Many low-cost NMR systems use a single coil system to transmit, and receive (Tx, and Rx respectively). However, in such a case, it is mandatory to have a switch which selects the transmission, or receiving phases (figure 2.21). Passive switch made with pin diodes or active switch can be used, but by doing so, an additional control pin is required, and the electronics

become more complex. Moreover, the switch needs to be fast enough to toggle quickly from the Tx to the Rx mode in order to record the FID from the beginning of the relaxation.
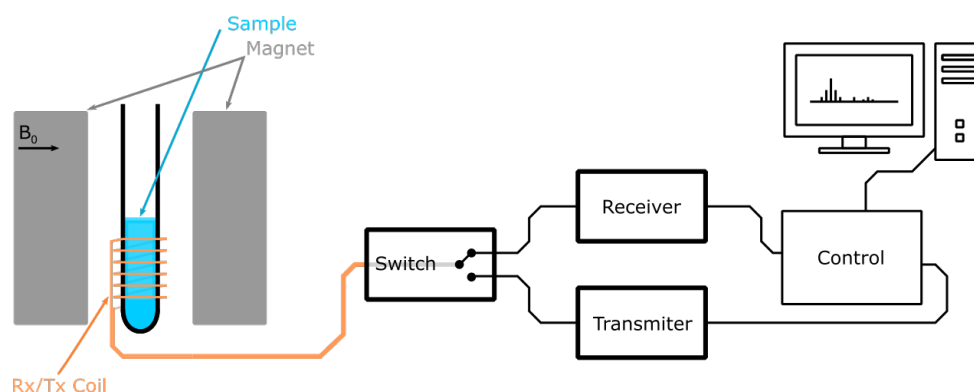
Figure 2.21: Principle of an NMR receiver system with one coil, a single coil, for transmitting and receiving.

In a two-coil system (figure 2.22), both coils are placed perpendicular to each other in such a way that no switch is required to isolate the receiver during the TX phase. Indeed, being perpendicular to the TX coil, the RX coil does not feel any magnetic field radiated by the TX coil. In practice, a small field is always sensed by the RX coil during the TX phase, but its power is sufficiently low not to deteriorate the receiver electronics.
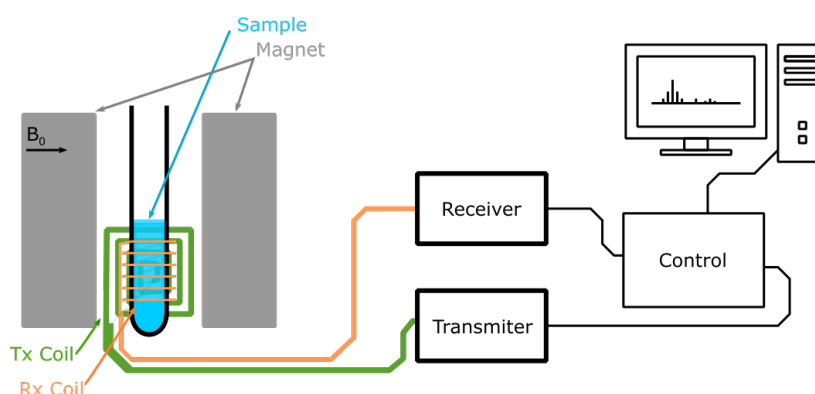
Figure 2.22: Principle of an NMR receiver system with two coils, one for transmitting, and one for receiving.

3.4   Static Field

The third key element of a NMR system is the magnet which has to produce an homogeneous B0 field in the whole sample volume. Such an homogeneity is very important in NMR. Indeed, if the B0 field is not the same throughout the sample, same molecules precess at different frequencies, and the corresponding spectral peak widens while the peak maximum lowers (for a given power in the peak corresponding to a given molecule concentration in the sample). ΔB_0 being the homogeneity deviation, the bandwidth over which the molecules will precess is simply:

$$\delta f = \frac{\gamma}{2\pi}\Delta B_0 \tag{2.32}$$

Having different relaxation frequencies, the phase coherence of the precessing spins is quickly lost during the relaxation phase, and the FID signal is drastically shortened leading to a relaxation time constant T_2^* lower than T_2, namely:

$$\frac{1}{T_{2*}} = \frac{1}{T_2} + \frac{\gamma}{2\pi}\Delta B_0 \tag{2.33}$$

The FID signal with inhomogeneity taken into account reads:

$$S_{FID}(t) = S_0 \cdot \cos(w_0 \cdot t) \cdot e^{\frac{-t}{T_2^*}} \tag{2.34}$$

Applying the fourrier transform to equation 2.34 to get the spectrum, we have :

$$s(t) = S_0.cos(2.\pi.f_0.t).e^{-\dfrac{t}{T_2^*}}.\Gamma(t) \xrightarrow{FT} \begin{aligned} S(f) &= S_0.\frac{1}{2}.\delta(f - f_0) * \dfrac{1}{\dfrac{1}{T_2^*} + j.2.\pi.f} \\[2em] S(f) &= \pm\frac{S_0}{2}.\left[\dfrac{1}{\dfrac{1}{T_2^*} + j.2.\pi.(f - f_0)}\right] \end{aligned}$$

the corresponding bilateral power spectrum in V^2/Hz is:

$$\pm|S(\omega)|^2 = \pm\frac{S_0^2}{4}.\left[\dfrac{1}{\dfrac{1}{T_2^{*2}} + (\omega - \omega_0)^2}\right]$$

leading to a maximum amplitude of the power spectrum at the Larmor frequency, given by:

$$|S(f_0)|^2 = \frac{S_0^2.T_2^{*2}}{4} \tag{2.35}$$

Therefore, for a lower T_2^* which is the case under B_0 inhomogeneity, peaks are lower and broader since the signal energy is spread over a wider frequency band. Thus, it is better to have T_2^* close to T_2 in an NMR experiment. The peak broadening of the power spectrum can be characterized by its Full Width at Half Maximum (FWHM) defined by (see figure 2.23):

$$FWHM = \frac{1}{T_2^*} \tag{2.36}$$

In practical, inhomogeneities may quickly lead to spectral peaks which overlap. In addition,

they can be below the noise level, making the NMR spectrum impossible to interpret. As a consequence, as we will see in the next chapter, the homogeneous B_0 magnet is really one of the trickiest element to build, especially in a low cost portable NMR probe.
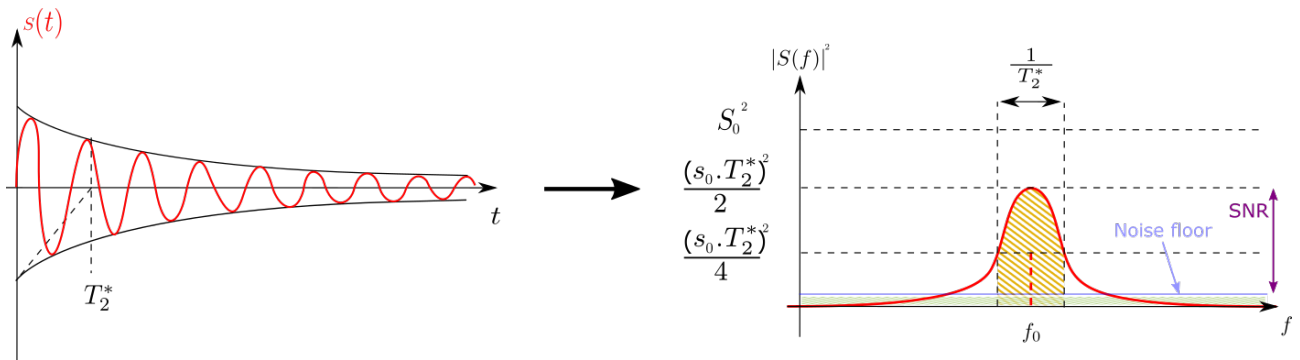
Figure 2.23: Unilateral power spectrum of a FID (twice the bilateral spectrum) with only one chemical component. The signal energy is represented in yellow. If it is spread too much, it will be under the noise floor, represented in blue.

3.5   Data Analysis Unit

The last key element of the receiver is the device that will receive the raw data and apply the Fourier transform to compute the spectrum and determine the compounds present in the sample. For a specific application this data analysis unit can be made on dedicated unit such as a FPGA [39]. However, it is also common to use a computer to process the data as it gives more flexibility to implement further data processing. In this PhD. work all data processing were done on computer. From the FID signal recording, we have computed its power spectrum using the method of the periodogram [82] (see Appendix):

$$\{P_0, P_1, \cdots, P_{N-1}\} = \frac{T_S}{T \cdot N} \cdot |FFT\{s_0, s_1, \cdots, s_{N-1}\}|^2 \qquad (2.37)$$

where T_S is the sampling period of the FID signal $s(t)$, N the number of samples, T the recording time window of $s(t)$, $FFT\{s_0, s_1, \cdots, s_{N-1}\}$ the Fast Fourier Transform of the series of the N FID samples $\{s_0, s_1, \cdots, s_{N-1}\}$, and $\{P_0, P_1, \cdots, P_{N-1}\}$ the estimation of the power spectral density of the FID signal at frequencies $0, f_s/N, \cdots, (N-1) \cdots f_s/N$.

$$*$$
$$*\quad *$$

Summary

This chapter has presented the theory behind nuclear magnetic resonance. After introducing the magnetic moment and its precession around the B0 field, the way this magnetic moment may be flipped by applying a RF wave at the Larmor frequency has been explained, first quantitatively,

then through the Bloch equations. This allowed introducing the Free Induction Decay signal from which the NMR spectrum is computed. Then the key elements that compose a NMR measurement system have been briefly presented. The next chapter discusses in details one of these key element, i.e. the magnet.

Chapter 3

The static magnetic field

1   Short theory on static magnetic field computation

As stated in section 3.4 of chapter 2, the homogeneity of the B_0 field in which the sample is placed has to be very good in order to get a usable NMR spectrum. The first part of this chapter deals with the B_0 static field to evaluate the possibility to build a low cost B_0 magnet for portable NMR spectrometers. In addition, within a portable NMR spectrometer, the electronics, i.e. the receiver, as well as the transmitter, are likely to be placed inside the magnet, and their behavior may be influenced by such a static field. To our knowledge, very few investigations on this issue have been carried out. So the second part of this chapter focuses on this topic, and shows that under very strong field, i.e. below 10T, CMOS electronics may easily be used.

In magnetism, two systems of unit are of common use. We thus remind them as well as the conversion table to switch from one to the other one. The first unit system is the International System of Units (SI system), which uses respectively Metres, Kilograms, and Seconds for length, mass, and time. It is also called MKS system. It succeeded the centimeter–gram–second system of units (*CGS* system) around 1886. Within CGS, several "sub-systems" units exist, including Gaussian units, the most common units used in magnetism today. CGS usually refers to CGS-Gaussian units, even if this naming is ambiguous. Table 3.1 shows the different units for SI and CGS systems, and table 3.2 the conversion factors where SI*Conversion factor = CGS [83].

Symbols	Description	SI	CGS
H	Magnetic field strength	Ampere per meter (A/m)	Oersted (Oe)
B	Flux density	Tesla(T)	Gauss (G)
M	Magnetization	A/m	electromagnetic unit per cubic centimeter (emu/cm^3)
ϕ	Flux	Weber (Wb)	Maxwell (Mx)

Table 3.1: Units used in magnetism in the SI and CGS systems.

Symbol	SI	Conversion factor	CGS
H	A/m	$4pi/10^3$	Oe
B	T	10^4	G
M	A/m	10^{-3}	emu/cm^3
Flux	Wb	10^8	Mx
$(BH)_{max}$	J/m^3	40π	GOe

Table 3.2: Table to convert SI to CGS units.

In free space, the $\vec{H}$ field, i.e. the magnetic field strength or magnetizing force, is linked to the magnetic induction $\vec{B}$ through the vacuum permeability μ_0:

$$\vec{B} = \mu_0 \cdot \vec{H} \tag{3.1}$$

In a material of magnetization $\vec{M}$, $\vec{M}$ contributes to the total magnetic induction $\vec{B}$, and adds up to $\vec{H}$, leading to the relation:

$$\vec{B} = \mu_0 \cdot (\vec{H} + \vec{M}) \tag{3.2}$$

Since we are interested in building a magnet which provides a static field $\vec{B_0}$, in addition to the magnetic induction Maxwell structural equation:

$$\nabla \cdot \vec{B} = 0 \tag{3.3}$$

the second Maxwell equation to be used in order to compute $\vec{B}$ once $\vec{M}$ is known is the Maxwell-Ampere equation (only valid under static conditions) that links locally $\vec{H}$ to the external current density ($\vec{J_{ex}}$), i.e. the possible current applied by the experimenter:

$$\nabla \times \vec{H} = \vec{J_{ex}} \tag{3.4}$$

It is worth noticing that if the magnet is built from ferromagnetic permanent magnets, as opposed to an electromagnet, $\vec{J_{ex}} = \vec{0}$, and the Maxwell-Ampere equation reads:

$$\nabla \times \vec{H} = \vec{0} \tag{3.5}$$

Equations 3.3 to 3.5 have to be completed by the boundary condition at the interface between two materials, i.e. material 1 and material 2. Noting ($\vec{H_1}$), the field in material 1, and ($\vec{H_2}$), the field in material 2, at the interface we have:

$$\vec{n_{12}} \times (\vec{H_2} - \vec{H_1}) = \vec{0} \tag{3.6}$$

Equations 3.1 to 3.6 allow to determine the distribution of $\vec{H}$, and then $\vec{B}$, in any given region of interest, once the magnetization of the material used to build the B_0 magnet is known. However, these equations cannot be solved analytically, but for very simple magnet geometries. We

therefore have to rely on Finite Element Simulations to determine $\vec{B}$, and we used the software *COMSOL$^{\circledR}$* in order to evaluate the possibility of building a low cost magnet for our portable NMR spectrometer.

2   Static field generation

To produce the static magnetic field various options may be used (figure 3.1):

- Resistive magnets are conventional electromagnets that do not use superconducting materials. They were used at the begining of NMR with CW-NMR, and were able to reach about 2,5T for a 5cm bore. Nevertheless, the sensitivity of CW-NMR was low and the stability of the magnetic field being related to the power electronics required to control the electromagnet was a critical issue [84, 74].

- Permanent magnets use rare earth materials (figure 3.8) and generate a permanent static magnetic field. Therefore, they do not require any power consumption, and can reach 1.5T in a 1cm bore [74]. They are usually used in relaxometry since a high homogeneity to perform NMR spectroscopy is tedious to realize with such magnets [85].

- Superconducting electromagnets were introduced to drastically improve the magnitude of the $\vec{B}_0$ field. They use a superconduction material with copper around it dedicated to field stabilization. The mostly used materials are type 2 superconductor like niobium-titanium (Nb$-$Ti). They allow to reach a field up to 15T [74]. Other improvement such as (Nb$_3$Sn) can operate at 20T to 25T. The counterpart of this technology is the need to cool the system for significant superconduction which drastically increases the cost of the magnet as well as the cost of its exploitation.

- Hybrid magnets combining super-conducting magnet technology and resistive magnet technology, can reach around 40T [86, 87]. At this time, the maximum achievable and usable magnetic field is a 45T field in a 32 mm Bore Hybrid Magnet (designed by the National High Magnetic Field Laboratory) [88].

Large magnets for industrial applications are usually resistive electromagnets. Superconductive and hybrid magnets are mainly used for high magnetic field in NMR application to increase spectral separation of molecules due to higher resonance frequencies (see equation 2.22), and higher magnetization hence, higher signal intensity (see equation 2.19). Electromagnets need to be power supplied. Therefore, for low-power applications the permanent magnets are more attractive [89]. However, permanent magnets exhibit poor homogeneity (critical parameter) and their field strength is limited. But they are compact, low cost, and need no maintenance. So despite their low intrinsic homogeneity, we decided to investigate the possibility of building a magnet structure using elementary permanent magnets for our portable NMR spectrometer. The use of permanent magnets dates back to 1950 with the accidental discovery of ferrite magnets.

Ten years later the first rare-earth magnets were produced and started dominating the market for their high magnetic field despite their cost and their brittleness. Permanent magnet research and development are still improving, especially to provide rare-earth-free permanent magnets for sustainability, and to improve magnetic and physical properties. This is one of the challenges driving portable NMR technology.
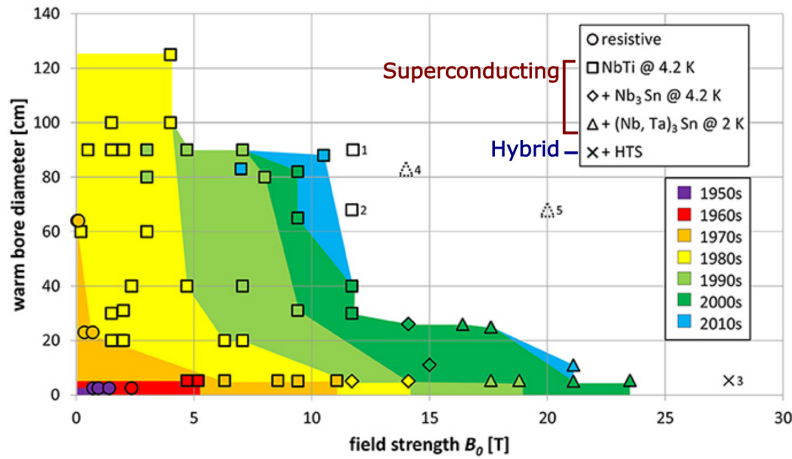

Figure 3.1: Field in NMR over the years depending on the technology, and the Bore diameter [74].

2.1   Magnet Material

Besides the permanent magnets arrangement, the choice of the magnet material is also very important. Different magnetic materials for permanent magnets exist. Permanent magnets represent 47,3 billion $US of the global magnet market only in the motor industry, and more than 10 billion $US in electronic industry in 2017 [90]. The most used materials for magnets are Ferrite, Aluminium-Nickel-Cobalt (AlNiCo or Al), Samarium-Cobalt (SmCo), and Neodymium-Iron-Boron (NdFeB) [91]. Additional materials are still under development to provide higher capabilities and also eco-friendly production due to the rarification of rare-earth materials.

In order to compare the magnetic properties of these materials (see table 3.3 below in section 2.3) we remind here the main physical properties used to characterize a magnetic material [92]:

- The remanence (B_R) is the strength of the magnetic field in Tesla (T). It is called remanence as it indicates the remaining magnetic induction of the material, after it has been magnetized to saturation, and with the external magnetization field removed. B_R is proportional to the remanent magnetization M_R by the permeability of free space μ_0.

$$B_R = \mu_0 \cdot M_R \qquad (3.7)$$

- The coercivity (Hc) is the value of the external magnetic field that has to be applied to reduce the magnetic induction B_R to zero, i.e. the material's resistance to becoming demagnetized under magnetic field. It is expressed in Oersted (Oe).

- The maximum energy product (BH_{max}) is the maximum amount of magnetic energy stored in the magnet.

- T_{max} represents the maximal temperature before the magnet loses its magnetic properties and can be reversible.

- The Curie temperature (TC) is the temperature at which the alignment of the atomic magnetic moment is broken. If the temperature reaches TC, the magnetization is irreversibly lost.

An important characteristic of a magnet is its hysteresis loop representing the nonlinear response of its magnetization M to an imposed external magnetic field H. Depending on the hysteresis loop, we speak about hard magnetic materials (such as Alnico, rare earth alloys, ferrite...) and soft magnetic materials (unalloyed iron, silicon iron for example) [92]. Magnetic materials are structured in areas of uniform magnetization named magnetic domains. During the magnet fabrication an external strong magnetic field is generally applied to provide all these magnetic domains with the same orientation, i.e. parallel to the applied magnetic field. In ferromagnetic materials, when the external field is suppressed, the magnetic domains remain aligned parallel, and the magnet exhibits a permanent magnetization that may be suppressed only with a strong magnetic field applied to the magnet in the opposite direction to its magnetization. In practice, such a strong field will be never encountered, and the magnet can thus be considered as permanent. Figure 3.2 represents an example of a magnet hysteresis loop where, from a demagnetized origin, an imposed magnetic field H irreversibly (green dotted lines) modifies the micro-structure of the magnetic domains inside the material. Initially magnetic domains are in a randomized state (a). If the external magnetic field H is sufficient to saturate the magnetization M of the material (Ms) ((a) to (b) in figure 3.2) then, when H goes back to zero, the remanence Mr remains ((b) to (b')). The coercivity Hc is the reverse field H needed to reduce the magnetization back to zero ((b') to (c) to (d)).
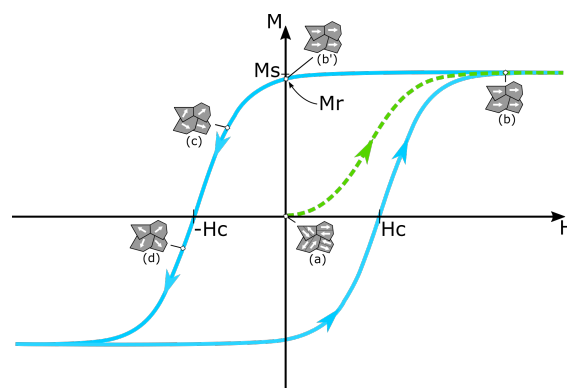

Figure 3.2: A typical magnet hysteresis loop where the configuration of magnetic domains inside the magnetic material are represented (adapted from [93]).

Magnetic materials are classified into two categories, hard and soft magnetic materials. Hard magnetic materials have a broad square hysteresis loop (figure 3.3-a), and are as consequence,

suitable for permanent magnets. Indeed, by applying a sufficient magnetic field to saturate the magnetization (i.e. applying H≥Ms) during their fabrication, they remain magnetized when the external H field is removed. In contrary, soft material have a narrow loop and a less steep slope. They lose their magnetization when H is removed (figure 3.3-b) [93]. These magnets are suitable for magnetic field concentrators.
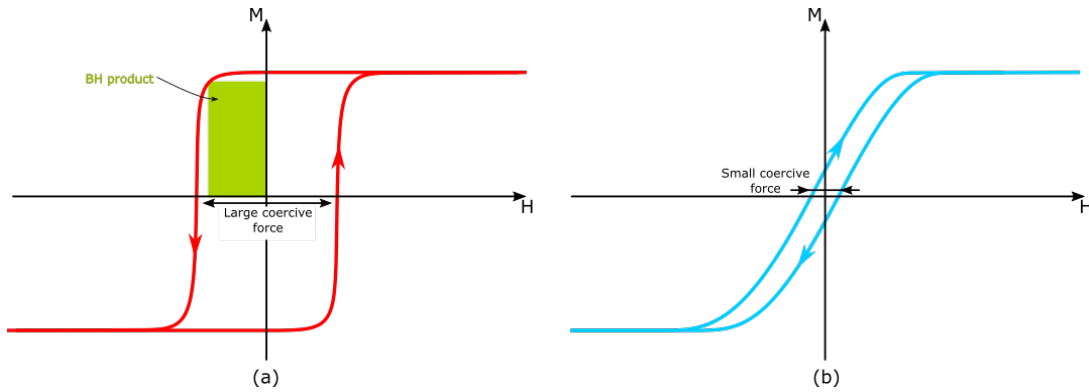

Figure 3.3: Hysteresis loop example for: (a) Hard magnetic material, (b) Soft magnetic material.

2.2 Halbach magnet structure

Several elementary permanent magnets can be combined in such a way that their magnetizations add up in order to get in a given Region of Interest (ROI) a quite homogeneous magnetic field whose magnitude is higher than the magnetization of the individual magnets. The magnet arrangement proposed by *Klaus Halbach* in 1979 [94] is a structure made from a single rare earth permanent magnet material with individual magnetic domains (figure 3.4) oriented over a circle as shown in figure 3.5. This configuration increases the magnetic field in the center whilst canceling it outside. At first, the magnet, which requires a complex material engineering to be realized, was not built for NMR. However, because of the relative field homogeneity in its center, the Halbach magnet structure was quickly adopted for NMR. Thanks to Raich and Blümer who proposed structures based on arrangement of individual magnets (figure 3.6), it is now widely used for its fast implementation and rapid prototyping [95]. Raich and Blümer called their structure Mandhalas (Magnet Arrangement for Novel Discrete Halbach Layout) but it is common to refer them as Halbach array, Halbach structure, or simply Halbach magnet.
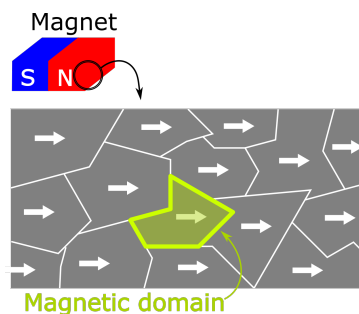
Figure 3.4: Magnetic domains in the magnet material where the arrow represents the magnetization of each magnetic domain.
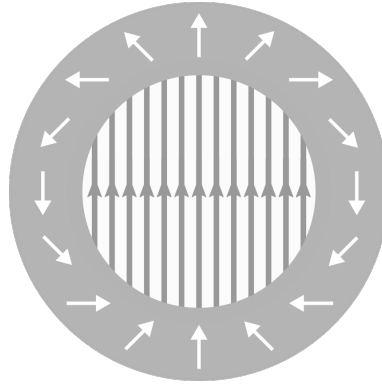
Figure 3.5: Original Halbach ring.
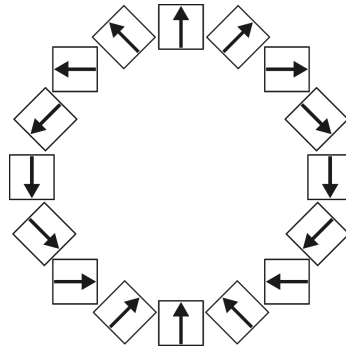
Figure 3.6: Halbach array with 16 square magnets.

The theory for the positionning of the elementary magnets in a Halbach array can be found in the litterature [95, 96, 97], and summarizes as follow:

For a number n of elementary square magnets, the center position $^c\vec{p}_i$ of each magnet, where $i = n - 1$, is computed with the following equation:

$$^c p_i := \begin{pmatrix} ^c y_i \\ ^c z_i \end{pmatrix} = r \begin{pmatrix} \sin \alpha_i \\ \cos \alpha_i \end{pmatrix} \tag{3.8}$$

where r is the radius of the Halbach array, and α_i the angle of the magnet $i = n - 1$. α_i is expressed as:

$$\alpha_i = \frac{2\pi \cdot i}{n} \tag{3.9}$$

where β_i is the magnetization angle of the ith magnet with respect to the z-axis:

$$\beta_i = 2\alpha_i \tag{3.10}$$

The size a of the elementary magnet is then chosen to have the denser arrangement of magnets in order to be as close as possible to the original Halbach array (figure 3.5). Computing the coordinates of the elementary square magnet i, where the corner position is given by the vector $^j\vec{p}_i$, with j is the corner label $1 < j < 4$ (see figure 3.7), we get:

$$^1p_i := \begin{pmatrix} ^1y_i \\ ^1z_i \end{pmatrix} = ^c p_i + \frac{a}{\sqrt{2}} \begin{pmatrix} \cos \xi_i \\ \sin \xi_i \end{pmatrix} \tag{3.11}$$

$$^2p_i := \begin{pmatrix} ^2y_i \\ ^2z_i \end{pmatrix} = ^c p_i + \frac{a}{\sqrt{2}} \begin{pmatrix} -\sin \xi_i \\ \cos \xi_i \end{pmatrix} \tag{3.12}$$

$$^3p_i := \begin{pmatrix} ^3y_i \\ ^3z_i \end{pmatrix} = ^c p_i + \frac{a}{\sqrt{2}} \begin{pmatrix} -\cos \xi_i \\ -\sin \xi_i \end{pmatrix} \tag{3.13}$$

$$^4p_i := \begin{pmatrix} ^4y_i \\ ^4z_i \end{pmatrix} = ^c p_i + \frac{a}{\sqrt{2}} \begin{pmatrix} \sin \xi_i \\ -\cos \xi_i \end{pmatrix} \tag{3.14}$$

where $\xi_i = \frac{p_i}{4} - 2\alpha_i$. The length of the magnet size can thus be obtained by solving the equation:

$$^4p_{\frac{n}{8}-1} + \lambda(^1p_{\frac{n}{8}-1} - ^4p_{\frac{n}{8}-1}) = ^3 p_{\frac{n}{8}-1} \tag{3.15}$$

which gives:

$$a = 2r\Xi(\frac{2\pi}{n}) \tag{3.16}$$

with:

$$\Xi(\frac{2\pi}{n}) = \frac{\cos\left(\frac{2\pi}{n}\right) - sin(\frac{2\pi}{n}) - \sqrt{2}\sin\left(\frac{\pi}{4} - 2(\frac{2\pi}{n})\right)}{2\cos\left(\frac{\pi}{4} - 2(\frac{2\pi}{n})\right) + \sqrt{2}} \tag{3.17}$$

The inner radius and outer radius are therefore given by the next two expressions:

$$r_{outer} = r(1 + \sqrt{2}\Xi(\frac{2\pi}{n})) \tag{3.18}$$

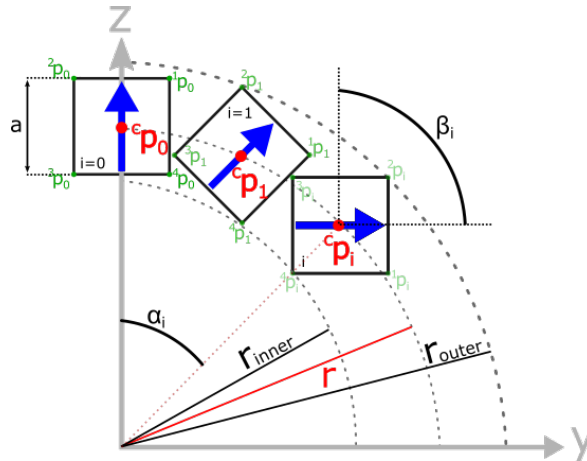$$r_{inner} = r(1 - \sqrt{2}\Xi(\frac{2\pi}{n})) \tag{3.19}$$

Figure 3.7: Halbach array geometrical parameters.

The approximate magnetization at the center of the Halbach array is given by [98]:

$$B_{apx} = B_r \cdot \ln \frac{R_{outer}}{R_{inner}}$$

(3.20)

Although more homogeneous than the stray field around a single elementary magnet, the magnetic field in the center of the Halbach array, i.e. in the R.O.I., is not perfectly homogeneous, and finite element simulation is required to assess the residual inhomogeneity, and evaluate if a simple Halbach array may be used for NMR spectroscopy. Before performing such simulation, we have to choose the magnetic material for the elementary square magnets.

2.3   Choice of the elementary magnet

For the targeted application we need a high magnetic remanence, coercivity and maximum energy product. Simply put, we need a high magnetic field that is not sensible to demagnetization as the elementary magnets will be very close to each other in the Halbach structure. We have listed the different materials that can be used, and their properties in table 3.3.

- Ferrite magnets: They are the most commercialized magnets. They are low-cost, very stable (i.e. the magnetic field does not change overtime due to temperature for example) and difficult to demagnetize. They are mainly used in electronic inductors, transformers, electromagnets... Nevertheless, they have a low remanence (see table 3.3) and therefore, provide less magnetic field than other materials.

- Alnico magnets (Al): They were developed in the 1930s. They are alloys of iron, cobalt, nickel and aluminium. Alnico magnets have great magnetic properties, but they lack physical properties as they are hard and brittle. Thus, costly machining is necessary to create a finished magnet with high tolerance [99]. Besides, the coercivity of Alnico is very low, and the magnet may be easily demagnetized (see table 3.3).

- Samarium-Cobalt magnets (SmCo): They were developed in 1960, and are used in high-end motors, cryogenic systems, NMR spectrometers... They are resistant to demagnetization, and have a good stability. They can provide a high magnetic field and are less subject to corrosion than a neodymium magnet. Thus, Cobalt magnets are mainly used in extreme working conditions and high temperature due to their high maximum temperature (see table 3.3).

- Neodymium magnets (NdFeB): They were developed in 1984 for the automotive industries. They are nowadays the most used type of rare earth magnets. They can reach a higher magnetic field than SmCo magnets (see table 3.3), and are lighter and cheaper, because Neodymium is more abundant than samarium. They are found in many applications that have no harsh environment, i.e. mobile phones, hard disk drives, NMR spectrometers...

Figure 3.8 summarizes the development and improvement in terms of energy product of these four materials over the last century.
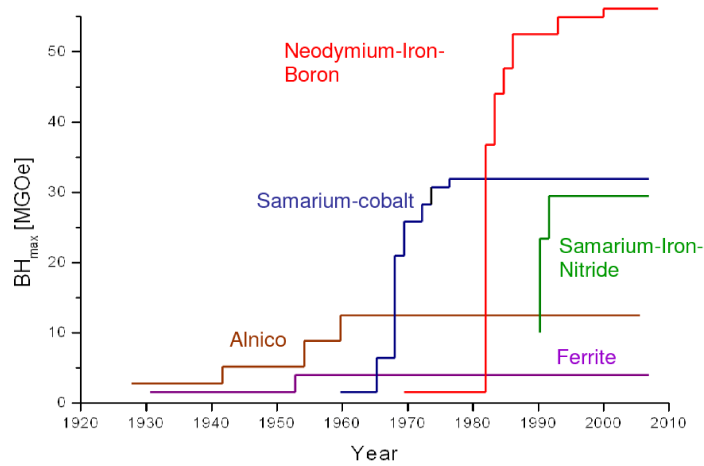
Figure 3.8: Development of permanent magnets over the last century with their maximum energy product [27].

Type	Br(T)	Hc(kOe)	BH max(MGOe)	T max (° C)	T Curie (° C)
Ferrite 8B	0.4	3	3.8	250°	450°
Alnico 5	1.1	0.6	4.25	450°	810°
SmCo (SC-3215)	1.12-1.18	8.9-10.1	31-32	248°	800°
NdFeB (N52)	1.44-1.48	10.5	49-53	60°	312°

Table 3.3: Magnetic properties of the typical magnets used in industry [91].

From the table 3.3 and the outlined properties, the relevant materials for a portable NMR spectrometer are SmCo and NdFeB (Samarium and Neodymium magnets). However, Neodymium is cheaper than Samarium, for approximately the same properties, and we will not use our magnet in harsh environments, so we chose to use Neodymium elementary magnets to build our Halbach structure.

2.4   Halbach magnet prototype

In order to assess the magnetic field strength and homogeneity we can reach with a simple Halbach magnet, we first simulated and then built a prototype with N52 Neodymium magnets (see table 3.3).

Simulations of different Mandhalas structures with various number of magnets can be found in the literature. Their homogeneity in ppm (part per million, $\Delta B_0/B_0$) is reported by Raich *et al* as well as Hung [95, 99] for circular and square elementary magnets as shown in the table 3.4. It is worth mentioning that in table 3.4 the ROI is around 25mm for all Halbach magnets, i.e. the magnet was bigger when using a low number of elementary magnets. This leads to very heavy

Halbach magnet (for instance, 75kg for the 4-magnet structure, the weight is not reported on the table) and thus not valuable commercially.

n	B(T)		Homogeneity (ppm)	
	Squares	Circles	Squares	Circles
4	0.7014	1.1705	727	88745
8	0.7475	0.6853	3517	164
16	0.3011	0.3553	857	23
32	0.1348	0.1795	110	7

Table 3.4: Summary of 2D simulations and geometric calculation of Mandhalas structures by Hung [99]. The result are similar to Raich *et al* [95].

Moreover, prototypes for NMR based on Halbach magnets that have been improved with complex shimming methods, and tedious modifications of the basic structures to greatly improve their homogeneity have also been reported by Hung [99]. Main results are summarized in table 3.5.

Reference	Homogeneity (ppm)	Mass (Kg)	ROI (mm)	Field Strengh (T)
Moresi and Magin [100]	10	4	3x3x5	0.6
Jachmann [101]	56	5	0.25x2	0.5
Danieli [102]	0.85	50	10x10	0.22
Hugon [103]	10	1.8	1.5x1.5	0.12
Windt [104]	200	3.1	5x5	0.57
Hung [99]	178	20	40x50	0.32
Unshimmed Raich and Blumer [95]	2500	11.4	18x18x30	0.3

Table 3.5: Comparison of existing Mandhalas [99].

In our application, we eventually target a portable NMR probe that could be integrated in a microfluid system. So our goal is to have a low-cost magnet with a very small R.O.I., typically of 2mm x 2mm x 2mm. We thus simulated a 8-magnet Halbach structure with an inner diameter of 25 mm, and compute the magnetic field strength and its homogeneity over a 2mm R.O.I. We used *COMSOL®* with the "Magnetic Field, No Current" (mfnc) toolbox. The choice of a 8-magnet structure was to have an easy first to build prototype, with a sufficiently strong field, but light and small enough to be carried easily. Although the use of circular elementary magnets seems to result in a better homogeneity (see table 3.4), we chose to use square magnets since it eases maintaining the magnets in their right positions inside the holder. Indeed, the Halbach structure is not a natural magnetic configuration, i.e. with the lowest possible magnetic energy, and strong repel forces are exerted between the magnets. Using round cross-section magnets requires to glue the magnets inside their holder cavities to avoid any rotation of the magnet, which make the fabrication of the Halbach structure quite difficult.

The Halbah simulation is based on 8 commercially available low cost magnets of a square cross section, with dimension of $12.8\text{mm} \times 12.8\text{mm} \times 60\text{mm}$ (see figure 3.9). The choice of a long

60mm magnet was to avoid boundaries effect in the center due to the finite ends of the magnets. In the simulation the Halbach magnet is surrounded by air and each elementary magnet is defined as N52 Neodymium with their material characteristics that was defined manually (see table 3.3). The magnetization direction and the geometric parameters are defined by equations 3.9 and 3.10 previously discussed. The inner diameter of the structure (see figure 3.9) has been made so each elementary elements are the closest to each other, as mentioned previously. However, the structure holding the magnet should be considered, hence, a small separation between the magnets to provide enough rigidity to the structure while setting up the magnets has been taken into account. 2mm walls were chosen between magnets leading to a minimum inner diameter of 25mm.

Figure 3.10 shows the field distribution in the R.O.I of 2mm x 2mm x 2mm, i.e. over +/- 1mm along each axis. The worst homogeneity is along the y-axis, with an inhomogeneity of 0.00176/6.989989 = 251ppm. As discussed in chapter 2, such an inhomogeneity is too high for practical NMR spectrometry. However, in [101] Jachmann reported a NMR spectrometry experiment with a MnCl$_2$ doped water sample in a B_0 field of 0.5T, and a field inhomogeneity of 450ppm. It results in a 10.5 kHz wide peak just above the noise level after 128 scans, but detectable. So we decided to fabricate our Halbach prototype in order to try to perform a first NMR experiment on a water sample with the integrated receiver we developed, and that is presented in chapter 6.
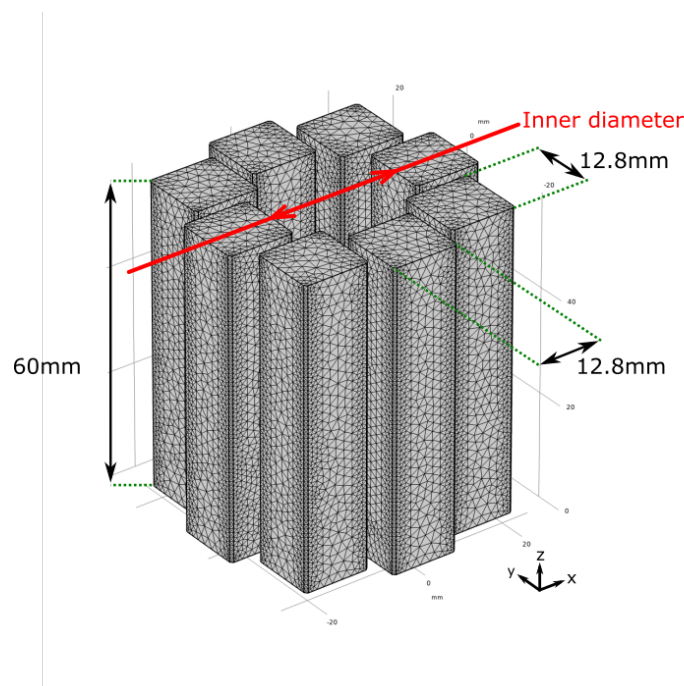

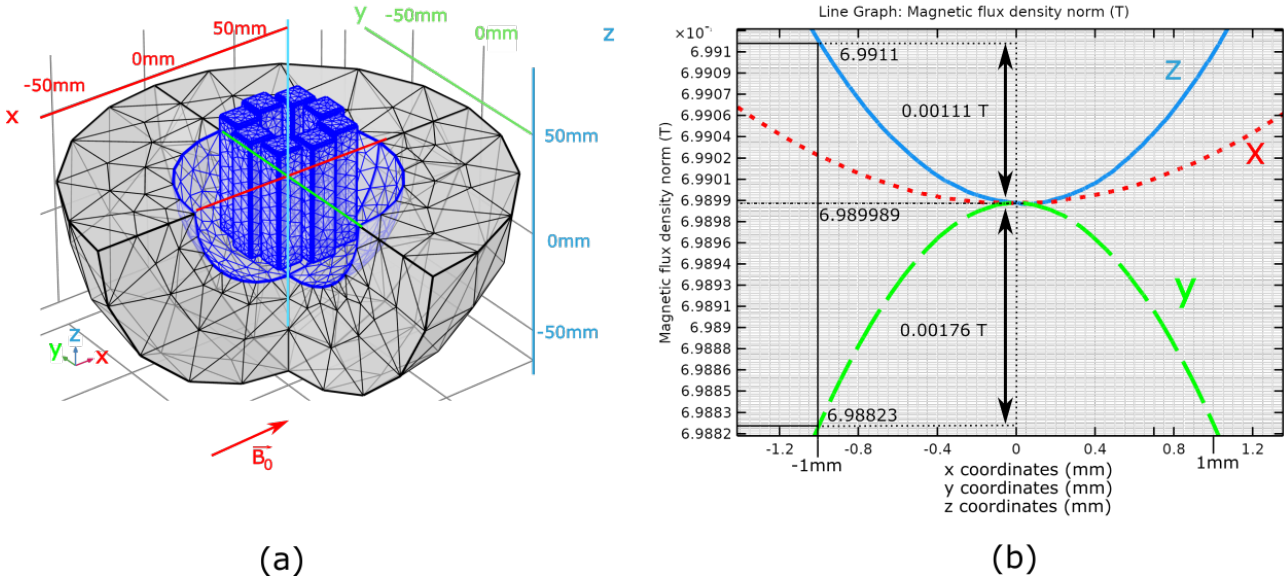Figure 3.9: 3D meshed view from *COMSOL®* for the Halbach magnet simulation, and its inner diameter represented.

Figure 3.10: (a) Meshed view of the Halbach structure (b) Magnetic field distribution along the x, y and z-axis, around the centered area of interest.

Each individual magnet of the experimental prototype has a square cross section and is similar to the magnets used in the simulation (12.8mm $\times$ 12.8mm $\times$ 60mm N52 magnets). Because of the strong repel that occurs between the adjacent magnets in the Halbach array, the holder needs to be sufficiently resistant. Therefore PETG material was chosen for 3D printing of the holder. It is a Glycol modified version of Polyethylene Terephthalate (PET) which is widely used for water bottle production. PETG is one of the various material that can be melted in fusion deposition modeling (FDM), i.e. 3D printing, to create rigid object with good impact resistance. Moreover, PETG has almost no warping during 3D printing (distortion of the print), therefore, it provides precise structure. Besides, PETG is easier to print with because it stick easily to the bed, i.e. the printing surface, and comes without the inconvenience of other 3D materials. The PLA (polylactic acid) can easily have a warping effect, i.e. the print bends during the printing process, and can be too fragile to hold the magnets compared to the same structure in PETG. Besides, ABS (Acrylonitrile butadiene styrene) needs a thermal controlled environment and a higher temperature to melt, thus requiring an advanced 3D printer, while PETG is compatible with almost all 3D printers. Besides, PETG is less toxic while printing [105]. The 3D model of the structure to hold the magnets was designed on *Freecad*, a free 3D design software, before slicing the model in another free software for 3D printing called Cura. We use the term slicing as it produces slices for the 3D printer corresponding to each deposition layer, before loading the created *.stl* file on the printer to print.

Figure 3.11 shows the prototype with the commercial 1D WT10A Hall effect magnetometer inserted at the center to measure the B_0 field. We measured a field of $674mT$, close to the expected $699mT$ provided by the simulation. The discrepancy may be due to temperature conditions, dispersion in the elementary magnet saturation fields, as well as magnetometer positioning and orientation. Unfortunately, the resolution of the WT10A is only $1mT$, like many other com-

mercial Hall effect magnetometers that are able to sustain a field of several hundreds of millitesla, and we are not able to measure the B_0 field distribution over the $\pm 1mm$ range of interest. However, the SMH team in which I worked for this PhD thesis has recently developed an integrated gradiometer with two 3D Hall effect sensors that should exhibit a resolution at least better than $50\mu T$ along the 3 axis x, y and z (see figure 3.12). The 3D magnetometer is under testing, and it is expected to be able to accurately determine the field distribution inside the Halbach structure, as well as the position where this field exhibits the best homogeneity, i.e. the point where its magnitude is maximum.

Figure 3.11: The Halbach magnet on the right and the *WT10A* magnetometer with 1mT resolution on the left.
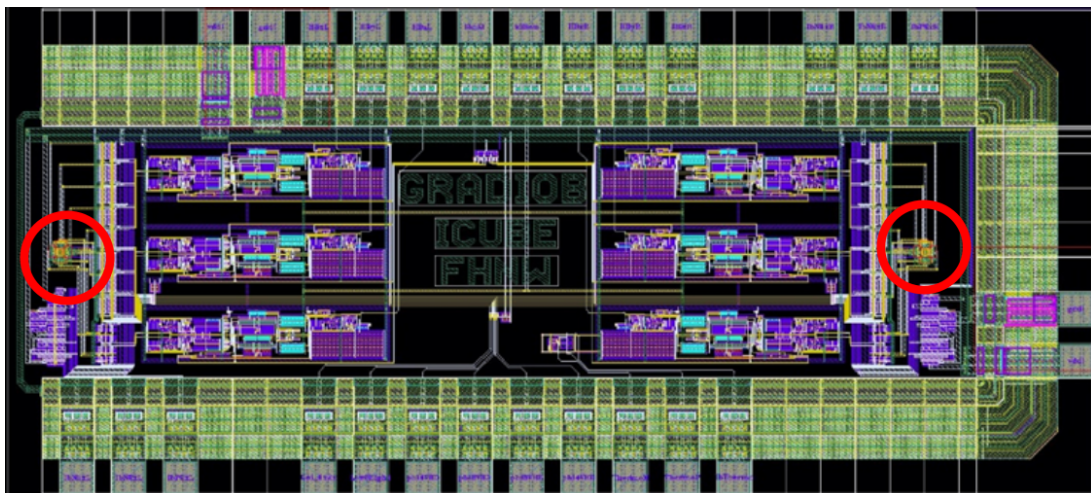
Figure 3.12: 3D CMOS integrated gradiometer. The two 3D Hall devices are separated by 2.5mm, and are operated with a specific spinning current technique for resolution improvement [106]. Hall device have a footprint of 50µm x 50µm and are highlighted in the red circles.

As discussed above, we tried to obtain a FID signal with our Halbach magnet prototype using a capillary tube of $1.8mm$, and the integrated receiver described in chapter 6. A solenoidal

coil to transmit the RF wave to the sample has been made, and matched to 50Ω to have a full power transmission. The RF wave was produced with a signal generator (The SML03 from Rohde & Schwarz®) and was amplified by a 10KHz to 100MHz RF Power amplifier from Amplifier Research®. A second coil were handwired around the capillary tube and connected to the receiver. Both coil were tuned to the Larmor frequency. Unfortunately we were not able to get a usable signal. It comes from several factors. First we did not know the exact position of the location where the B_0 field is maximum, and thus the most homogeneous area. In addition, the B_0 field value depends on temperature, and it was very difficult to know the exact value of the field, and thus the right resonance frequency, during our numerous tentatives to get a signal. We tried to sweep the frequency of the RF wave to find the right Lamor frequency, but the sweeping range was too wide, and may vary during the experiment due to temperature variation over the day. So we finally decided to used the magnet of a commercial NMR benchtop equipment, a Magritek 60 [107], as discussed in chapter 5. However, the preliminary results we obtained showed that the realization of a low-cost NMR magnet for portable NMR probe should be possible. It will require shimming coils for inhomogeneity compensation [108, 99, 77, 76], as well as a thermal sensor to adjust the frequency at which the electronics will sense the FID signal. Such a work is however out of the scope of this study.

3 Electronic and magnetic field compatibility

Twenty years ago, a few publications have reported parasitic effects on the electrical characteristics of Field Effect Transistors [109, 110]. However no satisfactory explanation were given, and no research was subsequently performed on the topic, certainly because the applications of such high fields are limited. We should also mention that many publications have reported electronic circuits that work as expected under magnetic field, especially under small or moderate fields. Although we may expect low effects of magnetic field on MOS transistor electrical characteristics when they are placed in field close to 1T, i.e. in field magnitudes we are dealing with portable NMR probes, we studied theoretically and experimentally the effect of strong magnetic fields on MOS transistors in order to predict possible deviations of their characteristics, as well as from which field magnitude these deviations may disturb the circuit behavior.

3.1 Theoretical background

The theory is presented with a NMOS transistor, but is readily applicable to PMOS transistors as well. In a NMOS transistor, when a positive voltage V_{DS} is applied, a longitudinal electric field E_l takes place in the channel, and electrons flow from the source to the drain. Noting ν their speed, when a magnetic field B is applied, the moving electrons feels the Laplace force:

$$F_L = -q \cdot E_l - q \cdot \nu \times B \tag{3.21}$$

The energy they acquire with F_L is lost in the silicon lattice through scattering, and the resulting equilibrium leads to an average electron velocity proportional to F_L:

$$\nu = \frac{\mu_n}{q} \cdot F_L = -\mu_n \cdot E_l - \mu_n \cdot \nu \times B \tag{3.22}$$

where μ_n is the electron mobility. The current density is then:

$$j = -n \cdot q \cdot \mu_n \cdot E_l - \mu_n \cdot j \times B \tag{3.23}$$

Using the relation $(U \times V) \times W = (U \bullet V) \cdot V - (V \bullet W) \cdot U$ where U, V and W are vectors, expression 3.23 can be solved to give j versus E_l and B:

$$j = \frac{\sigma_n \cdot E_l + \mu_n \cdot \sigma_n \cdot (E_l \times B)}{1 + \mu_n^2 \cdot B^2} \tag{3.24}$$

where $\sigma_n = n \cdot q \cdot \mu_n$ is the silicon conductivity.
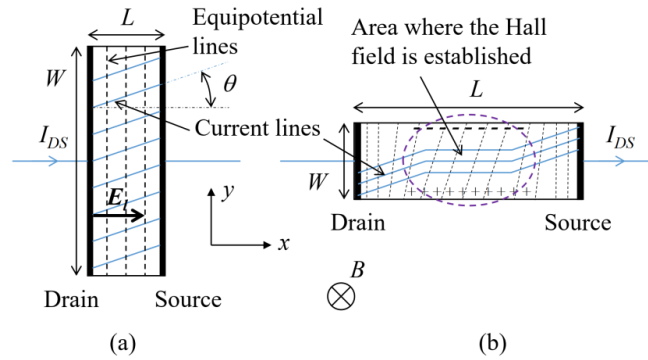
Figure 3.13: (a) short transistor, (b) long transistor, under magnetic field B

As seen in figure 3.13-a, for a short channel, i.e. a transistor with a small L/W ratio, the drift electric field in the channel, E_l, remains along the x axis, i.e. perpendicular to the equipotential lines formed by the source and drain that are assumed as ohmic contacts. Expression 3.24 shows that in this case the drift current is no longer aligned with E_l. It is tilt by the angle θ, where $tan(\theta) = \mu_n \cdot B$, and can be decomposed as a longitudinal component, j_x, and a perpendicular component, j_y:

$$j_x = \frac{\sigma_n \cdot E_l}{1 + \mu_n^2 \cdot B^2} \text{ and } j_y = \frac{\mu_n \cdot \sigma_n \cdot (E_l \times B)}{1 + \mu_n^2 \cdot B^2} \tag{3.25}$$

For a short channel the electrons which tend to accumulate on the lateral side, due to j_y, flow immediately back through the source and drain ohmic contacts. On the contrary for long transistors, i.e. when L/W is high, in the center of the channel the resistive path for the electrons to flow back through the source and drain is too high, and electrons accumulate on one side of the channel where a negative surface charge appears, while the other side exhibits a deficit of

electrons, i.e. a positive surface charge. This brings an electric field along y, the Hall field, and an electric force opposite to the Lorentz force. Finally, both forces are balanced, and the current lines remain along x in the center of the channel (see figure 3.13-b) while the electric field E_l is no longer aligned with x. A Hall voltage appears between the lateral sides of the MOS channel [111].

It is worth noticing that only the j_x component contributes to the drain to source current I_{DS}, which is expressed as [112, p.17].:

$$I_{DS} = KP_n \cdot \frac{W}{L} \cdot \left[V_{GS} - V_{Tn} - \frac{V_{DS}}{2} \right] \cdot V_{DS} \text{ for } V_{DS} \leq V_{GS} - V_{Tn} \tag{3.26}$$

and

$$I_{DS} = \frac{1}{2} \cdot KP_n \cdot \frac{W}{L} \cdot (V_{GS} - V_{Tn})^2 \text{ for } V_{DS} > V_{GS} - V_{Tn} \tag{3.27}$$

where V_{Tn} is the threshold voltage of the transistor, and KP_n the transconductance parameter given:

$$KP_n = \mu_n \cdot C_{ox} \tag{3.28}$$

with C_{ox} the gate capacitance per unit area.

So, for a small L/W transistor, the expression of j_x in equation 3.25 shows that under a magnetic field, the channel conductivity, respectively the carrier mobility, is reduced to an effective conductivity $\sigma_n(B)$, respectively an effective mobility $\mu_n(B)$, given by:

$$\sigma_n(B) = \frac{\sigma_n}{1 + \mu_n^2 \cdot B^2} \text{ and } \mu_n(B) = \frac{\mu_n}{1 + \mu_n^2 \cdot B^2} \tag{3.29}$$

As a consequence, for a small L/W transistor, the transconductance parameter has to be changed in the expression of the I_{DS} current by:

$$KP_n(B) = \frac{\mu_n}{1 + \mu_n^2 \cdot B^2} \cdot C_{ox} = \mu_n(B) \cdot C_{ox} \tag{3.30}$$

For long transistors, i.e. with a high L/W, rewriting equation 3.23 as:

$$E_l = \frac{j}{\sigma_n} + \frac{\mu_n}{\sigma_n} \cdot j \times B \tag{3.31}$$

shows that in the center of the channel, where j is aligned along x, the electric field is now the sum of a x-component given by $E_x = j/\sigma_n$ and a y-component given by $E_y = (\mu_n/\sigma_n) \cdot j \times B$. As a consequence, in the center, the channel conductivity is unaffected by the magnetic field and remains equal to σ_n. Of course, close to the drain and the source, this is no longer valid since the current lines are deflected (see figure 3.13-b).

To summarize, the deflection of the current lines lead to an effective mobility of the carriers given by $\mu_n/(1 + tan^2\theta)$ where θ is the deflection angle. For small L/W transistors, θ remains

constant along the short channel (see figure 3.13-a), equal to $\mu_n \cdot B$, and I_{DS}, which is proportional to KP_n, is simply reduced by the reduction factor (RF):

$$RF = 1/(1 + \mu_n^2 \cdot B^2) \approx 1 - \mu_n^2 \cdot B^2 \tag{3.32}$$

For high L/W transistor, θ varies along the channel and the computation of I_{DS} is more complex. However, since the current lines are only tilt at the tips of the channel, i.e. close to the source and the drain, as shown in figure 3.13-b, the relative effect of the magnetic field on the MOS electrical characteristics is much lower than for a short transistor.

3.2 Experimental results

In order to compare the theory we developed with the experiment, a chip which integrates various NMOS transistors, and has been fabricated in the AMS $0.35\mu m$ CMOS technology. We focused on two of these transistors [113]. Both are interdigitated with two legs, the first one, M_0, with $W/L = 20/20$, and the second one, M_1, with $W/L = 20/0.35$. Thus each leg of M_0 has a size of $10/20$, while each leg of M_1 a size of $10/0.35$. The chip was encapsulated in a DIL ceramic package whose metallic cap was removed since it was slightly attracted when placed in the strong magnetic field. It means that the cap features a small amount of ferromagnetic components (Fe, Ni, or Co) and would have deviated the magnetic field from its expected direction. The chip was thus placed on a small printed circuit board (PCB) featuring BNC connectors in order to connect an Agilent 4156C Semiconductor Parameter Analyzer to the transistors. The PCB was designed to fit into the small animal cradle in order to be easily moved inside the bore of a 7T Bruker® BioSpec 70/30 MRI scanner (see figure 3.14). The Agilent® 4156C was placed outside the shielded room where is located the MRI scanner, and was connected to the chip through coaxial cables.
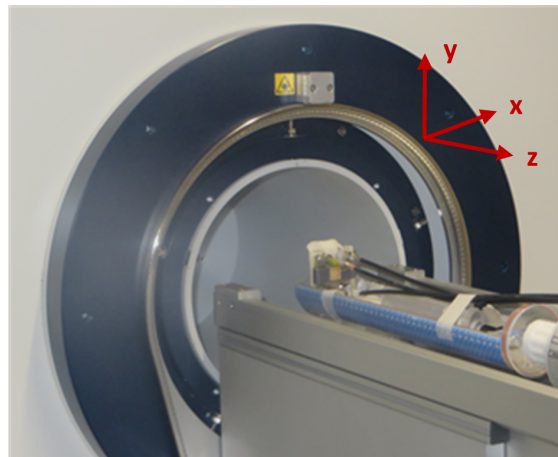

Figure 3.14: Chip under test in the MRI scanner, just before entering the scanner bore where a 7T field holds. The NMOS channel, i.e. the chip plane, is perpendicular to the magnetic field which is aligned with the scanner bore z-axis.

For several positions of the chip, the drain-to-source current versus gate-to-source voltage ($I_{DS} - V_{DS}$) of both transistors were recorded. First the chip was outside the scanner room, i.e. under the low earth magnetic field. We label this position P_0, the earth magnetic field being negligible. Then the characteristics were recorded (i) with the chip perpendicular to $B_0 = 7T$ (position $P_\perp$), i.e. with the chip placed vertically as shown in figure 3.14, B_0 being aligned along the z-axis, and (ii) with the chip placed horizontally (position $P_{//}$), i.e. with its plane parallel to B_0. In position $P_\perp$ the chip was also rotated by 90°, as well as flipped upside down, corresponding to another $P_{//}$ position, and whatever the $P_{//}$ position, no influence of the magnetic field was observed. On the contrary, in the $P_\perp$ position, a non-negligible influence was recorded. In addition, this influence has the same magnitude when the chip is flipped, i.e. rotated by 180° along the x-axis (see figure 3.14 for axis definition). Finally, from its $P_\perp$ position, the chip was also rotated by roughly 30° along the y-axis, as shown in figure 3.15. We label this position $P_{\perp 30}$. In this last position, a B_0 influence was also registered, but lower than in position $P_\perp$.
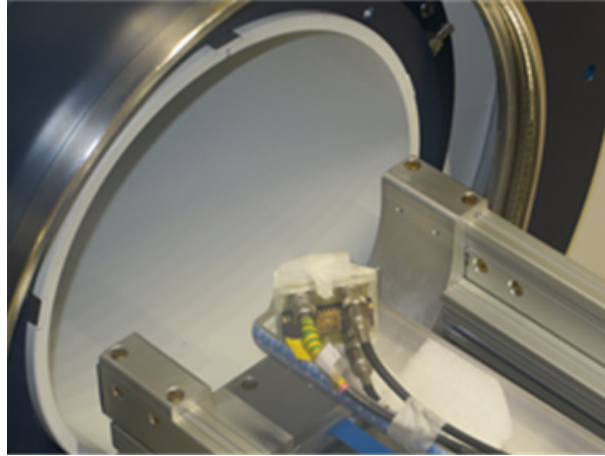
Figure 3.15: Chip in position $P_{\perp 30}$, just before entering inside the scanner bore.

The $I_{DS} - V_{DS}$ characteristic was recorded for $V_{DS} = 10mV$, and V_{GS} varying from $0V$ to $2V$. Such a measurement is reported in figure 3.16 for M_1 in position $P_\perp$. For $V_{GS} > V_{Tn} + 10mV$, the transistor is in linear regime and its current is expressed by equation 3.26 repeated here for convenience:

$$I_{DS} = KP_n \cdot \frac{W}{L} \cdot \left[V_{GS} - V_{Tn} - \frac{V_{DS}}{2} \right] \cdot V_{DS}$$

Taking the derivative dI_{DS}/dV_{GS} gives the slope:

$$\alpha = KP_n \cdot \frac{W}{L} \cdot V_{DS} = \mu_n \cdot C_{ox} \cdot \frac{W}{L} \cdot V_{DS} \tag{3.33}$$
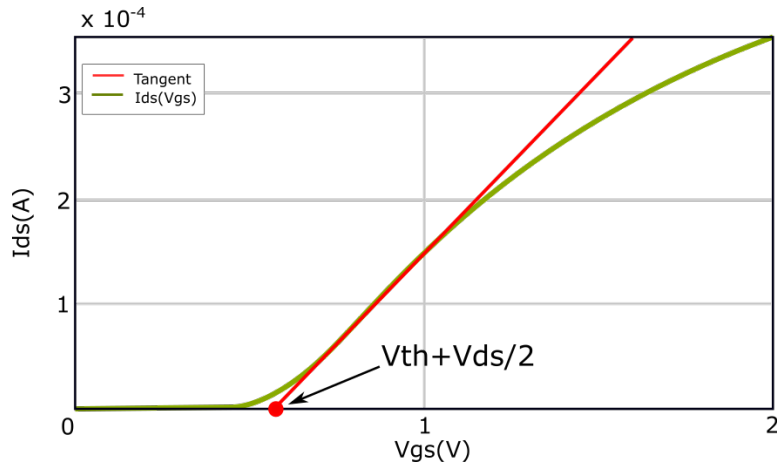
Figure 3.16: Measured $I_{DS} - V_{GS}$ characteristic of transistor M_1 in position $P_\perp$. V_{DS} has a constant value of $10mV$. The red straight line is the tangent to the $I_{DS} - V_{GS}$ curve at maximum slope.

When V_{GS} increases, the electrons are pushed towards the oxide-silicon interface and the carrier mobility is reduced due to surface scattering [114, p.142]. This well-known phenomenon explains why the slope α is not constant over the whole linear region. As seen in figure 3.16, it decreases when V_{GS} increases. Drawing the tangent to the $I_{DS} - V_{DS}$ curve with the maximum α slope (red straight line in figure 3.16) we can determine [114, p.156] (i) the transistor threshold voltage (V_{Tn}) by extrapolating the tangent till $I_{DS} = 0$, and (ii) the usual maximal transconductance parameter ($KP_n = \mu_n \cdot C_{ox}$), generally provided by the CMOS design kit, and used by the designer to determine by hand calculation the transistors' sizes once the biasing current is chosen. Instead of considering only the usual maximum value of α, we determined α for different values of V_{GS}, i.e. $V_{GS} = 0.6V, 0.8V, 1V, 1.2V$, and $1.5V$. Results are summarized in Table 3.6 for M_0 and in Table 3.7 for M_1 in positions P_0, $P_\perp$, and $P_{\perp 30}$.

V_{GS}	$\alpha(\mu A/V)$ M_0 in P_0	M_0 in $P_\perp$		M_0 in $P_\perp 30$	
		$\alpha(\mu A/V)$	$\frac{\Delta\alpha(P_\perp)}{\alpha(P_0)}$	$\alpha(\mu A/V)$	$\frac{\Delta\alpha(P_\perp 30)}{\alpha(P_0)}$
0.6	8.40	8.18	-2.62%	8.36	-0.48%
0.8	8.39	8.13	-3.10%	8.32	-0.83%
1	8.11	7.98	-1.60%	8.16	+0.62%
1.2	7.70	7.57	-1.69%	7.79	+1.17%
1.5	6.86	6.68	-2.62%	6.86	-0.07%

Table 3.6: Slope α for M_0(W/L=20/20) versus V_{GS} for relevant positions of the chip.

V_{GS}	$\alpha(\mu A/V)$ M_1 in P_0	M_1 in $P_\perp$		M_1 in $P_\perp 30$	
		$\alpha(\mu A/V)$	$\frac{\Delta\alpha(P_\perp)}{\alpha(P_0)}$	$\alpha(\mu A/V)$	$\frac{\Delta\alpha(P_\perp 30)}{\alpha(P_0)}$
0.6	410	374	-6.73%	381	-4.99%
0.8	396	370	-6.57%	378	-4.55%
1	330	313	-5.15%	317	-3.94%
1.2	271	259	-4.43%	263	-2.95%
1.5	199	193	-3.02%	196	-1.51%

Table 3.7: Slope α for M_1(W/L=20/0.35) versus V_{GS} for relevant positions of the chip.

It is worth to notice that $V_{Tn} \approx 560mV$ was not influenced by the strong magnetic field. On the contrary, α is reduced as shown in Tables 3.6 and 3.7 through the computation of the relative reduction factor $\Delta\alpha/\alpha(P_0) = (\alpha - \alpha(P_0))/\alpha(P_0)$. This is very clear for M_1, and this reduction is stronger on the short transistor, M_1, than on the long one, M_0. In addition, for a given biasing, the reduction of α is smaller when the transistor is in position $P_{\perp 30}$ than in $P_\perp$. The slight increase observed for M_0 in $P_{\perp 30}$ when $V_{GS} = 1V$ and $1.2V$ is not relevant. Indeed, α being a derivative, the error on its computation is amplified by the measurement noise. So, in position $P_{\perp 30}$, where the reduction of α is small, the computation noise is certainly higher than the magnitude of α change, i.e. close to $\pm 1\%$, which explains why the deviations on α observed for M_0 are not relevant.

For short transistors, i.e. for M_1, using equation 3.32, the relative reduction factor is expressed by:
$$\frac{\Delta\alpha}{\alpha(P_0)} = \frac{\alpha - \alpha(P_0)}{\alpha(P_0)} = \frac{\mu_n(B) - \mu_n(B=0)}{\mu_n(B=0)} \approx -\mu_n^2 \cdot B^2 \qquad (3.34)$$

from which we can determine the value of the electron mobility μ_n (see Table 3.8).

$V_{GS}(M_1)$	0.6V	0.8V	1V	1.2V	1.5V
$RRF = \Delta\alpha(P_\perp)/\alpha(P_0)$	-6.73%	-6.57%	-5.15%	-4.43%	-3.02%
$\mu_n(cm^2 \cdot V^{-1} \cdot s^{-1})$	370	366	324	300	248

Table 3.8: Electron mobility determination from the relative reduction factor $RRF = \Delta\alpha(P_\perp)/\alpha(P_0)$.

The experimental value of $370cm^2 \cdot V^{-1} \cdot s^{-1}$ for μ_n at low V_{GS}, i.e. $V_{GS} = 0.6V$, is a typical value of the mobility at the gate-oxide interface in a NMOS transistor. The reduction of μ_n with V_{GS} is also in very good agreement with the experiment [115]. Finally, to validate the theory which states that only the out of plane component of the magnetic field influences the transistor char-

acteristics, we simply computed the ratio of the reduction factor in position $P_{\perp 30}$ to the reduction factor in position $P_\perp$, i.e. $RRF(P_{\perp 30})/RRF(P_\perp)$.

It should be equal to $(\cos\beta)^2$, where β is the angle by which the chip was tilted along the y-axis to be placed in position $P_{\perp 30}$ (see figure 3.15). Results for M_1 are given in Table 3.9 where we get an average value of $(\cos\beta)^2 = 0.68$. It corresponds to $\beta = 35°$ which is in good agreement with the experiment, where the manual tilt of the chip was not very accurate (see figure 3.15).

$V_{GS}(M_1)$	0.6V	0.8V	1V	1.2V	1.5V
$RRF = \Delta\alpha(P_{\perp 30})/\alpha(P_1) = (\cos\beta)^2$	0.74	0.69	0.77	0.67	0.50
$\mu_n(cm^2 \cdot V^{-1} \cdot s^{-1})$	370	366	324	300	248

Table 3.9: Computations of $(\cos\beta)^2 = \Delta\alpha(P_\perp)/\alpha(P_0)$.

3.3 Discussion

We were able to show that as reported more than twenty years ago a strong magnetic field may have an influence on the electrical characteristics of MOS transistors. It comes from the deviation of the current lines inside the channel leading to an increase of the channel effective resistivity. This translates in a reduction of the transconductance parameter, and thus of the transconductance of the transistor. Only the out of plane component of the magnetic field influences the transistor behaviour, and a transconductance reduction close to 7% under a $7\,T$ field was measured for a short transistor biased with a small overdrive voltage $V_{GS} - V_{Tn}$. For a higher overdrive voltage, the transconductance reduction is smaller since this reduction is proportional to the square of the electron mobility, and the electron mobility is well known to be reduced under high V_{GS} voltage. Experiment are in good agreement with the theory, and more details can be found in [113, 115] where we also developed a first model that is valid in linear regime and strong inversion. This study shows that for portable NMR where the B_0 field will be around $1\,T$, we can neglect the influence of B_0 on the transistors behaviour. However, it should be noticed that since the influence is proportional to the square of the magnetic field, in NMR experiments using field such as $20\,T$, it may be very challenging to place CMOS electronics inside the NMR chamber. Indeed, the 7% transconductance reduction we observed under $7\,T$ translates into a 63% reduction. It is worth to also notice that using high mobility technology such as AsGa, where the electron mobility may be six times higher than in silicon, can be very challenging under strong magnetic. Finally, it should be noticed that the designer can mitigate the influence of the magnetic field by using high $V_{GS} - V_{Tn}$ overdrive voltage to take benefit from the mobility reduction with V_{GS}.

$$*$$
$$* \quad *$$

Summary

In this chapter, one of the key elements of the NMR portable probe, the magnet, was introduced. First a brief review of the theory on magnetic field was presented with the units and equations used in magnetism. Then, after analyzing the different magnet technologies, we showed that a good candidate for portable probe is a passive magnet based on a Halbach array. The design process of such a magnet, as well as the material to be used for the elementary magnets that constitute the array was presented. Then a 8-element Halbach array was designed, simulated, and fabricated using commercial elementary N52 Neodymium magnets. The measured magnetic field at its center is close to what we obtained in simulation. However, it was not possible to measure its inhomogeneity since such an experiment requires a better magnetometer that the commercial Hall sensor we have, as well as an improved experimental setup. Simulations have shown that shimming the Halbach array is mandatory to drastically improved the homogeneity that is a key parameter for NMR spectrometry. However, this preliminary study opens the way for a low-cost, light, and passive magnet suitable for portable NMR spectrometry. This chapter ends with a study done at the beginning of this PhD thesis, and discussing the influence of strong magnetic field on the electrical characteristics of MOS transistor. It is shown that an influence exists, and that its origin comes from the deviation of the current lines in the transistor channel when the channel senses an out of plane magnetic field. A simple model has been developed, and measurement performed under a field of 7T have demonstrated a reduction of the transconductance of NMOS transistors that can reach up to 7%. However, under moderate field of 1T, like in portable NMR, the magnetic field influence can be neglected.

Chapter 4

Nuclear Magnetic Resonance sensing head

In NMR, coils are used to transmit the NMR pulse $\vec{B}_1$ to flip the nuclear magnetization vector $\vec{M}$, and also to detect the transverse magnetization on the xy-plane, when the nuclei present in the sample are precessing during relaxation. Usually, in benchtop NMR, one coil acts as a receiver and transmitter alike, but some design integrates two coils, one to receive and another one to transmit. In the this last case, the transmitter coil is regularly called "Tx coil" as it transmits (Tx) the pulse, and the receiver (Rx) is known as "Rx Coil".

The purpose of the transmitting coil is to send an RF pulse to flip the magnetization vector to the desired angle. Consequently, the coil should transmit the pulse from an RF generator to the sample with the maximum efficiency at Larmor frequency. An RF coil has a specific frequency bandwidth at which it operates, and most of the coils are tuned for a specific nucleus. Carbon or hydrogen are predominantly used since they are two abundant nuclei. A pulsed RF source delivers the signal to a power amplifier that provides enough power to the coil. However, the coil has to be tuned at the right resonant frequency and, if necessary, matched to avoid reflections so the maximum power is transferred to the coil (i.e. B_1 without loss) and then to the sample.

To sense the transverse magnetization emitted by the sample during relaxation, we also use a coil because of its low resistivity, and therefore low thermal noise, as well as the possibility to tune it to a specific frequency, and then taking benefit from its quality factor and passive amplification. As already discussed in section 2.5 of chapter 2 (see equation 2.30), the relaxation field the receiving coil senses from an elementary volume of the sample at distance r from the coil is proportional to the field B_u the coil would produce in this elementary volume from a current of 1A flowing in the coil. When the distance r is high, $B_u \approx 0$, and the coil senses no signal from such a distant sample element. It is thus possible to define the field of view of the coil as the volume around it which gives a no negligible signal, i.e. a signal above the noise level. Likewise, the filling factor is defined as the ratio of the field of view of the coil to the whole sample volume.

1   Types of Coils

1.1   Volumetric coils

Volumetric coils have the intrinsic advantage of surrounding the sample, thus for regular NMR applications the coil can be placed around the NMR tube, leading to a filling factor close to one. They are designed to provide a very homogeneous excitation field inside the ROI and most of the time, also to operate as transmitter/receiver coils [116]. Solenoid coils are extensively used as its geometry produces a strong and relatively homogeneous magnetic field leading to a higher sensitivity. Some setups were reported with solenoid coils achieving 100pL range detection (figure 4.1) [117, 118].
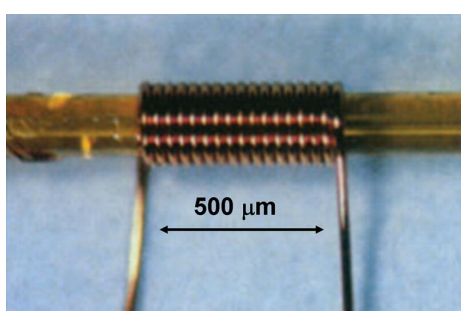

500 μm

Figure 4.1: Hand winded solenoidal coil measuring sub nL samples [119].

The impediment of such topography is the placement that requires to be perpendicular to the $\vec{B}_0$ axis (to have the 90° angle) for an NMR experiment, and in some setup can prove difficult to achieve.

1.2   Planar coils

Planar coils started to be used because of the necessity to measure smaller samples, at a time when solenoidal sub-nL coil were nearly impossible to realize due to the very thin enameled wire needed and the tedious handwork associated. The first usage is from Ackerman in 1980 [120]. His coil filing factor while observing a small sample was not sufficient, so he decided to use a planar coil in order to increase it and enhance its Signal to Noise Ratio (SNR). The planar topology is made from a conductor track in spirals above a substrate (epoxy, silicon or glass, for example on figure 4.2). Planar coils can also be obtained via standard lithographic processes from the microelectronic industry. Because of the coil geometry, the static magnetic field B_0 must be placed parallel to the coil surface. The main advantage of such geometry is the ability to attain very low sample volume and make surface test, for microfluidic experiments with 100-300nL sample volumes for example. Thanks to the CMOS technology, planar coils can be extremely miniaturized and exhibit high sensitivity. With all those advantages, it was possible to integrate them into miniaturized devices and provide sub-nL biological sample study [60].
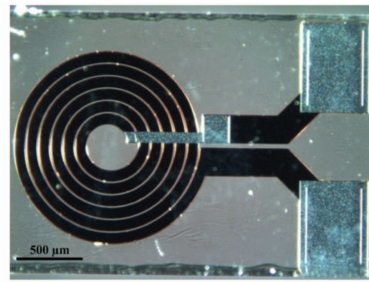
Figure 4.2: Planar microcoil with six windings with its underbridge and the pads visible [121].

1.3 Microslot and stripline

The stripline resonator shown in figure 4.3 and its downsized implementation, the microslot, has been created in 2007 in response to the problem of planar coils on semiconductor substrates that show lower signal sensitivity due to their geometry and low quality factor because of the electric losses in the substrate. Microslot provides a high quality factor, because of the cavity that separates the sensible stripline from the ground plane and permits a uniform B_1. Additionally, the susceptibility mismatch is minimized and such geometry has a high degree of integration with microfluidic [122, 25, 123]. The major disadvantage of such geometry is the difference between the sample and the design size. Indeed, at high NMR frequency, 300MHz for example, the design is around cm-sized and it is fixed for a given resonant frequency i.e. there is a need to adapt the sample size to the microslot/stripline.
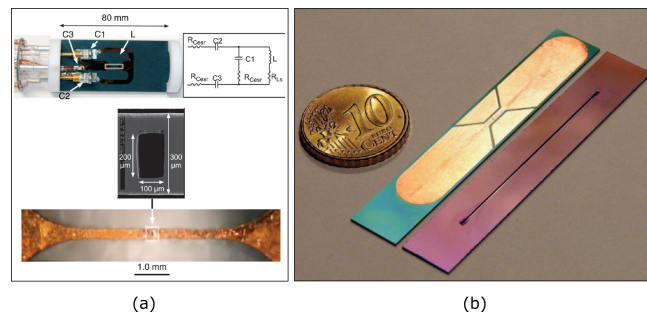

Figure 4.3: (a) Microslot probe with the detector area in white (b) Stripline design (the closest to the coin) and its encapsulation for a microfluidic chip [121, 124]

2 Signal to Noise Ratio and Limit of Detection

The Signal to Noise Ratio is a key parameter in NMR as it determines whether or not the relevant NMR spectrum will be detected and exploitable. As already stated, the maximum amplitude of the signal (in Volt) at the output of the receiving coil is expressed as (see equation 2.30 and 2.31):

$$S_0 = \eta \cdot w_L \cdot M_0 \cdot V_l \cdot B_u \tag{4.1}$$

where w_L is the Larmor frequency, η the coil filling factor, B_u its unitary field, V_l is the volume of the sample, and M_0 the magnetization vector for a nutation angle of 90° , i.e. at the beginning of the Free Induction phase.

In order to be exploitable, this signal amplitude has to be at least slightly above the noise level present at the output of the coil. As any resistive material, the receiving coil exhibits a thermal noise whose power spectral density $\overline{V_n^2}$ is proportional to the coil resistance, R_{coil}:

$$\overline{V_n^2} = 4 \cdot k \cdot T \cdot R_{coil} \tag{4.2}$$

Over the bandwith of interest Δf , which is typically a few Hertz in NMR (see discussion in chapter 2 on the chemical shift) the noise level at the output of the receiving coil is:

$$<V_n> = \sqrt{4 \cdot k \cdot T \cdot R_{coil} \cdot \Delta f} \tag{4.3}$$

As a consequence, the FID signal will be exploitable if S_0 is higher than $<V_n>$, in other words if the Signal to Noise Ratio (SNR) is higher than 1 [125, 126]:

$$SNR = \eta \frac{S_0}{\sqrt{4 \cdot k \cdot T \cdot R_{coil} \cdot \Delta f}} = \frac{\eta \cdot w_L \cdot M_0 \cdot V_l \cdot B_u}{\sqrt{4 \cdot k \cdot T \cdot R_{coil} \cdot \Delta f}} \tag{4.4}$$

It is worth noticing that the above SNR expression is optimistic since in practice we have also to consider the noise coming from the sample. Indeed, the thermal random motion of the spins inside the sample leads to an inductive noise signal at the output of the coil which adds up to the thermal noise coming from the resistance of the coil. As any thermal noise, the sample noise depends on the temperature of the sample. In addition, the receiving coil may sense any electromagnetic noise coming from the environment during the experiment. However, this last noise can be minimized by design. Finally, it is also important to be aware that the receiving electronic chain that follows the coil will also add its noise, especially the first Low Noise Amplifier. Equation 4.4 is thus the best SNR that can be achieved, and we may expect slightly worse value experimentally.

Although we did not focus our work on the design of the best coil, which could be a thesis work by itself, in order to be complete on this key topic of the receiving coil, it is important to mention here that R_{coil} is not determined by the simple expression of a resistance of length l, cross-section S, and made in material whose resistivity is ρ:

$$R = \rho \cdot \frac{l}{S} \tag{4.5}$$

Indeed equation 4.5 is only valid for a DC current. At RF frequency, the resistivity of the conductor is affected by the skin effect. This effect tends to push the carriers to the conductor's periphery as the frequency increases. Therefore the current is non-uniform in the wire and tends to circulate on the periphery over a distance called skin thickness and defined by the following

equation [127]:

$$\delta = \sqrt{\frac{1}{\pi \cdot \mu_0 \cdot \sigma \cdot f_0}} \tag{4.6}$$

where δ is the skin thickness, σ the conductor resistivity, μ_0 the vacuum permeability and f_0 the signal frequency (Hz).

It is common to find in literature analytical expression of the resistance taking the skin effect into account. The expression 4.7 gives the serial resistance Rs for a conductor of circular section and resistivity ρ [128].

$$Rs = \rho \cdot \frac{l}{\pi \cdot \delta} \tag{4.7}$$

In case of a planar coil the previous equation writes as follow:

$$Rs_{planar} = \frac{\rho \cdot l}{w \cdot \delta (1 - e^{\frac{-tm}{\rho}})} \tag{4.8}$$

with tm the metal thickness of the track, w its width, and l its length [127].

The second effect that induces a change in resistivity is called the proximity effect. This effect, in addition to the skin effect, corresponds to the influence of the tracks between them, which tends to push the carrier to one of the edges of the adjacent conductor. In the case of an inductor, the alternating current flowing through the conductor creates a turning field inducing eddy currents in the adjacent spire as shown in figure 4.4. Closer to the center of the coil, the magnetic field is stronger, hence the eddy current effect tends to become more important [129]. Moreover, the field created inside the conductor is opposite to the total field strength of the coil, which leads to a decrease in the inductance value as the operating frequency increases.
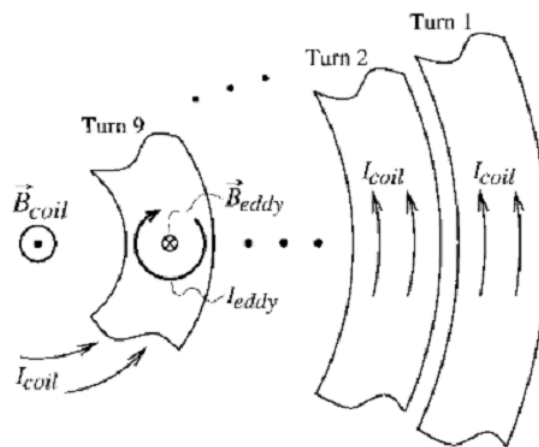

Figure 4.4: Representation of the eddy current effect between wires [130]

All those effects interact with each other making computation complicated. Therefore, using FEM simulation can prove beneficial in order to improve the coil design. For a first approach and

a rapid prototyping it is not necessary to go into such tedious task.

As it can be seen in equation 4.4, the SNR depends on the magnetization vector M_0, whose expression (see equation 2.19) is:

$$M_0 = \frac{N_s \cdot (\gamma \cdot \hbar)^2 \cdot s \cdot (s+1)}{3 \cdot k \cdot T} \cdot B_0 \tag{4.9}$$

It is proportional to the number of spins per unit volume N_s. As a consequence, for a given NMR probe, the SNR is proportional to the concentration of the substance that is analyzed. So, we define the limit of detection of the NMR probe, that is expressed in mol/l as:

$$LOD_c = \frac{c_c}{SNR} \tag{4.10}$$

where c_c is the concentration of the substance in mol/l. It may also be expressed in mol:

$$LOD_{mol} = \frac{mol}{SNR} \tag{4.11}$$

where mol is the amount of the substance in mole.

It is worth noticing that such definitions may vary from one author to another [131].

3   Impedance adaptation

Tuning and matching are necessary to get the best sensitivity for the receiver, and to optimize the power transmission to the transmitter coil. NMR coils are tuned at the Larmor frequency and matched to the impedance of the connected transmission lines. In other words, tuning means to adjust the resonant frequency, while matching means to adjust the impedance.

Concerning the transmitter, it is well known that to avoid any power reflection and ensure an optimal power transmission from the power amplifier (PA) to the transmitting coil, it is necessary for the PA to deliver its power to an impedance equal to the complex conjugate of its output impedance. Assuming the output impedance of the PA to be resistive, which is generally the case, the PA has to deliver its power to a resistive impedance equal to its output resistance. Most of the time the PA is connected to the transmitting coil through a transmission line, i.e. a coaxial cable whose characteristic impedance is equal to 50Ω. Thus the output resistance of the PA is also chosen equal to 50Ω. In addition, since the impedance of the coil is mainly inductive, a tuning/matching network placed between the coil and the transmission line is mandatory to make the impedance seen by the transmission line when looking to the coil equal to 50Ω at the Larmor frequency. We can also show that under such conditions, the transmitter head, i.e. the transmitting coil with its tuning/matching network resonate at the Larmor frequency.

On the receiver side figure 4.6, the picture is more complex. It is necessary to ensure, with a tuning/matching circuit, the best amplification of the tiny FID signal from the coil to the input of
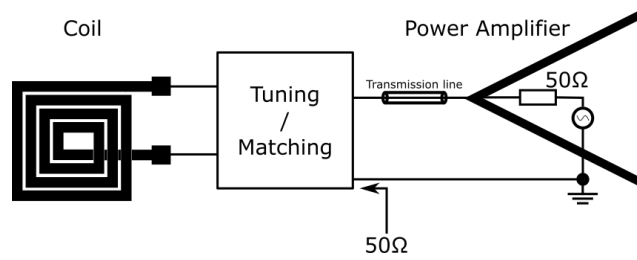
the LNA, which depends on the LNA input impedance Z_{LNA}.

Figure 4.5: Transmitter, where the coil is viewed as a 50Ω impedance resulting in an optimum power transfer to the sample.
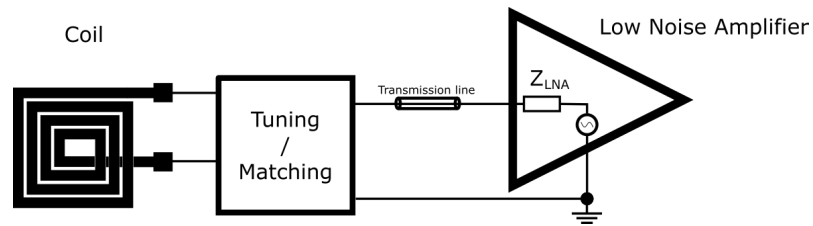

Figure 4.6: Receiver with its input impedance Z_{LNA}.

The receiver coil can be modeled with a very good approximation as an inductor L in series with a low value resistor R. When the low noise preamplifier (LNA) is in the vicinity of the coil, the coil is directly connected to the input of the LNA by simple, very short wires, and there is no need to consider the "transmission line" of the two connecting wires. On the other hand, at the Larmor frequency of the system, ω_L, if the LNA is placed far from the coil, typically at more than 1/10-th of the wavelength, it is usually connected to the coil via a coaxial cable, or other transmission line, of characteristic impedance 50Ω. This avoids interference from the measurement environment but also, by impedance matching, avoids the establishment of standing waves which can lead to a low amplitude of the signal at the LNA input if the input is in a node of the standing wave. It is important to note that, for this matching to be possible, the input impedance of the LNA must also be 50Ω, purely resistive, on the bandwidth of interest. This is the case for all commercial LNAs.

Thus, it is common in NMR to place a matching network at the output of the coil, and to connect it to the LNA via a coaxial cable, even if the distance between them is quite small. This matching circuit with the LNA usually consists of two capacitances C_1 and C_2 as shown in figure 4.7.
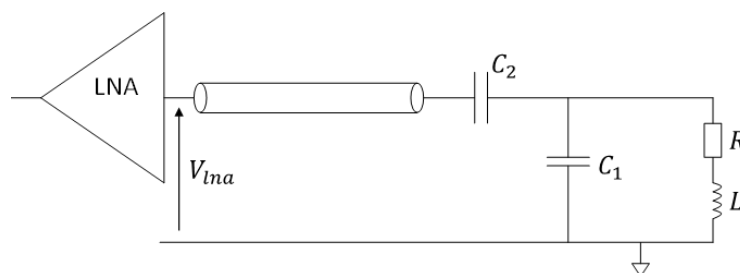

Figure 4.7: Measuring coil connected to the LNA via an matching/tuning network and a coaxial cable.

However, we are going to show that although it allows, at the Larmor frequency, to match the impedance of the link between the coil and the LNA, it does not provide the best achievable passive amplification from the coil to the LNA input. However, from a Signal-to-Noise ratio point of view, it is interesting to maximize this passive amplification factor, and we are going to show that this possible only if the LNA input impedance is infinite. In such a case however, the coil has to be placed close to the LNA and directly connected to it.

Suppose that at the Larmor frequency, the distance between the coil and the LNA is less than 1/10-th of the wavelength. In this case, neglecting the transmission line effect, the model of the sensing head reduces to that of figure 4.8. In this model, Z_{LNA} represents the input impedance of the LNA. As mentioned above, the input impedance of commercial LNAs is generally resistive, equal to 50Ω. Therefore, we will note R_{LNA} the input impedance of the LNA in order to remind that, on the LNA bandwidth, it is purely resistive. In figure 4.8, V_{fid} represent the RMS voltage of the FID at the output of the coil. It is assumed here that V_{fid} is purely sinusoidal at the Larmor frequency. In other words, it is assumed that T_2^* is very large, which does not detract from the generality of the demonstration. The term $\overline{V_{nlna}^2}$ represents the spectral density of noise from the LNA referred to the input of the LNA. Finally, the term $\overline{V_{ncoil}^2}$ represents the spectral density of thermal noise coming from the coil, i.e. related to its internal resistance R.
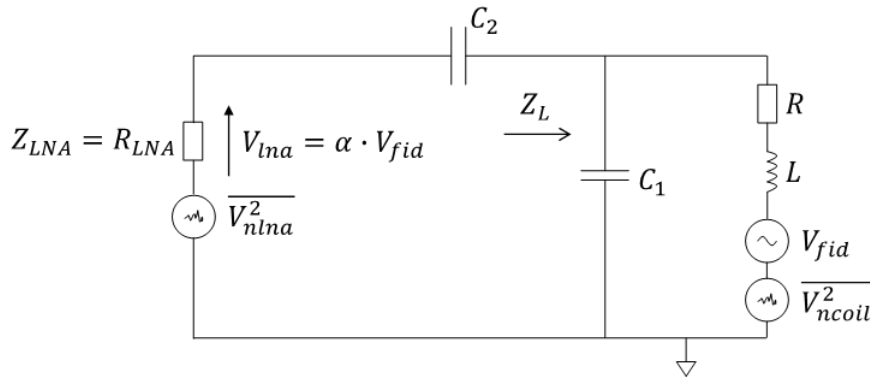

Figure 4.8: Model of the NMR measuring head in the case of a small distance between the LNA and the receiving coil.

The receiving coil is normally designed to have a good quality factor, $Q = (\omega_L \cdot L)/R$, at the Larmor frequency. We want to benefit from the resonance effect of the coil to amplify without any active component the signal V_{fid} around the Larmor frequency. The tuning circuit, classically made up of the capacitors C_1 and C_2 will therefore allow the coil to resonate and amplify by a factor α the signal V_{fid} seen at the input of the LNA, i.e. at the terminals of R_{LNA} the signal is $V_{lna} = \alpha \cdot V_{fid}$. We therefore seek to maximize α by playing on C_1 and C_2. However, it is important to note that as with the V_{fid} signal, $\sqrt{V_{ncoil}^2}$ is amplified by the same factor α. LNA and coil noises add up quadratically at the input of the LNA, leading to a total noise spectral density at the input of the LNA given by:

$$\overline{V_{ntot}^2} = \overline{V_{nlna}^2} + \alpha^2 \cdot \overline{V_{ncoil}^2} \tag{4.12}$$

The SNR of the system is therefore given by:

$$SNR = \frac{\alpha \cdot V_{fid}}{\sqrt{\overline{V_{nlna}^2} + \alpha^2 \cdot \overline{V_{ncoil}^2}}} \tag{4.13}$$

The maximization of α must lead to $\sqrt{\overline{V_{nlna}^2}}$ negligible in front of $\alpha \cdot \sqrt{\overline{V_{ncoil}^2}}$. Under these conditions, the SNR is optimal, equal to the intrinsic SNR of the coil:

$$SNR_{coil} = \frac{V_{fid}}{\sqrt{\overline{V_{ncoil}^2}}} \tag{4.14}$$

and the noise factor of the LNA (noise added by the LNA) is negligible.

We will first look for the value of the capacitance C_2 maximizing α for a given coil (R and L given) and a given but unspecified capacitance C_1. Of course, we place ourselves at the Larmor frequency, and we note at such a frequency $Z_L = R_L + j \cdot X_L$ the impedance seen from C_2 looking to the coil in parallel with C_1 (see figure 4.8). In this case, the model in figure 4.8, where we have removed the sources of noise since we are interested in the deterministic signal V_{fid}, reduces to the model in figure 4.9. The signal V_{eq} represents the signal across C_1 when the branch consisting of R_{LNA} and C_2 is absent (high impedance).
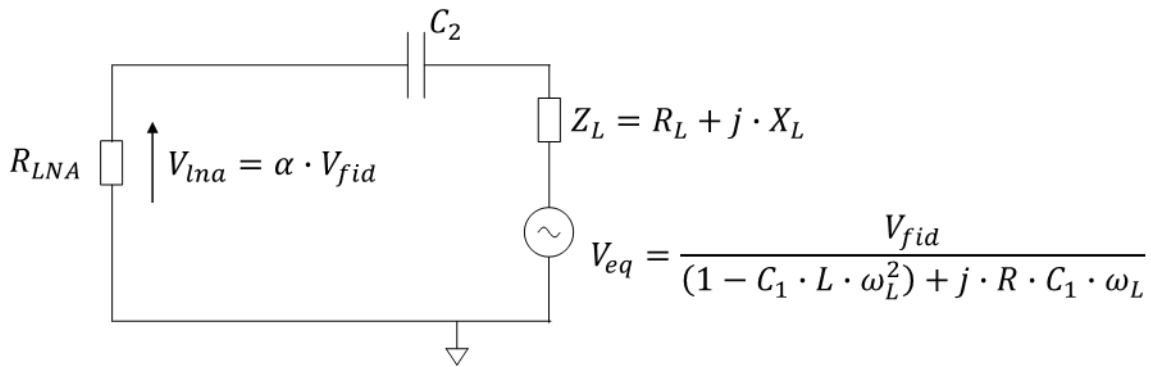

Figure 4.9: Equivalent diagram for the calculation of C_2 maximizing α.

It is important to note that R_L and C_L depend on C_1. A simple calculation gives:

$$V_{lna} = \frac{R_{LNA}}{R_{LNA} + R_L + j \cdot \left(X_L - \frac{1}{C_2 \cdot \omega_L}\right)} \cdot V_{eq} \tag{4.15}$$

In the previous expression only the term $\left(X_L - \frac{1}{C_2 \cdot \omega_L}\right)$ depends on C_2, and the maximization of V_{lna} by tuning C_2 asks to cancel this term, i.e. to choose:

$$C_2 = \frac{1}{X_L \cdot \omega_L} \tag{4.16}$$

With such a choice for C_2, V_{lna} now depends only on C_1:

$$V_{lna} = \frac{R_{LNA}}{R_{LNA} + R_L} \cdot V_{eq} = \frac{R_{LNA}}{R_{LNA} + R_L} \cdot \frac{V_{fid}}{(1 - C_1 \cdot L \cdot \omega_L^2) + j \cdot R \cdot C_1 \cdot \omega_L} \tag{4.17}$$

Note that if there is a transmission line, i.e. for instance a coaxial cable, between C_2 and the LNA, and if the input impedance of the LNA is equal to the characteristic impedance of the transmission line, then we are in the same situation as in figure 4.9 since from C_2, looking towards the LNA, we see a pure resistive impedance of R_{LNA}, typically equal to 50Ω as it is usually done in NMR receiver. So, what we are developing now is also valid for a coil linked to the LNA through a transmission line.

Now to find the value of C_1 that maximizes V_{lna} it is first necessary to express R_L, and thus X_L as a function of C_1 (at the Larmor frequency).

According to Figure 4.8, we have:

$$Z_L = \frac{R + j \cdot L \cdot \omega_L}{1 - C_1 \cdot L \cdot \omega_L^2 + j \cdot R \cdot C_1 \cdot \omega_L} \tag{4.18}$$

On the other hand, at the Larmor frequency, the quality factor of the coil is:

$$Q = \frac{\omega_L \cdot L}{R} \tag{4.19}$$

It should be reminded that the coil is normally designed to have a high quality factor at the Larmor frequency. We can then express Z_L by introducing Q in its expression:

$$Z_L = \frac{R + j \cdot Q \cdot R}{1 - R \cdot C_1 \cdot \omega_L \cdot Q + j \cdot R \cdot C_1 \cdot \omega_L} \tag{4.20}$$

where Q has a well defined value at the Larmor frequency (see equation 4.19). Noting $\alpha_1 = R \cdot C_1 \cdot \omega_L$, the only term depending on C_1 in the above expression of Z_L, we get:

$$Z_L = \frac{R + j \cdot Q \cdot R}{1 - \alpha_1 \cdot Q + j \cdot \alpha_1} = \frac{(R + j \cdot Q \cdot R) \cdot [(1 - \alpha_1 \cdot Q) - j \cdot \alpha_1]}{(1 - \alpha_1 \cdot Q)^2 + \alpha_1^2} \tag{4.21}$$

from which we deduce the expressions of R_L and X_L:

$$R_L = \frac{R}{(1 - \alpha_1 \cdot Q)^2 + \alpha_1^2} \tag{4.22}$$

$$X_L = \frac{Q \cdot R \cdot (1 - \alpha_1 \cdot Q) - \alpha_1 \cdot R}{(1 - \alpha_1 \cdot Q)^2 + \alpha_1^2} \tag{4.23}$$

Besides, in the expression of V_{eq} one can also introduce the terms Q and α_1. This leads us to the following expression for V_{lna}:

$$V_{lna} = \frac{R_{LNA}}{R_{LNA} + \frac{R}{(1-\alpha_1 \cdot Q)^2 + \alpha_1^2}} \cdot \frac{V_{fid}}{(1 - \alpha_1 \cdot Q) + j \cdot \alpha_1} \tag{4.24}$$

So we can now to maximize the module of V_{lna} by using the term α_1 which is the only one which depends on C_1 in the above expression for a given module of V_{fid}:

$$|V_{lna}| = \frac{1}{1 + \frac{R/R_{LNA}}{(1-\alpha_1 \cdot Q)^2 + \alpha_1^2}} \cdot \frac{|V_{fid}|}{\sqrt{(1 - \alpha_1 \cdot Q)^2 + \alpha_1^2}} \tag{4.25}$$

By introducing $X_1 = (1 - \alpha_1 \cdot Q)^2 + \alpha_1^2$, the above expression is simplified to:

$$|V_{lna}| = \frac{|V_{fid}|}{\sqrt{X_1} + \frac{R/R_{LNA}}{\sqrt{X_1}}} \tag{4.26}$$

It is easy to show that the denominator of the above expression has a minimum for $X_1 = R/R_{LNA}$ We can then determine if there is a value of C_1 allowing this condition. We must have:

$$\begin{aligned}
X_1 &= (1 - \alpha_1 \cdot Q)^2 + \alpha_1^2 = \frac{R}{R_{LNA}} \\
&\Leftrightarrow \alpha_1^2 \cdot (1 + Q^2) - 2 \cdot \alpha_1 \cdot Q + \left(1 - \frac{R}{R_{LNA}}\right) = 0 \\
&\Leftrightarrow \alpha_1^2 - 2 \cdot \frac{Q}{1 + Q^2} \cdot \alpha_1 + \frac{1 - R/R_{LNA}}{1 + Q^2} = 0 \\
&\Leftrightarrow \left(\alpha_1 - \frac{Q}{1 + Q^2}\right)^2 + \frac{(1 - R/R_{LNA}) \cdot (1 + Q^2) - Q^2}{1 + Q^2} = 0
\end{aligned} \tag{4.27}$$

For the previous equation to have a solution, it is necessary that:

$$(1 - R/R_{LNA}) \cdot (1 + Q^2) - Q^2 \leq 0 \tag{4.28}$$

which leads to:

$$R_{LNA} \leq (1 + Q^2) \cdot R \tag{4.29}$$

It is important to note that R is relatively small, a few Ohm, whereas Q can be relatively high, a few dozen. For example, for realistic values of $R = 5\Omega$ and $Q = 20$ we can find an optimum for the SNR if the input impedance of the LNA is lower than $2,005k\Omega$. This will be the case with a commercial LNA of input impedance 50Ω. We can also note that in this case, the amplitude of the signal at the input of the LNA, $|V_{lna}|$ is:

$$|V_{lna}| = \frac{|V_{fid}|}{2 \cdot \sqrt{R/R_{LNA}}} \tag{4.30}$$

Thus, the amplification factor α defined in figure 4.8 is only:

$$\alpha = \frac{\sqrt{R_{LNA}/R}}{2} \tag{4.31}$$

From this last equation, we deduce that R_{LNA} has to be chosen as large as possible, while checking that it is less than $(1 + Q^2) \cdot R$. However, it is also interesting to note that the condition on the ratio R_{LNA}/R (equation 4.29):

$$\frac{R_{LNA}}{R} \leq 1 + Q^2 \tag{4.32}$$

leads to a maximum value for α:

$$\alpha \leq \frac{\sqrt{1 + Q^2}}{2} \approx \frac{Q}{2} \tag{4.33}$$

Consequently, when R_{LNA} is relatively small, one cannot take full advantage of the quality factor of the coil, but can only benefit from 50% of the Q factor for passive amplification. In particular, this is the case when the coil has to be linked with a 50Ω transmission line to a commercial 50Ω LNA.

However, if R_{LNA} is greater than $(1 + Q^2) \cdot R$, especially if the input impedance of the LNA is infinite, then it is easy to show that the amplitude of V_{lna} is reduced by minimizing X_1. This is equivalent to choosing the term α_1 in such a way that $(1 - \alpha_1 \cdot Q)^2 + \alpha_1^2$ is minimum, that is:

$$-2 \cdot Q \cdot (1 - \alpha_1 \cdot Q) + 2 \cdot \alpha_1 = 0 \Leftrightarrow \alpha_1 = \frac{Q}{1 + Q^2} = R \cdot C_1 \cdot \omega_L \approx \frac{1}{Q} \tag{4.34}$$

and therefore to choose C_1 so that:

$$C_1 = \frac{1}{R \cdot \omega_L \cdot Q} = \frac{1}{\omega_L^2 \cdot L} \tag{4.35}$$

i.e. in such a way that the coil resonates at the Larmor frequency. In this case, X_1 is equal to:

$$X_1 = \frac{1}{1 + Q^2} \tag{4.36}$$

The amplitude of V_{lna} is thus given by:

$$|V_{lna}| = \frac{|V_{fid}|}{\sqrt{1/(1 + Q^2)} + \frac{R/R_{LNA}}{\sqrt{1/(1+Q^2)}}} \approx \frac{|V_{fid}|}{\frac{1}{Q} + Q \cdot \frac{R}{R_{LNA}}} \tag{4.37}$$

which can be written as:

$$|V_{lna}| \approx \frac{Q}{1 + Q^2 \cdot \frac{R}{R_{LNA}}} \cdot |V_{fid}| \tag{4.38}$$

From this last expression, we see that in terms of SNR, to take full advantage of the coil quality factor, an LNA with infinite input impedance should be chosen. In this case, the V_{fid} is amplified by a factor $\alpha = Q$ at the input of the LNA, and the SNR is optimal, close to the intrinsic SNR of the coil.

Finally, it is interesting to note that when X_1 is chosen minimal, i.e. equal to $1/(1 + Q^2)$, X_L is equal to 0 because the coil is resonating. Indeed:

$$
\begin{aligned}
X_L &= \frac{Q \cdot R \cdot (1 - \alpha_1 \cdot Q) - \alpha_1 \cdot R}{(1 - \alpha_1 \cdot Q)^2 + \alpha_1^2} = \frac{Q \cdot R \cdot \left(1 - \frac{Q^2}{1+Q^2}\right) = \frac{Q}{1+Q^2} \cdot R}{(1 - \alpha_1 \cdot Q)^2 + \alpha_1^2} \\
&= \frac{Q \cdot R \cdot \left(\frac{1+Q^1-Q^2-1}{(1-\alpha_1 \cdot Q)^2 + \alpha_1^2}\right)]}{(1 - \alpha_1 \cdot Q)^2 + \alpha_1^2} = 0
\end{aligned}
\tag{4.39}
$$

Consequently, under these conditions, i.e. when R_{LNA} is very high, even infinite, one has to choose $C_2 = 1/(X_L \cdot \omega_L)$ infinite, or simply, short-circuit C_2. The tuning circuit then reduces to a single capacitance C_1 which causes the coil to resonate at the Larmor frequency. Of course, such an SNR optimization is not possible with a coil which is linked to the LNA with a transmission line of 50Ω characteristic impedance since in this case, the input impedance of the LNA has to be equal to 50Ω.
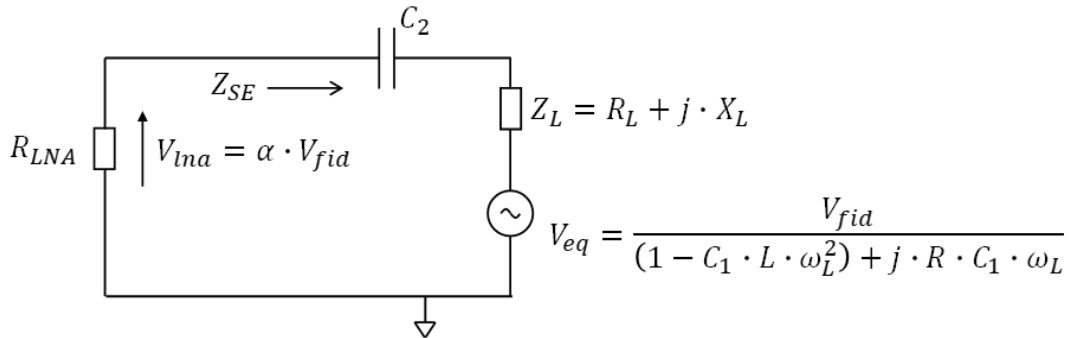

Figure 4.10: Definition of Z_{SE}

It is also interesting to compare the impedance Z_{SE} (see figure 4.10) seen from the LNA looking towards the sensing head, i.e. the tuning/matching network with the receiving coil, depending of the LNA input impedance, either $R_{LNA} = \infty$ or $R_{LNA} = 50\Omega$. When $R_{LNA} = \infty$, the tuning/matching network reduces to C_1 (C_2 short circuited) and C_1 is tuned to make the coil resonate. So Z_{SE} is simply equal to the small resistance of the coil:

$$
Z_{SE}(R_{LNA} = \infty) = R
\tag{4.40}
$$

On the contrary when $R_{LNA} = 50\Omega$, using equation 4.16 and 2.22, we have:

$$
Z_{SE} = R_L + j \cdot X_L - j \cdot \frac{1}{C_2 \cdot \omega_L} = R_L = \frac{R}{X_1}
\tag{4.41}
$$

Finally, since $X_1 = R/R_{LNA}$ when the sensing head is tuned/matched, we get:

$$Z_{SE} = R_{LNA} \tag{4.42}$$

It means that in this case, we are in the condition of optimal power transmission from the sensing coil to the input resistance of the LNA in order to ensure the best V_{lna} signal at the LNA input. This is exactly the same situation as for the transmitter previously discussed (see figure 4.5) where the impedance seen by the power amplifier when looking towards the transmitter head is equal to 50Ω. In the case where $R_{LNA} = \infty$, no power needs to be transmitted to the infinite input resistance of the LNA to have the best V_{lna} signal, and thus we do not need to be in the condition of optimal power transmission. It is worth noticing that this last situation provides the best SNR for the receiver.

In conclusion, when it is possible to directly link the receiving coil to the LNA, i.e. when the LNA is placed very close to the coil or, better, when the coil is co-integrated with its LNA on a single chip, we just need to link the coil to the LNA with a single C_1 capacitance, and the input impedance of the LNA has to be chosen infinite. Then, tuning C_1 to make the coil resonate at the Larmor frequency ensures the optimal SNR. On the other hand, when the coil is far away from the LNA, it is necessary to place at its output a tuning/matching network made of two capacitances C_1 and C_2, and to link this sensing head to the LNA through a coaxial cable. It is also mandatory to choose the input impedance of the LNA to be equal to the characteristic impedance of the coaxial cable. Then C_2 allows the impedance matching, while C_1 allows tuning the coil to provide the best signal, i.e. to make the sensing head resonate at the Larmor frequency. Notice that the optimal value of C_2 depends on C_1. In such a case, we are in the condition of an optimal power transmission from the coil to input resistance of the LNA.

Matching/Tuning in practice

In practice, the tuning is realized with a Vectorial Network analyzer (VNA), using either the wobble curve or the Smith chart (see figure 4.11). The wobble curve shows the reflection in dB at the input over a frequency range (see figure 4.11-a). Matching means that no power is reflected. Therefore, the lowest point of the wobble curve should be at the frequency of interest. It is common when tuning/matching to first adjust C_1 as it allows the tuning of the coil. It will easily move the lowest point of the curve close to the frequency of interest. Then adjusting C_2 will provide the matching, i.e. the lowest reflection. However, as already discussed, C_1 and C_2 being correlated, it is necessary to process step by step, adjusting C_1, then C_2, and repeat the adjustments until the best tuning/matching is obtained.

On the other hand, on a normalized Smith chart, the 50Ω is at the center of the chart on the real axis where the imaginary parts of the impedance cancel each other (see figure 4.11-b). To have a good tuning we need to be on this real axis, and to have a good matching we need to reach 50Ω and thus have the lowest reflection possible. By moving C_1 and C_2, as discussed

above, we can move the position of the point, which represents the impedance at the Larmor frequency, to the center of the chart. From experience, it is interesting to use first the wobble curve to roughly place the matching at the frequency of interest, i.e. the Larmor frequency, then use the Smith chart to finely tune the impedance to 50Ω.
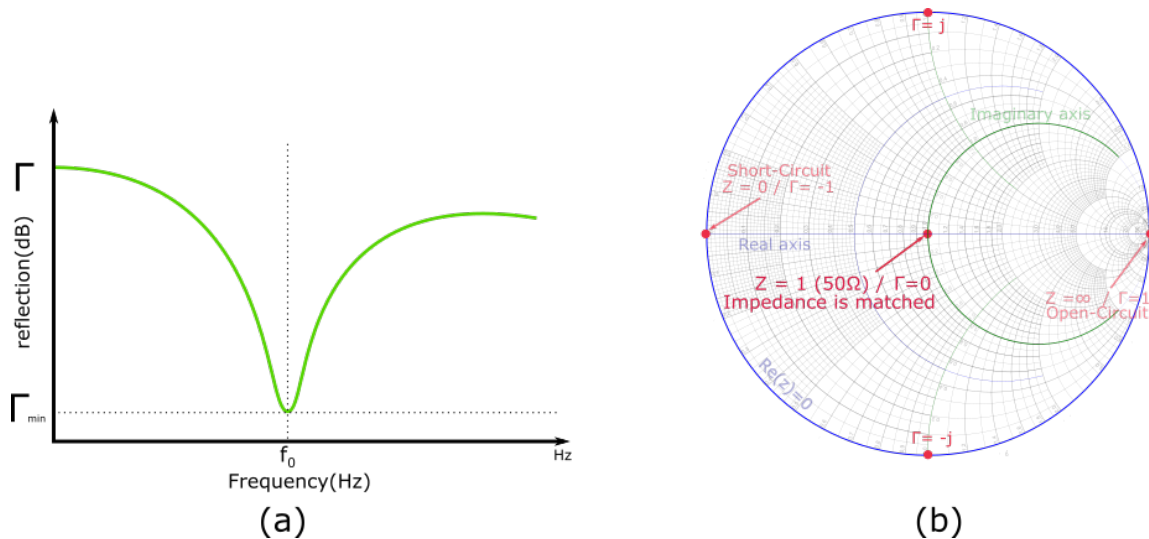

Figure 4.11: (a) Wobble curve where a coil is well matched at the frequency f_0, (b) Smith chart with its main parameters.

<div align="center">

*

*   *

</div>

Summary

This chapter has presented to the two key elements of the sensing head, i.e. the coil and its tuning/matching circuit, as well as the parameters that define the Signal-to-Noise ratio in NMR. The different types of coils have been briefly presented. When the geometrical constraints of the system allow volumetric coils to be used, the solenoidal coil is certainly the best choice since it wraps up the sample, providing a 100% fill factor. On the contrary, planar coils are good alternatives. Then the necessity of using a tuning/matching circuit between the coil and the input of the LNA was deeply discussed. It was demonstrated that the passive amplification that occurs when the coil is matched and tuned to the LNA input is limited to a relatively poor value, i.e. $\sqrt{R_{LNA}/R/2}$, when the LNA exhibits a finite input impedance, typically $R_{LNA} = 50\Omega$. In this case, a coaxial cable can be used to move the LNA far away from the coil. However, if the LNA can be placed close to the coil, no coaxial cable is required, and the best choice is to use a LNA with an infinite input impedance, which provides a passive amplification equal to the quality factor of the coil. In addition, in such a case, the tuning/matching circuit becomes a simple tuning capacitance.

Chapter 5

Discrete NMR receiver prototype

As we have shown in chapter 3, developing a portable magnet with a B_0 homogeneity compatible for NMR spectra acquisition is possible but requires possibly a whole PhD work. So, it was decided to use the magnet of a commercial benchtop NMR spectrometer, i.e. the Magritek 60. In addition, due to a long delay in chip delivery, and a design error that has limited the number of available chips as discussed in the next chapter, we decided not to use the integrated receiver we designed and fabricated, but to develop a discrete receiver from on-the-shelf components in order to perform our first NMR spectra acquisition, and assess if it is readily possible to detect water pollutants with a low cost NMR spectrometer. This chapter presents the Magritek 60 we used, as well as the discrete receiver we developed, and the first spectra we acquired.
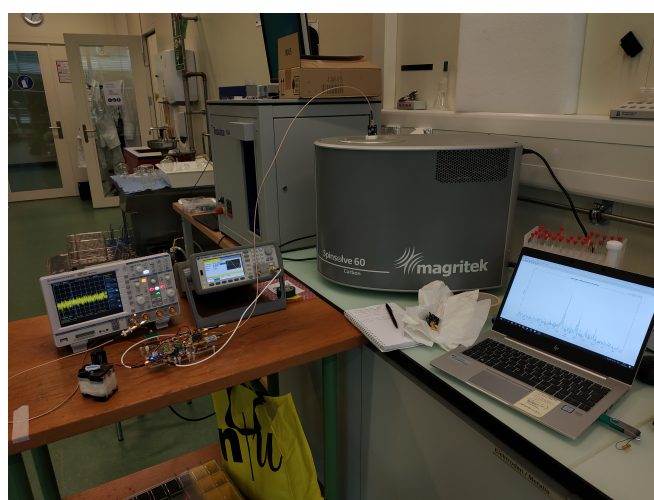
1   Magitrek benchtop characterization

Figure 5.1: View of the full setup.

As discussed in chapter 3, a simple Halbach array provides a field whose homogeneity is not sufficient to perform NMR spectroscopy. So, in order to validate the receivers we developed as well as our experimental procedure, we used the magnet of a Magritek 60 benchtop NMR [107],

as well as its transmitter. The Magritek 60 can be seen in figure 5.1 with the full experimental setup. The advantage of doing so is that it was also possible to compare the NMR spectra we acquired using our receiver with the NMR spectra acquired with the Magritek alone, i.e. using the Magritek receiver. The Magritek 60 has been designed to work at a Lamor frequency around 60 MHz. It means that its B_0 is around 1.5T. However, its exact value was not known. The equipment we used is owned by the University of Applied Science Northwest Switzerland (FHNW) (Fach-hochschule Nordwestschweiz, FHNW) in the city of Brugg in Switzerland. It is in a laboratory of chemistry, and used as a "plug and play" equipment. It means that no technical documentation about its internal architecture was available. In particular, we did not know where was the area of best field homogeneity, and in which direction the RF pulse was applied, as well as in which direc-tion the FID has to be sensed. In addition, the Magritek 60 uses a permanent magnet whose field value depends on temperature. It is thus placed in an air-conditioned room. However, although the Magritek 60 also features a system for temperature control, it was necessary to regularly shim it. The single information we had was that the bore where the tube containing the sample is placed has a diameter of 5 mm, and that the sample has to fill the tube up to a given level, as shown in figure 5.2. As a consequence, first, we had to characterize the main experimental parameters of the Magritek 60.
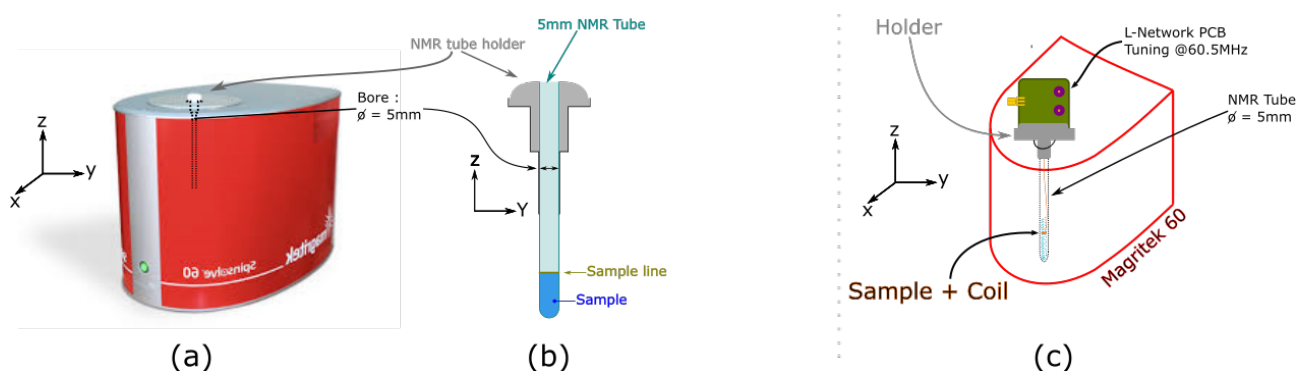

Figure 5.2: (a) The Magritek and the axis of reference, with the tube holder highlighted, (b) The holder with an NMR tube and the sample limit, (c) View of the Magritek with our probe. The tuning/matching circuit is highlighted.

As shown in figures 5.3 and 5.4, we used for that purpose a discrete receiver we developed, and the FID was acquired with an oscilloscope. Placed in a 5mm glass tube (see figure 5.5), the handmade receiving coil is connected to its tuning/matching network which is integrated on a small printed circuit board (PCB) placed at the input of the tube (see figures 5.2, 5.3, and 5.4). The tuning/matching circuit is linked to the Low Noise Amplifier (LNA) through a coaxial cable. The LNA is made of 3 commercial LNA in series, each one providing a gain close to 25dB. The amplification was limited to roughly 75dB since the room hosting the Magritek 60 contains many noisy equipments, and our discrete chain was quite sensitive to these perturbations. Increasing the amplification above 80 dB led to spurious signals at the output of the receiver and to difficulties to trigger correctly the FID signal. To mitigate the effect of these electromagnetic perturbations, a band-pass filter (50MHz to 70MHz) was placed right after the first LNA, allowing to easily trigger

the down-converted FID signal. Then, in order to be digitally converted by the oscilloscope, the signal is down-converted with a mixer, the Local Oscillator (LO) being provided from a RF generator. Finally, before entering the oscilloscope, the up-converted signals are removed thanks to a 500kHz anti-aliasing low-pass filter, which also helps in reducing the noise power.

Position of best magnet homogeneity

The best magnet homogeneity should be below the marker up to which chemists are required to fill the sample. This best position was confirmed by using a tube with a small amount of water, and moving its position inside the tube while acquiring the signal with the Magritek. The best signal was obtained when the sample is placed 3 mm below the marker. Hence, the coils were placed at this position for all experiments.

RF frequency and sensing direction

To know the frequency of the RF pulse as well as its direction, we used the two handmade coils shown in figure 5.5, one, the z-coil, to sense along the z-axis, the other one, the xy-coil, to sense along the x or y-axis, i.e. in the xy-plane. Axis directions are defined in figures 5.2 and 5.5. The RF pulse being strong, we didn't need to tune the coils which were directly connected to an attenuator and an oscilloscope. The coils were inserted in an empty 5 mm NMR tube (see figure 5.5) and placed at the best position defined previously, and the RF pulse sent by the Magritek was sensed. It was found that the transmitter is emitting in the xy-plane at a frequency of 60.502 MHz, we can say along the x-axis. This means that the B_0 field is perpendicular to this axis, i.e. either along the y-axis or the z-axis. The tube being along the z-axis, we finally assumed that B_0 should be along the y-axis, and that the FID has to be sensed along the z-axis. This was confirmed by doing an acquisition on a water sample with a tuned z-coil connected to our receiver prototype that is described below in details.
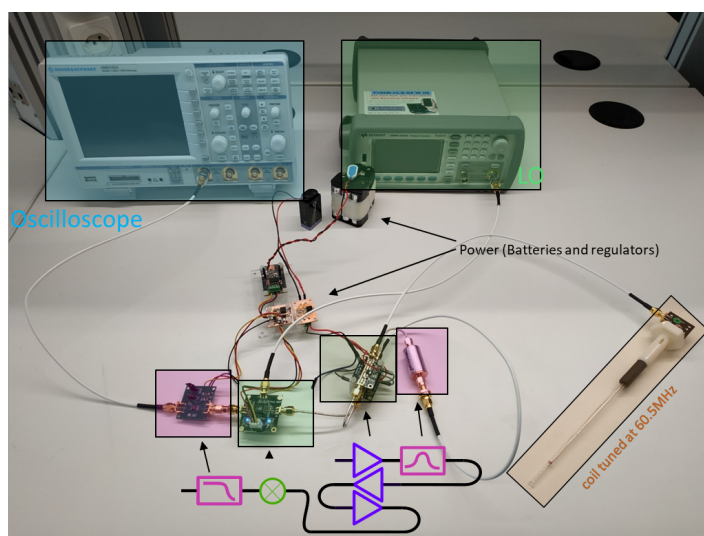

Figure 5.3: Split detailed view of the receiver and its connection to the oscilloscope and the RF generator that provides the reference signal of the mixer.
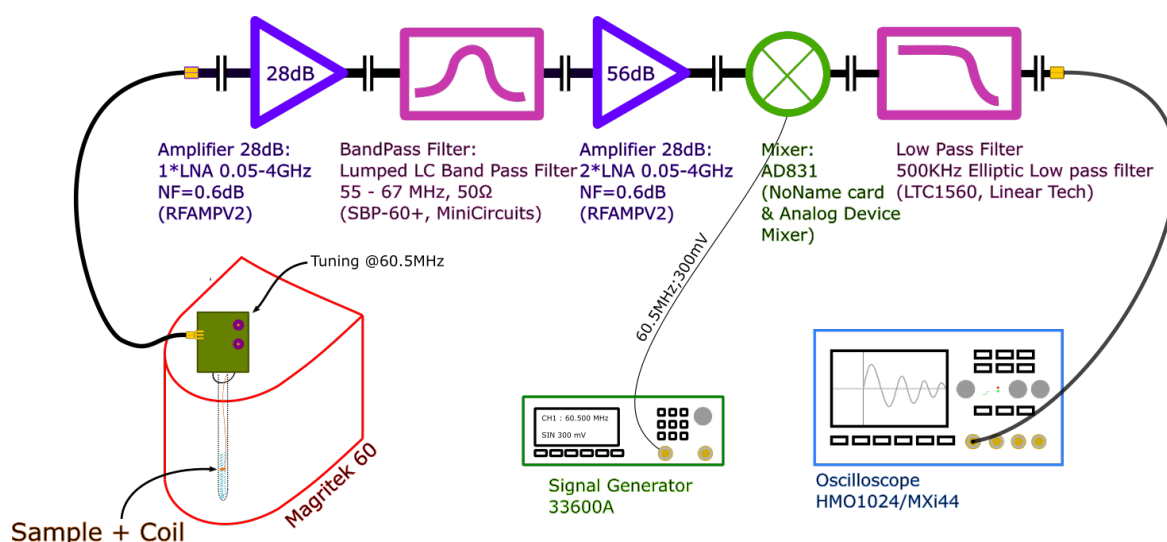
Figure 5.4: Detailed view of the setup with the different discrete components of the receiver.
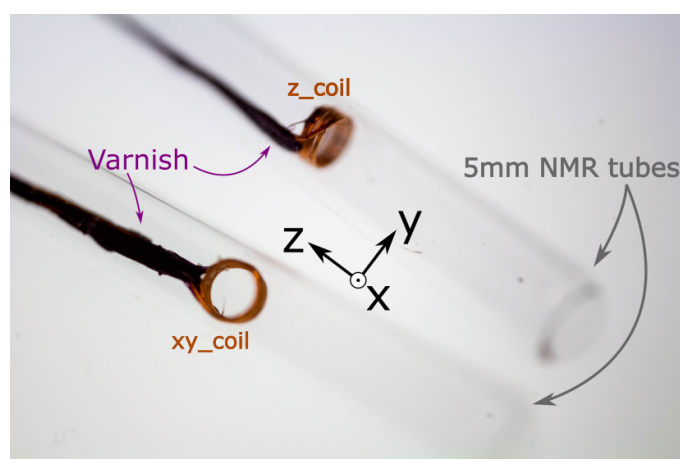

Figure 5.5: Coils used for the detection of the RF frequency transmission axis. Twisted wires are fixed with a varnish.

2 Discrete receiver prototype

The receiver is made of three key elements, the holder which has to maintain the tube and the receiving coil at the optimal position, the coil which has to be compatible with the chemical sample under test, and the receiving electronics which was already briefly discussed. These three key elements are now described in details.

2.1 Holder

To be able to maintain a 5 mm NMR tube inside the Magritek, a holder is provided with the Magritek, as shown in figure 5.6. It features a hole to easily slide the tube in it. So, a handmade z-coil could be inserted from the top to inside the tube. However, the holder tip is not adapted to easily fix the wires, and the coil may move. It is thus difficult to ensure that the coil is at the

best position inside the Magritek bore. In addition, the tuning/matching circuit has to be placed as close as possible to the coil, i.e. just at the tip of the holder (see figure 5.2-c), and the Magritek holder was not adapted to fix easily the tuning/matching circuit. So we fabricated our own holder.
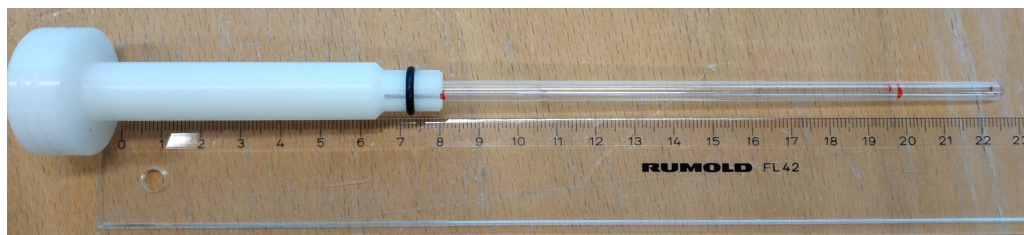

Figure 5.6: Magritek NMR tube holder with a 5mm NMR tube.

First holder prototype

The first holder prototype was 3D printed (see figures 5.7,5.8-a and 5.8-b) in an elastic material in such a way that the tube is maintained by compression. It was thus possible to easily remove it from the holder to fill it. A tuning/matching L-network PCB was placed on the top with the coil directly connected to it. This avoid any detuning. An acrylic backplate was placed on one side of the 3D printed elastic holder in order to screw the PCB without deforming the holder.
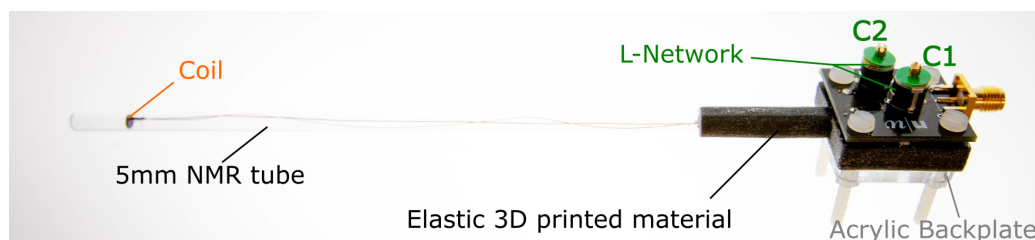

Figure 5.7: First holder prototype with a NMR tube featuring a z-coil. Capacitances C1 and C2 of the L-network tuning/matching circuit are highlighted..

Second holder prototype

In the first prototype, the wires' length was adjusted for the z-coil to be exactly at the optimal position for sensing. However, over time and refilling processes of the tube, the wires might move a little bit, and the best sensing position was lost. In addition, as shown in figure 5.8-a the elastic holder has a tendency to bend, and eventually the tube may shatter inside the Magritek. This has to be avoided! To get rid of these two drawbacks of the first prototype, two modifications were introduced. First, the coil wires have been made longer and were strapped on the back of the tuning/matching PCB, as shown in figure 5.8-c. Then, when required, the coil position can be moved and re-calibrated precisely, especially when the tube is changed. Second, the holder was printed with a rigid material for its upper part, and with an elastic material for its lower part, as shown in figure 5.9-a. The elastic lower part allows to maintain by a small compression the tube in the right position inside the holder, while the rigid part rests on the Magritek. This rigid part has

been designed with a large round base to be stable when it is positioned on the Magritek (see figure 5.9-a). Notice that the narrow protrusion on which the tuning/matching PCB is screwed has been printed in a less rigid material. Such a solution prevents any shattering of the tube inside the Magritek bore. Indeed, in case the coaxial cable which links the tuning/matching circuit to the preamplifier is inadvertently pulled, the PCB is pulled as well and may lead the protrusion to break. Then the coil slides ouside the tube, but the fragile tube would remains stable in its holder and would not break.
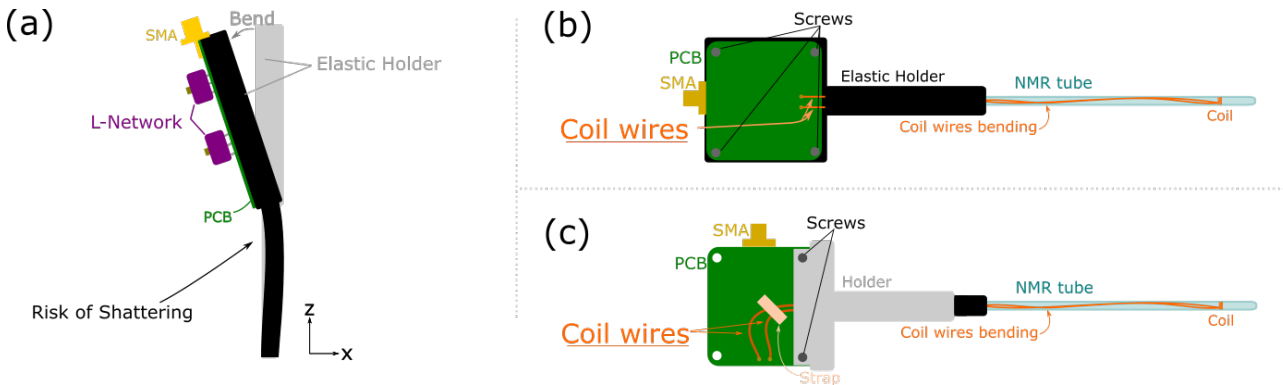

Figure 5.8: The different holders where the elastic material is represented in black, (a) The elastic holder bending issue, (b) First elastic holder, (c) Second holder prototype where the coil wires are strapped on the tuning/matching PCB.
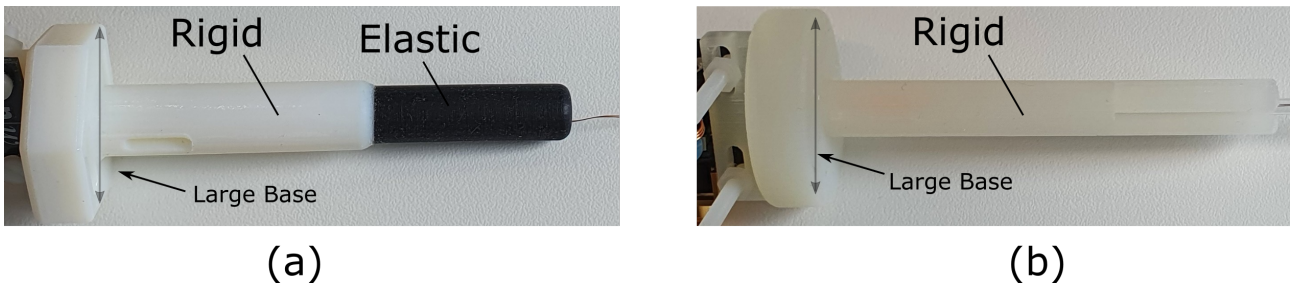
Figure 5.9: View of the two last holder prototypes, (a) second holder prototype with rigid and elastic material, (b) the latest improvement in rigid material only.

Third and last holder prototype

The main drawback of the second prototype was the elastic material that has a tendency to become sticky when temperature increases (hot summer temperatures). The fragile tube may thus be very difficult to remove from its holder. So finally, to avoid this issue, a new holder with rigid material only was printed. As shown in figure 5.9-b, it features slots in its lower part in order to maintain the tube with enough force but without breaking it. Besides, it has been printed vertically for precision. This ensures the glass tube is firmly held, and at the same time can slide easily without the risk of breaking when it is removed from the holder.

2.2   Receiving coil

Coil fabrication:

All coils we fabricated were hand-wired around a screwdriver, and the remaining wire that is inside and along the tube was twisted to improve rejection of external interferences. A varnish was then applied on the wires to fix them. The first coil made to detect the Larmor frequency of the Magritek had varnish only on the twisted wires (see figure 5.5). Indeed, the coil was hand-wired with enameled copper wire of 0.8 mm diameter, which is hard enough for the coil to keep its shape. The unitary field B_u discussed previously (see equation 2.30) allows to assess the coil sensitivity. Indeed, for a sufficiently long longitudinal coil we have:

$$B_u = \frac{B_1}{I} = \mu_0 \cdot \frac{N}{l} \tag{5.1}$$

where N is the number of turns, l the coil length, and μ_0 the vacuum permeability. So, using a small coil with many turns per unit of length, i.e. using wires with small diameter, improves the sensitivity. However, there is a limit to the wire length because of its resistance, as well as to the wire diameter because of the capacitive effect that will decrease the coil quality factor. Terman demonstrated that the best quality factor is for a coil whose length/diameter ratio is between 0.7 and 2.0 [128], a factor of 2.0 being the best because a longer coil provides a better homogeneity, thus improving the filling factor [132]. Besides, it is worth noticing that the proximity effect increases the resistance of the coil. Therefore, separating the wires a bit can be beneficial [128]. Hopefully, the resin covering enameled copper wire helps in lowering the proximity effect. Based on the above discussion, the next coil was fabricated with a 150 μm diameter enameled copper wire. Since the coil wire was not sufficiently rigid for the coil to naturally keep its shape, the coil and its tail twisted wires were coated with a nail varnish. Such a coil was used for our first NMR experiments in water and ethanol samples (see figure 5.10-a). However, in samples containing the acetonitrile eluent (CH_3CN), the varnish was slowly dissolved. Therefore, the varnish was replaced by an epoxy resin (DP125 3MScotch-Weld Epoxy Adhesive). It has to be noticed that the coil needs to be maintained during more than 150 minutes at room temperature for the resin to dry, so the fabrication was delicate. Moreover, because the epoxy may stick to the screw support after polymerization, leading to a difficult extraction of the screw, we fitted the screw with a thermoretractable sheath. The coil was then hand-wired on the sheath, the screw easily removed, as well as the thermoretractable sheath after shrinking it with hot air. The "epoxy coil" shown in figure 5.10-b was used for all subsequent experiments, especially for those with pesticide in acetonitrile solvent. Its geometrical and electrical characteristics are given in Table 5.1.
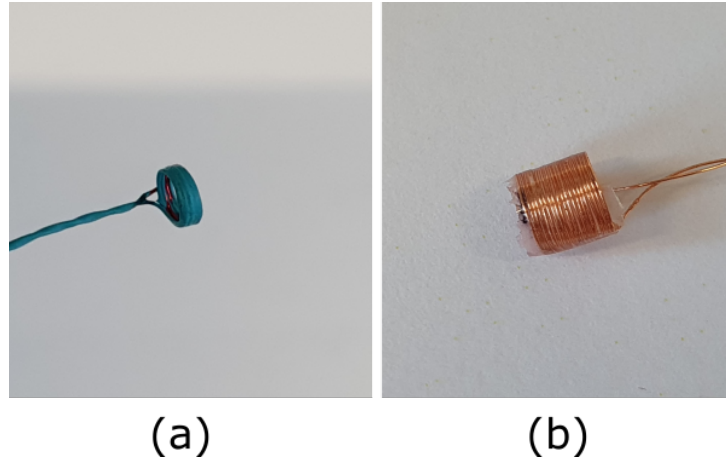
Figure 5.10: (a) Hand wired coil with varnish, (b) coil maintained by epoxy resin.

Coil	Varnish coil	Epoxy coil
Copper Wire	$130\mu m$ (bare), $150\mu m$ (enameled)	
N turns	5	21
Diameter	$3mm$	$3mm$
Length	$1mm$	$4mm$
Resistivity	0.8Ω	1.86Ω
Inductance	$450nH$	$630nH$

Table 5.1: Characteristics of the hand made coils.

Coil Matching

Since the discrete preamplifier could not be placed close to the coil, the receiver features a L-network tuning/matching circuit with two capacitances C_1 and C_2 that have to be adjusted. Using the model we developed in section 3 of chapter 4, we can determine the value of C_1 and C_2, once the electrical characteristics of the coil, i.e. R, L, and $Q = (\omega_L \cdot L)/R$, are known. Indeed, solving the second order equation 4.27, we get:

$$\alpha_1 = R \cdot \omega_l \cdot C_1 = \frac{Q \pm \sqrt{\frac{R}{R_{LNA}} \cdot (1 + Q^2) - 1}}{1 + Q^2}$$

$$\Leftrightarrow Q - \alpha_1 \cdot (1 + Q^2) = \pm \sqrt{\frac{R}{R_{LNA}} \cdot (1 + Q^2) - 1}$$

(5.2)

Equations 4.16, 4.23, and 4.27, lead to :

$$X_L = \frac{Q \cdot R \cdot (1 - \alpha_1 \cdot Q) - \alpha_1 \cdot R}{R/R_{LNA}} = \frac{1}{C_2 \cdot w_L}$$
$$\Leftrightarrow \left[Q - \alpha_1 \cdot (1 + Q^2) \right] \cdot R_{LNA} = \frac{1}{C_2 \cdot \omega_L}$$

(5.3)

Introducing equation 5.2 into 5.3, we obtain:

$$\frac{1}{C_2 \cdot \omega_L} = \pm R_{LNA} \cdot \sqrt{\frac{R}{R_{LNA}} \cdot (1 + Q^2) - 1}$$

(5.4)

since $C_2 \cdot \omega_L > 0$ we finally have :

$$Q - \alpha_1 \cdot (1 + Q^2) = \sqrt{\frac{R}{R_{LNA}} \cdot (1 + Q^2) - 1}$$

(5.5)

from which we get:

$$C_1 = \frac{Q - \sqrt{\frac{R}{R_{LNA}} \cdot (1 + Q^2) - 1}}{R \cdot \omega_L \cdot (1 + Q^2)}$$

(5.6)

$$C_2 = \frac{1}{R_{LNA} \cdot \omega_L \cdot \sqrt{\frac{R}{R_{LNA}} \cdot (1 + Q^2) - 1}}$$

(5.7)

Equations 5.6 and 5.7 were used to compute the value of C_1 and C_2, and variable capacitances whose span includes these values were mounted on the tuning/matching PCB. From a practical point of view, the matching was made with a vector analyzer, the Siglent® SVA1000X, to a pure 50Ω using the Smith chart and the wobble curve in reflection (S_{11}) as briefly discussed at the end of chapter 4. Indeed, the wobble curve mode allows to fastly approach the resonant frequency, and the Smith chart to find the optimal matching to 50Ω.

It is worth mentioning that for our experiments in water or ethanol, we simply performed tuning/matching at the laboratory, i.e. the coil being outside the tube. Introducing the coil inside the sample does not change drastically the tuning. On the contrary, for experiments in acetonitrile solvent, the permeability of the solvent was sufficiently different from the air permeability, and the tuning/matching was performed with the coil in the tube filled with the sample. Table 5.2 provides the tuning/matching capacitances determined from equations 5.6 and 5.7 for the two coils of Table 5.1.

Coil	Varnish coil	Epoxy coil
Q	212	128
C_1	$13.6 \ pF$	$9 \ pF$
C_2	$1.98 \ pF$	$2.15 \ pF$

Table 5.2: Tuning/matching capacitances.

2.3 LNA

Many equivalent RF low noise amplifier (LNA) boards are available on the market. We chose the RF AMP V2.0 from Walfront®. It is a 0.05-4GHz bandwidth LNA, with a noise factor of NF=0.6dB. The RF AMP V2.2 board is designed around the SPF5189Z from Qorvo® [133], a GaAs pHEMT low noise MMIC amplifier. It exhibits a high gain at 60MHz, i.e. $G_{dB} = 28dB$, and features a high linearity with an output power at $1dB$ compression point, and at 900MHz, of 22.4dBm. Assuming this conservative value of $22.4dBm$ for the output power at $1dB$ compression point even at 60MHz, i.e. at our frequency of interest, the amplifier begins to be non-linear for an input power of $-4.6dBm$. Such a power on a 50Ω input impedance corresponds to an input signal amplitude of $186mV$. Since the whole receiver features three cascaded LNA, this amplitude of $186mV$ has to be divided by G^2, where $G = 10^{G_{dB}/20} = 25$ is the gain in V/V of the LNA, in order to have an estimation of the maximum input signal the receiver can sustain before its non linearity may become an issue. With $G = 25dB$, we get a maximum admissible FID signal amplitude of $298\mu V$. The best signal we may expect is with a water sample. Using equations 2.19 and 2.31 with the characteristics of the coil (varnish coil – see Table 5.1), we can estimate the magnitude of this signal. Indeed, from equation 2.19, we have for the maximum magnetization of the sample under $B_0 = 1.5T$:

$$M_0 = \frac{3/4 \cdot N_S \cdot (\gamma \cdot \hbar)^2 \cdot B_0}{2 \cdot k \cdot T} = 5.06 \cdot 10^{-3} A/m \tag{5.8}$$

where $N_s = 6.68 \cdot 10^{28} m^{-3}$ is the protons density in water, $\gamma \cdot B_0 = 2\pi \cdot 60 \cdot 10^6 rad/s$, and $k \cdot T = 4 \cdot 10^{-21} V \cdot C$ at ambient temperature. The coil being a solenoid, its B_u is given by [125]:

$$B_u = \frac{\mu_0 \cdot N}{\sqrt{d^2 + l^2}} \tag{5.9}$$

where d is the coil diameter, l its length, and $\mu_0 = 4\pi \cdot 10^{-7} H/m$ is the permeability of water, assumed to be close to the permeability of free space. Using the characteristics of the "varnish coil", we get:

$$B_u = 1.99 \cdot 10^{-3} T/A \tag{5.10}$$

Finally, we can assume to a very good approximation that the sample volume is equal to the coil volume, that is:

$$V_L = \frac{\pi \cdot d^2}{4} \cdot l = 7.1 \cdot 10^{-9} m^3 = 7.1 \mu l \tag{5.11}$$

So, using equation 2.31, we get for the maximum voltage magnitude at the output of the coil for the water sample:

$$S_0 = \omega_0 \cdot M_0 \cdot V_L \cdot B_u = 27 \mu V \tag{5.12}$$

The coil being tuned and matched to the input impedance of the LNA, this amplitude is passively amplified by $\alpha = (\sqrt{R_{LNA}/R})/2 = 3.95$ (see equation 4.31 So, the maximum FID signal we may expect at our receiver input is $107 \mu V$, i.e. below $298 \mu V$, ensuring that the receiver will not saturate, and justifying this optimal choice of three cascaded LNA. It should be noticed that this value is optimistic because it assumes that all protons in the whole volume of the coil precess at the same Larmor frequency. Due to the unavoidable B_0 inhomogeneity, it is never the case, and the maximum amplitude of the FID signal decreases, while its spectrum peaks broaden.

In terms of noise, the noise factor of 0.6dB for an input impedance of $R_{LNA} = 50\Omega$ corresponds to an intrinsic noise of the LNA, referred at its input, σ_{lna}^2, of:

$$NF = 10 \cdot \log\left(\frac{\sigma_{in}^2 + \sigma_{lna}^2}{\sigma_{in}^2}\right) \Leftrightarrow \sigma_{lna}^2 = (10^{NF/10} - 1) \cdot \sigma_{in}^2 = (10^{NF/10} - 1) \cdot 4 \cdot k \cdot T \cdot R_{LNA} \tag{5.13}$$

In other words, the noise brought by the LNA, referred at its input, corresponds to the thermal noise of a resistance of $(10^{NF/10} - 1) \cdot R_{LNA} = 0.148 \cdot R_{LNA} = 7.4\Omega$. This value has to be compared to the noise brought by the coil when looking at the input of the LNA. As discussed in section 3 of chapter 4, this noise is the thermal noise coming from the coil resistance, $R = 0.8\Omega$ in our case (varnish coil), multiplied by α^2 (see equation 4.12) where α is the passive amplification once the coil is tuned and matched, i.e. $\alpha = 3.95$ here. So, at the input of the LNA, the noise coming from the coil is the thermal noise of a resistance of $\alpha^2 \cdot R = 12.5\Omega$. This value shows that the first LNA of the receiver, and thus the receiver, brings a slightly lower noise than the coil. As a consequence, such an LNA is well adapted for our sensing head.

It is worth to notice that the LNA data sheet provides all the characteristics used above at 900MHz, while we use the amplifier around 60MHz. However, we may be quite confident in our assessments since Matthias Ddus [134] reported for this amplifier a gain of 25dB around 60MHz and a NF of 1dB (see figure 5.11).
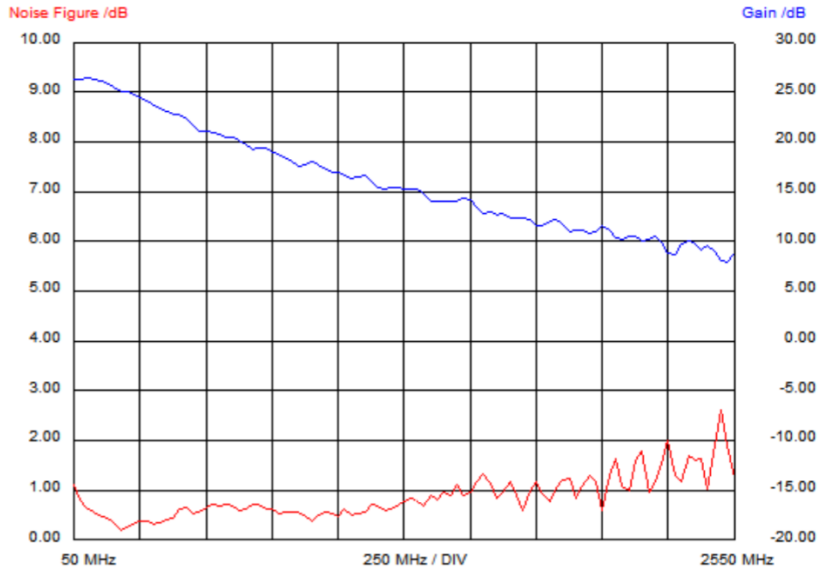
Figure 5.11: Noise factor and gain measurement of the MMIC SPF5189Z from Ddus [134].

The cascaded three RF AMP V2.0 LNAs are shown in figure 5.12, with the main characteristics of the SPF5189Z LNA reminded in Table 5.3.
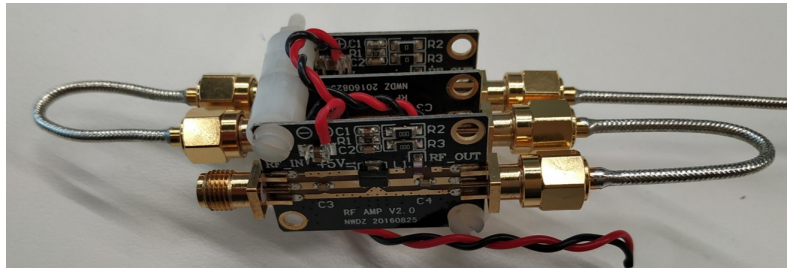

Figure 5.12: RF AMP V2.0 LNAs cascaded for the discrete prototype. Note that the band-pass filter placed after the first LNA is not shown here.

Gain	28dB
Noise Figure	0.6dB
P1dB	22.4dBm
Bandwidth	4GHz

Table 5.3: SPF5189Z main characteristics.

2.4   Mixer

It is not possible to convert in digital a signal at $60MHz$, at least with the accuracy required to compute the NMR spectrum. Indeed, it would require a minima a 8 bits ADC with a sampling frequency above $120MHz$! It is thus mandatory to down convert the FID signal to a much lower frequency allowing an easy digital conversion of the signal. We use a mixer for that purpose . An ideal mixer is a pure analog multiplier [135], as shown in figure 5.13. Denoting ν_{IF} the output

voltage of the mixer, ν_{RF} the radio frequency input voltage that has to be down converted, and ν_{LO} the local oscillator voltage whose frequency, f_{LO}, will be tuned to determine the low frequency of ν_{IF} we have:

$$\nu_{IF} = \nu_{LO} \times \nu_{RF} \tag{5.14}$$

The time domain multiplication leads to frequency shifts in frequency domain [136], with a down converted signal at frequency $f_{RF} - f_{LO}$, and a up converted signal at frequency $f_{RF} + f_{LO}$:

$$\nu_{IF}(t) = V_{LO} \cdot \cos(2\pi \cdot f_{LO} \cdot t) \times V_{RF} \cdot \cos(2\pi \cdot f_{IF} \cdot t)$$
$$\nu_{IF}(t) = \frac{V_{LO} \cdot V_{IF}}{2}[\cos(2\pi \cdot (f_{RF} - f_{LO}) \cdot t) + \cos(2\pi \cdot (f_{RF} + f_{LO}) \cdot t)] \tag{5.15}$$

We are interested by the down converted signal, leading to a FID signal at the output of the mixer at a frequency $f_{FID} = f_{IF} = f_L - f_{LO}$ where f_L is the Larmor frequency, roughly $60MHz$ in our case.

The down converted frequency f_{IF} has to be chosen above a few kilohertz in order to avoid placing the signal at very low frequency where $1/f$ noise dominates.
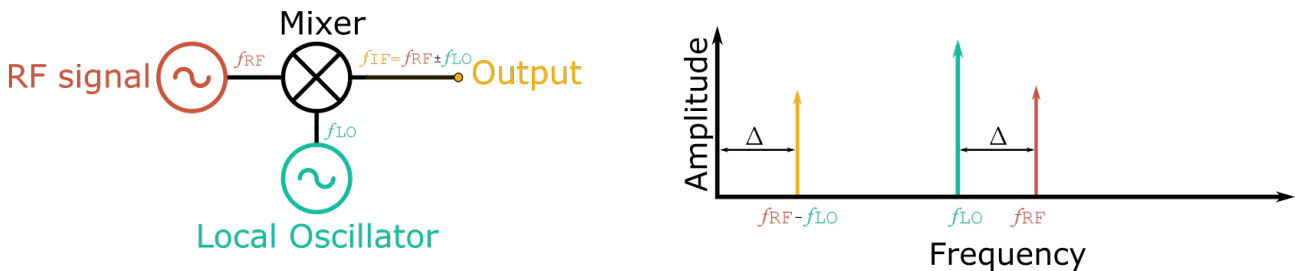

Figure 5.13: Down conversion principle.

In our receiver, we use the AD831 mixer from Analog Device (figure 5.14). It can sustain RF signal up to $500MHz$ and provide an IF signal between DC and $200MHz$. It has a gain of 0dB. Its 1dB compression point, i.e. the input RF power for which the output IF power is 1dB below the power it should have if the mixer does not saturate, is 10dBm. Assuming a strong NMR signal with an amplitude of roughly $100\mu V$ at the input of the LNA, i.e. a signal power of -70dBm, and a receiver gain of 3x25dB, lead to a RF signal at the input of the mixer of +5dBm, sufficiently below the 1dB compression point. It should be noticed again that this maximum signal power is optimistic. It will be always lower due to the B_0 inhomogeneity. We can thus neglect the non-linearity due to the mixer. The mixer being placed after the three cascaded LNA, its noise factor of 10.3dB is not an issue.
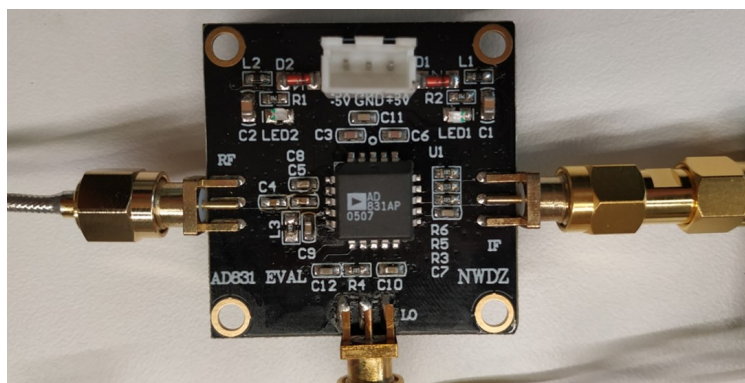
Figure 5.14: Mixer used in the discrete prototype to down convert the NMR signal.

2.5 Filters

As already discussed at the beginning of this chapter, a $50MHz - 70MHz$ bandpass filter was placed after the first LNA. It allows to drastically reduce the electromagnetic perturbations that are picked up by the sensing head, certainly by the tuning/matching circuit, and coming from the highly noisy environment of the experimental room where is located the Magritek 60 benchtop. The SIF-60 (see figure 5.15) from Mini-Circuits® was used because of its low-noise figure, that is less than 1dB, and its 50Ω input and output impedances.

Figure 5.15: Band-pass filter placed after the first LNA.

The $500kHz$ anti-aliasing low-pass filter placed right before the oscilloscope that acquires the FID signal is the LTC1560-1 from Linear Technology®. It is a 5th order elliptic filter in an SO-8 package that needs no external components. It was soldered on a PCB as shown on figure 5.16.
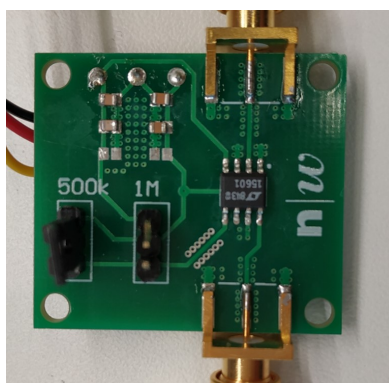

Figure 5.16: Anti-aliasing low-pass filter placed before the oscilloscope. It exhibits two selectable cutoff frequencies, 500kHz and 1MHz. We selected 500kHz.

2.6   Power supply

The different PCB circuits of the receiver were first powered through linear regulators that were supplied with a switching wall power supply. However, such power supply radiates parasitic electromagnetic waves that were perturbating the receiver. So we decided to simply power the different circuits with batteries, as shown in figure 5.3.

2.7   Receiver characterisation and limit of detection

Before carrying out the first NMR experiment, the receiver was electrically characterized. The local oscillator was tuned to down convert the Larmor frequency, i.e. $60.5017MHz$, to $17kHz$. Then, the input of the receiver was connected to a Keysight® 33621A RF generator, and its output to an oscilloscope. Due to the receiver high gain, around 80dB, three 20dB attenuators were placed at the output of the RF generator. Then a gain of 81dB, i.e. 11220 V/V, was measured at $60MHz$.

The noise floor was determined with a Siglent® SVA1000X spectrum analyser. The receiver input being connected to a 0Ω impedance, a noise floor of $4\mu V/\sqrt{Hz}$ around $17kHz$ was measured. It corresponds to the thermal noise of a 8Ω resistance at the input of the receiver, to be compared to the equivalent noise resistance of the LNA estimated at 7.4Ω from the data sheet (noise factor of 0.6dB).

From these results we can estimate the minimum signal the receiver can detect depending on the coil we use. Indeed, as discussed in section 2.3, the equivalent noise resistance at the input of the LNA is:

$$R_{neq} = \alpha^2 \cdot R_{coil} + R_{nlna} \tag{5.16}$$

where R_{coil} is the coil resistance, α is the passive amplification when the coil is tuned and matched to the 50Ω LNA input impedance, and R_{nlna} is the equivalent noise resistance of the LNA, i.e. 8Ω from the noise floor measurement. The minimum signal that can be detected, multiplied by α, has thus to be above the noise level $\sqrt{4 \cdot k \cdot T \cdot R_{neq}}$. So, the minimum signal the receiver can detect is:

$$S_{min} = \frac{\sqrt{4 \cdot k \cdot T \cdot R_{neq}}}{\alpha} \tag{5.17}$$

Table 5.4 gives R_{neq} for both coils we used as well as the passive amplification α when the coil is tuned and matched to the LNA, and finally the minimum signal that can be detected.

Coil	Varnish coil	Epoxy coil
R_{coil}	0.8Ω	1.86Ω
$\alpha = \dfrac{\sqrt{50\Omega/R_{coil}}}{2}$	3.95	2.6
R_{neq}	20.4Ω	20.6Ω
$\sqrt{4 \cdot k \cdot T \cdot R_{neq}}$	$5.7 \cdot 10^{-10}V/\sqrt{Hz}$	$5.7 \cdot 10^{-10}V/\sqrt{Hz}$
S_{min}	$144pV$	$219pV$

Table 5.4: Equivalent noise resistance R_{neq} at the input of the receiver (input of the first LNA), passive amplification, α, and minimum signal that can be detected, S_{min}, depending of the coil used.

It should be noted that the FID signal being proportional to the volume of the sample, i.e. to the coil volume here (see equation 2.31). Although the minimum detectable signal is lower for the varnish coil, it is better to use the epoxy coil since its volume is four times higher than the volume of the varnish coil. This is why varnish coil was only used for our first NMR experiment carried out on a water sample.

3   Experimental results

The targeted portable NMR probe focuses on two pollutants, atrazine and glyphosate. As discussed in section 3 of chapter 1, these pollutants will be concentrated in a polymer filter, and then possibly extracted with the acetonitrile eluent. In addition, atrazine is the pollutant providing the smallest signal. So due to limited access to the Magritek 60 benchtop, the equipment being regularly used by other teams, we tested atrazine in acetonitrile only. Before this test, we first acquired the NMR spectra of a tap water sample since water is known to provide a high and easy signal to be detected. Then, in order to validate the possibility for our system to discriminate between very close spectrum peaks, we acquired the NMR spectrum of an ethanol sample. Ethanol is easy to have and handle, and exhibits many peaks, among which some are separated only by 0.05 ppm. It is thus a good candidate for peak discrimination assessment. Finally, before acquiring the NMR spectrum of atrazine in acetonitrile, we first acquired the spectrum of acetonitrile alone. All spectra were acquired with our receiver as well as with the Magritek 60, and compared.

3.1   Experiment parameters and protocol

As already mentioned, the Magritek 60 was mainly used for its homogeneous magnet. However, we took also advantage of its transmitter to apply the RF pulse (Tx phase). The Tx time is automatically determined by the Magritek during its calibration. According to equation 2.21, it depends on the RF wave power, i.e. on B_1, and also on temperature. It is slightly below $20\mu s$, i.e. from $17\mu s$, up to $19\mu s$ when the room temperature increases. The signal at the output of the receiver was acquired with an oscilloscope, and the T_X phase was removed to keep only

the FID signal that were processed using MATLAB® to provide the NMR power spectrum. The acquisition time of the FID signal depends on the spectrum peak separation. Noting $\Delta\nu$ the smallest frequency of the peaks separation, the acquisition time needs to be higher than $1/\Delta\nu$:

$$AQ = 1/\Delta\nu \tag{5.18}$$

Among the different spectra we acquired, the ethanol spectrum has the smallest peaks separation, around 0.05ppm, i.e. corresponding to a frequency separation of 3Hz when the spectrometer is operated at 60MHz. So we chose an acquisition time larger than 330ms for all our experiments.

Noting $f_{FID} = f_{NMR} - f_{LO}$ the frequency of the down-converted NMR signal, where f_{NMR} is the NMR signal frequency, close to the Larmor frequency f_L, and f_{LO} is the mixer local oscillator frequency, the sampling frequency of the oscilloscope was chosen higher than twice f_{FID} according to the Shannon theorem. Then, the power spectrum of the FID was computed using the periodogram algorithm (see section 3.5 of chapter 2, and appendix). All spectra were drawn in V^2/Hz (power spectra) versus the chemical shift in ppm. This allows comparing spectra regardless of the B_0 value used for their acquisition. We have:

$$\text{chemical shift (ppm)} = \frac{(f_{signal} + f_{LO}) - f_L}{f_L} \cdot 10^6 \tag{5.19}$$

Finally, when appropriate, the FID acquisition was repeated and spectrum averaging was done in order to reduce the dispersion on the power spectrum calculation. The flowchart of figure 5.17 summarizes the signal processing performed with MATLAB.
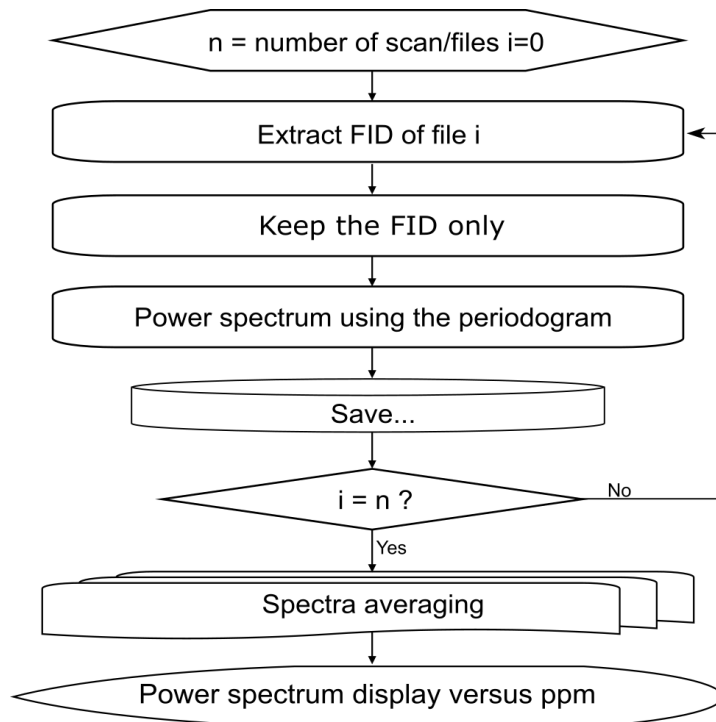

Figure 5.17: FID data processing with MATLAB.

3.2   Results

Water NMR spectrum

For this experiment, we used tap water and the varnish coil (see table 5.1). The mixer local oscillator was tuned in such a way that the down converted FID signal was around $2kHz$. Then the FID signal was acquired with a HMO1024 Rhodes & Schwartz® oscilloscope over 1s at a sampling frequency of $f_s = 5kHz$. The vertical sensitivity of the oscilloscope was set to $10mV$, allowing a vertical full range of $\pm40mV$ (height vertical divisions). The FID signal is shown in figure 5.18-a with its power spectrum in figure 5.18-b.
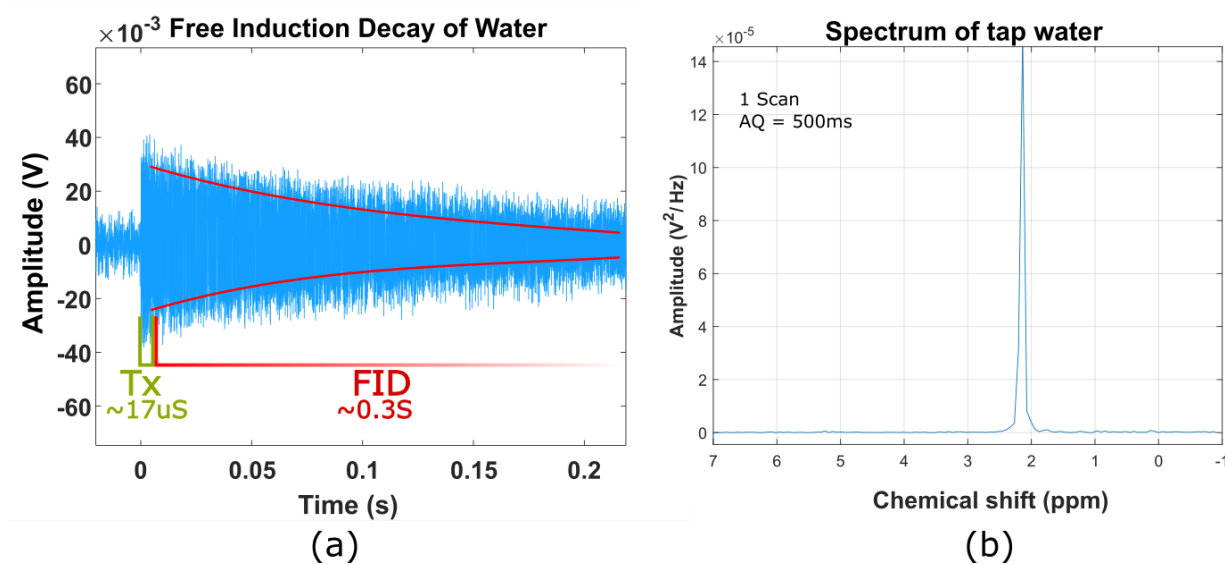

Figure 5.18: (a) Acquired water FID, and (b) its corresponding power spectrum.

From our discussion on the maximum signal the receiver can sustain before its non linearity may be an issue (see section 2.4 of this chapter), it should be noted that we may expect a much higher FID signal at the starting point of the FID. Indeed, assuming a perfectly homogeneous B_0 field, with the varnish coil, we assessed the NMR signal at the input of the first LNA to have a maximum amplitude of $107\mu V$, leading to a FID signal with an amplitude of $11220\times107\mu V = 1.2V$ at its starting point! Of course, because of the B_0 inhomogeneity, this maximum amplitude is much lower, but should be higher than the amplitude of the oscilloscope range, i.e. $40mV$. So the peak value of $1.4 \cdot 10^{-4}V^2/Hz$ is underestimated. However, we kept the oscilloscope vertical sensitivity to $10mV$ in order to be able to resolve the noise floor. This choice did not prevent from measuring the water chemical shift that is around +2ppm, same as it was on the Magritek.
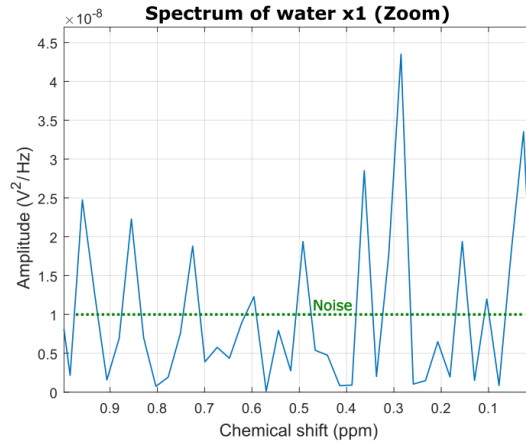
Figure 5.19: Noise floor of the tap water spectrum.

As seen in figure 5.19, where a zoom on the noise floor between 0 and 1 ppm is highlighted, the measured noise power may be estimated around $1 \cdot 10^{-8} V^2/Hz$. Referred at the input of the first LNA of the receiver, this noise floor becomes $1 \cdot 10^{-8}/11220^2 = 7.9 \cdot 10^{-17} V^2/Hz$. This noise floor has to be compared with the noise floor coming from the equivalent noise resistance, R_{neq}, evaluated to be 20.4Ω for the varnish coil (see section 2.7, this chapter, and table 5.4). However, it should be noticed that the sampling frequency of $5kHz$ is much below the $500kHz$ cutoff frequency of the 5th order low-pass filter placed right before the oscilloscope. In others words the thermal noise of R_{neq} is undersampled, and all the thermal noise power is folded back in the $F_s/2$ bandwidth [137]. As a consequence the measured noise floor is raised by the undersampling factor $N = 500kHz/(F_s/2) = 200$. It means that the expected measured noise floor at room temperature is:

$$\text{Expected noise floor } = N \times 4 \cdot k \cdot T \cdot R_{neq} = 200 \times 4 \times 25 \cdot 10^{-3} \times 1.6 \cdot 10^{-19} \times 20.4$$
$$\text{Expected noise floor } = 6.5 \cdot 10^{-17} V^2/Hz \tag{5.20}$$

which is very close to the $7.9 \cdot 10^{-17} V^2/Hz$ we measured.

This first experiment validates our measurement protocol, and our receiver.

Ethanol spectrum

For this experiment, as for all the other measurements, we used the epoxy coil (see table 5.1). We used also another oscilloscope, the 44Mxi from Lecroy®. In order to be able to resolve the ethanol peak separations that are close to 0.05ppm, i.e. $3Hz$, we acquired the FID over $500ms$. The vertical sensitivity of the oscilloscope was set to $2mV$, and its sampling frequency to 5Ms/s, i.e. $f_s = 5MHz$, much above the $500kHz$ cutoff frequency of the anti-aliasing filter placed right before the oscilloscope. It should be noticed that many equipments were working in the Magritek room during this experiment, leading to a quite noisy environment. Therefore, 10 acquisitions were performed, and the spectra were averaged. The spectrum acquired with the Magritek (1

scan) is shown in figure 5.20-a, while the power spectrum acquired with our receiver (average of 10 scans) is shown in figure 5.20-b.
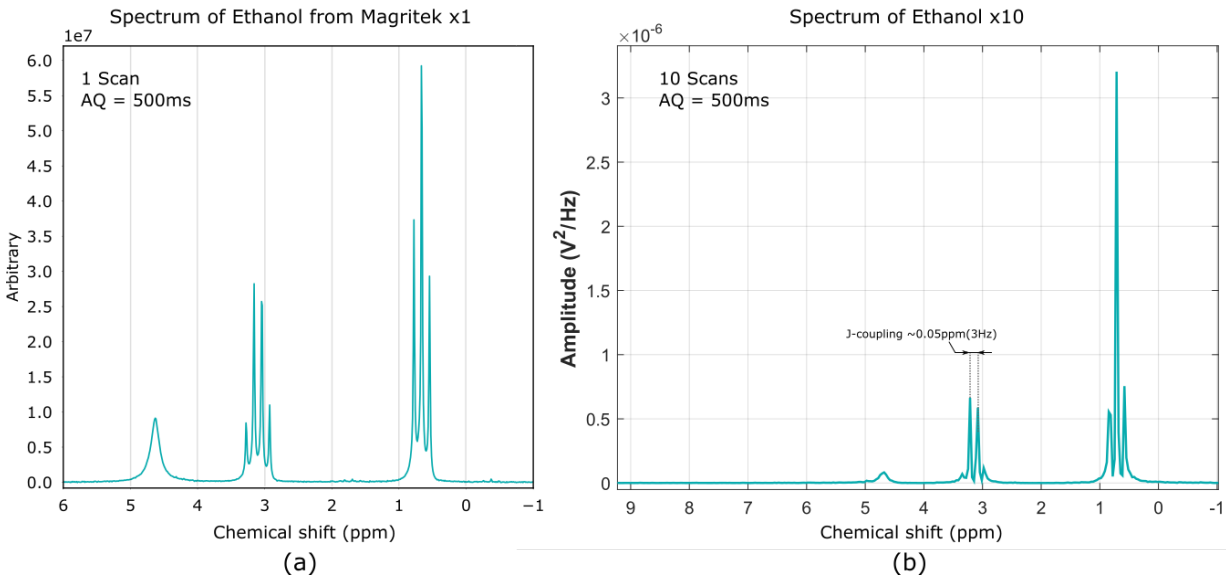

Figure 5.20: (a) Ethanol spectrum from the Magritek, 1 scan (b) Ethanol spectrum acquired with our receiver, 10 scans.

Both spectra are very close, and all peaks are identically resolved. It is not possible to compare the peaks' amplitudes since the vertical unit of the Magritek spectrum is not indicated. In order to determine the experimental noise floor, a zoom on the power spectrum of figure 5.20 from 5 to 9ppm is shown in figure 5.21.
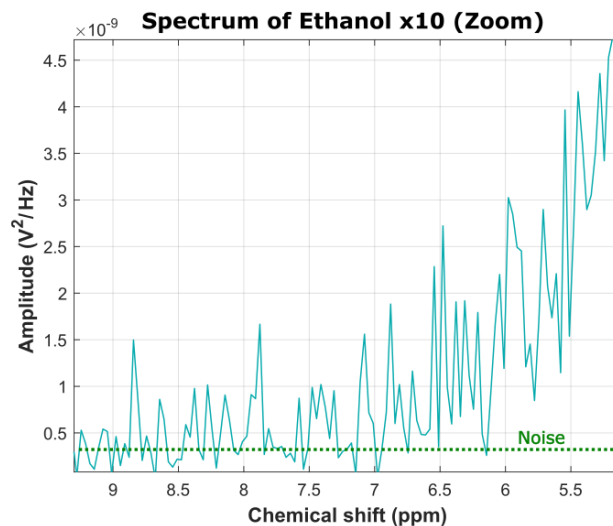
Figure 5.21: Noise of the ethanol spectrum.

It is difficult to say if the noise floor is readily reached at +9ppm. Assuming this is the case, we get a measured noise floor of $2.5 \cdot 10^{-10} V^2/Hz$ at the output of the receiver. Referred to the LNA input, we thus have a measured noise floor of $2.5 \cdot 10^{-10}/11220^2 = 2 \cdot 10^{-18} V^2/Hz$. It has to be compared to the expected noise floor of $3.3 \cdot 10^{-19} V^2/Hz$ at room temperature, coming

from the equivalent noise resistance that was estimated to be $R_{neq} = 20.6\Omega$ for the epoxy coil (see table 5.4). The higher measured noise floor than expected should be attributed to the noisy environment, and our receiver that is very sensitive to this noise. However, our receiver is able to resolve peak separation lower than 0.05ppm, which was what we wanted to validate with this experiment.

Acetonitrile spectrum

For this experiment, we used deuterated acetonitrile, the eluent that should be used in the portable pollutants probe. The main advantage of deuterated solvent is to avoid the dominance of the solvent spectrum as deuterium atoms resonate at a completely different frequency than the pollutants resonance frequencies. The acquisition time was set to $200ms$ with the same sampling frequency as for ethanol, i.e. $f_s = 5MHz$, and the same vertical sensitivity of $2mV$. It should be noticed that the measurement was carried out during the summer, on a very hot day, and that the Magritek was not able to do any new measurement after this one due to the room temperature. We were however able to perform 10 acquisitions that were averaged. In addition, like for the previous experiments, the environment was quite noisy due to many equipments working in the room. Figures 5.22 compares the spectrum from the Magritek with the spectrum acquired with our receiver. They are quite similar although not giving exactly the same chemical shift. This could be explained by the experimental conditions.

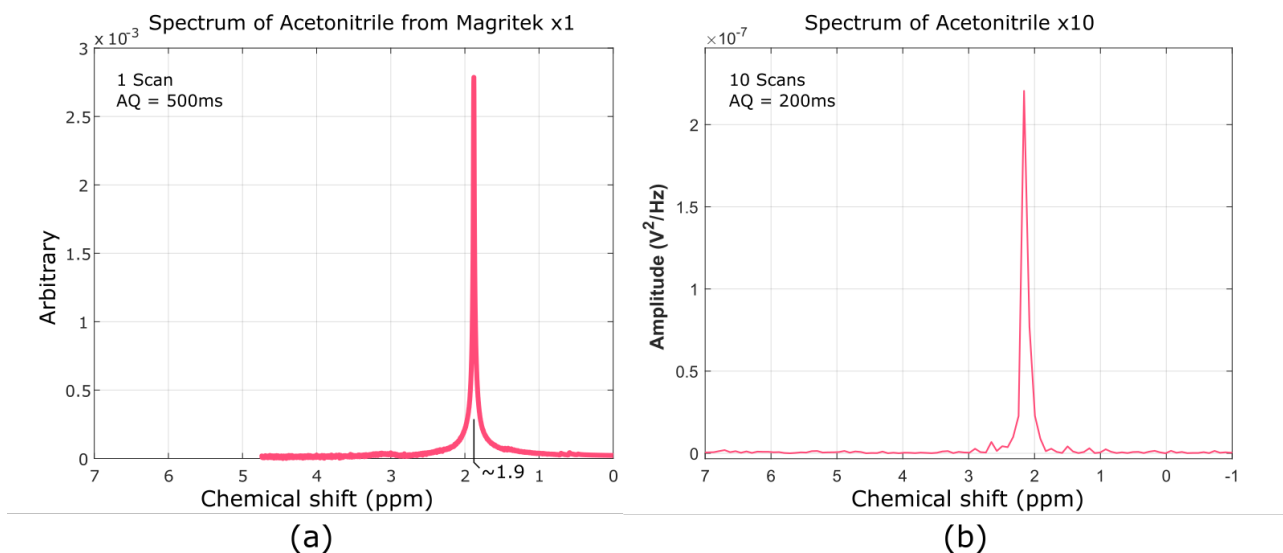Figure 5.22: (a) Acetonitrile spectrum from the Magritek, and (b) from the homemade receiver.

As for the noise floor of the previous experiment, this measurement (see figure 5.23) is more than one order of magnitude higher than the expected noise floor. Here again, this discrepancy between theory and experiment should be explained by the experimental conditions. However, acetonitrile is detectable.
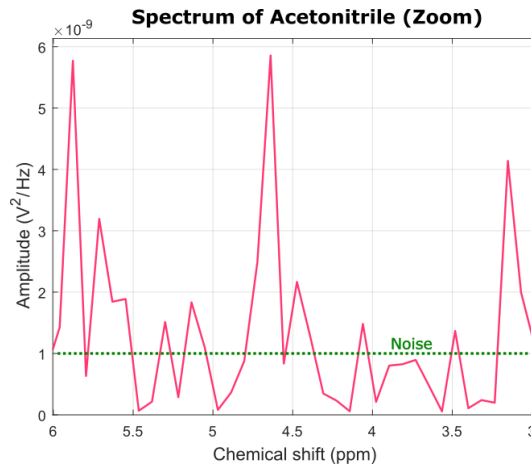
Figure 5.23: Noise floor of the Acetonitrile spectrum.

Atrazine in Acetonitrile spectrum

This last experiment was carried out to assess if atrazine, which is known to give a very small signal when observed with the Magritek, may be detectable with our receiver. Atrazine has a solubility up to 1mg/mL in acetonitrile [138]. So we use this high concentration for our experiment. This time, in order to be in the least noisy environment possible, the experiment was carried out early in the morning with only the Magritek switched on in the laboratory room. The acquisition time was set to 1s with a sampling frequency of $f_s = 2.5 MHz$, and the oscilloscope vertical sensitivity at its minimum value of $2mV$. In addition, 16 acquisitions were performed, and their spectra averaged. Figure 5.24-a shows the spectrum acquired with the Magritek, while figure 5.24-b shows the spectrum acquired with our receiver. Obviously, the Magritek is able to resolve the atrazine peaks, and exhibits a lower noise level than the spectrum acquired with our receiver. However, although it should be confirmed by more acquisitions, and certainly a higher averaging, the atrazine peaks seem also to be observable from the spectrum acquired with our receiver.
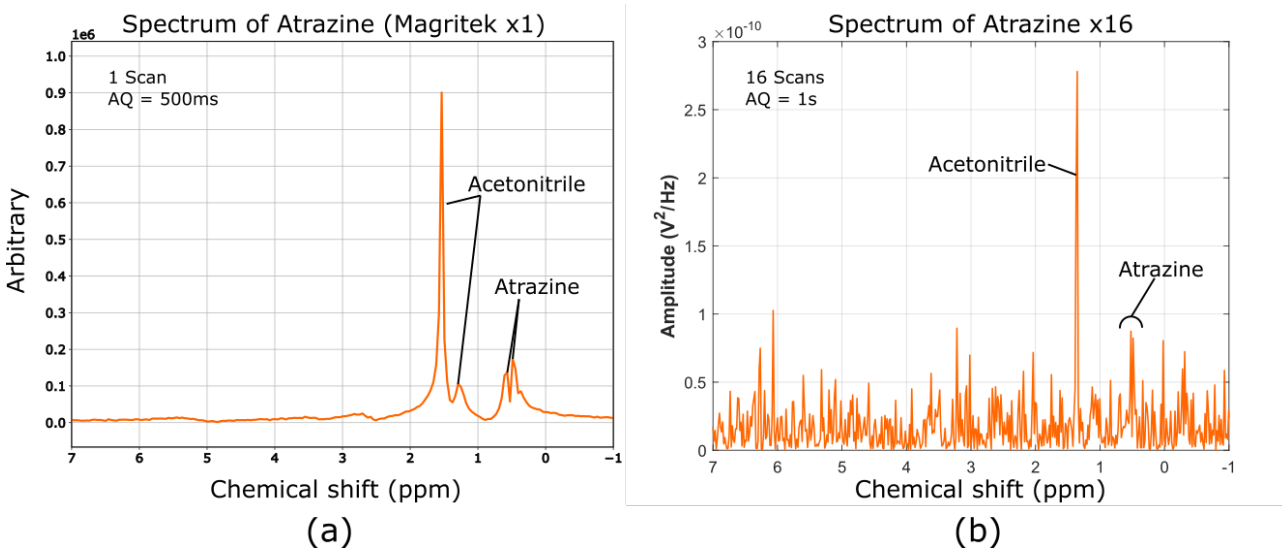

Figure 5.24: Acetronitrile and Atrazine comparison (a) from the Magritek (1 scans), (b) from the low-cost receiver (16 scans).

Finally, as shown in figure 5.25, the experimental noise floor is close to $2 \cdot 10^{-11} V^2/Hz$, corresponding to a noise floor at the input of the first LNA equal to $1.6 \cdot 10^{-19} V^2/Hz$, which is even better than the expected theoretical noise of $3.3 \cdot 10^{-19} V^2/Hz$ at room temperature. Nevertheless, experimental and theoretical noise floor are in good agreement, and validates the receiver model we developed.
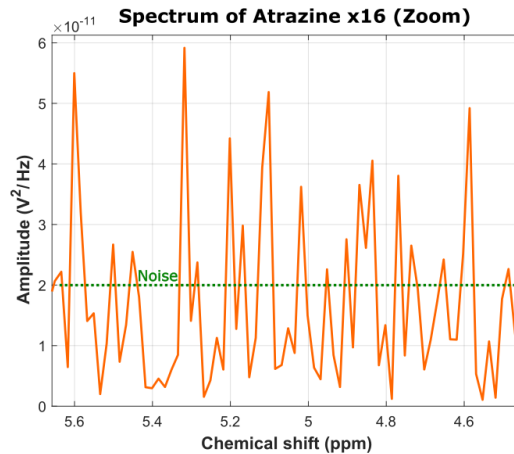
Figure 5.25: Noise floor of the Atrazine spectrum.

*

*   *

Summary

In this chapter, we presented the Magritek 60 benchtop NMR magnet we used to perform NMR spectrum acquisitions with the discrete receiver we developed. The discrete receiver was described in details, and its main electrical characteristics provided. The coils we developed was also presented, as well as the method we used to fabricate them, and to hold them on the Magritek in order to ensure a good repeatability of the numerous experiments we performed. Then experimental results we obtained with tap water, ethanol, acetonitrile, and finally atrazine in acetonitrile, were presented. These preliminary results show that it should be readily possible to detect pollutants with a simple portable NMR spectrometer, even if many technological developments have to be done before having a "plug and play" system.

Chapter 6

Integrated receiver prototype

We have shown in section 3 of chapter 4 that using a high input impedance LNA with a coil tuned at the Larmor frequency thanks to a single capacitance C_1 in parallel to the coil allows taking full advantage of the quality factor Q of the coil. This is only possible if the LNA can be placed directly at the output of the coil, and that no transmission line is required to connect the coil to the LNA.
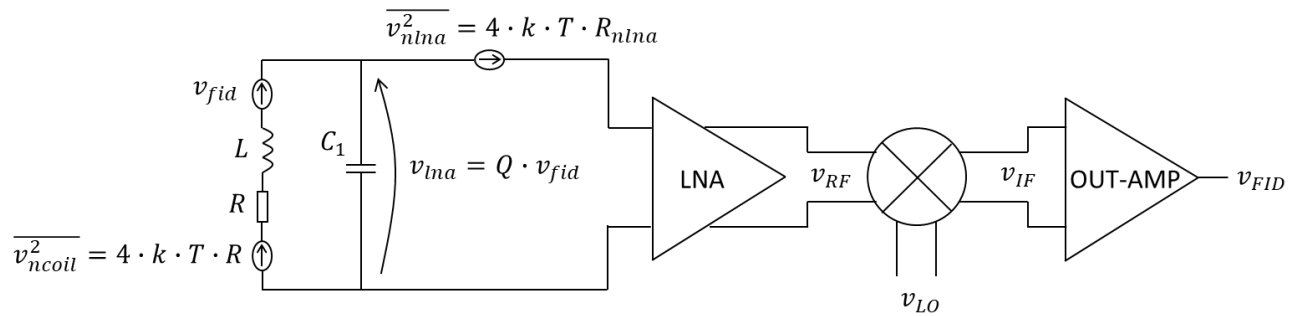

Figure 6.1: Integrated receiver prototype with its external coil and tuning capacitance C_1.

Indeed, as reminded in figure 6.1, in such a case, the inductive signal ν_{fid} at the output of the coil is passively amplified by the factor $\alpha = Q$ when picked up across C_1, i.e. at the input of the LNA. On the contrary, using a conventional tuning/matching circuit with a 50Ω transmission line to connect the coil to a 50Ω input impedance LNA reduces α to $\sqrt{50/R/2}$, where R is the coil resistance. This $\alpha = Q$ passive amplification has two main advantages. First, the whole amplifying chain of the receiver can be reduced to only one LNA, and possibly an output amplifier (see figure 6.1), but does not require three cascaded amplifiers as we did in the discrete receiver of chapter 5. This simplifies the receiver design, and reduces power consumption. The second advantage is that noise constraints for the LAN design are drastically lowered. Noting R_{nlna} the equivalent thermal noise resistance of the LNA referred to the LNA input, this noise resistance is divided by Q^2 when referred at the output of the coil. So, the equivalent thermal noise resistance at the output of the coil reads:

$$R_{neq} = R + R_{nlna}/Q^2 \tag{6.1}$$

However, this is R_{neq} which eventually determines the SNR of the receiver (see equation

):

$$SNR = \frac{\nu_{fid}}{\sqrt{4 \cdot k \cdot T \cdot R_{neq}}} \qquad (6.2)$$

As a consequence, choosing $R_{nlna}/Q^2 << R$, i.e. for instance $R_{nlna}/Q^2 = R/10$, makes the receiver to exhibit the best achievable SNR, which is the intrinsic SNR of the coil:

$$SNR = \frac{\nu_{fid}}{\sqrt{4 \cdot k \cdot T \cdot (R + R/10)}} \approx \frac{\nu_{fid}}{\sqrt{4 \cdot k \cdot T \cdot R}} = SNR_{coil} \qquad (6.3)$$

As an example, considering the epoxy coil whose resistance is $R = 1.86\Omega$ (see table 5.1), and quality factor is $Q = 128$ (see table 5.2), means that designing a LNA with an equivalent thermal noise resistance of:

$$R_{nlna} = \frac{Q^2}{10} \cdot R = 3k\Omega \qquad (6.4)$$

It is sufficient to provide the receiver with its best achievable SNR. Such an equivalent thermal noise resistance is very easy to get using a basic CMOS technology. On the contrary, for the same noise performance, a receiver using the epoxy coil tuned and matched to a 50Ω input impedance LNA, requires the equivalent thermal noise resistance of the LNA to be:

$$R_{nlna} = \frac{\alpha^2}{10} \cdot R = \frac{50/R}{4 \times 10} \cdot R = 1.25\Omega \qquad (6.5)$$

Such a low thermal noise resistance is very challenging to get, and requires to bias the LNA with a very high current (see LNA design below). This may quickly lead to power consumption issues.

In order to demonstrate a possible architecture of such a high impedance receiver, we designed in the low cost AMS CMOS $0.35\mu m$ technology the receiver of figure 6.1. It should be noticed that this receiver has been designed before the discrete receiver of chapter 5. It was expected to be mounted in a first portable NMR probe that would have been built around the 0.7T Halbach magnet presented in chapter 3. However due to the poor homogeneity of the Halbach magnet, and to a very long delay for the chip delivery, we decided to realize the discrete prototype that was used for our first NMR experiments in the Magritek magnet. The integrated receiver being expected to detect the very small NMR signal of atrazine and glyphosate pollutants in acetonitrile, its amplifying gain, i.e. excluding the Q amplification contribution, was set to 63dB. This gain is shared between the LNA (26dB) and the output amplifier (37dB), the mixer having a gain of 0dB. In addition, the receiver noise contribution was made negligible in front of the noise contribution of the coil that was assumed to have a Q factor higher than 100. The integrated circuit that was fabricated (see figure 6.2 for the circuit layout) features each sub-circuit of figure 6.1 alone in order to validate their design and main parameters. It features also a complete amplifying chain as shown in figure 6.1. First, the architectures of the three sub-circuits are discussed, and simulation results compared with measurements for the main parameters. Finally, the whole amplifying chain is characterized, and its possible use instead of the discrete receiver presented

in the previous chapter is discussed
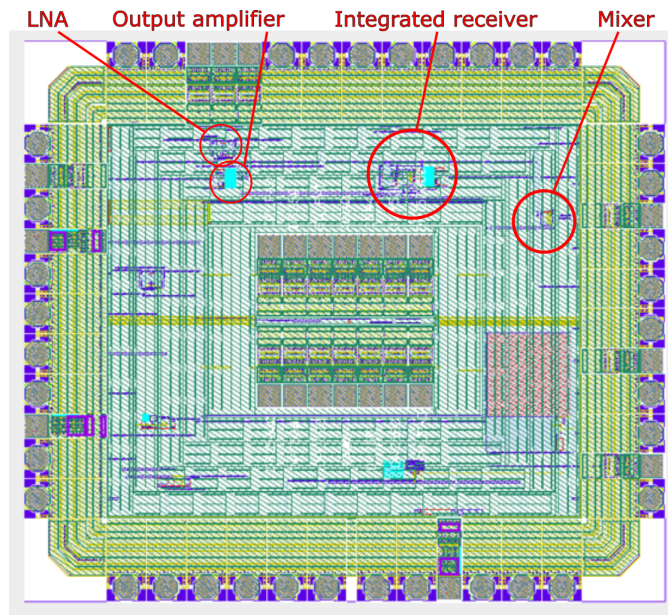
Figure 6.2: IC prototype in which the integrated receiver was implemented.

1 Low Noise Amplifier

1.1 Design
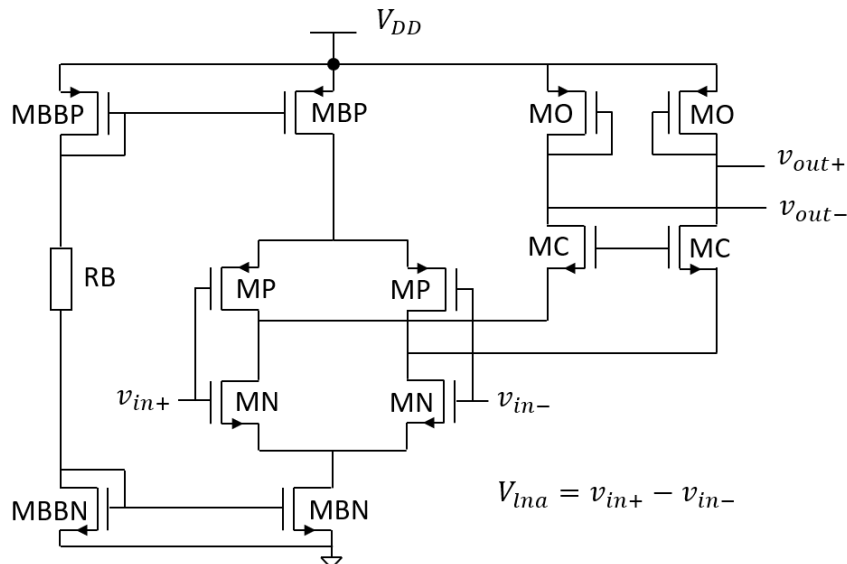
Figure 6.3: LNA architecture.

As shown in figure 6.3, we chose to use a fully differential version of the single ended LNA proposed by Anders in [44]. Its differential output is necessary to drive the mixer (see next section). This LNA uses a complementary input differential pair made of transistors MN and MP. Assuming the same transconductance for MN and MP, i.e. $g_{mMN} = g_{mMP}$, this architecture

has the advantage to double the LNA gain in comparison to an architecture using a single input differential pair. Indeed, its gain is:

$$G_{LNA} = (g_{mMN} + g_{mMP})/g_{mMO} \tag{6.6}$$

where g_{mMO} is the transconductance of the diode connected output transistor MO, while it would be g_{mMN}/g_{mMO} if the MP complementary pair was not introduced. It should be noticed that its limited input common mode range is the main disadvantage of such an input stage. However, it does not matter here since when the coil is connected at the input, we just need to bias one of both LNA inputs to $V_{DD}/2$, and all transistors will always remain in saturation due to the small $\nu_{lna} = Q \cdot v_{fid}$ at the LNA input (see figures 6.1 and 6.4).
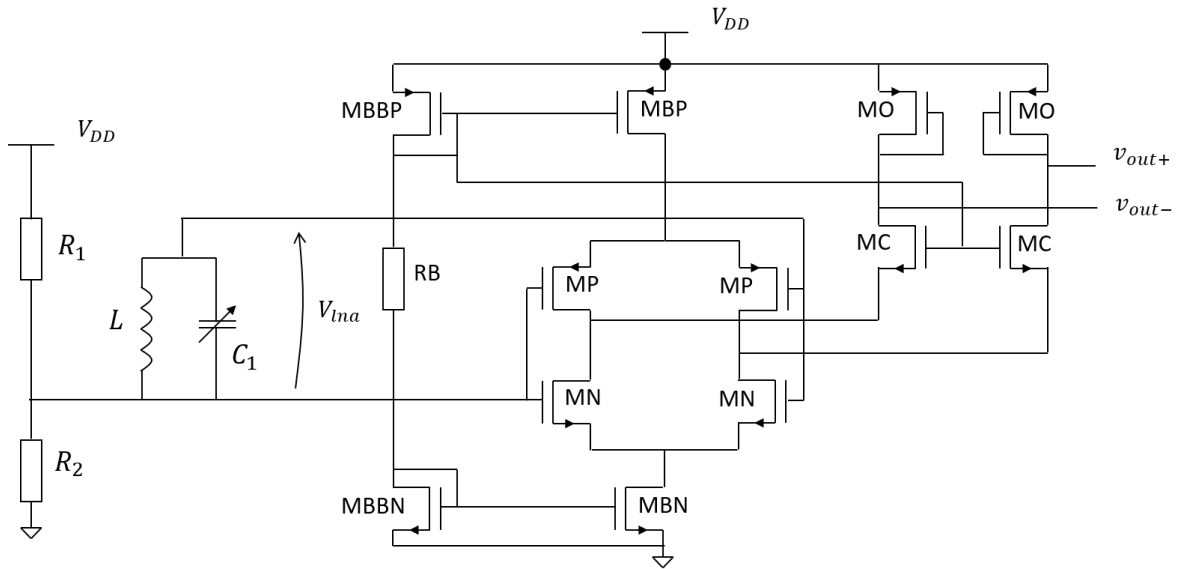

Figure 6.4: Biasing of the LNA input. R_1, R_2, C_1 and the coil, L, are external to the integrated receiver.

The cascode transistors MC isolate both output nodes from the capacitances at the common drains of MP and MN. As a consequence, the cutoff frequency of the pole at the output differential node is only determine by g_{mMO} and the input capacitance of the mixer, estimated to be $C_{MIX} \approx 100 fF$:

$$f_{lna} = \frac{g_{mMO}}{2 \cdot \pi \cdot C_{MIX}} \tag{6.7}$$

This frequency determines the -3dB bandwidth of the LNA that was set to 100MHz. In terms of noise, the cascode transistors do not contribute, while the output thermal current noises of each transistor MN, MP, and MO, i.e. $8/3 \cdot k \cdot T \cdot gm$, sum up at the output. Referred to the input of the LNA this current noise is divided by the square of the input transconductance $g_{mMN} + g_{mMP}$. This leads to an input equivalent noise of the LNA given by:

$$\overline{\nu_{lna}^2} = \frac{16}{3} \cdot k \cdot T \cdot \frac{g_{mMN} + g_{mMP} + g_{mMO}}{(g_{mMN} + g_{mMP})^2} = 4 \cdot k \cdot T \cdot R_{nlna} \tag{6.8}$$

As discussed above, R_{nlna} was chosen much lower than $Q^2 \cdot R$. Here, we set $R_{nlna} = 200\Omega$. Finally, the LNA was biased thanks to the simple voltage divider made of MBBN, MBBP, and RB, as shown in figure 6.3. Using equations 6.6, 6.7, and 6.8, the LNA was designed to have $G_{LNA} = 26dB$, $f_{lna} = 100MHz$ with a load capacitance $C_{MIX} = 500fF$, and $R_{nlna} = 200\Omega$. We chose the LNA to be able to drive an output capacitance of roughly $500fF$, i.e. higher than the integrated mixer input capacitance estimated to be $100fF$, because the LNA which is alone has to drive the $350fF$ capacitance of the RF output pad. This leads to the transistors' dimensions of table 6.1, and a power consumption of $722\mu A$, i.e. $I(MBN) = 710\mu A$, $I(MBBN) = 11\mu A$, and $I(MBP) = 293\mu A$.

	MN	MP	MO	MC	MBN	MBP	MBBN	MBBP	RB ($k\Omega$)
W (μm)	210	460	5	40	270	130	4	2	150
L (μm)	0.35	0.35	0.35	0.35	0.35	0.7	0.35	0.35	

Table 6.1: LNA sizing.

Figures 6.5a and 6.5b show respectively the simulated gain versus frequency of the LNA, and its noise power spectral density referred to its input.
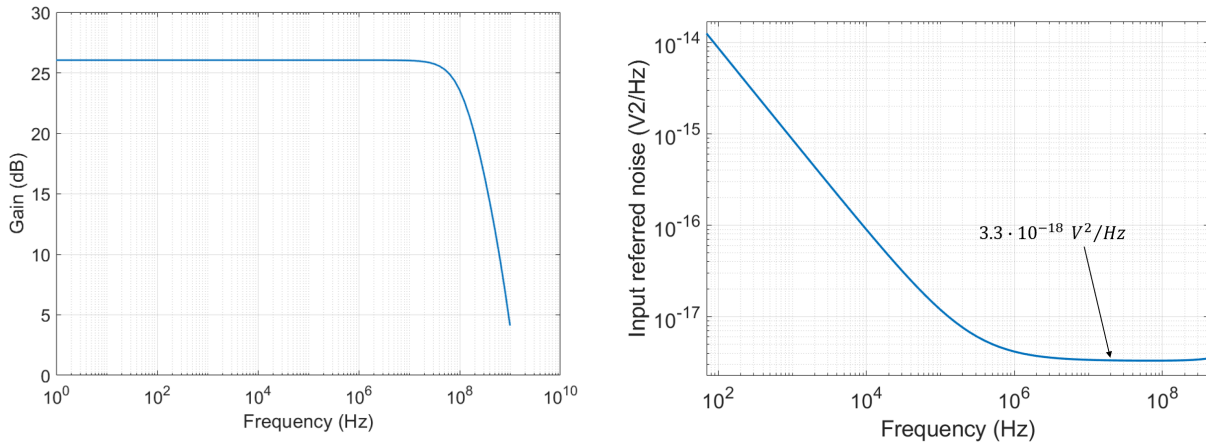
(a) LNA gain versus frequency with an output capacitive load of $500fF$.

(b) LNA power spectral density referred to its input.

Figure 6.5: LNA characteristics.

1.2 Experimental results obtained with the LNA alone:

The chip was directly bonded on a PCB to characterize the LNA alone. Each LNA output was connected to a high-speed buffer, i.e. the LMH6704 from Texas Instruments®, with a AC coupling whose high-pass cutoff frequency is 160 Hz ($10nF$ with $100k\Omega$). The buffer has a gain of 6 dB, a -3 dB bandwidth of 400 MHz, and a low noise floor of $2.3nV/\sqrt{Hz}$. Its input impedance is $1\,M\Omega$ in parallel to $1pF$. So, for the characterization, both output of the LNA are loaded as shown in figure 6.6. With such a loading, the simulation shows that the LNA gain is 25.5 dB, and its bandwidth

is limited to 45 MHz, against 100 MHz when loaded with only $100 fF$ as it is in the fully integrated amplifying chain.
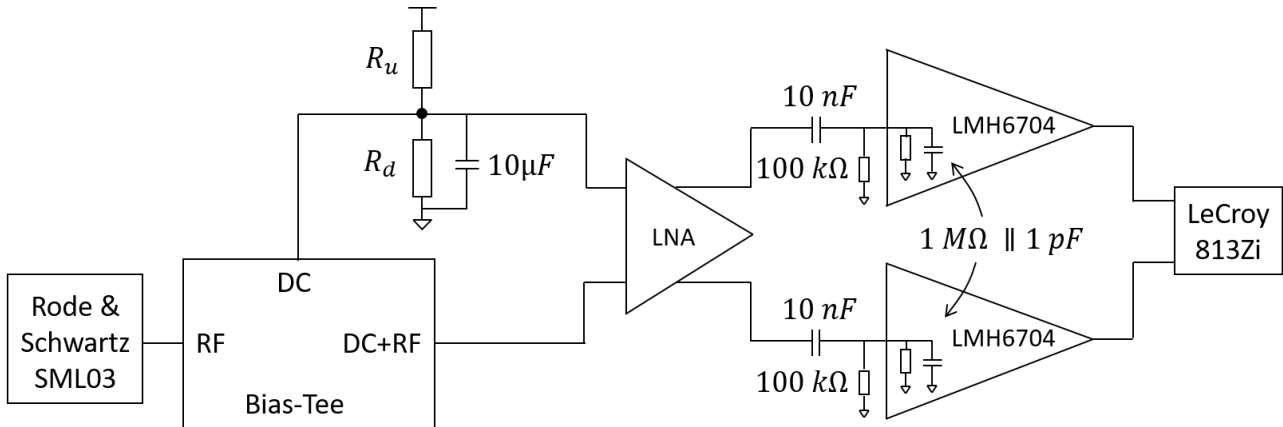
Figure 6.6: LNA input driving and output load configuration for electrical characterization

The chip being supplied by $V_{DD} = 3.3$ V, one of the input of the LNA was set to 1.65 V thanks to a resistive divider R_u/R_d (see figure 6.6), with $R_d = 1.74 k\Omega$. Then the 1.65 V DC voltage was picked-up with a SMA cable, and connected to the DC input of a ZFBT-4R2GW 0.1-4200 MHz Bias-Tee from Mini-Circuits®.

A RF signal of 16 mVpp was applied to the RF input of the Bias-Tee thanks to a Rode & Schwarz® SML03 9kHz-3.3GHz signal generator, and swept from 1MHz to 100MHz. In order to low-pass filter the RF leakage from the RF input of the Bias-Tee to its DC input, a $10\mu F$ capacitance was soldered in parallel to R_d. The DC+RF output of the Bias-Tee was then applied to the second LNA input. Thanks to this experimental setup, the LNA is differentially driven with a 16 mVpp RF signal around its optimal bias point of 1.65 V. Both LMH6704 outputs were finally recorded with a LeCroy® 4 channels Wave Master 813Zi 13GHz oscilloscope, from which the differential output signal amplitude, and thus the LNA gain was determined versus frequency.

Figure 6.7: Experimental setup for measurement of the LNA frequency response.

Figure 6.7 shows the experimental setup, and figure 6.8 the recorded experimental frequency response.
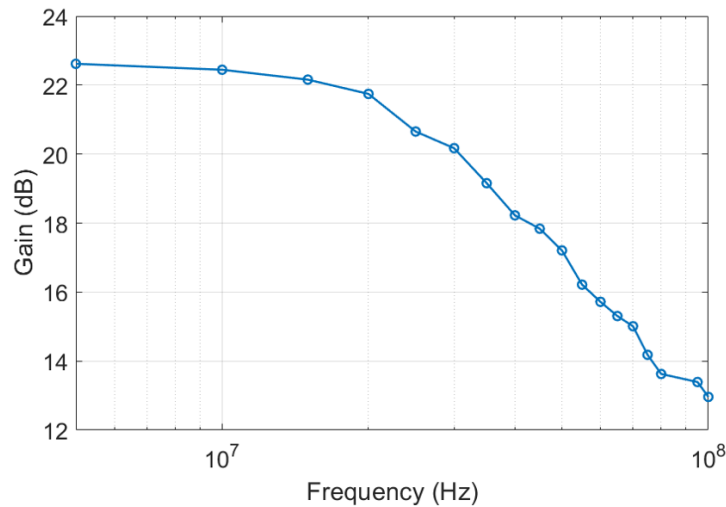
Figure 6.8: Measured LNA frequency response.

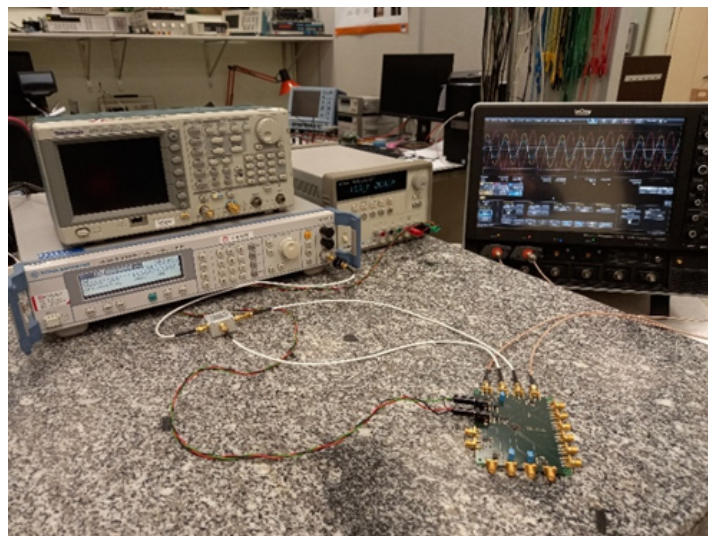The measured gain is 22.6 dB, and the -3dB bandwidth is 35 MHz. The measured bandwidth is lower than expected. However, it should be noted that this bandwidth is highly dependent on the actual input capacitance of the LMH6704, whose value is not accurately known. So, integrated in the complete amplifying chain, we may expect that the gain and the bandwidth of the LNA are close to the values targeted by design, i.e. 26 dB and 100 MHz.

The next and last LNA characteristic which is of paramount importance is its input referred noise. In order to measure this noise, the Bias-Tee previously used to inject the RF signal was removed, and both inputs of the LNA were short-circuited with a SMA cable. Then both LNA outputs buffered with the LMH6704 were connected to a two-channel SR560 Low-Noise Amplifier from STANFORD RESEARCH SYSTEM®. The SR560 allows converting the differential LNA output into a single-ended output, as well as amplifying by 20dB the noise signal. Then the SR560 output was connected to a Rode & Schwartz® FSP3 9kHz-3.3GHz spectrum analyzer to measure the output noise power spectral density. It should be noticed that the SR560 has a bandwidth limited to 1MHz. In addition, as shown in figure 6.5b, the corner frequency of the LNA noise power spectral density is around 2MHz. So, with this experimental setup, we were not able to determine the thermal noise floor, but were just able to verify that up to 1MHz, the 1/f noise dominates with a magnitude similar to the value obtained by simulation, which is the case. So we can expect than the noise floor is close to simulated one, i.e. close to $3.3 \cdot 10^{-18} V^2/Hz$ (see figure 6.5b) when referred to the LNA differential input.

2   Mixer

2.1   Design

The mixer we implemented is based on the widely used double-balanced CMOS Gilbert cell [139] shown in figure 6.9. The differential to single-ended output amplifier which directly follows the mixer, i.e. without any buffer in between, is also shown in figure 6.9 since it loads the mixer, and has to be considered to determine the gain of the mixer.
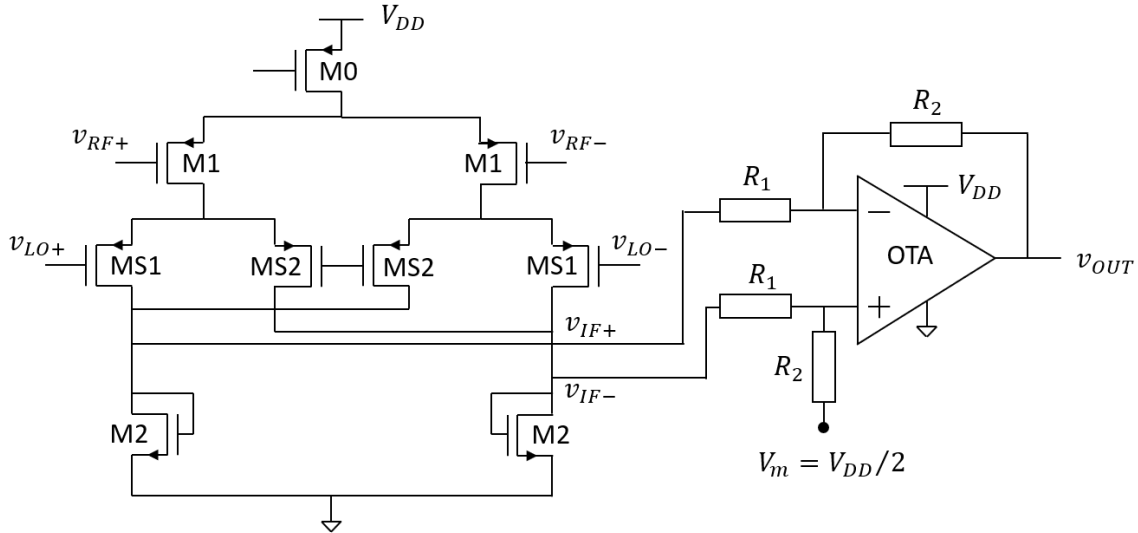
Figure 6.9: Mixer with the differential to single-ended output buffer.

The mixer is simply a self-biased input differential stage driven by the RF signal, i.e. the output of the LNA (see figure 6.1), and whose output is periodically switched thanks to the external local oscillator square voltage v_{LO} which drives the switching transistors MS1 and MS2. Both load transistors M2 are diode connected with a high overdrive voltage $V_{GS} - V_{Tn}$ in order for the biasing output point of the mixer to be close to $V_{DD}/2$. The output signal of the mixer, ν_{IF}, is then subsequently amplified by the differential to single-ended amplifier with a gain of $1 + R_2/R_1$ (see figure 6.9).

Since the overdrive voltage of M2 is high, its transconductance g_{m2} is low, much lower than $1/R_1 = 833\mu S$ (see below), and the static gain of the mixer is only determined by g_{m1} and R_1:

$$G_{MIX} = \frac{g_{m1}}{g_{m2} + 1/R_1} \approx \frac{g_{m1}}{1/R_1} = g_{m1} \cdot R_1 \qquad (6.9)$$

In order for the mixer to exhibit a gain close to 0 dB, we set $g_{m1} = 1/R_1 = 833\mu S$. Finally, due to the high overdrive voltage of M2 imposed by the mixer output biasing point of $V_{DD}/2$, $g_{m2} = 83\mu S$. It is worth to notice that the mixer gain would have been equal to $g_{m1}/g_{m2} = 10$ if the mixer was not loaded by the output amplifier.

The middle point V_m, which defines the virtual ground at the input of the operational transcon-

ductance amplifier (OTA) used to build the output amplifier, is set externally to $V_{DD}/2$, i.e. equal to the biasing point at the output of the mixer. We chose to set it externally in order to have testing flexibility.

It should be noticed that when switched by a square ν_{LO} voltage, the thermal noise of the mixer is unchanged [139], i.e. it remains equal to the thermal noise of the differential stage M1/M2. Indeed, under such a driving, the mixer is equivalent to a differential stage which is chopper stabilized at the local oscillator frequency, and it is well known that chopper stabilization does not changed the thermal noise level [137]. As a consequence, the mixer thermal noise, referred at the input of the mixer reads:

$$\overline{v_{nmix\_RF}^2} = \frac{16}{3} \cdot k \cdot T \cdot \frac{1}{g_{m1}} \cdot \left(1 + \frac{g_{m2}}{g_{m1}}\right) \approx \frac{16}{3} \cdot k \cdot T \cdot \frac{1}{g_{m1}} = 2.6 \cdot 10^{-17} V^2/Hz \qquad (6.10)$$

In the previous equation, the noise coming from the output amplifier, i.e. from R_1, R_2 and the OTA is not considered. It will be taken into account in the noise analysis performed in the output amplifier study below. Dividing by the squared LNA gain that we measured, i.e. $G_{LNA} = 22.6\,\text{dB} = 13.5$, the thermal noise contribution of the mixer referred at the LNA input gives:

$$\overline{v_{mix}^2} = \frac{\overline{v_{nmix\_RF}^2}}{G_{LNA}^2} = \frac{2.6 \cdot 10^{-17}}{13.5^2} = 1.4 \cdot 10^{-19} V^2/Hz \qquad (6.11)$$

which is negligible in comparison to the LNA noise contribution estimated at $3.3 \cdot 10^{-18} V^2/Hz$. The switches MS1 and MS2 were sized sufficiently large to behave close to ideal switches. Finally, it should be noticed that due to the presence of the small R_1 resistance, the mixer cutoff frequency is determined by R_1 and the output capacitance of the mixer equal to $C_{GS2}+C_{DS2}+C_{DS1}$. Simulation shows that the mixer bandwidth reaches more than 100MHz, a value sufficiently high for our application. The mixer transistors' sizes are listed in table 6.2, and its consumption is $I_0 = 134\mu A$, given by the current flowing through M0.

	M0	M1	MS1 and MS2	M2
W (μm)	115	60	30	5
L (μm)	0.35	0.35	0.35	20

Table 6.2: Mixer sizing.

2.2 Experimental results obtained with the mixer alone
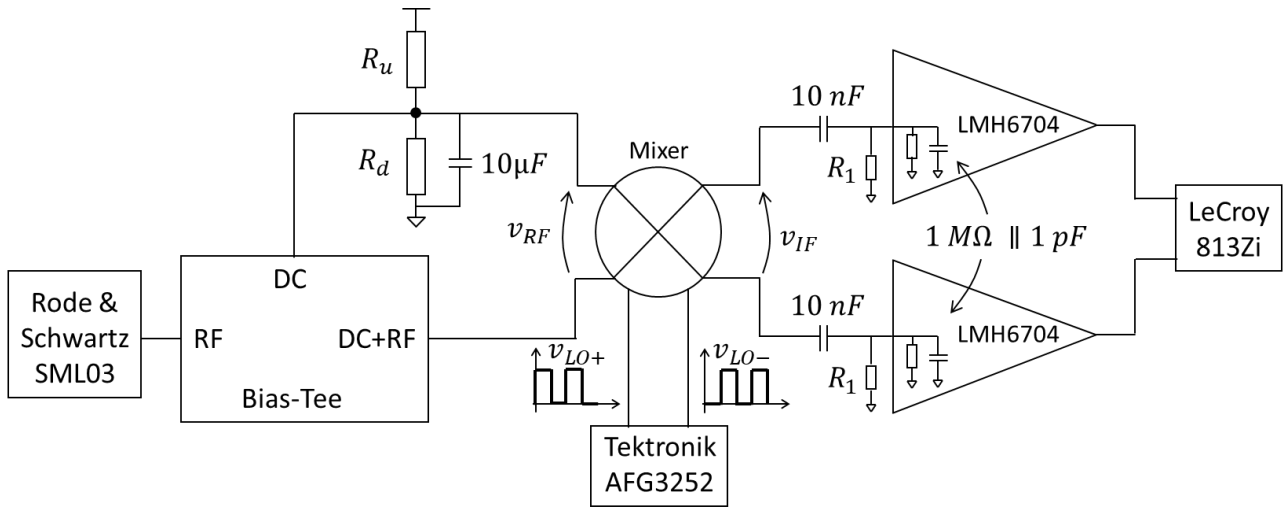
Figure 6.10: Measurement setup for mixer electrical characterization. R_1 is set to $1.2k\Omega$ for loaded mixer characterization, and to $100k\Omega$ for unloaded mixer characterization.

As for the LNA characterization, the RF signal generator SML03 (Rode & Schwartz®) was connected to the differential RF input of the mixer through the Bias Tee (see figures 6.1 and 6.10) to apply a ν_{RF} signal from $f_L = 1Mz$ to $100MHz$, plus $17KHz$. Both differential outputs were connected to a LMH6704 buffer through AC coupling. This AC coupling was set to 10 nF in parallel to $1.2k\Omega$ to characterize the gain versus frequency as if the mixer is loaded with the R_1 resistances of the output amplifier, and set to 10 nF in parallel to $100k\Omega$ to characterize the gain of the unloaded mixer. The amplitude of the RF signal was 130 mV for the unloaded mixer, and 260 mV for the loaded mixer. The local oscillator square signal, ν_{LO}, at frequency f_L was provided by a Tektronik® AFG3252 dual-channel arbitrary/function generator whose bandwidth is 240MHz. It should be noticed that above 100MHz, ν_{LO} is much more sinusoidal than square. Finally both LMH6704 buffer outputs were recorded with the LeCroy® 813Zi oscilloscope, from which the difference was computed, and the resulting down converted 17 kHz signal was visualized to determine the mixer gain versus the f_L frequency.

Figure 6.11: Gain versus frequency of the mixer loaded with $1.2k\Omega$ resistances.

Figure 6.12: Gain versus frequency of the unloaded mixer.

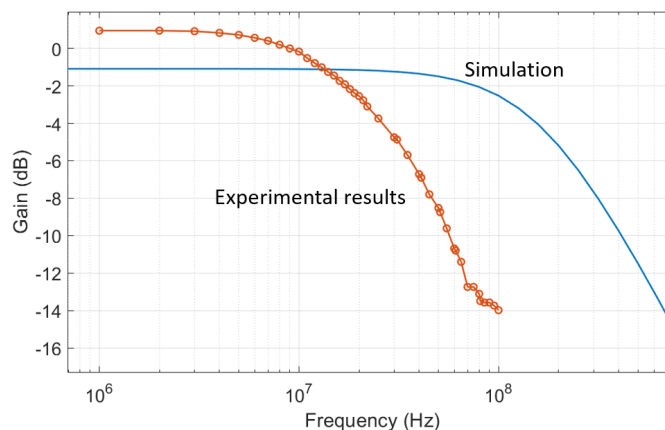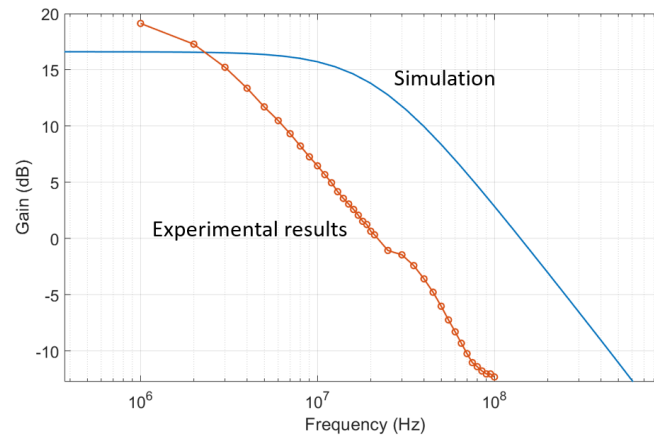Figures 6.11 and 6.12 show respectively the simulated and measurement results of the mixer gain versus frequency for the loaded and unloaded mixer. As expected under a $1.2k\Omega$ load, the gain is close to 0 dB, while it is close to 20 dB when it is unloaded. It should be noted that in both cases, the measured gain decreases faster than predicted by simulation. This can be explained by the shape of the local oscillator voltage wave, ν_{LO}. In simulation the gain is determined assuming ν_{LO} square, which is not the case in practice. During the switching phase, MS1 and MS2 are ON over a time window whose relative length is higher when frequency increases, i.e. when ν_{LO} looks like a sine wave instead of a square wave. However, when MS1 and MS2 are ON, the mixer gain is close to zero. So in practice the effective gain of the mixer is lower than the simulated gain, and the discrepancy between both gains increases with frequency. Because of that, the measured -3 dB bandwidth of the $1.2k\Omega$ loaded mixer is limited to 20 MHz. However, we will see that it does not prevent the whole receiver to work up to 60 MHz, even 80 MHz.

3 Output amplifier

3.1 Design

The output amplifier ensures the differential to single-ended conversion of the down converted FID signal, as well as its amplification with a gain that was set to 37 dB. Since the FID signal is typically down converted to a frequency around a few tens of kilohertz, the bandwidth of the output amplifier was limited to 200 kHz. So the output amplifier ensures also the low-pass filtering of the up converted signal. It was designed to drive easily an output capacitance of 25 pF in order for the receiver to be directly connected to an oscilloscope for signal acquisition. Its simulated gain versus frequency is shown in figure 6.13.
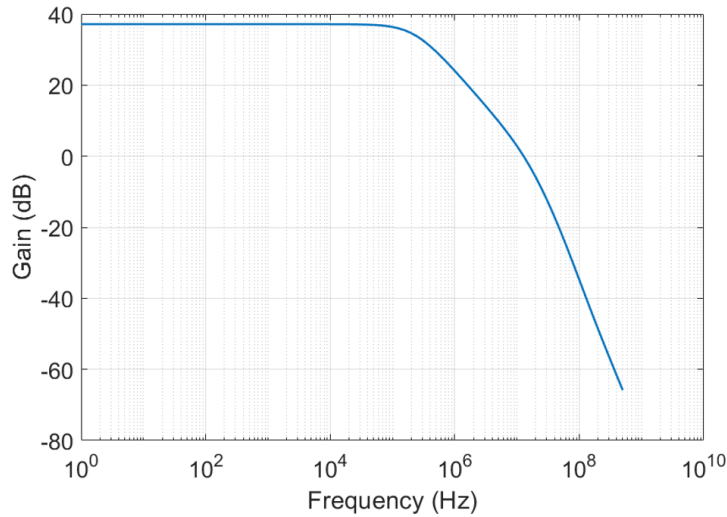
Figure 6.13: Simulated gain versus frequency of the differential to single-ended output amplifier loaded with 25pF.

The output amplifier uses a conventional architecture based on an Operational Transconductance Amplifier (OTA) fedback to provide a gain of $1 + R_2/R_1$, as shown in figure 6.9. The OTA is based on the widely used two-stage Miller compensated OTA shown in figure 6.14. It was designed with a conventional approach [140] and exhibits a static gain of 65 dB, a gain bandwidth product of 16 MHz, and an input referred thermal noise level of $5 \cdot 10^{-15} V^2/Hz$. Considering the LNA+MIXER gain of 20, it gives a simulated noise level referred to the LNA input equal to $5 \cdot 10^{-15}/20^2 = 12.5 \cdot 10^{-18} V^2/Hz$, a value four times higher than the LNA input noise. So at the input of the LNA, the simulated thermal noise level of the whole receiver is $15.8 \cdot 10^{-18} V^2/Hz$, which remains very small, much smaller than the intrinsic noise of the coil.

Table 6.3 provides the sizes of all transistors of the OTA. In addition, the circuit is biased with $13\mu A$ in M0 and $812\mu A$ in Mn.
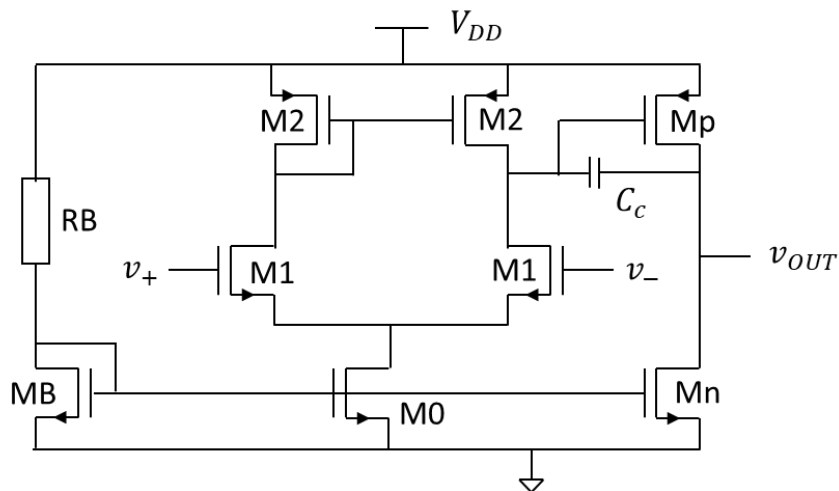
Figure 6.14: Miller compensated two-stage OTA used in the output amplifier.

	M0	M1	M2	Mn	Mp	MB	RB	Cc
W (μm)	1.4	2.8	20	84.3	400	1.4	$180k\Omega$	$150fF$
L (μm)	0.35	8	1.4	0.35	0.35	0.35		

Table 6.3: OTA sizing

3.2   Experimental results obtained with the output amplifier alone

For the measurement of its gain, the output amplifier was simply connected as shown in figure 6.15.
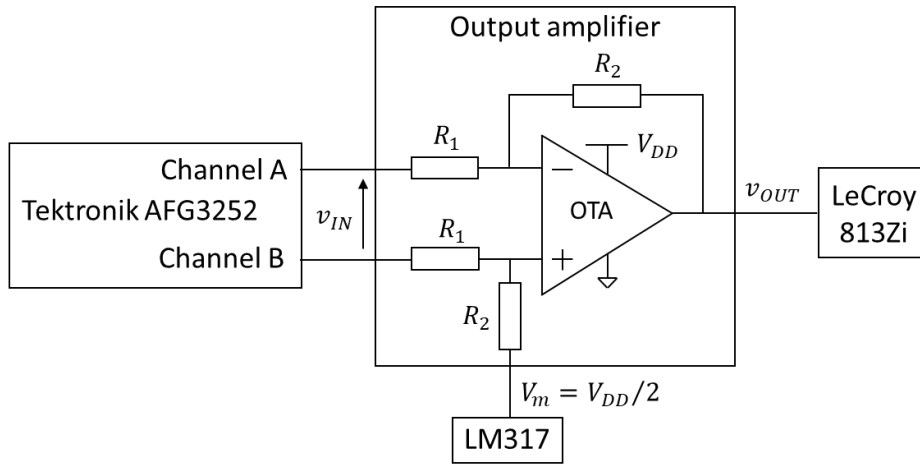
Figure 6.15: Experimental set-up for gain measurement of the output amplifier.

The $V_{DD}/2$ biasing point defining the virtual ground at the OTA input was applied thanks to a LM317 regulator soldered on the testing board. Then both inputs of the amplifier were connected to the dual channel Tektronik® AFG3252 function generator to apply a differential input of amplitude 5mV above a DC point of $V_{DD}/2 = 1.65$ V, and from 1 kHz to 4 MHz. The output was recorded with a LeCroy® 813Zi oscilloscope, from which the gain was determined. Figure 6.16 shows the experimental results. The static gain is 36.4 dB, very close to the expected 37 dB. The bandwidth is 350kHz, much more than the 200kHz that was targeted. This means that the actual gain bandwidth product is $350/200 = 1.75$ times higher than the simulated one. This GBW is given by [140]:

$$GBW = \frac{g_{m1}}{C_c} \tag{6.12}$$

So, the actual transconductance of M1, g_{m1}, is certainly higher than the expected one by simulation. This is readily possible when we consider the simple circuit made of MB and RB (see figure 6.14) we used to bias the OTA, where MB has a very small size of $W/L = 1.4/0.35$. For such transistor size we may have high fabrication dispersion, leading possibly here to a much higher biasing current than predicted in the differential input stage of the OTA, and thus a higher g_{m1}.
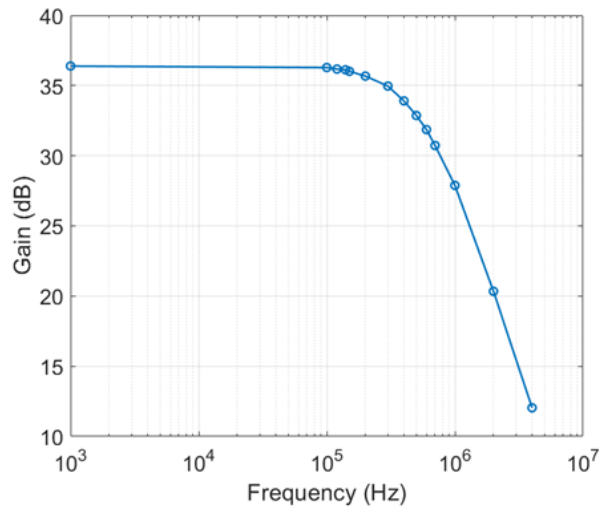
Figure 6.16: Measured gain versus frequency for the output amplifier.

For noise characterization of the output amplifier, we simply removed the AFG3252 in figure 6.15, and we short circuited both inputs of the amplifier with a SMA cable. The output of the amplifier was directly connected to an Agilent® 35670A dynamic signal analyzer to record the noise power spectral density. The result is shown in figure 6.17.
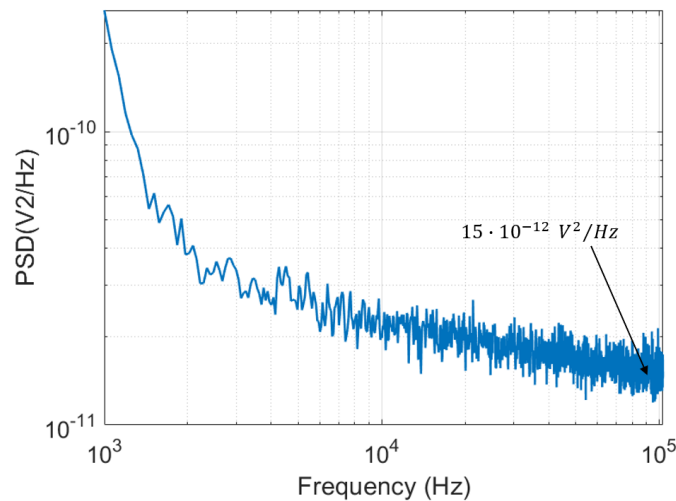
Figure 6.17: Measured output noise power spectral density of the output amplifier.

We see that over the 102.4 kHz measurement bandwidth of the Agilent®35670A, the noise is mainly a 1/f noise. This noise comes certainly from the LM317 (see figure 6.15). Anyway, from figure 6.17, we can say that the output thermal noise of the output amplifier is lower than $15 \cdot 10^{-12} V^2/Hz$, as expected by simulation. Considering the previous discussion on the actual value of g_{m1}, and reminding that the thermal noise is inversely proportional to $1/g_{m1}$, we certainly have an output thermal noise floor coming from the output amplifier close or lower than $15 \cdot 10^{-12}/1.75 = 8.5 \cdot 10^{-12} V^2/Hz$.

3.3   Characterization of the receiver

A second testing board, on which another CMOS chip was bonded, was used to characterize the complete receiver. All external components used to bias the receiver are the same as the ones used on the previous testing board dedicated to the characterization of the different elements of the receiver. For its gain characterization, the receiver was mounted as shown in figure 6.18.
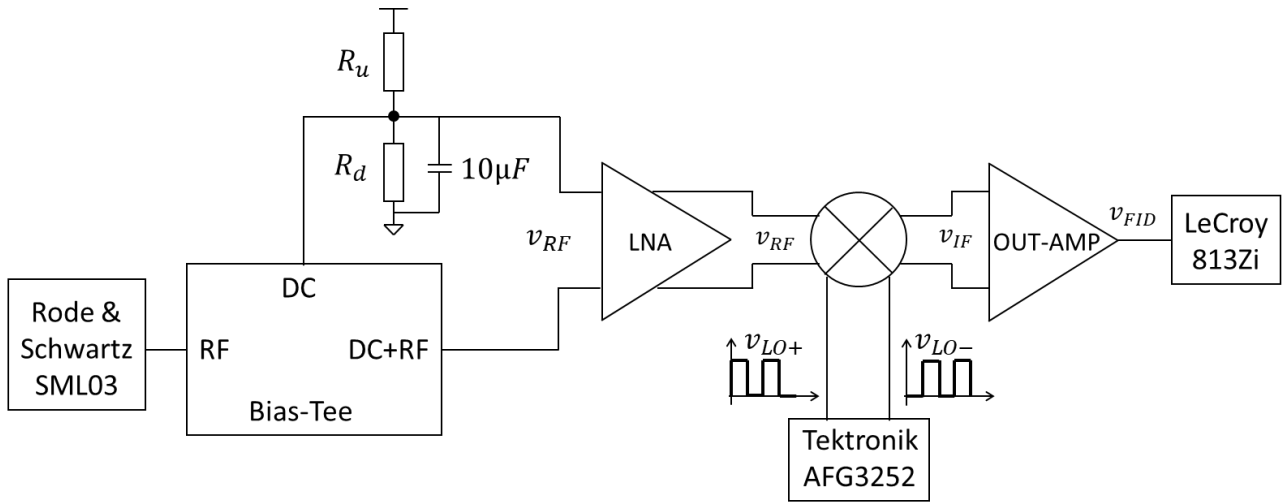
Figure 6.18: Experimental setup for receiver gain versus Larmor frequency.

As for the Mixer gain measurement, an input RF signal at $f_L + 17 kHz$, i.e. at the Larmor frequency plus 17 kHz, f_L ranging from 10 MHz to 100 MHz, was applied with the Rode & Schwartz® SML03 RF signal generator. The amplitude of the signal was set to 250 mV, and a 1/1000 attenuator was placed at the output of the SML03. The local oscillator signal, ν_{LO}, set at the Larmor frequency f_L was applied like for the mixer characterization, i.e. with the Tektronik® AFG3252. Then the output of the receiver was directly connected to the LeCroy® 813Zi to record the 17 kHz output signal amplitude, from which the gain was determined. Figure 6.19 shows the experimental result.
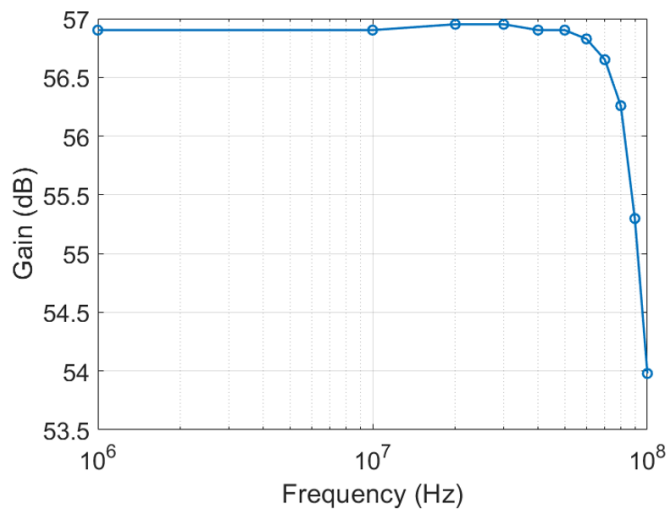
Figure 6.19: Measured receiver gain versus Larmor frequency.

The receiver gain is close to 57 dB over a bandwidth of 50 MHz, with a -3 dB bandwidth of 100 MHz. The gain result is close to the 60 dB that was expected by summing up the gains measured previously for the individual elements of the receiver. On the contrary, the -3 dB bandwidth of 100 MHz is much higher than expected since the characterization of the mixer alone, with its bandwidth of 20 MHz (see figure 6.11) should have reduced the receiver bandwidth to this value of 20 MHz. In fact, the mixer gain versus frequency of figure 6.11 was measured with the $R_1 = 1.2k\Omega$ resistances connected to a real ground, while in the receiver they are connected to the virtual ground of the output amplifier. Since this amplifier has a limited bandwidth of 350 kHz (see section 6.3), the differential input of the OTA behaves as a true virtual ground only up to roughly this frequency. Above this value, this is no longer valid, and the mixer is no longer loaded by a resistance of $1.2k\Omega$, but by a resistance which increases up to $R_1 + R_2 = 91.2k\Omega$. Under such a load, its gain increases (see figure 6.12), and compensates for the mixer gain decrease due to the non square v_{LO} signal. This is confirmed by looking at figure 6.20 where the simulated gain at the output of the mixer, the mixer being in the receiver amplifying chain, is shown. In this simulation, the switches of the mixer are set in one of both mixing phases, which is equivalent to having the mixer driven by a perfectly square ν_{LO} voltage. We clearly see that above 500 kHz, the gain increases, and that it remains above 26 dB up to 100 MHz. So up to roughly 100 MHz the mixer gain decrease due to the non square local oscillator voltage ν_{LO} is compensated by an increase due to the load seen by the mixer.
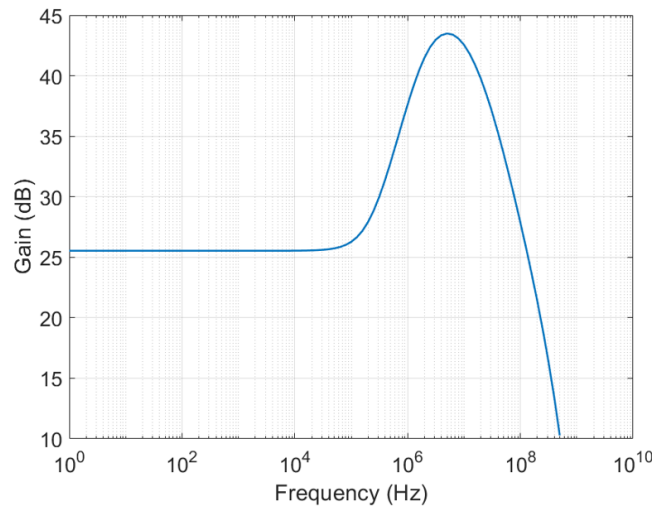
Figure 6.20: Gain versus frequency at the output of the mixer, the mixer being loaded by the output amplifier.

It is worth to notice that this gain compensation applies also for the noise spectrum at the output of the mixer. Figure 6.21 shows the simulated noise power spectral density at the output of the mixer when the mixer is in the receiver, i.e. when the mixer is loaded by the output amplifier, and its switches are set to one of both mixing phases. Such a spectrum is the spectrum at the output of the mixer when driven by a perfectly square ν_{LO} voltage at the Larmor frequency f_L, but unshifted around f_L. The figure shows also this noise when the LNA followed by the mixer are loaded by two resistances $R_1 = 1.2k\Omega$ and AC decoupled by a 10 nF capacitance, like in

figure 6.10, i.e. when the mixer gain is close to 0 dB up to 100 MHz. From these simulation results, we clearly see that the noise power spectrum at the output of the mixer is amplified between simulation and experimental results for 500 kHz and 100 MHz when the mixer is loaded by the output amplifier and driven by a perfectly square ν_{LO} voltage. On the contrary, it remains flat above 2 MHz, and up to 100 MHz, equal to the thermal noise at the output of the LNA, i.e. $1.1 \cdot 10^{-15} V^2/Hz$, when the mixer gain is close to 0 dB. So because of the gain compensation phenomenon, the noise at the output of the mixer in our experimental set up should be close to this last noise spectrum, where the mixer exhibits a gain of 0 dB up to 100 MHz, but for the high-pass filtering before 1 kHz due to the AC coupling with the 10 nF capacitance.
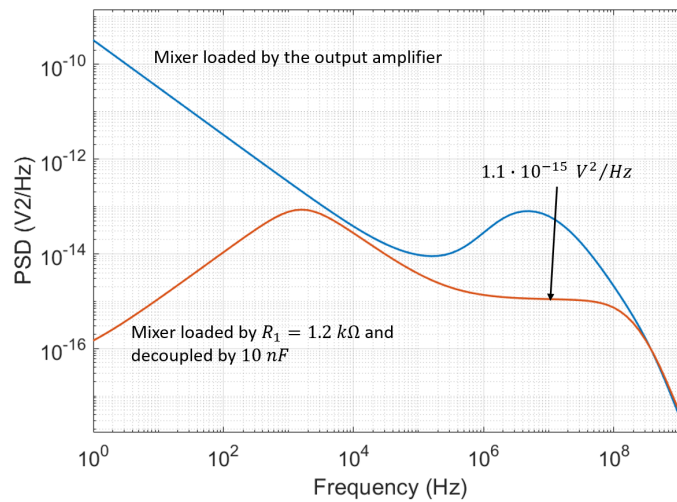
Figure 6.21: Simulated noise spectra at the output of the mixer depending on its load.

Due to the mixing at the Larmor frequency, f_L, this noise spectrum is shifted around f_L, as shown in figure 6.22. It is then amplified and low-pass filtered at 350 kHz by the output amplifier. Finally, in the bandwidth of interest of a few dozens of kHz, the noise spectrum at the output of the receiver is the sum of (i) this noise, i.e. the noise at the output of mixer around f_L amplified by the square of the output amplifier gain, and (ii) the output noise of the output amplifier.
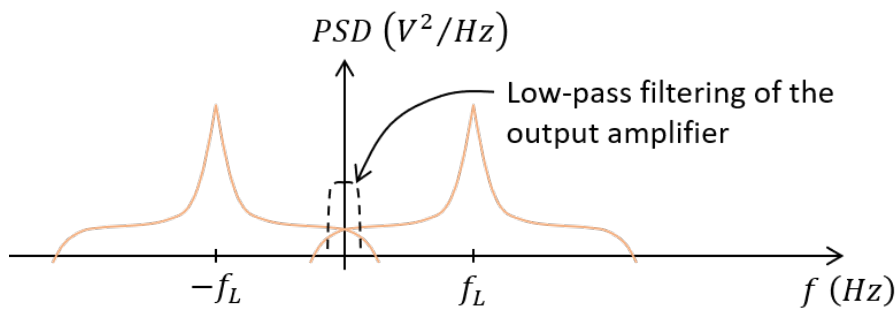
Figure 6.22: The noise spectrum at the output of the mixer.

For the noise characterization of the receiver, we just removed the Bias Tee at the input of the receiver, and we short circuited both inputs of the LNA with a SMA cable. Then the output

of the receiver was directly connected to the Agilent® 35670A dynamic signal analyzer to record the output noise spectrum. The experiment were carried out for $f_L =10MHz, 20MHz, 40MHz,$ $60MHz$, and $80MHz$, and the results are shown respectively in figures 6.23 to 6.27. First, it should be noticed that for all the measurements, the 1/f noise level is much lower than the 1/f noise that we measured at the output amplifier (see figure 6.17), and that we were expected to have at the output of the receiver. It means that on this second testing board, this 1/f noise coming mainly from the externally LM317 regulator used to set the mid-point V_m of the output amplifier is hopefully much lower than on the previous card used to characterize the output amplifier alone. The spectral line at 30 kHz that we observe on all spectra is a parasitic signal coming from the room in which the experiment was carried out, and in which many equipments were switched ON.
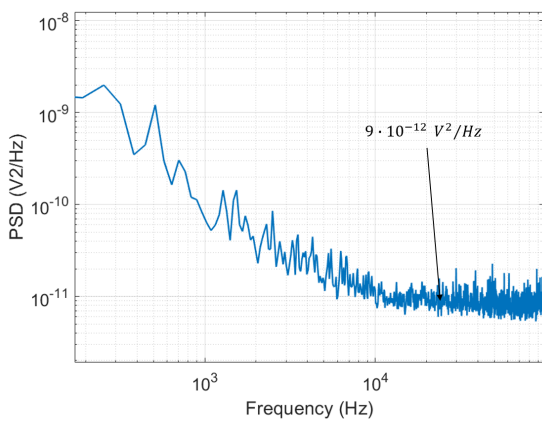
Figure 6.23: Receiver output noise spectrum at $f_L = 10MHz$.
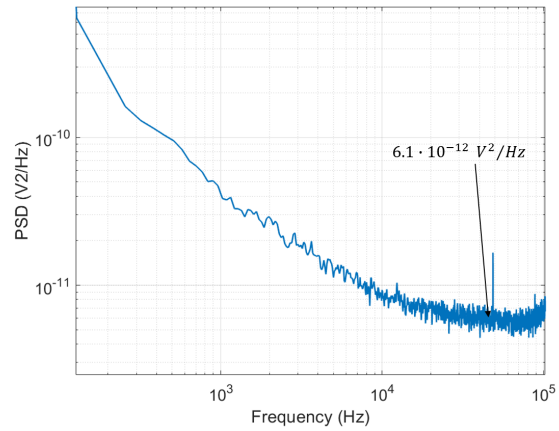
Figure 6.24: Receiver output noise spectrum at $f_L = 20MHz$.
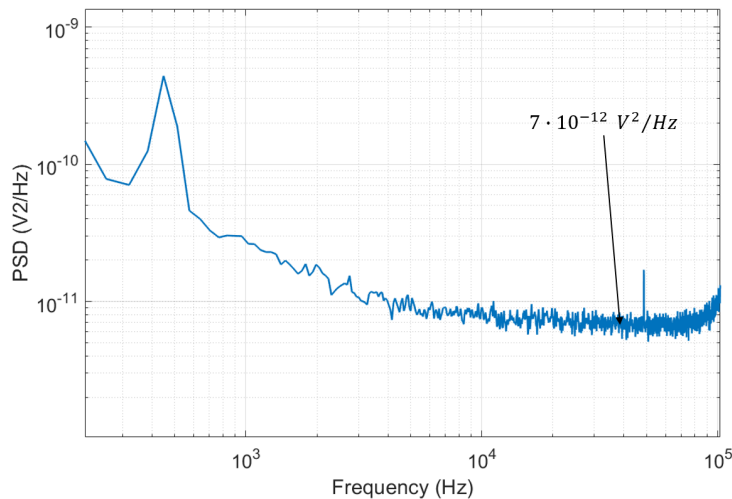
Figure 6.25: Receiver output noise spectrum at $f_L = 40MHz$.
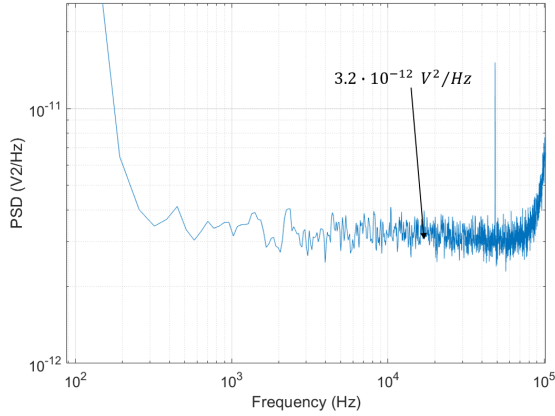
Figure 6.26: Receiver output noise spectrum at $f_L = 60MHz$.
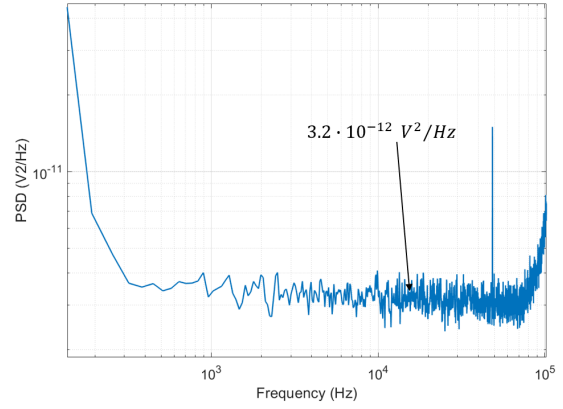
Figure 6.27: Receiver output noise spectrum at $f_L = 80MHz$.

It is interesting to note that above $f_L = 60MHz$, the thermal noise floor remains constant, equal to $3.2 \cdot 10^{-12}V^2/Hz$. At this frequency, as it can be seen in figure 6.21, the noise coming from the LNA-MIXER starts to decrease, and becomes lower than the thermal noise of the output amplifier. Therefore, $3.2 \cdot 10^{-12}V^2/Hz$ is certainly a good estimation of the output thermal noise of the output amplifier. It was estimated to $8.5 \cdot 10^{-12}V^2/Hz$ with the results obtained by the characterization of the output amplifier alone (see section 3), but it is obviously lower in this chip. Finally, when f_L decreases, the output noise level increases, as it is expected from figure 6.21. For instance, at $f_L = 10MHz$, the simulation of figure 6.21 gives a noise level of $1.1 \cdot 10^{-15}V^2/Hz$. This noise is amplified by the 36.4 dB of the output amplifier, i.e. by $66^2 = 4356$, leading to a noise level of $4.8 \cdot 10^{-12}V^2/Hz$ that has to be added to the $3.2 \cdot 10^{-12}V^2/Hz$ noise density coming from the output amplifier. We thus get an output noise level estimation of $8 \cdot 10^{-12}V^2/Hz$, that has to be compared to the $9 \cdot 10^{-12}V^2/Hz$ measured noise level (see figure 6.23).

In conclusion, looking at 60 MHz, i.e. at the Larmor frequency of the NMR experiments we performed in chapter 5 with our discrete receiver, we have for our integrated receiver a gain of 56.8 dB, i.e. 692, and an output noise level of $3.2 \cdot 10^{-12}V^2/Hz$. Referred at the receiver input, this noise is divided by 692^2, which gives an input noise level of $6.7 \cdot 10^{-18}V^2/Hz$. If this receiver is connected to the epoxy coil we used in chapter 5, whose Q factor is 128, when referred at the input of the coil, the noise is divided by Q^2. So at the input of the coil the receiver contributes to a noise level of $4.1 \cdot 10^{-22}V^2/Hz$. Such a noise is negligible in comparison to the thermal noise of the coil, $3 \cdot 10^{-20}V^2/Hz$, coming from its 1.86Ω intrinsic resistance. So, if we had used this receiver, the system would have exhibited its best SNR, which is the intrinsic SNR of the coil. Unfortunately, we were not able to perform such an experiment, first by lack of time, but also because of a lack of CMOS chips. Indeed, as it can be seen in figure 6.2, the chip contains in its center a pad ring to test several elementary devices. One of these devices was a varicap suitable to integrate the C_1 tuning capacitance. The other devices were linked to another research project. Unfortunately, a design error in this central pad ring introduced a short circuit between V_{DD} and the ground, making the chip unusable a priori. However hopefully, the short circuit was easily spotted, and by scratching with a tiny needle the surface of the chip (see figure 6.28), we

were able to disconnect the central pad ring from the external one, making the receiver working. However, only 4 chips were saved.
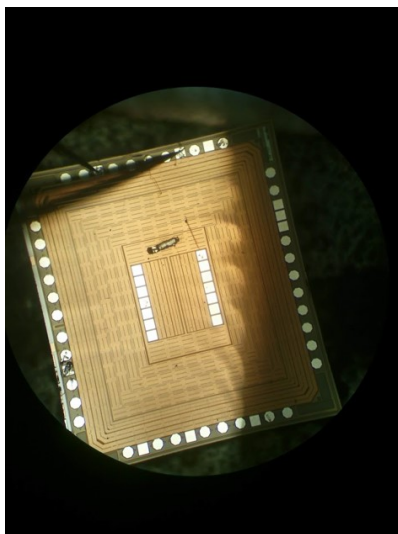
Figure 6.28: Photography of the repaired CMOS chip.

$$*$$
$$* \qquad *$$

Summary

This last chapter has presented the integrated receiver we designed and fabricated in the low cost CMOS AMS $0.35\,\mu$m technology. It was designed with an infinite input impedance to take full advantage of the quality factor of the coil. First the architecture of the receiver was presented, and the design and experimental characterization of its three sub-circuits, the Low Noise Amplifier, the mixer, and the output amplifier, were discussed in details. Finally, the whole receiver has been characterized. The experimental results show that combined with the epoxy coil used in chapter 5, this integrated receiver allows to get the best Signal-to-Noise Ratio that is achievable, i.e. the intrinsic SNR of the coil. It thus opens the way to develop a portable NMR spectrometer once a compact and homogeneous magnet will be available.

Chapter 7

Conclusion and prospective

The aim of this PhD work, which was done partly at ICube laboratory, in Strasbourg (France), and partly at IM2 Institute, in Muttenz (Switzerland), was to assess the possibility of developing a low-cost portable Nuclear Magnetic Resonance spectrometer that can be easily deployed in distribution water stations for continuously monitoring the feared presence of pollutants such as atrazine or glyphosate. The availability of such a probe would be a great improvement in the following up of the quality of water, since nowadays, the test of water sample may be done only once year, or even less frequently, in some areas of European countries. In the first chapter, after presenting the context of NMR, we described the general concept of the portable pollutants NMR probe which will be developed in the framework of an Interreg European project in which ICube and IM2 are partners. This PhD work is a pre-study that was somehow at the genesis of this project. Then a state of the art of the miniaturized NMR systems existing in the scientific literature was presented. Most of these systems are relaxometers, and not spectrometers, certainly because NMR spectrometry requires a very high homogeneity of the B_0 portable magnet in order to be able to resolve the NMR spectrum peaks. The second chapter dealt with the theory behind the nuclear magnetic resonance, and described the different functional elements that compose a NMR measurement system, i.e. the sensing head made of a coil with its tuning/matching circuit, the receiver which amplifies the tiny FID signal, the transmitter which makes the sample resonating, the magnet, and finally the unit which analyses the data. Next chapters address these key elements of the NMR system with the target of developing a portable NMR probe.

Chapter 3 is focused of the issues in developing the magnet, as well as on a study to assess the possible influence of high magnetic field on electronic components that will be placed inside the magnet. After a short reminding of the theory behind magnetic material and magnetic field simulation, a structure that is widely adopted in the literature, i.e. the Halbach array, was studied in details to assess the possibility of using it as a portable magnet. We thus designed, simulated, and fabricated a 8-element Halbach magnet. The preliminary results we obtained show that it is possible to get a B_0 close to 1T, and that the experimental B_0 field we measured for our structure, around 700mT, is close to the one we simulated. However, simulations have shown that to have a highly homogeneous B_0 field, it is mandatory to shim B_0. Unfortunately, these

developments were out of the scope of this PhD work, initially more focused on developing the electronics. So we decided to postpone this development for the next Interreg project, and to use the magnet of a commercial benchtop NMR system, a Magritek®60, to demonstrate the possibility of detecting pollutants with a low-cost receiving electronics. At the end, as we expect to have the electronics very close to the sensing coil, so inside the magnet, we also performed a theoretical, and experimental study of the influence of strong magnetic fields on the electrical characteristics of MOS transistors. A simple model has been developed and measurements were made under the 7T B_0 field of a Magnetic Resonance Imaging scanner available at ICube. We concluded that under the moderate field of a portable NMR spectrometer, i.e. around 1 T, the influence can be readily neglected. The next chapter deals with the sensing head, i.e. the coil and its tuning/matching circuit, as well as the key parameters that define the Signal-to-Noise ratio in NMR spectrometry. The different types of coils that exist have been briefly discussed, showing that when the geometrical constraints of the probe allow its use, the solenoidal coil is a very good choice, not to say the best, since its filling factor is close to 100%, and its sensing area is well defined. The tuning and matching of the coil to the input port of the Low Noise Amplifier, i.e. to the input port of the receiver, was then deeply discussed. A model has been developed, and it was shown that the best choice is to use a LNA with an infinite input impedance since it allows to benefit from the quality factor of the coil to passively amplify the FID signal before its amplification with the LNA. In this case, it is very easy, even with a low-power consumption, and thus medium quality LNA, to get the best Signal-to-Noise Ratio that we can have with a NMR receiver, i.e. a SNR equal to the intrinsic SNR of the coil. However, with such a high input impedance LNA, we cannot use a coaxial cable to connect the coil to the LNA. As a consequence, the receiver electronics has to be placed very close to the coil.

Commercial radio frequency LNAs exhibit all a 50Ω input impedance. So in order to show that high impedance LNA are relevant to build a NMR probe that would exhibit a very high SNR, we developed a low-cost CMOS chip on which a receiver with a high input impedance was integrated. Unfortunately, the very long delay for its delivery, close to one year, led us to develop a discrete receiver with commercial LNAs, and use it to perform our first NMR experiments in the magnet of a commercial Magritek®60, with the aim to show that the atrazine pollutant can be detected using this low-cost receiver. Chapter 5 presents this discrete receiver, as well as the two solenoidal coils we built. All details are given on the different electronic sub-circuits of the receiver, on the fabrication steps of the coils, as well as on the sensing head holder. Then NMR spectra were acquired with this discrete receiver on tap water, ethanol, acetonitrile, and atrazine in acetonitrile. These spectra were compared with the spectra acquired directly with the Magritek®60. Both spectra are in very good agreements, although the discrete receiver needs to be improved in terms of its susceptibility to electromagnetic perturbations. Finally, although it has to be confirmed by the averaging of more measurements, atrazine seems to be detectable with such a low-cost probe. The last chapter presents the high input impedance CMOS receiver we developed. Since all its sub-circuits were also integrated alone on the chip, it was possible to characterize each one individually. The electronic architecture we implemented to reach the required specifications for

each sub-circuit was presented, and experimental results compared with the expected electrical specifications. Finally, the whole receiver was tested, and the experimental results we obtained were discussed on the light of the results obtained on the individual sub-circuits. Finally, we have shown that this low-power, low-cost integrated receiver is able to detect a NMR signal up to a Larmor frequency of 100 MHz, with a negligible noise contribution when it is directly connected to the coils developed in chapter 5. It should be noted that we were not able to build a complete NMR probe that could be used in the Magritek®60 because of the limited number of CMOS chips, and also due to lack of time.

These preliminary results show that it should be readily possible to build a low-cost portable NMR spectrometer to detect pollutants in water. However, many additional technological developments are required yet. First a new CMOS chip has to be sent to fabrication. We could take this opportunity to (i) improve the architecture of the receiver, and (ii) co-integrate the tunable capacitance which is required to make the coil resonating at the Larmor frequency. In addition, since the chip will be inside the magnet, we could add a thermal sensor in the chip to sense the temperature of the magnet, and adjust the Larmor frequency of the receiver to the B_0 variation due to thermal effects. An integrated Hall magnetometer could also be used for such a purpose. The second technological development to address is the transmitter. The realization of RF pulses can be done with a programmable Direct Digital Synthesizer (DDS). A pre-study was done by Bachelor students I supervised, and they were able to demonstrate the generation of non-selective RF pulses. This first prototype of this programmable generator of RF pulses has also be extended to selective pulse shapes, although its physical implementation is not done yet. As discussed for the receiving coil in chapter 4, the transmitting coil has to be tuned and matched to the output resistance of the power amplifier that is necessary to develop yet, and that will be placed just after the DDS to provide the power to the TX coil. The last development, which is required, and which is certainly the most critical, is the magnet that needs to have a very high B_0 homogeneity over the volume of the sample, typically over one cubic millimetre. As shown in chapter 3, the Hallbach array needs to be shimmed. This shimming can be done passively, using additional magnets carefully placed [102], or actively with tunable currents in shimming coils [141]. It would be also interesting to look at the possibility of using electromagnets that have the advantage to provide the possibility of changing the B_0 magnitude. Whatever, we hope that this PhD work will be a useful starting point for the development of low cost portable NMR spectrometers for water pollutants detection.

APPENDIX

Computation of the power spectral density of a noise signal with the method of the periodogram

We consider a real signal $x(t)$ with a finite mean power, recorded over the time window T. It is named $x_T(t)$. It may be a sine wave or a noise signal. It is worth to notice that when this signal is considered over an infinite duration, its energy is infinite. On the contrary, when it is recorded on a finite time window T, it has a finite energy which is expressed as:

$$E(x_T) = \int_{-\infty}^{+\infty} x_T(t)^2 \cdot dt$$

The Fourier transform of $x_T(t)$ gives :

$$FT_{x_T}(f) = \int_{-\infty}^{+\infty} x_T(t) \cdot e^{-j \cdot 2\pi \cdot f \cdot t} \cdot dt = \int_{0}^{T} x_T(t) \cdot e^{-j \cdot 2\pi \cdot f \cdot t} \cdot dt$$

If we consider now the series of the N samples of $x_T(t)$ sampled at frequency $f_s = 1/T_s$, with $T_s = T/N$, i.e. the samples $x0$, $x(T/N)$, $x(2 \cdot T/N)$,..., $x((N-1) \cdot T/N)$, the Fourier transform of $x_T(t)$ can be approximated by:

$$DTFTx_T(f) = \sum_{k=0}^{k=N-1} x_k \cdot e^{-j \cdot 2\pi \cdot f \cdot \frac{k \cdot T}{N}} \cdot \frac{T}{N} \text{ where } x_k = x\left(k \cdot \frac{T}{N}\right)$$

This approximation of the spectrum of $x_T(t)$ is a continuous function of the frequency variable f. In addition, it is worth to notice that this approximated spectrum is a periodic function of period f_s. Indeed, it is the spectrum of $x_T(t)$ sampled at frequency f_s. The simplest way of representing this spectrum is to compute it for different values of the frequency f, between $f = 0$ and $f = f_s$. In practice, we use to represent it for N values of f evenly distributed, i.e. for $f = 0$, $f = f_s/N$, $f = 2 \cdot f_s/N$,..., $f = N - 1 \cdot f_s/N$.

Note : The spectrum that is plotted for these N frequency values is the sampled version of $DFTx_T(f)$. When we compute its inverse Fourier transform, we get a periodic version of $x_T(t)$, i.e. a signal corresponding to $x_T(t)$ shifted by $k \cdot T$ where $k \in \mathbb{Z}$. It means that the power spectral density (PSD) that we compute with the periodogram corresponds to the PSD of the periodic

version of $x_T(t)$. Thus we get for $f = i \cdot \frac{f_s}{N}$:

$$DTFT x_T \left(f = i \cdot \frac{f_s}{N} \right) = \sum_{k=0}^{k=N-1} x_k \cdot e^{-j \cdot 2\pi \cdot i \cdot \frac{k}{N}} \cdot \frac{T}{N} = T_s \cdot \sum_{k=0}^{k=N-1} x_k \cdot e^{-j \cdot 2\pi \cdot i \cdot \frac{k}{N}} = T_s \cdot DFT(x_0, ..., x_{n-1})$$

where $DFT(x_0, ..., x_{n-1})$ is the Discrete Fourier Transform of the series of numbers $(x_0, ..., x_{n-1})$. This Discrete Fourier Transform can be easily computed with the Fast Fourier Transform algorithm or *FFT*. In addition, the Parseval theorem states that for a signal of finite energy $v(t)$, we have:

$$\int_{-\infty}^{+\infty} v^2(t) \cdot dt = \int_{-\infty}^{+\infty} |FTv(f)|^2 \cdot df$$

In other words, the signal energy is the integral of the squared module of its Fourier transform. It is worth to notice that this theorem is only true for a signal with a finite energy. It is thus valid for a signal which is the recording on a finite time window T of a signal of finite mean power, like a sine wave or a noise signal. So, for $x_T(t)$ we can write:

$$E(x_T) = \int_{-\infty}^{+\infty} x_T^2(t) \cdot dt = \int_{-\infty}^{+\infty} |FT_{x_T}(f)|^2 \cdot df$$

We can thus compute an approximated value of the energy of $x_T(t)$ by :

$$E(x_T) = \sum_{i=0}^{N-1} |DFT x_T(f_i)|^2 \cdot \frac{f_s}{N} = \frac{f_s}{N} \cdot \sum_{i=0}^{N-1} |T_s \cdot DFT(x_0, ..., x_{n-1})|^2$$

which can be written:

$$E(x_T) = T_s^2 \cdot \frac{f_s}{N} \cdot \sum_{i=0}^{N-1} |DFT(x_0, ..., x_{n-1})|^2 = \frac{T_s}{N} \cdot \sum_{i=0}^{N-1} |DFT(x_0, ..., x_{n-1})|^2$$

The series $\{(T_s/N) \cdot |DFT(x_0, ..., x_{n-1})|^2\}$ is named the periodogram of $x_T(t)$. By summing this series of numbers, we get an approximated value of the energy of $x_T(t)$. So, the series $\{(T_s/N) \cdot |DFT(x_0, ..., x_{n-1})|^2\}$ is an approximation of the spectral density of energy of $x_T(t)$. Now, if $x_T(t)$ represents the recording over a finite time window, T, of the signal $x(t)$ with a finite mean power, we just need to divide by T to get an estimation of the mean power of $x(t)$:

$$\langle P(x) \rangle = \frac{T_s}{T \cdot N} \cdot \sum_{i=0}^{N-1} |DFT(x_0, ..., x_{n-1})|^2$$

So, dividing by T the periodogram provides an estimation of the mean power spectral density, simply named power spectral density (PSD), of $x(t)$. In conclusion, the series of numbers $\{(T_s/(T \cdot N) \cdot |DFT(x_0, ..., x_{n-1})|^2\}$ where $DFT(x_0, ..., x_{n-1})$ is generally computed by Fast Fourier Transform, and it is the periodogram that we computed to estimate the power spectral density of all the FID signals we have measured in chapter 5.

Bibliography

[1] W. C. Li, "Occurrence, sources, and fate of pharmaceuticals in aquatic environment and soil," 2014.

[2] C. M. Lee, P. Palaniandy, and I. Dahlan, "Pharmaceutical residues in aquatic environment and water remediation by TiO2 heterogeneous photocatalysis: a review," *Environmental Earth Sciences*, vol. 76, no. 17, 2017.

[3] C. A. Hoga, K. V. Reche, F. L. Almeida, V. R. Reis, R. P. Cordeiro, A. Anadón, and F. G. Reyes, "Development and validation of an analytical method for the determination of 17β-estradiol residues in muscle of tambaqui (Colossoma macropomum Cuvier, 1818) by LC-MS/MS and its application in samples from a fish sexual reversion study," *Journal of Chromatography B: Analytical Technologies in the Biomedical and Life Sciences*, vol. 1128, p. 121774, oct 2019.

[4] S. J. Khan, T. Wintgens, P. Sherman, J. Zaricky, and A. I. Schäfer, "Removal of hormones and pharmaceuticals in the Advanced Water Recycling Demonstration Plant in Queensland, Australia," *Water Science and Technology*, vol. 50, pp. 15–22, sep 2004.

[5] J. Bartram and S. Cairncross, "Hygiene, sanitation, and water: Forgotten foundations of health," *PLoS Medicine*, vol. 7, no. 11, pp. 1–9, 2010.

[6] World Health Organization, *Safe water, better health. 2019 update*. 2019.

[7] WHO and Unicef, "Global Water Supply and Sanitation Assessment 2000 Report," *Water Supply*, p. 87, 2000.

[8] U. Holzgrabe, "Quantitative NMR spectroscopy in pharmaceutical applications," aug 2010.

[9] E. Zieminska, B. Toczylowska, D. Diamandakis, W. Hilgier, R. K. Filipkowski, R. Polowy, J. Orzel, M. Gorka, and J. W. Lazarewicz, "Glutamate, glutamine and GABA levels in rat brain measured using MRS, HPLC and NMR methods in study of two models of autism," *Frontiers in Molecular Neuroscience*, vol. 11, no. November, pp. 1–19, 2018.

[10] A. Kadjo, N. Baxan, A. Briguet, D. Graveron-Demilly, L. Fakri-Bouchet, R. Cespuglio, and C. Rousset, "In vivo animal NMR studies using implantable micro coil," in *IST 2008 - IEEE Workshop on Imaging Systems and Techniques Proceedings*, pp. 294–296, IEEE, 2008.

[11] Y. Liu, N. Sun, H. Lee, R. Weissleder, and D. Ham, "CMOS mini nuclear magnetic reso-
nance system and its application to biomolecular sensing," in *Digest of Technical Papers -
IEEE International Solid-State Circuits Conference*, vol. 51, I E E E, 2008.

[12] A. Y. Luaibi, A. J. Al-Ghusain, A. Rahman, M. H. Al-Sayah, and H. A. Al-Nashash, "Non-
invasive blood glucose level measurement using nuclear magnetic resonance," *2015 IEEE
8th GCC Conference and Exhibition, GCCCE 2015*, pp. 1–4, 2015.

[13] John L. Smith, "The Pursuit of Noninvasive Glucose : " Hunting the Deceitful By John L .
Smith Fourth Edition : Revised and Expanded Preface to the Fourth Edition," p. 145, 2011.

[14] A. P. Sobolev, F. Thomas, J. Donarski, C. Ingallina, S. Circi, F. Cesare Marincola, D. Capi-
tani, and L. Mannina, "Use of NMR applications to tackle future food fraud issues," 2019.

[15] J. Kim, B. Hammer, and R. Harjani, "A 5-300MHz CMOS transceiver for multi-nuclear NMR
spectroscopy," in *Proceedings of the Custom Integrated Circuits Conference*, IEEE, 2012.

[16] U. Holzgrabe, B. Diehl, and I. Wawer, *NMR Spectroscopy in Pharmaceutical Analysis*.
2008.

[17] J. D. Taylor, P. J. Gilbert, M. A. Williams, W. R. Pitt, and J. E. Ladbury, "Identification of
novel fragment compounds targeted against the pY pocket of v-Src SH2 by computational
and NMR screening and thermodynamic evaluation," *Proteins: Structure, Function and
Genetics*, vol. 67, pp. 981–990, jun 2007.

[18] J. Vazquez, L. Tautz, J. J. Ryan, K. Vuori, T. Mustelin, and M. Pellecchia, "Development
of molecular probes for second-site screening and design of protein tyrosine phosphatase
inhibitors," *Journal of Medicinal Chemistry*, vol. 50, pp. 2137–2143, may 2007.

[19] J. Kim, B. Hammer, and R. Harjani, "A low power CMOS receiver for a tissue monitoring
NMR spectrometer," in *IEEE Symposium on VLSI Circuits, Digest of Technical Papers*,
pp. 221–222, IEEE, 2010.

[20] J. M. Macdonald, O. Schmidlin, and T. L. James, "In vivo monitoring of hepatic glutathione
in anesthetized rats by 13C NMR," *Magnetic Resonance in Medicine*, vol. 48, pp. 430–439,
sep 2002.

[21] L. Fakri-Bouchet, "Implantable Microcoil for In-vivo Magnetic Resonance Spectroscopy,"
International Journal of Biosensors & Bioelectronics, vol. 3, sep 2017.

[22] J. B. Haun, T. J. Yoon, H. Lee, and R. Weissleder, "Magnetic nanoparticle biosensors," may
2010.

[23] K. M. Lei, H. Heidari, P. I. Mak, M. K. Law, F. Maloberti, and R. P. Martins, "A Handheld
High-Sensitivity Micro-NMR CMOS Platform With B-Field Stabilization for Multi-Type Bio-
logical/Chemical Assays," *IEEE Journal of Solid-State Circuits*, vol. 52, pp. 284–297, jan
2017.

[24] N. Sun, T. J. Yoon, H. Lee, W. Andress, R. Weissleder, and D. Ham, "Palm NMR and 1-chip NMR," in *IEEE Journal of Solid-State Circuits*, vol. 46, pp. 342–352, jan 2011.

[25] M. Grisi, G. Gualco, and G. Boero, "A broadband single-chip transceiver for multi-nuclear NMR probes," *Review of Scientific Instruments*, vol. 86, no. 4, pp. 1–8, 2015.

[26] A. Dupré, K. M. Lei, P. I. Mak, R. P. Martins, and W. K. Peng, "Micro- and nanofabrication NMR technologies for point-of-care medical applications – A review," mar 2019.

[27] H. Lee, T. J. Yoon, J. L. Figueiredo, F. K. Swirski, and R. Weissleder, "Rapid detection and profiling of cancer cells in fine-needle aspirates," *Proceedings of the National Academy of Sciences of the United States of America*, vol. 106, no. 30, pp. 12459–12464, 2009.

[28] A. Y. Luaibi, A. J. Al-Ghusain, A. Rahman, M. H. Al-Sayah, and H. A. Al-Nashash, "Noninvasive blood glucose level measurement using nuclear magnetic resonance," in *2015 IEEE 8th GCC Conference and Exhibition, GCCCE 2015*, 2015.

[29] Y. Parlak and N. Guzeler, "Nuclear magnetic resonance spectroscopy applications in foods," *Current Research in Nutrition and Food Science*, vol. 4, pp. 161–168, oct 2016.

[30] E. Hatzakis, "Nuclear Magnetic Resonance (NMR) Spectroscopy in Food Science: A Comprehensive Review," jan 2019.

[31] W. Zia, "Advances in Compact Magnetic Resonance : Devices , Methodologies , and Investigations," 2016.

[32] M. de la Santé, "Bilan De La Qualite De L'Eau Au Robinet Du Consommateur Vis-a-Vis Des Pesticides En 2013," pp. 1–14, 2015.

[33] Swissinfo, "Banned pesticide found in Swiss drinking water," 2020.

[34] D. Issadore, C. Min, M. Liong, J. Chung, R. Weissleder, and H. Lee, "Miniature magnetic resonance system for point-of-care diagnostics," *Lab on a Chip*, vol. 11, no. 13, pp. 2282–2287, 2011.

[35] E. W. McFarland and A. Mortara, "Three-dimensional NMR microscopy: Improving SNR with temperature and microcoils," *Magnetic Resonance Imaging*, vol. 10, no. 2, pp. 279–288, 1992.

[36] J. E. Stocker, T. L. Peck, S. J. Franke, J. Kruse, M. Feng, and R. L. Magin, "Development of an integrated detector for NMR microscopy," in *Annual International Conference of the IEEE Engineering in Medicine and Biology - Proceedings*, vol. 17, pp. 843–844, 1995.

[37] G. Boero, C. De Raad Iseli, P. A. Besse, and R. S. Popovic, "An NMR magnetometer with planar microcoils and integrated electronics for signal detection and amplification," *Sensors and Actuators, A: Physical*, vol. 67, no. 1-3, pp. 18–23, 1998.

[38] G. Boero, J. Frounchi, B. Furrer, P. A. Besse, and R. S. Popovic, "Fully integrated probe for proton nuclear magnetic resonance magnetometry," *Review of Scientific Instruments*, vol. 72, no. 6, pp. 2764–2768, 2001.

[39] I. L. Dalal, A. L. Kirpalani, and F. L. Fontaine, "A low-cost scalable multichannel digital receiver for magnetic resonance imaging," in *Annual International Conference of the IEEE Engineering in Medicine and Biology - Proceedings*, pp. 1897–1900, 2006.

[40] L. S. Fan, S. S. Hsu, J. D. Jin, C. Y. Hsieh, W. C. Lin, H. C. Hao, H. L. Cheng, K. C. Hsueh, and C. Z. Lee, "Miniaturization of magnetic resonance microsystem components for 3D cell imaging," in *Digest of Technical Papers - IEEE International Solid-State Circuits Conference*, pp. 2005–2007, 2007.

[41] J. Anders and G. Boero, "A low-noise CMOS receiver frontend for MRI," in *2008 IEEE-BIOCAS Biomedical Circuits and Systems Conference, BIOCAS 2008*, pp. 165–168, 2008.

[42] N. Sun, "CMOS RF Biosensor Utilizing Nuclear Magnetic Resonance," *IEEE Journal of Solid-State Circuits*, vol. 44, no. 5, p. 1629, 2009.

[43] A. Hassibi, A. Babakhani, A. Hajimiri, and S. Member, "A Spectral-Scanning Nuclear Magnetic Resonance," *Ieee Journal of Solid-State Circuits*, vol. 44, no. 6, pp. 1805–1813, 2009.

[44] J. Anders, G. Chiaramonte, P. SanGiorgio, and G. Boero, "A single-chip array of NMR receivers," *Journal of Magnetic Resonance*, vol. 201, no. 2, pp. 239–249, 2009.

[45] J. Anders, P. Sangiorgio, and G. Boero, "A fully integrated IQ-receiver for NMR microscopy," *Journal of Magnetic Resonance*, vol. 209, no. 1, pp. 1–7, 2011.

[46] J. B. Haun, C. M. Castro, R. Wang, V. M. Peterson, B. S. Marinelli, H. Lee, and R. Weissleder, "Micro-NMR for rapid molecular analysis of human tumor samples," *Science Translational Medicine*, vol. 3, no. 71, 2011.

[47] V. Badilita, K. Kratt, N. Baxan, J. Anders, D. Elverfeldt, G. Boero, J. Hennig, J. G. Korvink, and U. Wallrabe, "3D solenoidal microcoil arrays with CMOS integrated amplifiers for parallel MR imaging and spectroscopy," in *Proceedings of the IEEE International Conference on Micro Electro Mechanical Systems (MEMS)*, pp. 809–812, IEEE, 2011.

[48] E. Danieli and B. Blümich, "Single-sided magnetic resonance profiling in biological and materials science," *Journal of Magnetic Resonance*, vol. 229, pp. 142–154, 2013.

[49] W. P. Wu, R. S. Lu, X. L. Zhou, and Z. H. Ni, "The nuclear magnetic resonance probe based on a printed circuit board planar microcoil," in *2013 IEEE International Conference on Applied Superconductivity and Electromagnetic Devices, ASEMD 2013*, no. 51175083, pp. 169–172, 2013.

[50] J. Anders, J. Handwerker, M. Ortmanns, and G. Boero, "A fully-integrated detector for NMR microscopy in 0.13μm CMOS," in *Proceedings of the 2013 IEEE Asian Solid-State Circuits Conference, A-SSCC 2013*, pp. 437–440, 2013.

[51] D. Zhao, K. M. Lei, P. I. Mak, M. K. Law, and R. P. Martins, "Design considerations of a low-noise receiver front-end and its spiral coil for portable NMR screening," in *IEEE Asia-Pacific Conference on Circuits and Systems, Proceedings, APCCAS*, vol. 2015-Febru, pp. 403–406, 2015.

[52] K. M. Lei, P. I. Mak, M. K. Law, and R. P. Martins, "NMR–DMF: A modular nuclear magnetic resonance–digital microfluidics system for biological assays," *Analyst*, vol. 139, no. 23, pp. 6204–6213, 2014.

[53] D. Ha, N. Sun, J. Paulsen, Y. Song, Y. Tang, S. Hong, and D. Ham, "Integrated CMOS spectrometer for multi-dimensional NMR spectroscopy," in *Midwest Symposium on Circuits and Systems*, vol. 2017-Augus, pp. 1085–1088, 2017.

[54] TREJO ROSLLO Josué, *Contribution à l'amélioration de la Sensibilité d'un Micro-récepteur RMN Implantable*. PhD thesis, 2014.

[55] H. Pourmodheji, E. Ghafar-Zadeh, and S. Magierowski, "Dual-path NMR receiver using double transceiver microcoils," in *Proceedings of the Annual International Conference of the IEEE Engineering in Medicine and Biology Society, EMBS*, vol. 2015-Novem, pp. 7107–7110, 2015.

[56] H. Y. Chen, Y. Kim, P. Nath, and C. Hilty, "An ultra-low cost NMR device with arbitrary pulse programming," *Journal of Magnetic Resonance*, vol. 255, pp. 100–105, 2015.

[57] H. Pourmodheji, E. Ghafar-Zadeh, and S. Magierowski, "Active nuclear magnetic resonance probe: A new multidiciplinary approach toward highly sensitive biomolecoular spectroscopy," in *Proceedings - IEEE International Symposium on Circuits and Systems*, vol. 2015-July, pp. 473–476, 2015.

[58] K. M. Lei, P. I. Mak, M. K. Law, and R. P. Martins, "A μnMR CMOS Transceiver Using a Butterfly-Coil Input for Integration with a Digital Microfluidic Device Inside a Portable Magnet," *IEEE Journal of Solid-State Circuits*, vol. 51, no. 10, pp. 2274–2286, 2016.

[59] H. Pourmodheji, E. Ghafar-Zadeh, and S. Magierowski, "A multidisciplinary approach to high throughput nuclear magnetic resonance spectroscopy," *Sensors (Switzerland)*, vol. 16, no. 6, 2016.

[60] M. Grisi, *Broadband single-chip transceivers for compact NMR probes*. PhD thesis, 2017.

[61] J. Handwerker, M. Perez-Rodas, M. Ortmanns, K. Scheffler, and J. Anders, "Towards CMOS-based in-vivo NMR spectroscopy and microscopy," in *Proceedings - IEEE International Symposium on Circuits and Systems*, pp. 0–3, 2017.

[62] N. Hossein-Zadeh, M. Daliri, S. Magierowski, and E. Ghafar-Zadeh, "A novel fully differential NMR transciever," in *2018 IEEE Life Sciences Conference, LSC 2018*, pp. 13–16, 2018.

[63] A. Louis-Joseph and P. Lesot, "Designing and building a low-cost portable FT-NMR spectrometer in 2019: A modern challenge," 2019.

[64] N. Bloembergen, E. M. Purcell, and R. V. Pound, "Relaxation effects in nuclear magnetic resonance absorption," *Physical Review*, vol. 73, no. 7, pp. 679–712, 1948.

[65] J. A. Fessler, "Advantages of NMR Imaging," 2003.

[66] Rex Tayloe, "Introduction to NMR in the earth's magnetic field Student manual 2," 2010.

[67] C. Kittel, "Kittel, Charles - Introduction To Solid State Physics 8Th Edition," 2011.

[68] H. D. Hill and R. E. Richards, "Limits of measurement in magnetic resonance," *Journal of Physics E: Scientific Instruments*, vol. 1, pp. 977–983, oct 1968.

[69] M. Balci, "3 - chemical shift," in *Basic 1H- and 13C-NMR Spectroscopy* (M. Balci, ed.), pp. 25 – 85, Amsterdam: Elsevier Science, 2005.

[70] M. Balci, "4 - spin–spin splitting in 1h-nmr spectra," in *Basic 1H- and 13C-NMR Spectroscopy* (M. Balci, ed.), pp. 87 – 133, Amsterdam: Elsevier Science, 2005.

[71] A. J. Dingley, F. Cordier, and S. Grzesiek, "An introduction to hydrogen bond scalar couplings," *Concepts in Magnetic Resonance*, vol. 13, no. 2, pp. 103–127, 2001.

[72] R. Valiulin, *NMR Multiplet Interpretation*. De Gruyter, oct 2019.

[73] A. Zheltikov, "Understanding NMR Spectroscopy, James Keeler, John Wiley & Sons Ltd, Chichester, 2005, pp. 459, paperback, ISBN: 0470017872," *Journal of Raman Spectroscopy*, vol. 37, pp. 1456–1456, dec 2006.

[74] E. Moser, E. Laistler, F. Schmitt, and G. Kontaxis, "Ultra-high field NMR and MRI-the role of magnet technology to increase sensitivity and specificity," *Frontiers in Physics*, vol. 5, no. AUG, pp. 1–15, 2017.

[75] P. Blümler and F. Casanova, "CHAPTER 5: Hardware developments: Halbach magnet arrays," *New Developments in NMR*, vol. 2016-Janua, no. 5, pp. 133–157, 2016.

[76] P. Yu, Y. Xu, Z. Wu, Y. Chang, Q. Chen, and X. Yang, "A low-cost home-built NMR using Halbach magnet," *Journal of Magnetic Resonance*, vol. 294, pp. 162–168, 2018.

[77] Y. Hibino, K. Sugahara, Y. Muro, H. Tanaka, T. Sato, and Y. Kondo, "Simple and low-cost tabletop NMR system for chemical-shift-resolution spectra measurements," *Journal of Magnetic Resonance*, vol. 294, pp. 128–132, 2018.

[78] B. Shapira and L. Frydman, "Spatially encoded pulse sequences for the acquisition of high resolution NMR spectra in inhomogeneous fields," *Journal of Magnetic Resonance*, vol. 182, no. 1, pp. 12–21, 2006.

[79] D. I. Hoult, "The principle of reciprocity in signal strength calculations - A mathematical guide," *Concepts in Magnetic Resonance*, vol. 12, no. 4, pp. 173–187, 2000.

[80] J. F. Jacquinot and D. Sakellariou, "NMR signal detection using inductive coupling: Applications to rotating microcoils," *Concepts in Magnetic Resonance Part A: Bridging Education and Research*, vol. 38 A, pp. 33–51, mar 2011.

[81] A. J. Ilott and A. Jerschow, "Aspects of NMR reciprocity and applications in highly conductive media," *Concepts in Magnetic Resonance Part A: Bridging Education and Research*, vol. 47A, no. 2, pp. 1–8, 2018.

[82] J.-L. L. Jacques Max, *Méthodes et techniques de traitement du signal et applications aux mesures physiques*. 5th ed., 1996.

[83] Goldfarb, "Magnetic Units Conversion," 1985.

[84] R. Freeman and G. A. Morris, "The Varian story," *Journal of Magnetic Resonance*, vol. 250, pp. 80–84, 2015.

[85] A. McDowell and E. Fukushima, "Ultracompact NMR: 1H spectroscopy in a subkilogram magnet," *Applied Magnetic Resonance*, vol. 35, no. 1, pp. 185–195, 2008.

[86] H. J. Schneider-Muntau, "High field NMR magnets," *Solid State Nuclear Magnetic Resonance*, vol. 9, no. 1, pp. 61–71, 1997.

[87] Z. Gan, H. T. Kwak, M. Bird, T. Cross, P. Gor'kov, W. Brey, and K. Shetty, "High-field NMR using resistive and hybrid magnets," *Journal of Magnetic Resonance*, vol. 191, no. 1, pp. 135–140, 2008.

[88] J. R. Miller, "The NHMFL 45-T hybrid magnet system: Past, present, and future," *IEEE Transactions on Applied Superconductivity*, vol. 13, no. 2 II, pp. 1385–1390, 2003.

[89] M. Abele, "Structures of Permanent Magnets," 1993.

[90] Marketsandmarkets, "Soft Magnetic Materials Market by Material Type (Soft Ferrite, Electrical Steel, Cobalt), Application (Motor, Transformer, Alternator), End User Industry (Automotive, Electronics & Telecommunications, Electrical) - Global Forecast to 2026," 2017.

[91] E. P. Furlani, "Materials," in *Permanent Magnet and Electromechanical Devices*, ch. 1, pp. 1–72, Elsevier, 2001.

[92] D. Jiles, *Introduction to Magnetism and Magnetic Materials*, vol. 29. 1991.

[93] J. M. Coey, *Magnetism and magnetic materials*, vol. 9780521816. 2010.

[94] K. Halbach, "Design of permanent multipole magnets with oriented rare earth cobalt material," *Nuclear Instruments and Methods*, vol. 169, no. 1, pp. 1–10, 1980.

[95] H. Raich and P. Blümler, "Design and construction of a dipolar Halbach array with a homogeneous field from identical bar magnets: NMR mandhalas," *Concepts in Magnetic Resonance Part B: Magnetic Resonance Engineering*, vol. 23, no. 1, pp. 16–25, 2004.

[96] P. Campbell, *Permanent Magnet Materials and their Application*. Cambridge University Press, jul 1994.

[97] S. T. Sonawane and M. Meribout, "Halbach array design targeting nuclear magnetic resonance," *International Conference on Electronic Devices, Systems, and Applications*, pp. 1–4, 2017.

[98] A. R. Insinga, C. R. Bahl, R. Bjørk, and A. Smith, "Performance of Halbach magnet arrays with finite coercivity," *Journal of Magnetism and Magnetic Materials*, vol. 407, pp. 369–376, 2016.

[99] D. P. Hung, *Développement d'aimant bas champ pour RMN Portable: Conception et construction*. PhD thesis, 2015.

[100] G. Moresi and R. Magin, "Miniature permanent magnet for table-top NMR," *Concepts in Magnetic Resonance Part B: Magnetic Resonance Engineering*, vol. 19, no. 1, pp. 35–43, 2003.

[101] R. C. Jachmann, D. R. Trease, L. S. Bouchard, D. Sakellariou, R. W. Martin, R. D. Schlueter, T. F. Budinger, and A. Pines, "Multipole shimming of permanent magnets using harmonic corrector rings," *Review of Scientific Instruments*, vol. 78, no. 3, 2007.

[102] E. Danieli, J. Perlo, B. Blümich, and F. Casanova, "Small magnets for portable NMR spectrometers," *Angewandte Chemie - International Edition*, vol. 49, no. 24, pp. 4133–4135, 2010.

[103] C. Hugon, F. D'Amico, G. Aubert, and D. Sakellariou, "Design of arbitrarily homogeneous permanent magnet systems for NMR and MRI: Theory and experimental developments of a simple portable magnet," *Journal of Magnetic Resonance*, vol. 205, no. 1, pp. 75–85, 2010.

[104] C. W. Windt, H. Soltner, D. V. Dusschoten, and P. Blümler, "A portable Halbach magnet that can be opened and closed without force: The NMR-CUFF," *Journal of Magnetic Resonance*, vol. 208, no. 1, pp. 27–33, 2011.

[105] P. Azimi, D. Zhao, C. Pouzet, N. E. Crain, and B. Stephens, "Emissions of Ultrafine Particles and Volatile Organic Compounds from Commercially Available Desktop Three-Dimensional Printers with Multiple Filaments," *Environmental Science and Technology*, vol. 50, no. 3, pp. 1260–1268, 2016.

[106] L. Osberger, V. Frick, and L. Hébrard, "Four-phase bi-current spinning current on shallow vertical Hall sensor," *Procedia Engineering*, vol. 120, no. September, pp. 120–123, 2015.

[107] "Magritek : https://magritek.com/2016/03/14/magritek-launch-the-spinsolve-60-series-of-60-MHz-benchtop-nmr-spectrometers/."

[108] B. Manz, M. Benecke, and F. Volke, "A simple, small and low cost permanent magnet design to produce homogeneous magnetic fields," *Journal of Magnetic Resonance*, vol. 192, no. 1, pp. 131–138, 2008.

[109] J. R. Bodart, B. M. Garcia, L. Phelps, N. S. Sullivan, W. G. Moulton, and P. Kuhns, "The effect of high magnetic fields on junction field effect transistor device performance," *Review of Scientific Instruments*, vol. 69, no. 1, pp. 319–320, 1998.

[110] P. Phothimat and M. Awipi, "Effect of high magnetic field on transistor characteristics with applications to SEU testing," in *Conference Proceedings - IEEE SOUTHEASTCON*, pp. 338–339, 1998.

[111] R. S. Popović, "Hall-effect devices," *Sensors and Actuators*, vol. 17, pp. 39–53, may 1989.

[112] B. Razavi, *Design of Analog CMOS Integrated Circuits*. 2005.

[113] L. Hebrard, D. V. Nguyen, D. Vogel, J. B. Schell, C. Po, N. Dumas, W. Uhring, and J. Pascal, "On the influence of strong magnetic field on MOS transistors," *2016 IEEE International Conference on Electronics, Circuits and Systems, ICECS 2016*, pp. 564–567, 2017.

[114] Y. Tsividis and C. McAndrew, "Operation and Modeling of the Mos Transistor," p. 750, 1988.

[115] D. V. Nguyen, L. Werling, C. Po, N. Dumas, M. Madec, W. Uhring, L. Hebrard, L. Fakri-Bouchet, J. Pascal, and Y. Wadghiri, "Modeling the effect of strong magnetic field on n-type MOSFET in strong inversion," *2018 25th IEEE International Conference on Electronics Circuits and Systems, ICECS 2018*, pp. 637–640, 2019.

[116] B. Gruber, M. Froeling, T. Leiner, and D. W. Klomp, "RF coils: A practical guide for non-physicists," *Journal of Magnetic Resonance Imaging*, vol. 48, no. 3, pp. 590–604, 2018.

[117] D. A. Seeber, R. L. Cooper, L. Ciobanu, and C. H. Pennington, "Design and testing of high sensitivity microreceiver coil apparatus for nuclear magnetic resonance and imaging," *Review of Scientific Instruments*, vol. 72, no. 4, pp. 2171–2179, 2001.

[118] A. G. Webb, "Radiofrequency microcoils for magnetic resonance imaging and spectroscopy," *Journal of Magnetic Resonance*, vol. 229, pp. 55–66, 2013.

[119] D. L. Olson, T. L. Peck, A. G. Webb, R. L. Magin, and J. V. Sweedler, "High-resolution microcoil 1H-NMR for mass-limited, nanoliter-volume samples," *Science*, vol. 270, no. 5244, pp. 1967–1970, 1995.

[120] D. G. G. &. G. K. R. Joseph J. H. Ackerman, Thomas H. Grove, Gordon G. Wong, "Mapping of metabolites in whole animals by 31P NMR using surface coils," *Nature*, vol. 283, pp. 167–170, 1980.

[121] A. P. Kentgens, J. Bart, P. J. Van Bentum, A. Brinkmann, E. R. Van Eck, J. G. Gardeniers, J. W. Janssen, P. Knijn, S. Vasa, and M. H. Verkuijlen, "High-resolution liquid- and solid-state nuclear magnetic resonance of nanoliter sample volumes using microcoil detectors," *Journal of Chemical Physics*, vol. 128, no. 5, 2008.

[122] G. Finch, A. Yilmaz, and M. Utz, "An optimised detector for in-situ high-resolution NMR in microfluidic devices," *Journal of Magnetic Resonance*, vol. 262, pp. 73–80, 2016.

[123] J. D. Trumbull, I. K. Glasgow, D. J. Beebe, and R. L. Magin, "Integrating microfabricated fluidic systems and NMR spectroscopy," *IEEE Transactions on Biomedical Engineering*, vol. 47, no. 1, pp. 3–7, 2000.

[124] Y. Maguire, I. L. Chuang, S. Zhang, and N. Gershenfeld, "Ultra-small-sample molecular structure detection using microslot waveguide nuclear spin resonance," *Proceedings of the National Academy of Sciences of the United States of America*, vol. 104, no. 22, pp. 9198–9203, 2007.

[125] D. I. Hoult and R. E. Richards, "The signal-to-noise ratio of the nuclear magnetic resonance experiment. 1976.," *Journal of magnetic resonance (San Diego, Calif. : 1997)*, vol. 213, no. 2, pp. 329–343, 2011.

[126] Z. Ali, D. P. Poenar, and S. Aditya, "Design of planar microcoil-based NMR probe ensuring high SNR," *AIP Advances*, vol. 7, no. 9, 2017.

[127] C. P. Yue, C. Ryu, J. Lau, T. H. Lee, and S. S. Wong, "A physical model for planar spiral inductors on silicon," in *Electron Devices Meeting, 1996. IEDM'96., International*, pp. 155–158, IEEE, 1996.

[128] Terman, "Radio Engineers handbook," *McGraw-Hill*, 1943.

[129] A. Ghannam, *Conception et intégration" above IC" d'inductances à fort coefficient de surtension pour applications de puissance RF*. PhD thesis, Université Paul Sabatier-Toulouse III, 2010.

[130] A. M. Niknejad, *Analysis, simulation, and applications of passive devices on conductive substrates*. PhD thesis, UNIVERSITY of CALIFORNIA at BERKELEY, 2000.

[131] L. A. Currie, "Detection and quantification limits: origins and historical overview1Adapted from the Proceedings of the 1996 Joint Statistical Meetings (American Statistical Association, 1997). Original title: "Foundations and future of detection and quantification limi," *Analytica Chimica Acta*, vol. 391, no. 2, pp. 127–134, 1999.

[132] J. Mispelter, M. Lupu, and A. Briguet, *NMR Probeheads for Biophysical and Biomedical Experiments*. 2015.

[133] Qorvo, "Spf5189Z Datasheet," pp. 1–11, 2006.

[134] M. Ddus, "Low noise broadband amplifier based on SPF5189Z," pp. 1–6, 2018.

[135] C. Poole and I. Darwazeh, "Microwave mixers," *Microwave Active Circuit Analysis and Design*, pp. 589–616, 2016.

[136] M. S. Manavadaria, "Frequency Down Conversion Using Mixer and Its Simulation," no. 1, pp. 114–118, 2014.

[137] C. Enz and G. Temes, "Circuit techniques for reducing the effects of op-amp imperfections: autozeroing, correlated double sampling, and chopper stabilization," *Proceedings of the IEEE*, vol. 84, no. 11, pp. 1584–1614, 1996.

[138] S. Certiprep, "Pesticide Guide to Solubility," Tech. Rep. 0, 2016.

[139] S. S. Rout and K. Sethi, "Design of high gain and low noise CMOS gilbert cell mixer for receiver front end design," *Proceedings - 2016 15th International Conference on Information Technology, ICIT 2016*, no. December, pp. 1–5, 2017.

[140] G. Palmisano, G. Palumbo, and S. Pennisi, "Design procedure for two-stage CMOS transconductance operational amplifiers: A tutorial," *Analog Integrated Circuits and Signal Processing*, vol. 27, no. 3, pp. 179–189, 2001.

[141] G. Bringout and T. M. Buzug, "A robust and compact representation for magnetic fields in magnetic particle imaging," *Biomedizinische Technik*, vol. 59, no. 2, pp. S675–S678, 2014.

Communications

National communications

●POSTER: "ETUDE DE L'INFLUENCE D'UN FORT CHAMP MAGNETIQUE SUR LES TRANSISTORS MOS" D-V. Nguyen, L. Werling, N. Dumas, W. Uhring, L. Hébrard, *GDR SOC SIP, BORDEAUX, JUNE 2017*

●POSTER: "INFLUENCE D'UN CHAMP MAGNETIQUE FORT SUR LES TRANSISTORS MOS", L. Werling, D-V. Nguyen, N. Dumas, W. Uhring, L. Fakri-Bouchet, L. Hébrard, *GDR SOC², PARIS, JUNE 2018*

●ARTICLE: CONCEPTION D'UN CIRCUIT INTEGRE POUR L'ANALYSE MICRO-RMN DANS UN LABORATOIRE SUR PUCE, D-V. Nguyen, N. Dumas, M. Madec, W. Uhring, L. Hébrard, *15 EMES JOURNEES PEDAGOGIQUES DU CNFM, SAINT-MALO, NOVEMBER 2018*

International communications

●ARTICLE: "INFLUENCE D'UN CHAMP MAGNETIQUE FORT SUR LES TRANSISTORS MOS", L. Hébrard, D-V. Nguyen, D. Vogel, J-B. Schell, C. Po, N. Dumas, W. Uhring, J. Pascal, *ICECS, MONACO, DECEMBER 2016*

●TALK: "ANALYSE DETAILLE DE L'INFLUENCE DES CHAMPS FORT SUR LES TRANSISTORS MOS", D-V. Nguyen, L. Werling, C. Po, N. Dumas, M. Madec, W. Uhring, L. Hébrard, L. Fakri-Bouchet, J. Pascal, Y. Wadghiri, *ICECS, BORDEAUX, DECEMBER 2018*

Report

●REPORT: "A DETECTOR FOR PESTICIDES IN DRINKING WATER", J. Pascal, D.-V. Nguyen, M. Olesinska, P. Shahgaldian, N. Karlen, E. Weingartner, and D. Matter , *ANNUAL REPORT 2019, UNIVERSITY OF BASEL*

National workshop

●TALK + POSTER: "CONCEPTION D'UNE SONDE POUR LA SPECTROSCOPIE PAR RESONANCE MAGNETIQUE NUCLEAIRE", D-V. Nguyen, L. Werling, J. Pascal, N. Dumas, W. Uhring, L. Fakri-Bouchet , L. Hébrard, *JNRDM, STRASBOURG, NOVEMBER 2017*

●POSTER: "CONCEPTION D'UNE SONDE POUR LA SPECTROSCOPIE PAR RESONANCE MAGNETIQUE NUCLEAIRE", D-V. Nguyen, L. Werling, J. Pascal, N. Dumas, W. Uhring, L. Fakri-Bouchet, L. Hébrard, *JNRDM, MONTPELLIER, JUNE 2019*

International workshop

●POSTER : "INFLUENCE D'UN CHAMP MAGNETIQUE FORT SUR LES TRANSISTORS MOS", L. Hébrard, D-V. Nguyen, D. Vogel, J-B. Schell, C. Po, N. Dumas, W. Uhring, J. Pascal, *ÉCOLE D'ETE "NAMIS", FREIBURG, OCTOBER 2017*

Duc-Vinh NGUYEN

Sonde portable de spectroscopie par résonance magnétique nucléaire

Résumé:

La spectroscopie de Résonance Magnétique Nucléaire (RMN) permet de détecter de manière fiable plusieurs composés chimiques au sein d'un même échantillon qui peut être liquide ou solide. Elle est très utilisée en chimie et commence à l'être de plus en plus en médecine, voire dans le domaine de la qualité alimentaire. Il est donc envisageable de l'utiliser aussi pour détecter les polluants de l'eau et suivre en continu la qualité de l'eau. Toutefois les spectromètres RMN sont généralement des appareils chers et volumineux. En conséquence, leur déploiement au sein d'un réseau de distribution d'eau nécessite le développement d'un spectromètre dédié, portable et facilement installable au sein des stations de distribution. Dans ce contexte, ce travail de thèse étudie les défis à surmonter pour réaliser un tel spectromètre portable, capable de détecter certains polluants très néfastes de l'eau, comme l'atrazine ou le glyphosate.

Mots clefs : RMN portable, détections de polluants, sonde, pesticides, spectromètre RMN, micro-électronique, CMOS

Abstract:

Nuclear Magnetic Resonance (NMR) spectroscopy allows a reliable detection of chemical compounds in a sample that can be liquid or solid. It is widely used in chemistry, and becomes more and more used in medicine, even in the field of food quality. It may thus be used for the detection of water pollutants, and for the continuous monitoring of water quality. However, NMR spectrometers are expensive and bulky. So, their dispatching among a water distribution network asks for the development of a specific and portable spectrometer, that may be easily installed in a water station. In this context, this PhD work studies the challenges to face to realize such a portable spectrometer, able to detect very harmful pollutants, such as atrazine and glyphosate.

Keywords: Portable NMR, pollutants detection, probe, pesticides, NMR spectrometer, micro-electronics, CMOS

Résumé

Sonte portable de spectroscopie par résonance magnétique nucléaire

NGUYEN DUC-VINH 16/12/2020

1. Introduction et contexte

La résonance magnétique nucléaire (RMN) est un outil puissant pour la détection des éléments chimiques. Elle permet de déterminer avec précision la composition d'un échantillon, et constitue l'outil de référence dans plusieurs domaines nécessitant une connaissance approfondie de l'échantillon observé. De l'industrie pharmaceutique, en passant par l'environnement, à la santé et au contrôle alimentaire, chacun de ces domaines utilise de plus en plus les spectromètres RMN pour tester leurs produits. Une grande tendance permettant l'amélioration des mesures par RMN est d'augmenter toujours et encore le champ magnétique sous lequel sont fait les mesures. Plus le champ est intense, plus le signal RMN est fort. Cependant, outre la "chasse aux Tesla", une autre tendance est à la miniaturisation des dispositifs de mesure, comme c'est le cas dans le monde électronique et instrumental. Cette miniaturisation permet de réduire le coût des systèmes de RMN de façon considérable. Les entreprises pharmaceutiques visent à contrôler la pureté de leurs médicaments, mais aussi de pouvoir, lors de la phase de conception, tester des molécules dans un délai très court et ainsi faire de multiples combinaisons avec une sensibilité plus élevée que celle qu'ils utilisent actuellement. La spectrométrie RMN se positionne en techniques alternatives très intéressant pour le test et l'identification d'espèces chimiques. Cela permet ainsi d'améliorer les lignes de production par une analyse continue, c'est-à-dire en passant d'un système de production discontinue à un système de production continue (souvent impossible dans la production biotechnologique) [1,2]. En ce qui concerne les enjeux de santé, la santé est certainement le domaine où les systèmes de RMN développent le plus. Il est possible d'effectuer un suivi in vivo, consistant à suivre l'évolution des maladies en temps réel pour mieux comprendre leur développement. L'utilisation d'animaux de laboratoire génétiquement modifiés (comme des rats par exemple) auxquels sont inoculés des maladies humaines connues, permet d'observer métabolites du cerveau et suivre, par exemple l'évolution de la maladie d'Alzheimer pendant que l'animal est encore en vie [3]. Cela permet d'éviter la morbidité actuelle des analyses de stade lors de l'utilisation de la biopsie, c'est-à-dire la prise un morceau de tissu à chaque stade de la maladie que l'on souhaite observer. La méthode de la biopsie nécessite un plus grand nombre d'animaux à sacrifier (un par étape d'observation) et représente également un coût important, alors que l'exploration in-vivo

permet la durée de l'expérience tout en ayant une observation en temps réel du développement de la maladie. De plus, la mort et la biopsie de l'animal peuvent affecter les éléments observables, c'est pourquoi les techniques in-vivo sont préférables. Un autre exemple d'application dans le domaine des soins de santé est le la détection du cancer, qui se développe également rapidement. Grâce à la protéine avidine, par exemple, il devient possible de détecter la présence de cellules cancéreuses [4]. Il est également possible d'observer la différents éléments chimiques contenus dans le sang pour diagnostiquer des maladies telles que la maladie de Lyme ou l'anémie. Ainsi, la RMN, avec le développement d'outils de dépistage portables et rapides, permettra une gestion plus rapide et plus efficace dans le diagnostic des patients, et cela à un coût moindre, luttant ainsi contre la saturation des établissements de santé et les déserts médicaux. L'analyse des aliments par RMN est également très récente. Le contrôle de la qualité du miel et du vin sont deux exemples qui attirent de plus en plus l'attention [5]. En effet, la possibilité d'obtenir des résultats rapides sur le l'origine, la composition et la pureté, en ne prélevant qu'un très petit échantillon, présente un intérêt pour de nombreux aliments pour garantir la qualité de leurs produits.

En raison des enjeux écologiques contemporains, une autre facette récente de l'utilisation de la RMN est le domaine de l'environnement. La résonance magnétique nucléaire devrait permettre de détecter les polluants dans l'eau provenant de produits phytosanitaires qui contaminent l'eau potable. C'est également le cas de la dialyse, où il pourrait être possible d'observer les eaux rejetées. Ce travail de doctorat apporte sa contribution dans ce domaine en explorant la possibilité de concevoir un spectromètre RMN portable pour la détection des polluants dans l'eau.

La directive européenne 2008/105/CE des parlements européens et du Conseil européen a établi la norme de qualité de l'eau pour la santé humaine. Une liste de surveillance en résultant comprend 63 composés chimiques prioritaires. Cependant, il reste difficile d'obtenir des exigences élevées car il est difficile d'obtenir une quantité substantielle de mesures quantitatives décentes. Le contrôle de la qualité de l'eau est assuré par des laboratoires accrédités, directement à partir des sources d'eau et des réseaux de distribution. Néanmoins, la faible fréquence de contrôle, qui est directement liée au bassin versant et à la taille de la population, entraîne de graves risques pour la santé. Par exemple, les sites de distribution de petite taille ne sont testés que tous les 10 ans. Par conséquent, les déversements accidentels de pesticides ne peuvent être détectés à temps. En France, on estime que 680 000 personnes ont consommé en 2013 de l'eau non testée [6]. Bien que la qualité de l'eau en Europe occidentale tende à être satisfaisante, certains événements ont affecté la population. Avec l'augmentation de la population les exigences futures en matière de sécurité se resserrent, ainsi la nécessité de disposer de capteurs de polluants d'eau moins chers et plus performants se renforce.

Des appareils commerciaux détectant la pollution de l'eau sont déjà disponibles. Des mesures continues de température, de pH, de conductivité ou de turbidité sur le réseau de distribution d'eau sont effectuées. Toutefois, en ce qui concerne les mesures des composés chimiques,

c'est-à-dire les principales traces de polluants potentiels, les différentes méthodes de mesure qui ont été publiées et démontrées impliquent des équipements encombrants (spectroscopie de masse) ou un environnement réglementé (biocapteurs), qui utilise des consommables coûteux. Le laboratoire ICube (Université de Strasbourg, France), en collaboration avec l'Institut Génie Médical et Informatique Médicale (IM2 - Haute école spécialisée - FHNW, Muttenz, Suisse), le laboratoire BSC (Université de Strasbourg, France), l'Institut de (Université des sciences appliquées - HFU, Furtwangen, Allemagne), le laboratoire IMTEK (Université de Fribourg, Allemagne), et le département de chimie de l'Université technique de Kaiserlautern (Allemagne) a récemment proposé une alternative qui peut être facilement généralisable à différents polluants. Cette alternative devra être suffisamment petit pour être utilisé sur le terrain et abordable pour être déployé à grande échelle afin de surveiller la pollution de l'eau en temps réel et de prévenir les risques. Tous ces points font de la RMN un candidat parfait pour être économiquement viable.

Ce travail de doctorat, qui a été effectué au cours de ses trois premières années à ICube, et pour sa dernière année à l'IM2, est en partie à l'origine d'un nouveau projet de sonde sur les polluants, et fournit une pré-étude sur la possibilité de détecter les polluants de l'eau par spectrométrie RMN portable. Dans un premier temps nous souhaitons nous concentrer sur deux polluants à savoir le glyphosate, qui est vendu comme herbicide à large spectre mais qui est fortement controversé, ainsi que l'atrazine, le deuxième plus herbicide largement utilisé après le glyphosate en 2014 (aux États-Unis). En Europe, les recherches menées sur cet herbicide semblent montrer un facteur de problèmes de santé pour les petits animaux puisqu'il provoque des réactions mutagènes et des dysfonctionnements hormonaux. Quant à Dans certains pays comme la France, l'atrazine a été interdite. Bien entendu, les concentrations de polluants acceptables doivent être très faible. C'est pourquoi, avant d'être détectés par spectrométrie RMN, les polluants doivent être concentrés. Cette concentration se fera par le biais d'un polymère à empreinte moléculaire où l'eau circule, un polymère spécifique permettant de piéger les polluants. Ensuite, un éluant, c'est-à-dire l'acétonitrile, est utilisé pour rincer le polymère, et en extraire les polluants très concentrés qui seront analysés par RMN spectrométrie. Dans le chapitre 2 je présente brièvement un historique et décrit les équations nécessaires à la compréhension de la RMN, suivi d'une bibliographie des différents systèmes présentés dans la littérature. Le chapitre 3 se concentre sur le champ magnétique statique. Le chapitre 4 aborde l'élément sensible en RMN, la bobine. Cela nous amène alors au chapitre 5 mettant en avant les réalisations effectuées pendant la thèse, à savoir le récepteur discret, puis dans le chapitre 6 le récepteur intégré.

2. La résonance magnétique nucléaire

2.1 Principe théorique de le RMN

Pauli a introduit la notion de spin comme un moment angulaire intrinsèque des particules élémentaires, c'est-à-dire que les particules élémentaires subiraient un mouvement

de rotation sur elles-mêmes. Les Fermions (Quarks et Leptons) sont des particules élémentaires (c'est-à-dire des particules sans sous-particules) qui tournent sur elles-mêmes. Ainsi, nous pouvons définir le spin d'un électron, l'un des six Leptons, comme $\overrightarrow{s_e}$. Les protons et les neutrons sont eux-mêmes composés de Quarks ayant des charges différentes q, possédant également un spin. Les neutrons et les protons possèdent un spin, $\overrightarrow{s_n}$, $\overrightarrow{s_p}$ respectivement, qui sont la somme de tous les moments angulaires des quarks qui les composent. Le moment magnétique $\mu_e, \mu_n \; et \; \mu_p$ de l'électron, du neutron et du proton respectivement est lié au moment angulaire intrinsèque de la particule par le rapport gyromagnétique γ. Ce rapport peut être considéré comme une mesure quantitative de la "force magnétique" de la particule. Elle est définie comme :

$$\overrightarrow{\mu_x} = \gamma \cdot \overrightarrow{s_x} = \gamma \cdot \hbar \cdot \sqrt{s(s+1)} \cdot \overrightarrow{u_x}$$

Où $\overrightarrow{u_x}$ est un vecteur unitaire dans la direction de $\overrightarrow{\mu_x}$. L'état quantique d'une particule en dehors d'un champ magnétique est dit dégénéré, c'est-à-dire que l'on peut trouver plusieurs états quantiques distincts au même niveau d'énergie. En d'autres termes, un élément (particule, noyau, molécule) avec un moment angulaire de $\vec{s}$, et un nombre de spin s ont 2s + 1 possible les états quantiques (aussi appelés multiplicité, issue de la première règle du Hund). Avec l'application d'une champ magnétique B0 il y a une levée de la dégénérescence, séparant les valeurs des énergies disponibles en plusieurs niveaux correspondant au nombre d'états quantiques. Ceci est à l'origine de l'effet Zeeman anormal qui apparaît lorsque la rotation totale est non nulle. En RMN, nous utilisons principalement le protium 1H, l'isotope du proton, que nous appelons donc la RMN du proton. Pour le protium, le nombre de spins est s = 1/2, donc le nombre d'états potentiels pour ce noyau est 2s + 1 = 2.

De plus, comme s est non nul, il existe un moment magnétique nucléaire $\vec{\mu}$, et sous un champ magnétique, il crée un couple $\vec{\tau} = \vec{\mu} \wedge \overrightarrow{B_0}$ qui modifie l'état énergétique du protium par $E = \pm\vec{\mu} \cdot \overrightarrow{B_0}$ selon l'état quantique α ou β. Sous un tel couple, le noyau subit une précession autour de l'axe du champ. C'est le même principe qu'une toupie soumise au champ gravitationnel. Un noyau au niveau énergétique Eα peut passer au niveau énergétique Eβ s'il absorbe une énergie correspondant à la hauteur potentielle de la barrière :

$$\Delta E = \gamma \cdot \hbar \cdot B_0$$

Comme le noyau atomique ne peut avoir que deux niveaux d'énergie différents, il peut passer de l'un à l'autre soit en gagnant l'énergie ΔE soit en la libérant, ces échanges étant associés à un rayonnement électromagnétique. Ce phénomène est à la base de la résonance magnétique nucléaire. La relation de Planck nous permet d'associer l'énergie à la fréquence de l'onde électromagnétique par la relation fondamentale :

$$E = h.\nu$$

La fréquence ν_0 de l'onde impliquée lors de la résonance magnétique nucléaire est donc :

$$\nu_0 = \frac{\Delta E}{h} = \gamma \cdot \frac{B_0}{2} \cdot \pi$$

$\omega_0 = \nu_0/2\pi$ Correspond à ce que l'on appelle la fréquence de Larmor, c'est-à-dire la fréquence de commutation d'un niveau d'énergie à l'autre. La résonance de l'échantillon en RMN est obtenue par l'application d'une radiofréquence (RF) qui est une onde électromagnétique. L'interaction entre l'onde d'excitation RF, et les noyaux des molécules à l'étude étant à la base de l'expérience RMN. Ainsi dans une expérience de RMN, c'est la précession d'un grand nombre de protons magnétiques qui se trouvent dans l'échantillon testé qui est détectée. Ainsi, nous mesurons la valeur moyenne des moments magnétiques de l'échantillon $\vec{M}$ et une interprétation macroscopique du résultat est nécessaire. Lorsque aucun champ magnétique n'est appliqué, la moyenne de $\vec{M}$ est égale à zéro, et aucun signal RMN n'est détectable. Lorsqu'un champ magnétique statique $\overrightarrow{B_0} = \overrightarrow{B_{0_z}}$ est appliqué, les composantes z des moments magnétiques sont quantifiées avec deux valeurs possibles et la minimisation de l'énergie rompt l'équilibre, un vecteur de magnétisation nette non nul M apparaît. Ce phénomène est appelé le paramagnétisme nucléaire (figure 1). Au zéro absolu, le moment magnétique des atomes est parfaitement aligné avec le champ magnétique. Cependant, dans le cadre d'une expérience en conditions normales de température et de pression, c'est-à-dire à la température T, l'agitation thermique des moments magnétiques doit être prise et conduit à une magnétisation nette exprimée par la loi de Curie.
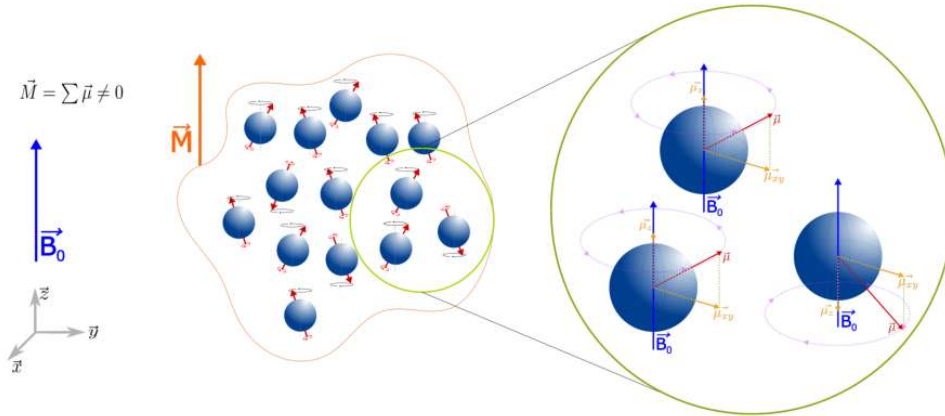

Figure 1: Représentation du paramagnétisme nucléaire.

Si le moment magnétique est parallèle ou antiparallèle au champ magnétique statique appliqué, il est nécessaire de fournir ou de récolter l'énergie du noyau. Cela peut se faire à l'aide d'un dispositif électromagnétique générant une onde à la fréquence de Larmor, définie par son amplitude et sa durée. Appliquée perpendiculairement à $\overrightarrow{B_0}$, cette onde de radiofréquence (RF) fait basculer $\vec{M}$ d'un angle proportionnel à l'amplitude, et la fenêtre temporelle de l'excitation. En effet, dans ces conditions, la composante magnétique de la RF nommée B1, applique un couple constant sur le vecteur d'aimantation puisqu'elle tourne à la même fréquence que le vecteur $\vec{M}$, c'est-à-dire à la fréquence de Larmor (figure 2).

Une fois que l'onde RF est arrêtée, l'aimantation revient à l'équilibre de façon exponentielle avec deux temps de relaxation en fonction de la composante de $\vec{M}$ que nous mesurons, c'est-à-dire le temps de relaxation longitudinale T1 lorsque Mz est détecté, et le temps de relaxation transversale T2 lorsque Mx ou My est détecté. Ces phénomènes sont liés aux molécules présentes dans l'échantillon observé, et donc, liées à l'environnement du spin. Il y à la relaxation longitudinale de Mz avec la constante de temps T1, et la composante transversale, Mx ou My. Cette dernière décroît de manière exponentielle avec une constante de temps T2 appelée temps de relaxation des spins (figure 3). Le signal résultant est un sinus qui s'atténue avec le temps, appelé le Free Induction Decay (FID). D'un point de vue général, il provient des interactions d'un ensemble de spins se déphasant les uns les autres. En spectroscopie, le $Mxy(t)$ est mesuré. Lorsque différentes molécules sont présentes, en raison de leur environnement local, elles présentent des fréquences de Larmor légèrement différentes. Cela signifie que différents FID sont superposés. Par conséquent, pour distinguer les différentes molécules, il est judicieux de transformer le signal du domaine temporel au domaine des fréquences. Ce faisant, nous pouvons distinguer les différentes fréquences dans le FID total, puis, en différenciant les composés présents dans l'échantillon par spectroscopie.
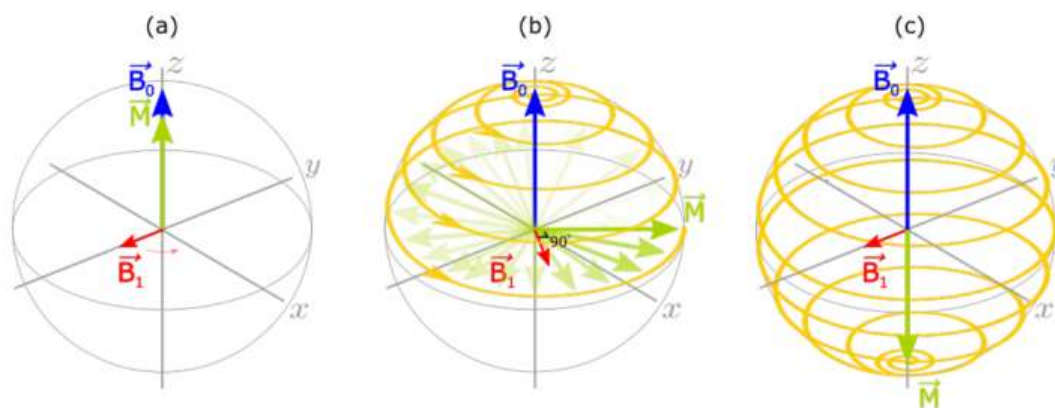

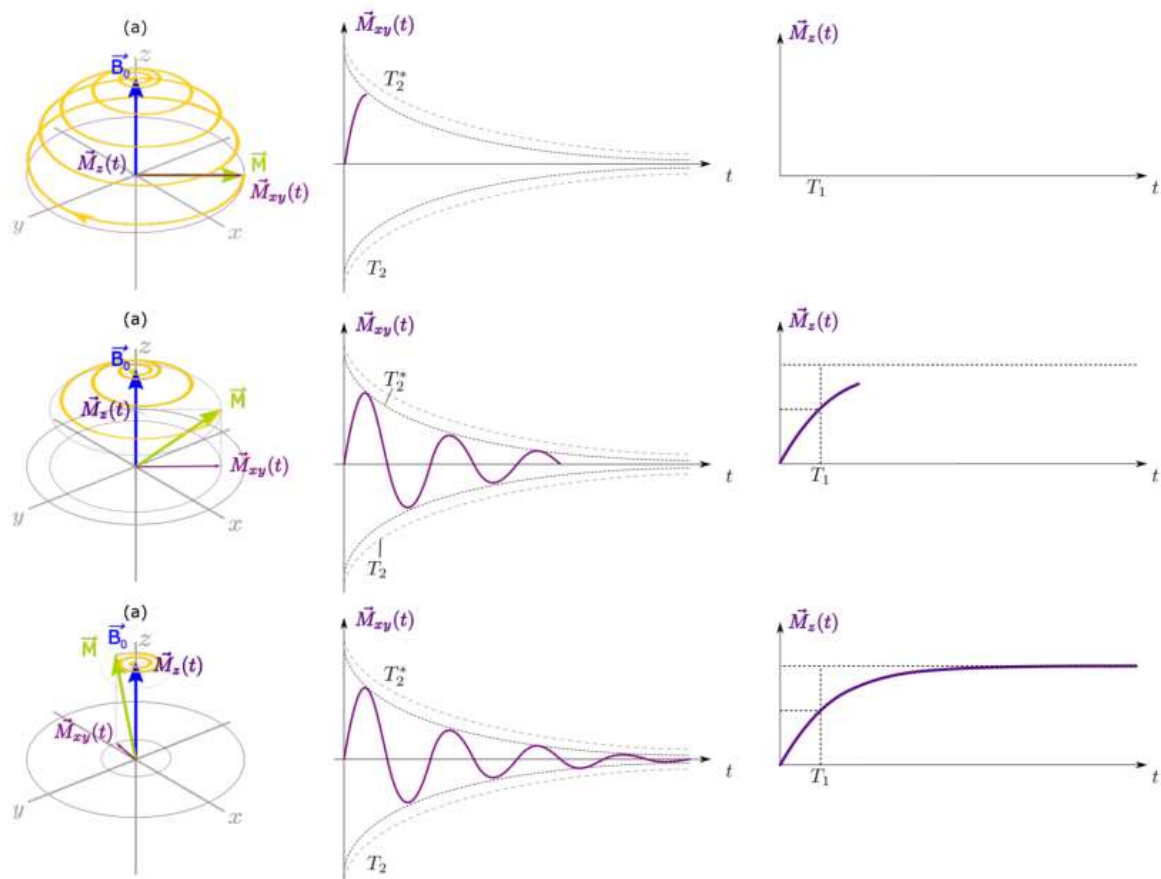*Figure 2: Effet de l'onde RF sur le vecteur de magnétisation global M.*

Figure 3: Représentation des deux relaxations, longitudinale et transversale, en fonction du temps.

2.3 Chaine instrumentale

Afin d'acquérir un signal à partir de l'échantillon, nous devons utiliser une bobine de réception. Cet élément a besoin qui doit être soigneusement construit et réglé pour détecter le petit signal de RMN. L'un des points clés de la construction de la bobine du récepteur consiste à la faire résonner à la fréquence de Larmor. Puis un préamplificateur amplifie le petit signal du FID à la sortie de la bobine de détection, éventuellement sans ajouter de bruit pour obtenir un rapport signal/bruit (SNR) élevé. C'est pourquoi le premier élément actif rencontré par le signal RMN à l'intérieur du canal du récepteur est un amplificateur à faible bruit (LNA). Comme tout amplificateur, le LNA a un produit de gain/bande passante fini (GBW). Le FID étant un signal RF (fréquence de Larmor à B0=1T est de 42MHz), le GBW fini limite le gain du préamplificateur, qui est généralement compris entre 20dB et 40dB. Afin d'obtenir un signal de sortie qui peut être converti numériquement pour l'analyse des données, une amplification ultérieure est nécessaire. Toutefois, en raison de la limitation du GBW, une conversion à une fréquence inférieure d'abord réalisée grâce à un mélangeur. L'amplificateur suivant peut donc amplifier fortement le signal. De plus, à la sortie de la bobine réceptrice, le bruit provenant du mélangeur et de l'amplificateur est fortement atténué grâce au gain du préamplificateur. En conséquence, ces sous-blocs n'ont pas besoin d'être conçus faible bruit. Néanmoins, nous devons garder à l'esprit que le signal FID converti en aval peut rester à une fréquence

supérieure à quelques kilohertz afin d'éviter toute fréquence de bruit faible (bruit 1/f) qui est toujours présent dans l'électronique. Une fois amplifié, on peut ajouter un filtre pour rejeter toutes les fréquences autour de la fréquence convertie en fréquence basse. Ensuite, le signal est converti avec un convertisseur analogique au numérique (ADC) avant d'être traité grâce à un ordinateur qui déterminera la Spectre RMN.

Quant à L'émetteur applique l'impulsion RF. Il doit être capable d'effectuer une impulsion rapide, c'est-à-dire de transmettre suffisamment de puissance en peu de temps. Tout d'abord, le signal RF doit être généré avant d'être transmis à l'échantillon, le signal RF est amplifiée par un amplificateur de puissance, et appliquée à la bobine émettrice avec une puissance de sortie adéquate pour fournir une fenêtre de fréquence d'observation souhaitée pour l'échantillon. La bobine de l'émetteur doit être et adaptés pour fournir une conversion maximale sans perte d'énergie.

Le troisième élément clé d'un système de RMN est l'aimant qui doit produire une image homogène de B0 dans l'ensemble du volume de l'échantillon. Une telle homogénéité est très importante en RMN. En effet, si le champ B0 n'est pas le même dans tout l'échantillon, les mêmes molécules précessent à des fréquences différentes, et le pic spectral correspondant s'élargit tandis que le pic maximum diminue (pour une puissance donnée dans le pic correspondant à une concentration donnée de molécule dans l'échantillon). En pratique, les inhomogénéités peuvent rapidement conduire à des pics spectraux qui se chevauchent. En outre, ils peuvent être inférieurs au niveau de bruit, ce qui rend le spectre RMN impossible à interpréter. Par conséquent, l'aimant B0 homogène est en réalité un l'élément le plus délicat à construire, en particulier dans une sonde RMN portable à faible coût.

Le dernier élément clé est le dispositif qui recevra les données brutes et appliquera la Transformation de Fourier pour calculer le spectre et déterminer les composés présents dans l'échantillon. Tous ces éléments sont visibles sur la figure 4.
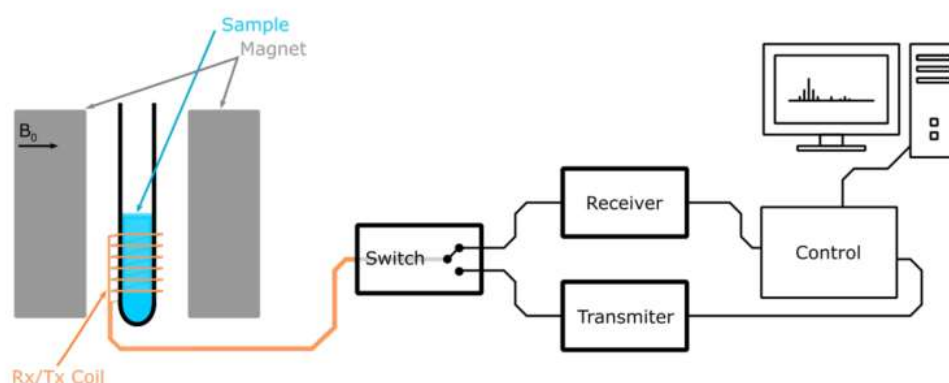

Figure 4: Principe d'une expérience RMN avec une seule bobine.

3. Champ magnétique statique

Les applications industrielles utilisent généralement des électroaimants résistifs. Les aimants supraconducteurs et hybrides sont principalement utilisés pour les champs magnétiques élevés dans les applications de RMN afin d'augmenter la séparation spectrale des molécules en raison de fréquences de résonance plus élevées et une magnétisation plus élevée, donc une intensité de signal plus élevé. Les électro-aimants doivent pour être alimenté en énergie. Par conséquent, pour les applications de faible puissance, les aimants permanents sont plus attractifs. Cependant, les aimants permanents présentent une faible homogénéité (paramètre critique) et leur force de champ est limitée. Mais ils sont compacts, peu coûteux et ne nécessitent aucun entretien. Alors malgré leur faible homogénéité intrinsèque, nous avons décidé d'étudier la possibilité de construire une structure magnétique utilisant des aimants permanents élémentaires pour notre spectromètre RMN portable.

Plusieurs aimants permanents élémentaires peuvent être combinés afin que leurs aimantations s'additionnent pour obtenir dans une région d'intérêt (ROI) donnée un champ magnétique assez homogène champ dont l'amplitude est supérieure à la magnétisation des aimants individuels. L'aimant L'arrangement proposé par Klaus Halbach en 1979 [7] est une structure composée d'un seul un matériau d'aimant permanent terrestre avec des domaines magnétiques individuel orientés en cercle. Cette configuration augmente le champ magnétique au centre tandis que en l'annulant à l'extérieur. Dans un premier temps, l'aimant, qui nécessite une ingénierie matérielle complexe pour être réalisé, n'a pas été construit pour la RMN. Cependant, en raison de l'homogénéité relative du champ en son centre, la structure de l'aimant de Halbach a été rapidement adoptée pour la RMN. Grâce à Raich et Blümer qui ont proposées une structure basée sur la disposition des aimants individuels comparable à celle réalisé par Halbach, il est maintenant largement utilisé pour sa mise en œuvre rapide et son prototypage rapide. Raich et Blümer ont appelé leur structure Mandhalas (Magnet Arrangement for Novel Discrete Halbach Layout), mais il est commun de le désigner sous le nom de structure de Halbach ou simplement aimant de Halbach. J'ai donc conçu un aimant visible sur la figure 5, en m'appuyant sur cette base afin d'observé la possibilité d'utiliser cette structure par la suite.

Les résultats de simulation ainsi que ceux obtenu après conception montre bien que l'aimant n'est pas utilisable en l'état mais présente un intérêt pour une future conception avec shimming actif ou passif.

Une autre étude vient alors compléter ce chapitre sur l'aimantation. En effet, il y a vingt ans, quelques publications ont fait état d'effets parasites sur les caractéristiques électriques des transistors à effet de champ [8,9]. Cependant, aucune explication satisfaisante n'a été donnée, et aucune recherche n'a été effectuée par la suite sur le sujet, certainement parce que les applications de ces champs élevés sont limitées. Il convient également de mentionner que de nombreuses publications ont fait état de des circuits qui fonctionnent comme prévu sous champ magnétique, en particulier sous des champs faibles ou modérés. Bien que l'on puisse

s'attendre à de faibles effets du champ magnétique sur les caractéristiques électriques des transistors MOS lorsqu'ils sont placés dans un champ proche de 1T, c'est-à-dire dans des magnitudes de champ dont nous avons affaire Nous avons étudié théoriquement et expérimentalement l'effet des champs magnétiques forts sur MOS afin de prévoir les écarts éventuels de leurs caractéristiques, ainsi que de quelle amplitude de champ ces déviations peuvent perturber le comportement du circuit. Il est démontré qu'une l'influence existe, et que son origine vient de la déviation des lignes de courant dans le transistor lorsque le canal détecte un champ magnétique hors du plan. Un modèle simple a été développé, et les mesures effectuées dans le cadre d'un champ de 7T ont démontré une réduction de la transconductance des transistors NMOS qui peut atteindre jusqu'à 7%. Cependant, sous des conditions de 1T, comme dans la RMN portable, l'influence du champ magnétique peut être négligée.

Figure 5: Image de l'aimant conçu avec son support PETG, et sa magnétisation en son centre mesuré par le magnétomètre WT10A.

4. Bobines de RMN

Les bobines sont utilisées pour transmettre l'impulsion de RMN B_1 afin de basculer le vecteur de magnétisation nucléaire $\vec{M}$, et aussi pour détecter l'aimantation transversale dans le plan xy, lorsque les noyaux présents dans l'échantillon pendant la relaxation. Habituellement, en RMN expérimentale, une bobine fait office de récepteur et d'émetteur, mais certaines conceptions intègrent deux bobines, l'une pour la réception et l'autre pour transmettre. Dans ce dernier cas, la bobine émettrice est régulièrement appelée "bobine Tx" car elle transmet (Tx) l'impulsion, et le récepteur (Rx) est connu sous le nom de "bobine Rx". Le but de la bobine émettrice est d'envoyer une impulsion RF pour basculer le vecteur de magnétisation vers l'angle souhaité. Par conséquent, la bobine devrait transmettre l'impulsion d'un générateur RF avec une efficacité maximale à la fréquence de Larmor. Une bobine RF a une fréquence spécifique à laquelle il fonctionne, et la plupart des bobines sont réglées pour un noyau spécifique. Le Carbone ou l'hydrogène sont principalement utilisés car ce sont deux noyaux abondants. Une source RF pulsée délivre le signal à un amplificateur de puissance qui fournit suffisamment de puissance à la bobine. Cependant, la bobine doit être réglé à la bonne fréquence de résonance et, si nécessaire, adapté pour éviter les réflexions de manière la

puissance maximale est transférée à la bobine (c'est-à-dire B_1 sans perte) puis à l'échantillon. Pour détecter la magnétisation transversale émise par l'échantillon pendant la relaxation, nous utilisons également une bobine en raison de sa faible résistivité, et donc de son faible bruit thermique, ainsi que la possibilité de régler à une fréquence spécifique, tout en profitant de son facteur de qualité et de son amplification passive. Il est possible de définir le champ de vision de la bobine comme le volume autour d'elle qui donne un signal non négligeable, c'est-à-dire un signal supérieur au niveau de bruit. De plus, le facteur de remplissage est défini comme le rapport entre le champ de vision de la bobine et le volume total de l'échantillon et un paramètre non négligeable d'une bobine.

Ce chapitre 4 présente ainsi les deux éléments clés de la tête de détection, c'est-à-dire la bobine et son ainsi que les paramètres qui définissent le rapport signal/bruit en RMN. Les différents types de bobines sont brièvement présentés, bobine volumique, planaire, microslot et stripline, avec un léger historique de leur conception ainsi que leur utilité habituelle. Nous en déduisons que lorsque les contraintes géométriques de la permettent d'utiliser des bobines volumétriques, la bobine solénoïdale est certainement le meilleur choix puisqu'il enveloppe l'échantillon, fournissant un facteur de remplissage de 100 %. Dans le cas contraire, ou la détection se ferait sur une surface, par exemple, une détection sur un animal ou dans un canal micro fluidique les bobines planes sont une bonne alternative. Ensuite, la nécessité d'utiliser un circuit d'accord/correspondance entre la bobine et l'entrée de la LNA fait l'objet d'une discussion approfondie avec plusieurs cas. Il est démontré que l'amplification passive qui se produit lorsque la bobine est adaptée et accordée à l'entrée LNA est limitée à une valeur relativement faible lorsque le LNA présente une impédance d'entrée finie, généralement RLNA = 50Ω. Dans ce cas un câble coaxial peut être utilisé pour éloigner le LNA de la bobine. Cependant, si le LNA peut être placé à proximité de la bobine, aucun câble coaxial n'est nécessaire et le meilleur choix est d'utiliser un LNA avec une impédance d'entrée infinie, qui fournit une amplification passive égale au facteur de qualité de la bobine. Dans ce cas, le circuit d'accord/adaptation devient un simple circuit d'accord capacitance. Comme il est montré dans le chapitre 3, le développement d'un aimant portable avec une homogénéité B_0 compatible pour l'acquisition de spectres RMN est possible mais nécessite éventuellement tout un travail de doctorat. Ainsi, il a été a décidé d'utiliser l'aimant d'un spectromètre RMN de banc commercial, le Magritek 60. En outre, en raison d'un long retard dans la livraison des puces et d'une erreur de conception qui a limité le nombre de de puces disponibles, comme nous le voyons dans le chapitre suivant, nous avons décidé de ne pas utiliser le récepteur intégré que j'ai conçu et fabriqué, mais de développer un récepteur discret à partir de composants du commerce afin de réaliser notre première acquisition de spectres RMN, et d'évaluer s'il est possible de détecter les polluants de l'eau avec un spectromètre RMN à faible coût. Ce chapitre présente le Magritek 60 utilisé, ainsi que le récepteur discret que nous avons mis au point et les premiers spectres acquis (un exemple figure 6).
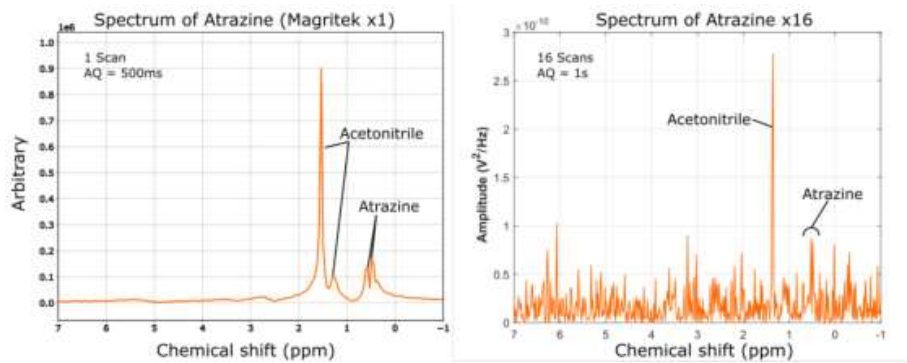
Figure 6: Spectre de l'acétonitrile avec atrazine, (a) sur le Magritek 60, (b) depuis la chaine de réception discrète.

5. Récepteur RMN discret

Dans ce chapitre 5, j'ai présenté l'aimant RMN du banc Magritek 60 que j'ai utilisé pour effectuer les acquisitions de spectre RMN avec le récepteur discret développé, visible sur la figure 7.
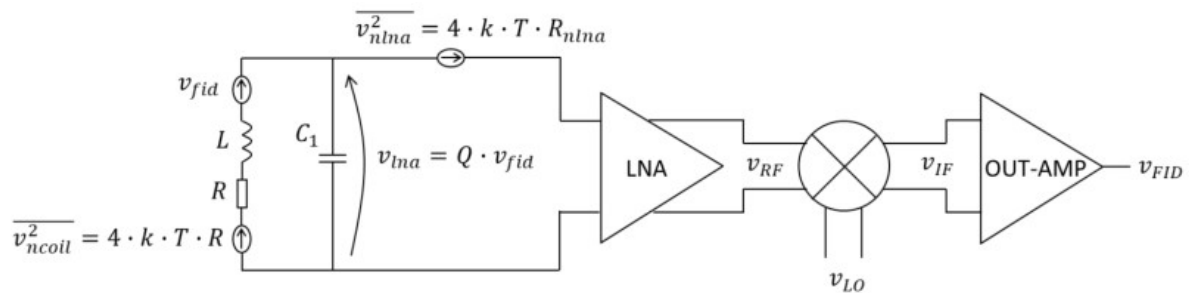

Figure 7:Recepteur intégré avec une bobine externe.

Les premiers positionnements des bobines afin de déterminer le bon placement dans le banc de mesure est présenté, puis le récepteur discret est décrit en détail, de sa conception aux différentes étapes de réalisation ainsi que ses principales caractéristiques électriques. Les bobines que j'ai développées sont également présentées, ainsi que la méthode utilisée, notamment l'impression 3D, pour les fabriquer et les maintenir sur le Magritek afin d'assurer une bonne répétabilité des nombreuses expériences réalisées. Je présente ensuite les résultats expérimentaux obtenus avec l'eau du robinet, l'éthanol, l'acétonitrile et enfin l'atrazine dans l'acétonitrile (Figure 6), en exposant les spectres obtenus avec le Magritek en comparaison des spectres obtenus par ma chaine discrète. Ces résultats préliminaires montrent qu'il devrait être possible de détecter facilement les polluants avec un simple spectromètre RMN portable, même si de nombreux développements doivent être faits avant de disposer d'un système "plug and play". Je montre dans la section 3 du chapitre 4 que l'utilisation d'un LNA à haute impédance d'entrée avec une bobine accordée à la fréquence de Larmor grâce à une capacité unique C1 en parallèle avec la bobine permet de prendre l'avantage du facteur de qualité Q de la bobine. Cela n'est possible que si le LNA peut être placé directement à la sortie de la bobine, et qu'aucune ligne de transmission n'est nécessaire pour relier la bobine au LNA. En effet, dans un tel cas, le signal inductif v_{fid} à la sortie de la

bobine est amplifiée passivement par le facteur α = Q lorsqu'il est captée à travers C1, c'est-à-dire à l'entrée de le LNA. Au contraire, l'utilisation d'un circuit de syntonisation/adaptation classique avec une transmission 50Ω pour connecter la bobine à une impédance d'entrée de 50Ω réduit α à q50/R/2, où R est la résistance des bobines. Cette α = Q amplification passive présente deux avantages principaux. Premièrement, l'ensemble de la chaîne d'amplification du récepteur peut être réduite à un seul LNA, et éventuellement à un amplificateur de sortie, mais ne nécessite pas trois amplificateurs en cascade comme nous l'avons fait dans le récepteur discret du chapitre 5. Cela simplifie la conception du récepteur et réduit la consommation d'énergie. Le deuxième avantage est que les contraintes de bruit pour la conception du réseau local sont considérablement réduites. Notant que R_{nlna} la résistance au bruit thermique équivalente du LNA par rapport à l'entrée du LNA, cette résistance au bruit est divisée par Q2 lorsqu'il est rapporté à la sortie de la bobine. Ainsi, la résistance équivalente au bruit thermique à la sortie de la bobine se lit :

$$R_{neq} = R + R_{nlna}/Q^2$$

Cependant, c'est R_{neq} qui détermine finalement le SNR du récepteur :

$$SNR = \frac{v_{fid}}{\sqrt{4 \cdot k \cdot T \cdot R_{neq}}}$$

En conséquence, le choix de $\frac{R_{nlna}}{Q^2} \ll R$, c'est-à-dire par exemple $\frac{R_{nlna}}{Q^2} = \frac{R}{10}$, fait que, pour présenter le meilleur rapport signal-bruit possible, qui est le rapport signal-bruit intrinsèque de la bobine nous avons :

$$SNR = \frac{v_{fid}}{\sqrt{4 \cdot k \cdot T \cdot (R + R/10)}} = SNR_{coil}$$

A titre d'exemple, en considérant une de mes bobines, celle appelé bobine d'époxy dont la résistance est R = 1.86Ω et le facteur de qualité est Q = 128, signifie que la conception d'un amplificateur bas-bruit (LNA) avec une résistance de bruit thermique de :

$$R_{nlna} = \frac{Q^2}{10} \cdot R = 3k\Omega$$

Cela est suffisant pour fournir au récepteur son meilleur rapport signal-bruit (SNR) possible. Ce bruit en résistance équivalente bruit thermique est très facile à obtenir en utilisant une technologie CMOS de base. Au contraire, pour les mêmes performances de bruit, un récepteur utilisant la bobine d'époxy accordé et adapté à une entrée 50Ω d'impédance LNA, exige une résistance au bruit thermique équivalente à celle du LNA :

$$R_{nlna} = \frac{\alpha^2}{10} \cdot R = \frac{\frac{50}{R}}{4 \cdot 10} \cdot R = 1.25\Omega$$

Une résistance de bruit thermique aussi faible est très difficile à obtenir, et nécessite de biaiser le LNA avec un courant très élevé. Cela peut rapidement entraîner une trop forte consommation d'énergie.

6. Récepteur intégré

Afin de démontrer une architecture possible d'un tel récepteur à haute impédance, j'ai conçu dans la technologie AMS CMOS 0,35μm à faible coût, le récepteur discret présenté par la suite. Il doit être noté que ce récepteur a été conçu avant le récepteur discret du chapitre 5. Il a été conçu afin de l'utiliser dans une première sonde RMN portable qui aurait été construite autour de l'Aimant de Halbach 0,7T présenté au chapitre 3. Cependant, en raison de la faible homogénéité de l'aimant de Halbach et du délai très long de livraison de la puce, nous avons décidé de réaliser le prototype qui a été utilisé pour nos premières expériences de RMN dans l'aimant Magritek. Le système intégré du récepteur devrait détecter le très petit signal RMN des polluants atrazine et glyphosate dans l'acétonitrile, son gain d'amplification, c'est-à-dire en excluant la contribution d'amplification Q, a été fixé à 63dB. Ce gain est partagé entre le LNA (26dB) et l'amplificateur de sortie (37dB), le mélangeur ayant un gain de 0dB. En outre, la contribution du bruit du récepteur a été rendue négligeable devant le bruit contribution de la bobine dont on a supposé un facteur Q supérieur à 100. L'intégration du circuit fabriqué comporte chaque sous-circuit séparément afin de valider leur conception et leurs principaux paramètres. Il comporte également une chaîne d'amplification complète. Dans ce chapitre, les architectures des trois sous-circuits sont tout d'abord examinées, et des résultats de simulation comparés aux mesures des principaux paramètres. Enfin, l'ensemble la chaîne d'amplification est caractérisée, et son utilisation possible au lieu du récepteur discret est présentée. Ce dernier chapitre présente ainsi le récepteur intégré que j'ai conçu et fabriqué dans la technologie CMOS AMS 0,35 μm. Il a été conçu avec une impédance d'entrée infinie pour prendre l'avantage du facteur de qualité de la bobine. L'architecture du récepteur est d'abord présentée, et la conception et la caractérisation expérimentale de ses trois sous-circuits, l'amplificateur à faible bruit, le Mixer et l'amplificateur de sortie sont discutés en détail. Enfin, l'ensemble du récepteur est caractérisé. Les résultats expérimentaux montrent que, combiné avec la bobine d'époxy utilisée dans le chapitre 5, ce récepteur intégré permet d'obtenir le meilleur rapport signal/bruit possible, c'est-à-dire le SNR intrinsèque de la bobine. Il ouvre ainsi la voie au développement d'un spectromètre RMN portable une fois qu'un aimant compact et homogène sera disponible.

7. Conclusion et prospectives

Viens alors la conclusion de cette thèse qui reprends les divers éléments clefs, ainsi qu'une prospective. En effet, Ces résultats préliminaires montrent qu'il devrait être possible de construire facilement un Spectromètre RMN pour détecter les polluants dans l'eau. Cependant, de nombreux autres développements technologiques sont encore nécessaires. Tout d'abord, une nouvelle puce CMOS doit être envoyée en fabrication. Cette nouvelle

fabrication permettra (i) d'améliorer l'architecture du récepteur, et (ii) de co-intégrer la capacité accordable nécessaire pour faire résonner la bobine à la fréquence de Larmor. De plus, puisque la puce sera à l'intérieur de l'aimant, nous pourrions ajouter un capteur thermique dans la puce pour détecter la température de l'aimant, et ajuster la fréquence de Larmor du récepteur à la variation B0 due aux effets thermiques. Un magnétomètre à effet Hall intégré pourrait également être utilisé à cette fin. Le deuxième développement technologique à aborder est l'émetteur. La réalisation d'impulsions RF peut se faire à l'aide d'un synthétiseur numérique direct (DDS) programmable. Une pré-étude a été réalisée par des étudiants en licence que j'ai supervisés, et ils ont pu démontrer la génération de RF non sélectifs des impulsions. Ce premier prototype de ce générateur programmable d'impulsions RF a également été étendu à des formes d'impulsions sélectives, bien que sa mise en œuvre physique ne soit pas encore terminée. Comme on l'a vu pour les la bobine de réception au chapitre 4, la bobine d'émission doit être accordée et adaptée à la sortie résistance de l'amplificateur de puissance qu'il est nécessaire de développer encore, et qui sera placé juste après le DDS pour fournir l'énergie à la bobine TX. Le dernier développement, qui est nécessaire, et qui est certainement le plus critique, est l'aimant qui doit avoir une très grande homogénéité de B0 sur le volume de l'échantillon, généralement plus d'un millimètre cube. Comme indiqué au chapitre 3, le tableau de Hallbach doit être homogénéisé (shimming). Ce shimming peut être effectué de manière passive, en utilisant des aimants soigneusement placés [10], ou activement avec des courants accordables dans des bobines de shimming [11]. Il est également intéressant d'examiner la possibilité d'utiliser des électro-aimants qui ont l'avantage et la possibilité de modifier la magnitude B0. Quoi qu'il en soit, nous espérons que ce travail de doctorat est un point de départ utile pour le développement de spectromètres RMN portables à faible coût pour la détection des polluants dans l'eau.

_____

Bibliographie :

[1] U. Holzgrabe, "Quantitative NMR spectroscopy in pharmaceutical applications," aug 2010.
[2] E. Zieminska, B. Toczylowska, D. Diamandakis, W. Hilgier, R. K. Filipkowski, R. Polowy, J. Orzel, M. Gorka, and J. W. Lazarewicz, "Glutamate, glutamine and GABA levels in rat brain measured using MRS, HPLC and NMR methods in study of two models of autism," Frontiers in Molecular Neuroscience, vol. 11, no. November, pp. 1–19, 2018.
[3] A. Kadjo, N. Baxan, A. Briguet, D. Graveron-Demilly, L. Fakri-Bouchet, R. Cespuglio, and C. Rousset, "In vivo animal NMR studies using implantable micro coil," in IST 2008 – IEEE Workshop on Imaging Systems and Techniques Proceedings, pp. 294–296, IEEE, 2008.
[4] Y. Liu, N. Sun, H. Lee, R. Weissleder, and D. Ham, "CMOS mini nuclear magnetic resonance system and its application to biomolecular sensing," in Digest of Technical Papers - IEEE International Solid-State Circuits Conference, vol. 51, I E E E, 2008.
[5] A. P. Sobolev, F. Thomas, J. Donarski, C. Ingallina, S. Circi, F. Cesare Marincola, D. Capitani, and L. Mannina, "Use of NMR applications to tackle future food fraud issues," 2019.
[6] M. de la Santé, "Bilan De La Qualite De L'Eau Au Robinet Du Consommateur Vis-a-Vis Des Pesticides En 2013," pp. 1–14, 2015.
[7] K. Halbach, "Design of permanent multipole magnets with oriented rare earth cobalt material," Nuclear Instruments and Methods, vol. 169, no. 1, pp. 1–10, 1980
[8] J. R. Bodart, B. M. Garcia, L. Phelps, N. S. Sullivan, W. G. Moulton, and P. Kuhns, "The effect of high magnetic fields on junction field effect transistor device performance," Review of Scientific Instruments, vol. 69, no. 1, pp. 319–320, 1998.
[9] P. Phothimat and M. Awipi, "Effect of high magnetic field on transistor characteristics with applications to SEU testing," in Conference Proceedings - IEEE SOUTHEASTCON, pp. 338–339, 1998.
[10] E. Danieli, J. Perlo, B. Blümich, and F. Casanova, "Small magnets for portable NMR spectrometers," Angewandte Chemie - International Edition, vol. 49, no. 24, pp. 4133–4135, 2010.
[11] G. Bringout and T. M. Buzug, "A robust and compact representation for magnetic fields in magnetic particle imaging," Biomedizinische Technik, vol. 59, no. 2, pp. S675–S678, 2014